

University of Alberta

Comprehensive study of the abrasive wear and slurry erosion behavior of an expanded system of high chromium cast iron and microstructural modification for enhanced wear resistance

by

Reinaldo Javier Chung

A thesis submitted to the Faculty of Graduate Studies and Research
in partial fulfillment of the requirements for the degree of

Doctor of Philosophy

in

Materials Engineering

Chemical and Materials Engineering

© Reinaldo J. Chung
Spring 2014
Edmonton, Alberta

DEDICATION

To my wife, Diana, who encourages and inspires me everyday making life the most beautiful journey. For her affection, patience, understanding, and companion of many hours, days and nights of work.

To my kids, Alana and Derek, for the many laughs that lighted up my days during the challenge of graduate school and work, while waiting patiently and joyfully for our time together.

To my parents, Marleny and Francisco, who taught me the value of knowledge and education, and to work hard for the things we want to achieve.

ABSTRACT

High chromium cast irons (HCCIs) have been demonstrated to be an effective material for a wide range of applications in aggressive environments, where resistances to abrasion, erosion and erosion-corrosion are required. For instance, machinery and facilities used in mining and extraction in Alberta's oil sands suffer from erosion and erosion-corrosion caused by silica-containing slurries, which create challenges for the reliability and maintenance of slurry pumping systems as well as other processing and handling equipment.

Considerable efforts have been made to determine and understand the relationship between microstructural features of the HCCIs and their wear performance, in order to guide the material selection and development for specific service conditions with optimal performance. The focus was previously put on a narrow group of compositions dictated by ASTM A532. However, with recent advances in casting technology, the HCCI compositional range can be significantly expanded, which potentially brings new alloys that can be superior to those which are currently employed.

This work consists of three main aspects of study. The first one is the investigation of an expanded system of white irons with their composition ranging from 1 to 6 wt.% C and 5 to 45 wt.% Cr, covering 53 alloys. This work has generated wear and corrosion maps and established correlation between the

performance and microstructural features for the alloys. The work was conducted in collaboration with the Materials Development Center of Weir Minerals in Australia, and the results have been collected in a database that is used by the company to guide materials selection for slurry pump components in Alberta oil sands and in other mining operations throughout the world. The second part consists of three case studies on effects of high chromium and high carbon, respectively, on the performance of the HCCIs. The third aspect is the development of an approach to enhance the wear resistance of HCCIs by microstructural modification through addition of strong carbide-forming elements to produce eutectic microstructures reinforced with in-situ formed foreign carbides. Very promising results have been obtained in lab, which demonstrates that the approach is feasible and effective in tailoring HCCIs for improved performance.

ACKNOWLEDGEMENT

To Dr. Dongyang Li, my supervisor and friend, who gaved me the opportunity to pursue my doctoral study. For his constant encouragement, guidance, insight, and advice.

To Xihu Tang, my colleague and research partner on this project, for his effort, teamwork, and numerous fruitful discussion and feedback.

To Weir Minerals, specially to Kevin Dolman and Brook Hinckley, for the opportunity to work in this project, sharing ideas, and all their support.

To Carmen Teran, my manager at Suncor, for her support and understanding on the completion of this thesis and in the beginning of my career in Oil Sands at Suncor Energy.

To Dr. Reginald Eadie, and Dr. Weixing Chen, the supervisory committee, for all their support, advice and valuable time.

To Dr. Leijun Li, Dr. Chong-Qing Ru, and Dr. Marcello Papini, the committee members, for their valuable time, expertise, and for kindly agreeing to serve on my committee.

To Lily Laser for her kindness, encouragement, and help from the beginning to the end of my studies.

To the instrument and machine shop technicians, specially to Walter Boddez, Richard Cooper, Clark Bicknell, Dave Parlin, and James McKinnon, for their endless support and assistance with the equipment maintenance and design.

TABLE OF CONTENTS

1	INTRODUCTION	1
1.1	Bibliography	6
2	LITERATURE REVIEW	9
2.1	Oil sands extraction overview	9
2.1.1	Oil sands characteristics	9
2.1.2	Overview of the oil sands extraction process	10
2.1.3	Typical wear resistant materials used in oil sands extraction	13
2.2	High chromium cast iron	15
2.2.1	Classification of high chromium cast irons	16
2.2.2	Effect of alloying elements on the high chromium cast irons	17
2.2.3	Microstructure of high chromium white irons	23
2.2.4	Heat treatment for HCCIs	28
2.2.5	Toughness and microstructure	30
2.3	Wear modes, mechanisms, and HCCI's performance	33
2.3.1	Sliding wear	33
2.3.2	Abrasive Wear	34
2.3.3	Slurry Erosion	37
2.4	Improving the performance of HCCIs	42
2.5	Bibliography	52
3	MICROSTRUCTURE/WEAR MAPPING – General behavior of HCCI.....	66
3.1	Experimental techniques	66
3.1.1	Alloy preparation	71
3.1.2	Microstructural characterization and micromechanical properties ...	71
3.1.3	Abrasion testing	72
3.1.4	Slurry erosion testing	75
3.1.5	Electrochemical testing	78
3.2	Microstructure.....	79
3.2.1	Microstructures that began solidification from primary austenite (γ).....	81
3.2.2	Microstructures that began solidification from primary ferrite ($\alpha\delta$)	83
3.2.3	Microstructures developed from primary M_7C_3 carbides	85
3.3	X-ray characterization	91
3.4	Phase microchemistry	93

3.5	Carbide volume fraction	100
3.6	Hardness	103
3.7	Wear behavior	105
3.7.1	Dry abrasion (three-body)	105
3.7.2	Slurry erosion	111
3.8	Corrosion behavior	121
3.9	Conclusions and recommendations.....	125
3.10	Bibliography	129
4	VARIATIONS IN MICROSTRUCTURE OF HIGH CHROMIUM CAST IRONS AND RESULTANT CHANGES IN RESISTANCE TO WEAR, CORROSION AND CORROSIVE WEAR	132
4.1	Experimental procedure.....	133
4.2	Results and discussion	136
4.2.1	X-Ray diffraction and SEM observation	136
4.2.2	Wear resistance	140
4.2.3	Corrosion rate and passivation behavior.....	142
4.2.4	Corrosive wear	147
4.3	Conclusions.....	149
4.4	Bibliography	150
5	MICROSTRUCTURE OF HIGH (45 WT%) CHROMIUM CAST IRONS AND THEIR RESISTANCE TO WEAR AND CORROSION.....	152
5.1	Experimental details.....	153
5.1.1	Materials	153
5.1.2	Characterization	153
5.1.3	Abrasive wear testing.....	154
5.1.4	Corrosion testing	154
5.1.5	Erosion-corrosion testing	155
5.2	Results and discussion	157
5.2.1	Microstructure and chemical analysis.....	157
5.2.2	Abrasive wear resistance of HCCIs	161
5.2.3	Corrosion resistance.....	164
5.2.4	Erosion-corrosion resistance of HCCIs	167
5.3	Conclusions.....	169
5.4	Bibliography	171

6	ABNORMAL EROSION – SLURRY VELOCITY RELATIONSHIP OF CHROMIUM CAST IRON WITH HIGH CARBON CONCENTRATIONS...	173
6.1	Experimental procedure	174
6.1.1	Sample preparation	174
6.1.2	Slurry erosion testing	175
6.1.3	Electrochemical testing	177
6.1.4	Characterization and mechanical properties	178
6.2	Results and discussion	179
6.2.1	Microstructure	179
6.2.2	Slurry erosion	185
6.2.3	Abnormal behaviour of hypereutectic alloys during slurry erosion	188
6.3	Conclusions	196
6.4	Bibliography	196
7	EFFECTS OF TITANIUM ADDITION ON MICROSTRUCTURE AND WEAR RESISTANCE OF HYPEREUTECTIC HIGH CHROMIUM CAST IRON FE-25WT.%CR-4WT.%C	198
7.1	Experimental details.....	199
7.2	Results and discussion	202
7.2.1	Microstructure and its variation with Ti addition	202
7.2.2	Effect of titanium on hardness and wear behaviour of the alloy	209
7.3	Conclusions	214
7.4	Bibliography	215
8	MICROSTRUCTURE REFINEMENT OF HYPEREUTECTIC HIGH CR CAST IRONS USING HARD CARBIDE-FORMING ELEMENTS FOR IMPROVED WEAR RESISTANCE.....	218
8.1	Experimental details.....	219
8.2	Results and discussion	222
8.2.1	Microstructure of the base HCCI Fe-25Wt.%Cr-4Wt.%C	222
8.2.2	Microstructure of the modified HCCI alloys with added carbide-forming elements	225
8.2.3	Effects of the carbide-forming elements on hardness and wear behavior of the modified HCCI series	240
8.3	Conclusions	246
8.4	Bibliography	247

9 OVERALL CONCLUSIONS, POSSIBLE FURTHER RESEARCH TOPICS, AND CONTRIBUTION	249
9.1 Conclusions	249
9.2 Further research topics	251

LIST OF TABLES

Table 2.1: HCCI classification according to ASTM A532.....	16
Table 2.2: Hardness of various carbides	20
Table 2.3: Invariant liquidus reactions in the Fe rich corner of the C-Cr-Fe system.	26
Table 2.4: Hardness of common minerals and various ferrous matrix phases. ...	43
Table 3.1: Actual chemical analysis of the cast plate samples produced.	68
Table 3.2: Summary of phases and crystallographic data encountered through X-ray diffraction patterns.	91
Table 3.3: Fracture toughness values of various samples and typical ranges for carbon steel and aluminum alloys.	112
Table 4.1: Corrosion potentials (CP, mV) of HCCIs in tap water and 0.5 mol/L H ₂ SO ₄ solution	143
Table 6.1: Chemical composition of cast irons under study.....	174
Table 6.2: Microhardness and volume fractions of microstructural components.	183
Table 7.1: Samples with titanium additions.....	200
Table 7.2: Melting and solidification conditions in the arc furnace.	200
Table 7.3: Microhardness of different phases present in the alloys.....	210
Table 8.1: Modified HCCI samples produced.	220
Table 8.2: Melting and solidification conditions (in an arc melting furnace). ...	221
Table 8.3: Microchemistry of phases in the base and eutectic HCCIs (without addition of other carbide-forming elements) determined by SEM-EDS, and their respective volume fractions.	225
Table 8.4: Microchemistry of V-HCCI phases determined by EDS, and their volume fractions.....	228

Table 8.5: Microchemistry of phases in Nb-HCCI determined by EDS and their volume fractions..... 232

Table 8.6: Microchemistry of the B-HCCI phases determined by EDS, and their respective volume fraction. 236

Table 8.7: Microchemistry of the Mo-HCCI phases determined by EDS, and their respective volume fraction. 239

LIST OF FIGURES

Figure 1.1: Average number of publications in high chromium cast irons per year - obtained through two major search databases.	3
Figure 1.2: Comparison of the typical commercial HCCIs and the expanded system proposed and studied.	4
Figure 2.1: Schematic representation of an oil sand particle.	9
Figure 2.2: Overview of the oil sands extraction process: (A) ore processing plant; (B) separation plant.	11
Figure 2.3: Overview of wear resistant materials used in oil sands extraction.	14
Figure 2.4: Effect of carbon content on impact toughness of a 15%Cr HCCI. ...	18
Figure 2.5: Fe rich corner of the C-Cr-Fe liquidus surface.	24
Figure 2.6: Relationship between the eutectic composition and the overall C and Cr content.	27
Figure 2.7: Typical heat treatment of high chromium alloys to produce the desired matrix without cracking.	28
Figure 2.8: Microstructure of a 27% Cr white cast iron: a) as cast; b) after destabilization.	29
Figure 2.9: Schematic of sliding wear.	34
Figure 2.10: Schematic of abrasive wear: (A) two-body; (B) three-body.	35
Figure 2.11: Schematic of abrasive wear mechanisms.	36
Figure 2.12: Schematic of solid particles erosion.	37
Figure 2.13: A HCCI worn impeller after 3 months of use in oil sands slurry pumps.	38
Figure 2.14: Platelets mechanism that controls the mass loss of an eroding surface. (A) formation of the platelets; (B) and (C) forging of the platelets by repeatedly impingements; (D) platelets just before being knocked off from the surface by particle impingement.	39

Figure 2.15: Schematic sequence for erosion.	40
Figure 3.1: Sample IDs for the expanded HCCI alloys produced for wear and corrosion mapping.	67
Figure 3.2: Particle size distribution of the Ottawa sand, AFS 50-70, used for dry abrasion tests.	73
Figure 3.3: Comparison of Ottawa Sand AFS 50–70 used for abrasion tests (left) with typical oil sands tailings solids (right)	74
Figure 3.4: Particle size distribution of the silica sand, AFS 12-50, used for slurry erosion tests.	76
Figure 3.5: A SEM micrograph of the silica sand used for the slurry erosion tests.	76
Figure 3.6: A schematic diagram of the slurry pot apparatus.	78
Figure 3.7: Iron rich corner of the metastable Fe-Cr-C liquidus surface showing the set of carbon and chromium compositions investigated in this work	80
Figure 3.8: Hypoeutectic microstructure of alloy 15-2, at two different magnifications, obtained through SEM backscattered. The resulting microstructure features primary austenite (γ) surrounded by eutectic precipitation of austenite (γ) and M_7C_3	82
Figure 3.9: Hypoeutectic microstructures of alloy 5-1 at two magnifications (SEM backscattered). The microstructure consists of primary austenite (γ) surrounded by eutectic precipitation of austenite (γ) and M_3C carbides.	83
Figure 3.10: Microstructure of alloy 15-1, at two different magnifications (SEM backscattered). The microstructure consists of peritectic formation of austenite (γ) and M_7C_3 carbides from the liquid- ferrite ($\alpha\delta$) reaction.	84
Figure 3.11: Microstructure of alloy 40-2, at two different magnifications (SEM backscattered). The resulting microstructure features primary ferrite ($\alpha\delta$) and eutectic $M_{23}C_6$ carbides.	85
Figure 3.12: Hypereutectic microstructure of alloy 25-4, at two different magnifications (SEM backscattered). The resulting microstructure features primary M_7C_3 carbides surrounded by eutectic colonies of austenite (γ) and M_7C_3	86

Figure 3.13: Hypereutectic microstructure of alloy 15-6, at two different magnifications (SEM backscattered). The resulting microstructure feature primary M_7C_3 carbide core with a peritectic M_3C carbide shell, surrounded by peritectic austenite (γ).....	87
Figure 3.14: Hypereutectic microstructure of alloy 45-4, at two different magnifications (SEM backscattered). The resulting microstructure features primary M_7C_3 carbide core with a peritectic $M_{23}C_6$ carbide shell, surrounded by peritectic austenite (γ) partially transformed to martensite after heat treatment.	88
Figure 3.15: Pseudo eutectic diagram for the 15 wt.% Cr series showing the liquidus and solidus lines obtained by the thermal analysis during solidification.	89
Figure 3.16: Microstructural evolution from a hypoeutectic, eutectic, and hypereutectic state of the 15 wt.% Cr series as carbon nominal composition increases from 1 to 6 wt.% C: (a) 1 wt.% C; (b) 2 wt.% C; (c) 3 wt.% C; (d) 4 wt.% C; (e) 5 wt.% C; (f) 6 wt.% C.....	90
Figure 3.17: X-ray diffraction patterns of various samples corresponding to distinct microstructural configurations presented in section 3.2.	92
Figure 3.18: Variations in the chromium content in M_7C_3 carbides with increasing chromium and carbon overall concentrations.	95
Figure 3.19: Variations in chromium content in the ferrous matrix with increasing chromium and carbon overall concentrations.	95
Figure 3.20: Chromium partition coefficient (K_{Cr}) as a function of nominal chromium composition for hypoeutectic, eutectic, and hypereutectic carbon series.	96
Figure 3.21: Variations in Manganese content in M_7C_3 with increasing chromium and carbon overall composition.	97
Figure 3.22: Variations in Manganese content in the ferrous matrix with increasing chromium and carbon overall composition.	98
Figure 3.23: Manganese partition coefficient (K_{Mn}) as a function of nominal chromium composition for various carbon compositional series.	98

Figure 3.24: Silicon content in the ferrous matrix with increasing chromium and carbon overall composition.....	99
Figure 3.25: Effects of carbon and chromium overall concentrations on the carbide volume content.	101
Figure 3.26: Comparison of measured carbide volume fraction with those predicted with an empirical equation proposed by Maratrays and one derived in this work (polygonal 2D).	102
Figure 3.27: Effects of carbon and chromium on bulk hardness of various compositional series studied.	104
Figure 3.28: Bulk hardness as a function of the carbide volume content for various chromium series featuring martensitic/retained austenite and ferritic matrix.....	104
Figure 3.29: Dry abrasion results (ASTM G65 Procedure A for various HCCI series.	105
Figure 3.30: Relation between the Cr/Fe ratio and micro-hardness of the primary M_7C_3 carbide.	107
Figure 3.31: Relationship between Cr/Fe ratio and micro-hardness of the ferrous matrix.	109
Figure 3.32: Abrasion performance as a function of bulk hardness.	110
Figure 3.33: Abrasion performance as a function of carbide volume fraction ...	110
Figure 3.34 Slurry erosion at low (15°), medium (45°), and high (90°) impingement angle for three different samples having near eutectic microstructures.....	112
Figure 3.35: SEM images of the worn surfaces of alloy 25-1, after slurry erosion in neutral slurry and 5 m/s slurry velocity, at different impingement angles: (a) 15°; (b) 45°; (c) 90°.	113
Figure 3.36: Slurry erosion weight loss as a function of overall C content for various Cr-series: (a) 45° impingement, 5 m/s; (b) 45° impingement, 6.5 m/s.....	115
Figure 3.37: Severe carbide fracturing under slurry erosion at 5 m/s, 45° impingement angle. Both micrographs show the same location on backscatter mode (left) and secondary electrons (right).	116

Figure 3.38: Typical slurry velocity – erosion behavior observed for most HCCI samples investigated.	117
Figure 3.39: An abnormal slurry velocity – erosion behavior observed for a subgroup of alloys featuring lower wear rates as the slurry velocity increased.	118
Figure 3.40: Comparison of the slurry erosion performance of hypoeutectic alloys featuring martensitic and ferritic matrixes.	119
Figure 3.41: Comparison of worn surfaces of two hypoeutectic samples featuring martensitic matrix (a) and ferritic matrix (b). SEM images after slurry erosion in pH=12 slurry, 5 m/s slurry velocity, 45°. pH=12 was used to suppress the corrosion effect and observe the pure mechanical damage.....	120
Figure 3.42: Comparison of dry abrasion (three-body) performance of hypoeutectic alloys featuring martensitic and ferritic matrixes.	120
Figure 3.43: Comparison of worn surfaces of two hypoeutectic samples featuring martensitic matrix (a) and ferritic matrix (b). SEM images after dry abrasion testing.....	121
Figure 3.44: Effect of overall carbon composition on polarization resistance for various chromium series.	123
Figure 3.45: Effect of overall chromium composition on polarization resistance for various carbon series.	124
Figure 3.46: SEM micrographs of the corroded surface after electrochemical testing in tap water: (a) 15-1 (b) 15-3; (c) 15-6.	125
Figure 4.1: Schematic illustration of the apparatus for corrosive wear tests	136
Figure 4.2: XRD patterns of as-casted HCCIs with different nominal carbon contents	137
Figure 4.3: SEM images of HCCIs specimens with different nominal carbon contents (A~F: 1, 2, 3, 4, 5 and 6 wt%)	138
Figure 4.4: The volume fraction of carbides in HCCIs with respect to the nominal carbon content.	139
Figure 4.5: Chemical compositions of the ferrous matrix of HCCIs	140

Figure 4.6: Effects of nominal carbon content on the wear resistance of HCCIs.	141
Figure 4.7: The corrosion rates of HCCIs in tap water (A) and 0.5 mol/L H ₂ SO ₄ solution (B)	143
Figure 4.8: Anodic polarization plots: (A) HCCIs in tap water; and (B) 0.5 mol/L H ₂ SO ₄	146
Figure 4.9: The corrosive wear resistance of HCCIs in tap water and 0.5 mol/L H ₂ SO ₄ solution	148
Figure 5.1: Schematic illustration of the slurry-pot erosion tester.....	156
Figure 5.2: Back-scattered Electron images of 45-series of HCCIs (A-F: with varied nominal carbon of 1, 2, 3, 4, 5 and 6wt%, respectively)	159
Figure 5.3: Volume fraction of total carbides in 45-series of HCCIs.....	159
Figure 5.4: XRD patterns of 45-series of HCCIs (A-F: with nominal carbon of 1, 2, 3, 4, 5 and 6wt%, respectively).....	160
Figure 5.5: Effects of nominal carbon on the wear resistance of 45-series of HCCIs	162
Figure 5.6: Micro-hardness of carbides and matrix in 45-series of HCCIs	163
Figure 5.7: Effects of nominal carbon on the corrosion resistance of 45-series of HCCIs in tap water at various pH levels.....	165
Figure 5.8: The measured overall concentration of chromium in 45-series of HCCIs and the free chromium in their ferrous matrix	166
Figure 5.9: Effects of nominal content of carbon on the erosion-corrosion resistance of 45-series of HCCIs in corrosive slurry at pH3, 5 and 7, respectively	167
Figure 6.1: Particle size distribution of the silica sand used for the slurry erosion testing.....	175
Figure 6.2: Schematic diagram of the slurry pot apparatus.	177

Figure 6.3: Back-scattered electron (BSE) micrographs of alloys being studied: A. 10-1; B. 10-3; C. 10-5; D. 15-1; E. 15-3; F. 15-6; G. 25-1; H. 25-3; I. 25-6.....	180
Figure 6.4: Liquidus projection of the Fe-Cr-C system in the Fe-rich corner.	181
Figure 6.5: X-ray diffraction patterns of the alloy series being studied.	183
Figure 6.6: EDX compositional mapping of the ferrous matrix of the three HCCIs with 25wt.%Cr. The colour intensities reflect the levels of chromium (green) and carbon (pink).....	184
Figure 6.7: Slurry erosion behaviour at four different slurry velocities for the alloys under study.	186
Figure 6.8: Comparison of slurry erosion performance of the three high carbon hypereutectic HCCIs at 2.5 m/s and 5 m/s in three different slurries: pH7, pH12 (adjusted with NaOH), and low dissolved oxygen (DO).....	190
Figure 6.9: Cyclic polarization results obtained for the 25wt.%Cr compositional series. (A) 25-1, pH7; (B) 25-3, pH7, (C) 25-6, pH7; (D) 25-1, pH12; (E) 25-3, pH12; (F) 25-6, pH12.	193
Figure 6.10: Effect of stirring on the cyclic polarization behavior of alloy 25-6.	194
Figure 6.11: Worn surface of alloy 25-6 after 2.5 m/s - slurry erosion testing at two different pH levels: (A) pH7; (B) pH12.....	194
Figure 6.12: Surface roughness of 15-1 and 15-6 as a function of the erosion time.	195
Figure 6.13: The compositional zone of HCCIs shown corresponds to high sensitivity to localized electrochemical attack at fluid velocities below 5 m/s in neutral slurries.....	195
Figure 7.1: Representative optical micrographs of ingots with different amounts of titanium addition: (a) 0 wt.% Ti; (b) 1 wt.% Ti; (c) 2 wt.% Ti; (d) 6 wt.% Ti.....	203
Figure 7.2: XRD diffraction patterns of the HCCI with: (a) no titanium addition, and (b) 6 wt.% Ti.	204

Figure 7.3: Representative backscatter images and EDS patterns of primary phases and TiC in some of the samples under study: (a) 0 wt.% Ti; (b) 2 wt.% Ti; (c) 6 wt.% Ti; (d) Hypoeutectic HCCI of Fe – 25 wt.% Cr – 2 wt.% C.....	205
Figure 7.4: An experimental phase diagram obtained through the collection of the thermal history of solidification of a variety of HCCI's	206
Figure 7.5: Volume fractions of primary phases and total carbides (primary and eutectic M_7C_3) in samples under study.	208
Figure 7.6: Changes in the bulk hardness and sliding wear volume loss of Fe - 25 wt.% Cr - 4 wt.% C with different amount of added titanium.....	212
Figure 8.1: (A) Backscatter SEM image of the base HCCI, Fe-25Wt.%Cr-4Wt.%C, consisting of needle-like coarse primary M_7C_3 carbides and a eutectic ferrous matrix; (B) Liquidus projection of the Fe-Cr-C system.	224
Figure 8.2: XRD diffraction pattern of the base HCCI, Fe-25Wt.%Cr-4Wt.%C, which contains M_7C_3 carbides and austenite.....	224
Figure 8.3: Microstructures of Vanadium added HCCI Series. (A) Sample V1 – Hypereutectic HCCI; (B) Sample V3 – Near-eutectic HCCI without distinguishable primary M_7C_3 carbides; Sample V4 – Hypoeutectic HCCI with fine carbides and a primary austenitic matrix.	226
Figure 8.4: (A) High magnification SEM (backscatter) micrograph of the near-eutectic V-HCCI sample (V3); (B) Representative diffraction patterns of samples V1 and V3.	227
Figure 8.5: High magnification EDS compositional mapping of the sample V3 showing the microstructural distribution of Fe (red), Cr (green), and V (blue).	228
Figure 8.6: Microstructures of the Niobium added HCCI Series. (A) Nb1 – Hypereutectic, (B) Nb3 – Near-eutectic HCCI without distinguishable primary M_7C_3 carbides., (C) Nb4 – Hypoeutectic HCCI consisting of austenitic matrix (γ) and fine NbC.....	230
Figure 8.7: (A) A high magnification SEM (backscatter) micrograph of the near-eutectic Nb-HCCI sample (Nb3); (B) Representative diffraction patterns of two Nb-HCCI alloys (Nb1 and Nb3).....	231

Figure 8.8: High magnification EDS compositional maps of sample Nb3 showing the distributions of Fe (red), Cr (green), and Nb (blue).....	232
Figure 8.9: Microstructure of the Boron added HCCI series. (A) B1 - Hypereutectic HCCI; (B) B3 - Hypereutectic HCCI with nucleated boride phase. (C) B4 - Hypereutectic HCCI featuring primary M_7C_3 and boride phase.	233
Figure 8.10: (A) High magnification SEM (backscatter) micrograph of sample B3; (B) Representative diffraction patterns of samples B1 and B3.....	235
Figure 8.11: High magnification EDS compositional maps of sample B3, showing distributions of Fe (red), Cr (green), and B (blue).	236
Figure 8.12: Microstructures of the Mo-added HCCI Series. (A) Mo1 – Hypereutectic HCCI; (B) Mo3 – Near-eutectic HCCI without distinguishable primary M_7C_3 carbides; (C) Mo4 – Hypoeutectic HCCI with a primary austenitic matrix.	237
Figure 8.13: (A) A high magnification SEM (backscatter) micrograph of sample Mo3; (B) Representative diffraction patterns of samples Mo1 and Mo3.	238
Figure 8.14: High magnification EDS compositional maps of sample Mo3 showing the microstructural distribution of Fe (red), Cr (green), and Mo (blue).	239
Figure 8.15: Bulk hardness measurements obtained for the modified HCCI alloys series being studied.	241
Figure 8.16: Pin-on-disc test results for the modified HCCI alloys under study as a function of the concentration of equivalent carbon, estimated based on the amount of added carbide-forming element.	243
Figure 8.17: Worn surfaces of the modified HCCI samples. (A) Mo-HCCI sample Mo3; (B) B-HCCI sample B4; (C) V-HCCI sample V3; (D) Nb-HCCI sample Nb3. Features are indicated as: micro-cracking (arrow); V (voids), delamination (D), micro-fatigue (F) and plowing (P).....	245

1 INTRODUCTION

Wear is the most predominant and aggressive failure mechanism for material loss in the Alberta Oil Sands surface mining operation. The extreme wear conditions result from the abrasive nature and large quantities of silica sand contained in the oil sands deposits being mined, transported and processed [1-3]. This has been a great challenge for the reliability and maintenance of machinery and equipment that typically have short lifecycles [4]. In addition to these already demanding conditions, the process has gradually become more corrosive and consequently the synergistic damage from the combined mechanical and chemical interaction. Synergistic erosion and corrosion is now a dominant wear mechanism in bitumen extraction. The increasing corrosivity of oil sands slurry is attributed to oxygen saturation at higher operating pressures (longer piping distances), and accumulation of chlorides and other salts in the process recycle water as less fresh water intake is used in order to reduce the environmental impact [5, 6].

In extraction, the main areas of concern involve slurry pump components, slurry pipelines, and breaker screens. These are within the highest cost maintenance items for oil sands operators, where annual budgets for maintenance and repairs can exceed \$450 million per year [4]. Slurry pump lifespan ranges from three to nine months while piping components life varies between 6 months to 4 years, depending on rotations, materials, components, and operating conditions [6].

High chromium white irons (HCCIs) have been used extensively in slurry pump components such as in casing and impellers, in piping components exposed to high wear such as bends, elbows and reducers, and also in breaker screens, wear liners, nozzle inserts, cyclofeeders, and cyclones [1, 2, 4, 5, 7-10]. They generally feature chemical compositions ranging from 12 to 27 wt.%Cr and 2.4 to 3.6 wt.%C, with those two elements comprising the principal alloying additions [1]. They are classified according to ASTM A532/532M “Standard Specification for Abrasion-Resistant Cast Irons” or their equivalent in other international standards.

The first patent of HCCIs was filed by Becket in 1917 covering the 25-30 wt.% Cr, 1.5-3 wt.% C and 3wt.% Si (maximum). Among these alloys, the 27 wt.% Cr - 2.75 wt.%C was considered to be the most important [8]. Since then, HCCIs have been an important engineering material in a wide range of industries including hard rock mining, minerals and chemical processing, paper, sugar cane, and hot rolling mill work [11-13]. Ninety years later they are still widely used and there have been considerable efforts made to continuously improve their wear and corrosion performance and to better understand microstructural features that fundamentally determine the performance of the alloys under distinctive operating conditions [14-18]. This includes not only their cast products, but also hard facing weld overlays that are extensively used to protect assets against wear [8, 19].

Figure 1.1 shows an average number of publications under “high chromium cast irons” since 1990 from two important search databases. Even though this search may not account for all technical journals, proceedings, and local publications, it is still evident that HCCIs is an important industrial R&D topic and have gained greater popularity in recent years. Related investigations are conducted by research groups from academia, government institutes, and industry worldwide.

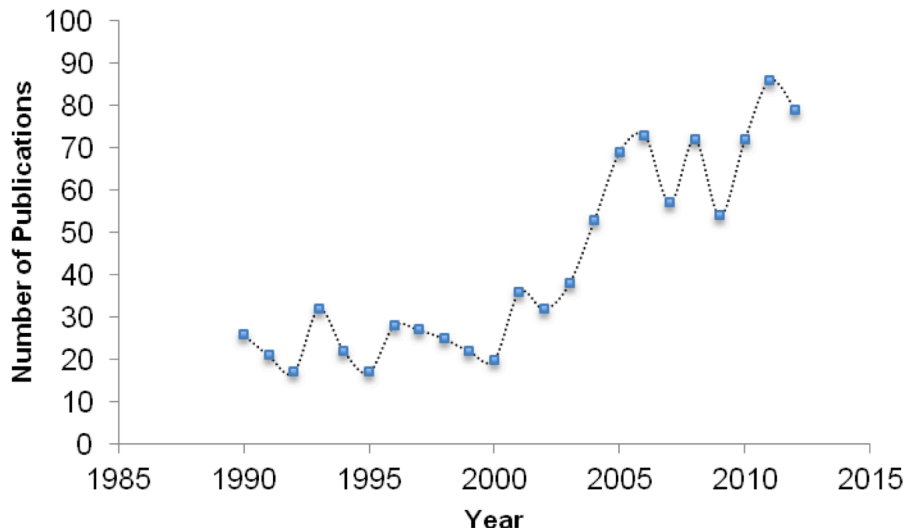


Figure 1.1: Average number of publications on high chromium cast irons per year - obtained through two major search databases.

Recent development of casting technology by Weir Minerals, an Australian manufacturer of cast irons, has made it possible to considerably expand the compositional range of white cast irons for a large scale production, as depicted in figure 1.2. In particular, concentrations of the carbon and chromium

can be extended to considerably higher levels, levels at which high reject and scrap rates limited their production in the past [1]. The wear behavior of the expanded compositional range of HCCIs and its correlation with microstructure are however not fully understood, although experimentally the expansion has been demonstrated to be very promising. It is thus of great interest for the industry to better understand mechanisms to permit effective guidance in both material selection for specific services and R&D efforts on tailoring existing HCCIs for further improvement in anti-wear performance. Understanding the microstructure-property relationship and identifying effective approaches for material improvement are main objectives of this thesis research.

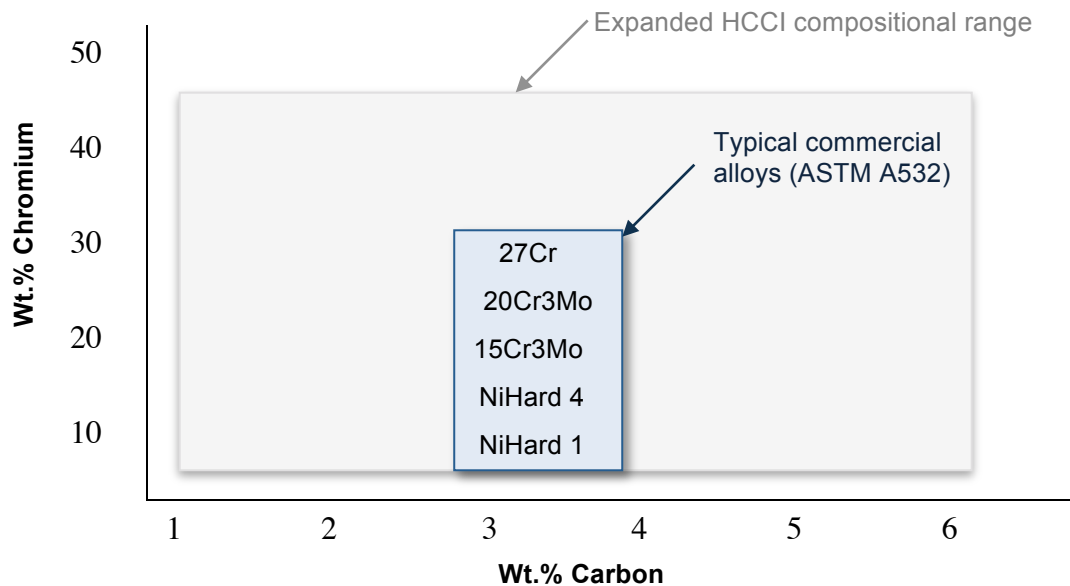


Figure 1.2: Comparison of the carbon and chromium typical content in commercial HCCIs and the expanded system proposed and studied in this work.

This thesis comprises three areas of study which are organized in the following structure:

Chapter one presents a brief introduction to wear in oil sands operation, their economic importance, and the use of HCCIs as one of the materials of choice to withstand the extreme and diverse conditions in which they operate. Chapter two provides a brief review of the bitumen extraction process in the oil sands industry and relevant wear issues, and introduces the high chromium cast irons with the most relevant literature.

Chapter three reports the development of wear mapping for the extended HCCI compositional range and correlation with their microstructural features. This work was conducted in collaboration with the Materials Development Center of Weir Minerals in Australia, and the results have been prepared in a database that is currently used by the company to aid the materials selection for slurry pump components used in the Alberta oil sands and in other mining operation throughout the world. Chapter four reports studies on the general erosion-corrosion behavior of HCCIs through the 30 wt.% Cr alloy series, which has attracted attention in oil sands in recent years. Chapters five and six present two case studies focused on the particular wear and corrosive wear behavior of the new HCCIs with high chromium (45wt.%) and high carbon (5~6wt.%) respectively. Based on the understanding of the entire HCCI system, chapter seven presents an approach for further improving their wear resistance by microstructural refinement through controlled additions of hard carbide-forming

elements to produce near-eutectic reinforced structures, which has shown promising results in lab testing and may lead to an step change in performance.

Finally, chapter eight presents an overall summary of the wear behavior of the expanded HCCI system, the influence of the principal alloying elements and microstructural characteristics, and the developed approach for microstructural refinement through in-situ formation of reinforcement carbides yielding eutectic microstructures.

1.1 Bibliography

1. Llewellyn, R.J., S.K. Yick, and K.F. Dolman, *Scouring erosion resistance of metallic materials used in slurry pump service*. *Wear*, 2004. **256**(6): p. 592-599.
2. Llewellyn, R., *Resisting wear attack in oil sands mining and processing*. *Cim Bulletin*, 1997. **90**(1012): p. 75-82.
3. J. Llewellyn, R.A.H., Robert; Du, JunRong, *Assessment of Materials for Gouging Abrasion Applications*. NRC Publications Archive (NPArc).
4. M. Anderson, S.C., and S. Hoskins, *Improving reliability and productivity at Syncrude Canada Ltd. through materials research: past, present, and future*, in *CIM Bulletin*. 2004.
5. Jones, M. and R.J. Llewellyn, *Erosion-corrosion assessment of materials for use in the resources industry*. *Wear*, 2009. **267**(11): p. 2003-2009.
6. Parent, L.L. and D.Y. Li, *Wear of hydrotransport lines in Athabasca oil sands*. *Wear*, 2013. **301**(1-2): p. 477-482.

7. Demello, J.D.B., M. Durandcharre, and S. Hamarthibault, *Solidification and solid-state transformations during cooling of chromium-molybdenum white cast irons*. Metallurgical Transactions A-Physical Metallurgy and Materials Science, 1983. **14**(9): p. 1793-1801.
8. Hinckley, B., et al., *Sem investigation of heat treated high-chromium cast irons*. Materials Forum, 2007. **32**: p. 55-71.
9. Tian, H.H., G.R. Addie, and K.V. Pagalthivarathi, *Determination of wear coefficients for erosive wear prediction through Coriolis wear testing*. Wear, 2005. **259**(1-6): p. 160-170.
10. Tabrett, C.P., I.R. Sare, and M.R. Ghomashchi, *Microstructure-property relationships in high chromium white iron alloys*. International Materials Reviews, 1996. **41**(2): p. 59-82.
11. Hanlon, D.N., W.M. Rainforth, and C.M. Sellars, *The rolling/sliding wear response of conventionally processed and spray formed high chromium content cast iron at ambient and elevated temperature*. Wear, 1999. **225**: p. 587-599.
12. Farah, A.F., O.R. Crnkovic, and L.C.F. Canale, *Heat treatment in high Cr white cast iron Nb alloy*. Journal of Materials Engineering and Performance, 2001. **10**(1): p. 42-45.
13. Zumelzu, E., et al., *Microstructural characteristics and corrosion behaviour of high-chromium cast iron alloys in sugar media*. Protection of Metals, 2003. **39**(2): p. 183-188.
14. Bedolla-Jacuinde, A., S.L. Aguilar, and B. Hernandez, *Eutectic modification in a low-chromium white cast iron by a mixture of titanium, rare earths, and bismuth: I. Effect on microstructure*. Journal of Materials Engineering and Performance, 2005. **14**(2): p. 149-157.
15. Laird, G. and G.L.F. Powell, *Solidification and solid-state transformation mechanisms in Si alloyed high-chromium white cast irons*. Metallurgical Transactions A, 1993. **24**(4): p. 981-988.
16. Dogan, O.N. and J.A. Hawk, *Effect of carbide orientation on abrasion of high Cr white cast-iron*. Wear, 1995. **189**(1-2): p. 136-142.

17. Eiselstein, L.E., O.A. Ruano, and O.D. Sherby, *Structural characterization of rapidly solidified white cast-iron powders*. Journal of Materials Science, 1983. **18**(2): p. 483-492.
18. Ikeda, M., et al., *Effect of molybdenum addition on solidification structure, mechanical-properties and wear resistivity of high chromium cast irons*. Isij International, 1992. **32**(11): p. 1157-1162.
19. Llewellyn, R. and C. Tuite, *Hardfacing fights wear in oil sands operation*. Welding Journal, 1995. **74**(3): p. 55-60.

2 LITERATURE REVIEW

This chapter is divided into three sections. The first part provides a brief review of the bitumen extraction process in oil sands operation and the wear resistant materials currently use. The second part consists of a review of the most relevant literature in HCCIs, microstructure and properties. The last section provides a review of the wear phenomena, different mechanisms, and HCCI wear performance.

2.1 Oil sands extraction overview

2.1.1 Oil sands characteristics

Oil sand consists of a mixture of sand covered by two layers: salty water and bitumen, as depicted by figure 2.1 The two layers make up near 16% (by weight) depending on the quality of the ore [1]. As the water is transported to the ponds in the tailing slurry, and then reused as cold and hot process water, the chloride content of the water layer is an important parameter that is monitored due to the direct effect on the corrosivity of the water and therefore reliability of equipment. The pond recycle water ranges from 400 to 1,000 mg/L of chlorides and has been steadily increasing over the years.



Figure 2.1: Schematic representation of an oil sand particle [1].

The mineral particle size distribution is typically reported as the D_{50} and in some cases D_{80} . They represent the particle sizes at which 50% and 80% of solids by weight pass that sieve opening size, respectively [2]. A typical D_{50} content is near 180 μm [1, 3]. Other oil sand characteristic includes the fine content (particles $< 40 \mu\text{m}$), clay content, and coarse solids content. The settling rate in the slurry is an important process factor that has to be maintained lower than the flow velocity in the pipe, otherwise sanding (or setting of the solids) will occur. Certainly the particle size distribution and their angularity are critical factors in the wear of components and material response. Even though the morphology of the sand particles change from batch to batch, a mixture of rounded and angular distributions has been reported with a D_{50} mostly maintained below 210 μm to avoid setting of the coarse sand in the pipe [3-5].

2.1.2 Overview of the oil sands extraction process

The oil sands extraction process separates the bitumen from the sand. This is carried out throughout a number of sub-processes typically handled in different plants, as depicted by figure 2.2(A) for the ore preparation and by figure 2.2(B) for the bitumen separation. In principle they are simple, but it becomes a challenge due to the large amount of material being processed and the resultant rapid thickness loss of equipment due to wear and corrosion. Because of this, several lines or production trains are used, each requiring other support lines such as air, steam, and process and seal water.

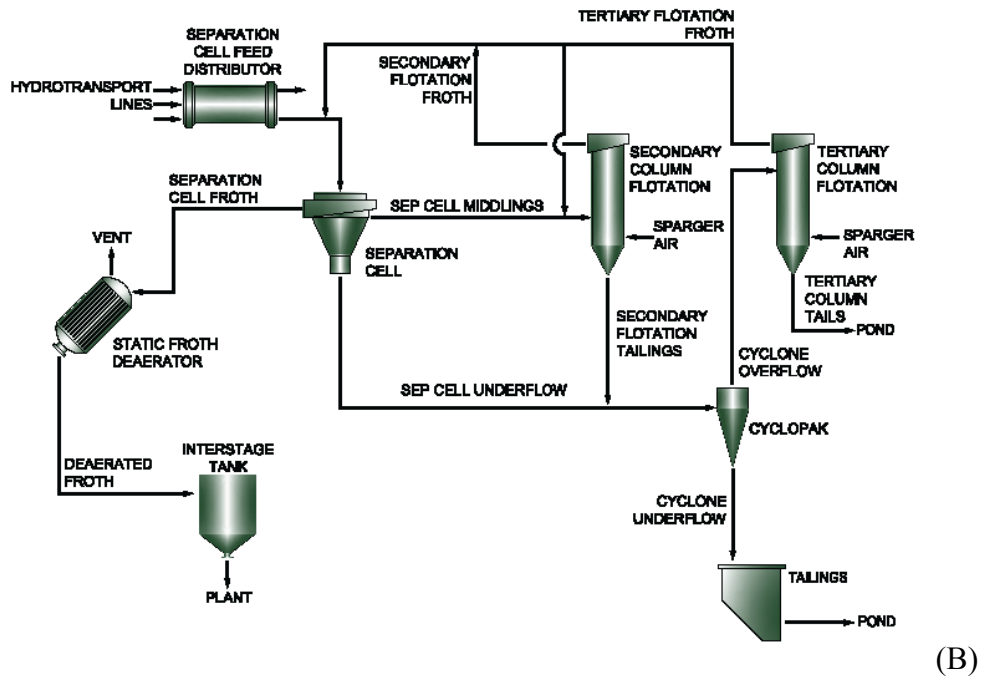
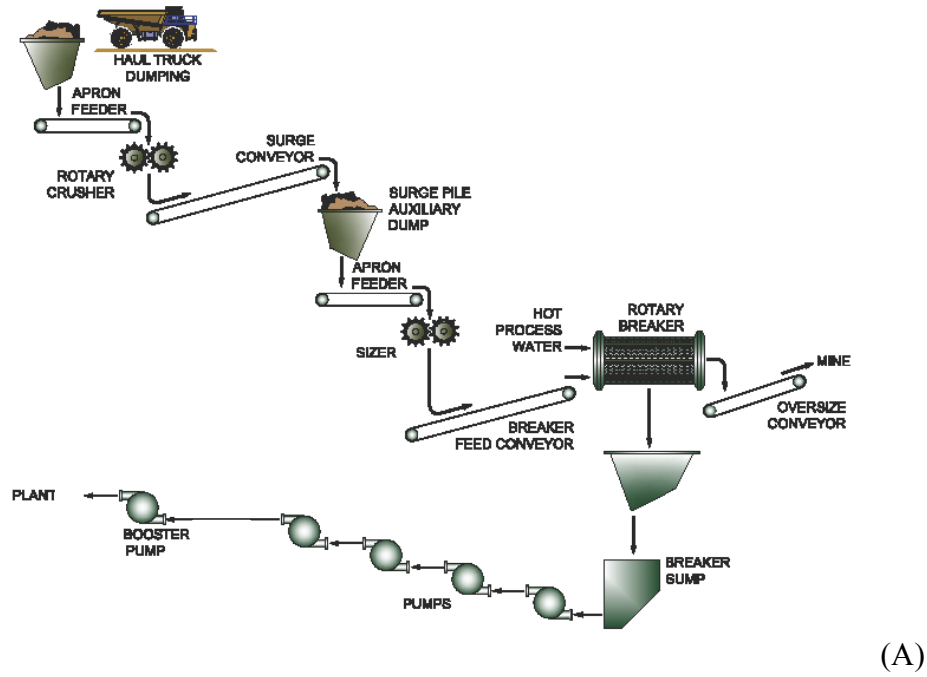


Figure 2.2: Overview of the oil sands extraction process [1]: (A) ore processing plant; (B) separation plant.

The extraction process begins at the feed hoppers where the mined oil sand is dumped by trucks and then transported through a system of apron feeders and conveyor belts. In order to reduce the oil sand particle size, rotary crushers and sizers are used in the process before slurring in the rotary breakers by addition of hot process water (60-95°C) and chemicals (if used). The slurry that passes through the breaker screens - opening size ranging from 2 to 6 in. - is collected into sumps or pump boxes where is pumped to the separation plants through kilometers of hydro transport pipelines. Multiple centrifugal pumps connected in series are often required to transport the slurry, and depending on distance and elevation, booster pump stations are utilized partway through the lines [1, 3, 6].

The slurry feed from the hydrotransport lines is processed in the primary separation cells, where about 80% of the bitumen is recovered as it floats off the top of the cell as froth. The froth layer contains near 23wt.% water and 12 wt.% fine mineral (approximately, depends on operator). The air content of the froth is reduced in static deaerators before being transported for downstream removal of water and minerals (i.e. sand and fines) [1]. Most of the remaining bitumen is recovered by secondary separation loops from another stream off the primary separation cell called middlings, which is located under the froth layer where the slurry does not have enough air content or is attached to fine minerals which prevents it from floating to the froth layer. The recovered bitumen from the secondary separation cell floats off the top as froth and is pumped back into the

primary separation cell feed [1]. The tails from the secondary column flotation may be processed through tertiary flotation cells to increase the bitumen recovery before all the under flow tailings are collected in sumps and pumped to tailings ponds by centrifugal slurry pumps [1, 6].

When tertiary flotation columns or cells are utilized, cyclopacks may be used upstream to force separation of heavy material (i.e. sand) by spinning the slurry so the heavy material is pushed to the sides and lighter material such as clays, water, and bitumen flow to the center and leave at the top as overflow. All tailings are collected in pump boxes and finally transported to the ponds.

2.1.3 Typical wear resistant materials used in oil sands extraction

White iron in its different forms (cast products, overlays, and bimetallics) is extensively used to extend the lifespan of components being severely exposed to slurry erosion and abrasion throughout the oil sands extraction process.

The following figure provide an overview of the typical wear resistant materials used in extraction, which shows the importance of white iron related products and their massive used in oil sands. Domite is the trade name of a commercial HCCI and CCO refers to iron based chromium carbide overlays which are all HCCI in its weld overlay form.

Ore Processing Plants (OPP)				
		Equipment	Component/Location	Material
1		Dump Hopper	Body	Carbon steel
			Interior Lining	Domite/400 BHN Plate
2		Grizzly Sizer	Frame	Carbon Steel
			Screen	CCO Plate
3		Apron Feeders	Return Rollers	Neoprene impact rollers
			Carrying Rollers	D11 CAT
			Pans (Flights)	TSE 355 Steel
4		Rotary Crusher/Sizer	Liner	CCO
			Segments / Ring Caps	AISI 4325 Modified*
			Teeth	WC Cladding
5		Feed Conveyor	Head Pulley (Shell)	ASTM A516 - GR50 Steel
			Head Pulley (Disc)	ASTM A148-90/60 Casting
			Conveyor Belt	Rubber embedded steel cable
			Lagging (Head, Feed & Reclaim)	Neoprene ACR 4254
			Lagging (Head, Stacking)	Polyurethane CP3400
			Lagging (Tail)	Polyurethane CP3400
6		Surge Pile Auxiliary Dump	Body	A36/44W Carbon Steel
			Liner	Domite
7		Rotary Breaker	Breaker Frame	AISI 1018 / ASTM 572 Gr. 50
			Screen Frame	CS w/400 BHN liners
			Screen Plates	400 BHN CS / WI Blocks / CCO / WCO
			Feed End Paddles	Carbon Steel / 400 BHN / Domite
			Trunnion Roller	1070-1080 CS
			Lifters	400 BHN
8		Product Chutes	Body	A36/44W Carbon Steel
			Interior Lining	Rock Box / CCO & WCO
9		Breaker Pump Box	Body	A36/44W Carbon Steel
			Interior Lining	CCO Bottom / Stainless Steel 304
10		Transport Lines	Material	API 5L Gr. B
			Interior Lining	CCO
11		Slurry Pump	Casing	ASTM A532 CL.III Typ-A
			Lining	ASTM A532 CL.III Typ-A
			Shaft	4150S
			Shaft Sleeve	WC Cladding
			Impeller	ASTM A532 CL.III Typ-A

Separation Plants				
		Equipment	Component/Location	Material
1		Separation Cell	Body	G40.21-38W
			Interior Lining at Outlet Nozzle	CCO
			Nozzle	WI Insert
2		Froth Line	Material	Carbon Steel
			Liner	-
3		Middlings Line	Body	Carbon Steel
			Interior Lining	Neoprene VN72
4		Tails Pumps	Casing	ASTM A532 CL.III Typ-A
			Shaft	AISI 4150
			Impeller	ASTM A532 CL.III Typ-A
5		Cyclone	Cone Body	WI 600BHN
			Apex	WI 600BHN
6		Cyclone Overflow Piping	Material	ASTM A53 Gr.B, ERW
			Interior Lining	Neoprene VN72
7		Cyclone Underflow Piping	Material	API 5L Gr BM
			Interior Lining	CCO
8		Scavenger Banks / Secondary Flotation Cells	Body	Carbon Steel
			Liner	304 Stainless Steel
			Agitator	Rubber Coated
			Dart Valve	Solid Rubber
9		Scavenger Banks / Tertiary Flotation	Body	Carbon Steel
			Liner	304 Stainless Steel
			Agitator	Rubber Coated
			Dart Valve	Solid Rubber
10		Tailings Pump Box	Body	Carbon Steel
			Liner	CCO at bottom & Stainless Steel 304 up to above liquid line
			Outlet Nozzle	WI Insert
11		Froth Pump Box	Casing	A36/44W Carbon Steel
			Liner	CCO at bottom
			Outlet Nozzle	CCO
12		Offset Pipes Between Tails Pumps	Material	Neoprene VN72 Hose
13		Tails Pipe	Body	API 5L Gr. BM
			Liner	CCO Lined

Figure 2.3: Overview of wear resistant materials used in oil sands extraction.

As it can be seen in figure 2.3, white iron is used as plate and overlay in hoppers, chutes, screens, pumpboxes, and sizers/crushers case liners; also white iron castings are the materials of choice in slurry pump casing and impellers, in piping sleeves and nozzles inserts, and in centrifugal cast bimetallic pipe. For instance, slurry pumps are known to be one of the largest maintenance cost item in extraction. Mostly the cast white iron used fall within 2.4 to 3.6 wt.% C and 25 to 27 wt.% Cr, while the overlays extends the carbon content to 5wt.% C. For dry applications white iron plate liners generally feature 15 to 20 wt.% Cr with carbon below 3.7 wt.% and molybdenum between 2.5 to 3 wt.%

2.2 High chromium cast iron

High chromium cast iron (HCCI) is a type of white iron. The word “white” has been historically used to define such cast irons that have two distinct characteristics: 1) fracture surface appears to have a white color as it occurs along the carbide phase; and 2) there is no graphite as all the carbon is tied up as carbide and in the ferrous matrix phase [7-9]. HCCI features the highest Cr content in the high-alloy white cast iron alloys, which gives them an excellent hardenability, wear and corrosive wear resistance even at high temperature while maintaining toughness to withstand impact during the wear process. These type of alloys are therefore recognized as to have the best combination of toughness and abrasion resistance attainable among the white irons [7, 10].

2.2.1 Classification of high chromium cast irons

The HCCIs are classified into Class II and III by ASTM A532/A532M-10 according to their chemical composition and hardness requirement, as listed in table 2.1.

Table 2.1: HCCI classification according to ASTM A532 [7].

Class	Type	Hardness (HB)	Composition (Wt.%)					
			Cr	C	Mn (max)	Si (max)	Ni (max)	Mo (max)
I	A	550-600	1.4-4.0	3.0-3.6	1.3	0.8	3.3-5.0	1
I	B	550-600	1.4-4.0	2.5-3.0	1.3	0.8	3.3-5.0	1
I	C	550-600	1.1-1.5	2.9-3.7	1.3	0.8	2.7-4.0	1
I	D	400-600	7.0-11.0	2.5-3.6	1.3	1.0-2.2	5.0-7.0	1
II	A	400-600	11.0-14.0	2.4-2.8	0.5-1.5	1	0.5	0.5-1.0
II	B	400-600	14.0-18.0	2.4-2.8	0.5-1.5	1	0.5	1.0-3.0
II	C	400-600	14.0-18.0	2.8-3.6	0.5-1.5	1	0.5	2.3-3.5
II	D	400-600	18.0-23.0	2.0-2.6	0.5-1.5	1	1.5	1.5
II	E	400-600	18.0-23.0	2.6-3.2	0.5-1.5	1	1.5	1.0-2.0
III	A	400-600	23.0-28.0	2.3-3.0	0.5-1.5	1	1.5	1.5

The class II refers to chromium-molybdenum irons containing 11 to 23 wt.% Cr and up to 3 wt.% Mo. They are considered the hardest of all grades of white irons and can be heat treated to reach their maximum abrasion resistance and toughness. The class III of HCCIs are widely used for general purpose and when

certain corrosion resistance is required. The chromium composition is typically between 25 wt.% and 28 wt.% with up to 1.5 wt.% Mo [7, 11, 12].

Other standards such as the international ISO 21988 maintain a similar classification but have adopted wider compositional range with chromium ranging from 11 to 40 wt.% and carbon from 1.8 to 3.6 wt.% except for the 30 to 40 wt.%Cr designation that allows up to 5.5 wt.% C. The expansion on the HCCI compositional range has been driven by improvement in foundry technology that has made it technically and economically viable [4, 13].

2.2.2 Effect of alloying elements on the high chromium cast irons

2.2.2.1 *Carbon*

Carbon is the main responsible for increasing hardness and to some extent wear resistance. As the carbon content is increased, the volume fraction of carbides in the HCCI microstructure increases rapidly having a more prominent effect than any of the other alloying elements. The increase on the carbide volume fraction is at the expense of the fracture toughness, and hardenability, making the HCCI more brittle. The relationship between impact toughness and carbon for a 15 wt.%Cr HCCI is shown in figure 2.4 [14].

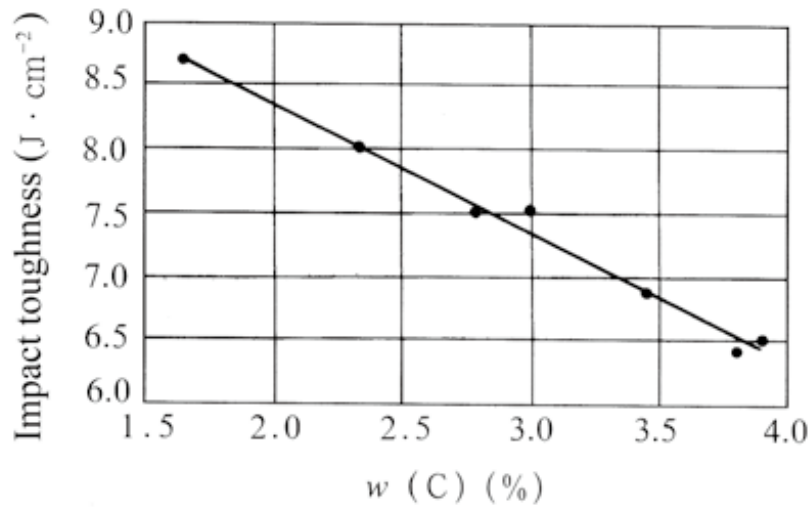


Figure 2.4: Effect of carbon content on impact toughness of a 15%Cr HCCI [14].

2.2.2.2 Chromium

Even though chromium is fundamental in HCCIs, its effect on hardness and wear resistance is less pronounced than carbon. The addition of chromium reduces the graphitization potential due to the higher tendency of formation of chromium carbides (large negative free energy Gibbs) and consequently producing a ferrous matrix-carbide microstructure characteristic of white irons [7, 9]. The chromium mostly reacts with carbon to form carbides and also partitions into the ferrous matrix where it can provide passivation capability to the HCCIs [15, 16]. Only 16 wt.% Cr in the ferrous phase has been found to be sufficient to develop an stable and sound passive oxide layer of a $\text{FeO} \cdot \text{Cr}_2\text{O}_3$ type on the matrix surface proving good corrosion resistance for aqueous environments such as in slurry erosion[16]. The chromium also helps stabilizing the microstructure at

high temperature and consequently maintaining its wear resistance [17-20]. It has been found that chromium strengthens both the carbide phase and the matrix.

In HCCIs, carbon and chromium are the more important alloying elements. In fact, empirical equations have been obtained to attempt to predict the carbide volume fraction and chromium levels in the ferrous matrix based on the carbon and chromium bulk composition. Maratray's equation [20] is one of the most common and widely used:

$$\text{Mass fraction of carbides} = \%C \ 12.33 + \%Cr \ 0.55\% - 15.2 \quad \{ 2.1 \}$$

Likewise, the Cr composition in the ferrous matrix was estimated:

$$\text{Mass fraction of Cr in metal matrix} = 1.95 \times (Cr/C)\% - 2.47. \quad \{ 2.2 \}$$

The equation depicts the less pronounced effect of chromium on the amount of carbides in the HCCI microstructure [20, 21]. Consequently, increasing the carbon composition is a most effective approach to increase the carbides and wear resistance. The equations can serve as a quick reference for determining possible or expected percentage of total carbides in the microstructure and chromium in the ferrous matrix. However, the equations do not address other important solidification parameters such as pouring temperature and cooling rates, which also influence the resultant microstructure [20].

With increasing Cr content, the structure and properties of the chromium carbide are changed from M_3C to M_7C_3 or $M_{23}C_6$ complex chromium carbides - where M represents chromium, and other elements that can partition into the carbide phase such as iron, and molybdenum [22-25]. Not all the carbides feature similar morphology [26-28]. M_7C_3 carbides solidify to form isolated carbides such as primary carbides, whereas also form a continuous network within the interdendritic spaces as eutectic carbides. M_3C and $M_{23}C_6$ carbides have been observed as interconnected rods or plates [29-31]. Isolated carbides are more effective in forcing cracks into the ferrous matrix when they can be arrested [32]. M_7C_3 has been found to possess the highest hardness among various chromium carbides, making it the best choice for wear protection [29, 33, 34]. Table 2.2 presents the hardness for the different carbide species and common minerals found in mining ore.

Table 2.2: Hardness of various carbides [14, 34, 35].

Carbide	Hardness (HV)
Complex chromium carbide, M_7C_3	1,200 – 1,800
Complex chromium carbide, M_3C	1,300
Complex chromium carbide, $M_{26}C_3$	1,140 – 1,500
Molybdenum carbide, Mo_2C	1,500
Tungsten carbide, WC	2,000 – 2,400
Vanadium carbide, VC)	2,460 – 3,150
Titanium carbide, TiC	2,000 – 3,200
Niobium carbide	2,400 – 2,850
Boron carbide, B_4C	1,800 – 3,500

2.2.2.3 Molybdenum:

When the molybdenum is added to the HCCI, it has no effect on the liquidus surface. It partitions into all the different HCCI's constituent phases. However, when its bulk content exceeds 2 wt.%, it also produces molybdenum carbides consuming about 50% of the Mo added [7, 36]. Depending on the Cr/C ratio, the hard Mo_2C or Mo_6C carbides solidify in the last liquid through a eutectic solidification preferentially along grain boundaries between the primary ferrous phase (austenite or ferrite) and the chromium carbides [37]. Higher Cr/C ratios (>10) lead to the formation of Mo_6C carbides instead of Mo_2C . Mo is typically added to HCCI in between 0.5 and 3.5 wt.% [20]. As the amount of Mo is increased, the hardenability and the strength of the ferrous matrix after heat treatment are improved due to suppression of perlite formation and reinforcement by secondary carbide precipitation [38].

Ikeda et al. [19] demonstrated that the high temperature wear resistance of hypoeutectic HCCI (Cr/C=5) modified with Mo was enhanced under sliding wear conditions when Mo_2C was formed. More recently, Scandian et al. [39] studied hypoeutectic HCCIs with higher Cr/C ratio modified with Mo where Mo_6C instead of Mo_2C was formed. Sliding wear at room temperature showed improvement in the wear resistance, mainly attributed to the fact that the ferrous matrix transformed from ferrite to austenitic/martensitic. Under abrasion conditions, Inthidech et. al. [40] found that the improvement in the wear

resistance with Mo addition was not consistent in two different type tests performed.

2.2.2.4 Minor elements

Minor elements sometimes used in HCCIs such as Mn, Si, and Cu have very little effect on the liquidus surface and therefore on the solidification path [41]. Like Mo, Mn, and Ni also suppress the perlitic transformation stabilizing the austenite phase. In the case of Mn, it partitions into both the chromium carbide phase and the ferrous matrix, in which it contributes to higher volume of retained austenite. This, in some cases, has been found to be beneficial for strength and toughness after heat treatments [42-44]. On the contrary, Si and Cu preferentially partitions into the ferrous matrix which is detrimental for their wear resistance. The addition of Si is rather limited due to the effect of increasing graphitization potential, inhibiting the carbide formation [45]. The Mn in HCCI is generally 1wt.% maximum and mostly used for deoxidation in the casting process. Copper is not as common in HCCIs as in other types of high allow white cast irons, where generally does not exceed 2.5 wt.%. Combined with Mo has been reported to be effective for hardenability. Higher amount of Cu can be detrimental due to the large volume of retained austenite that can be promoted.

Elements such as phosphorus and sulphur are intrinsic in the manufacturing process of cast irons. For low quality irons they can be as high as 0.15 wt.% and are significantly less for high-quality iron. As in steels, the sulphur

content is balanced by the effect of manganese due to the large tendency of iron and sulphur to form iron sulphide (FeS), which form at grain boundaries and is rather detrimental. On the contrary, MnS, is harmless due to its distribution within grains. The optimum ratio between manganese and sulphur for avoiding the formation of FeS structures has been described with the following relationship [7]:

$$\% \text{ Mn} = \% \text{ S} \times 1.7 + 0.15 \quad \{ 2.3 \}$$

It is essential to have a strict control of others minor elements, such as aluminum, antimony, arsenic, bismuth, lead, magnesium, cerium, and calcium since they can be detrimental to the microstructure and properties of the HCCI [7-9].

2.2.3 Microstructure of high chromium white irons

Under solidification conditions near equilibrium where slow cooling rates occur, such as those in large casting, the microstructural evolution can be predicted from the metastable Fe-Cr-C phase diagram [4, 10, 20, 29, 46-56]. This diagram is of paramount importance in metallurgy due to the large number of iron castings and steels based on alloying with C and Cr. Several studies have been conducted to investigate the liquidus reactions and extension on the phases in the liquidus surface [55-59]. In particular, the extension of the $M_{23}C_6$ carbide domain has long been discussed with contradicting results. While some authors claimed

not been fully completed and the U3 temperature is reached, which would occur near equilibrium conditions, a quasi-peritectic reaction completes the solidification forming a double layer or duplex carbide morphology with a M_7C_3 core and M_3C shell produced by the reaction between the liquid and the M_7C_3 carbides, which is more commonly seen at high carbon concentrations such those used in iron based chromium carbide weld overlays [13, 20, 29, 38, 54, 55, 62]. A fourth step in the solidification may also take place where the last liquid is solidified as ledeburitic M_3C carbides and γFe . In addition to the chemical composition of the alloys, the cooling rate will also dictate if all the reactions will occur, as reported by Thorpe and Chicco [55]. In reality, cooling rates that deviate from the equilibrium conditions will complete the solidification with the second step, eutectic γFe and M_7C_3 carbides precipitation after the primary solidification. Duplex carbides morphologies can still be attained under this condition after heat treatments where the M_3C shell features faceted interfaces with respect to the primary γFe [20, 29, 55, 63, 64].

Some of the new “hyperchromes” or hyper eutectic HCCIs solidify with M_7C_3 , hexagonal shaped (cross section) long needles of primary carbides that extend throughout the melt as shown by Bedolla et. al [41] using a deep etching technique. When their correspondent solidification sequence intersects the U2-U3 line, the remaining liquid solidifies as previously described for the hypoeutectic alloys.

As it can be seen in the liquidus surface, multiple reactions may take place depending on the solidification sequence, leading to a variety of possible microstructures. The invariant liquidus reactions in the Fe rich corner of the C-Cr-Fe metastable system are summarized in table 2.3.

Table 2.3: Invariant liquidus reactions in the Fe rich corner of the C-Cr-Fe system.

Temperature		
Symbol	(C)	Reaction
U1	1283	$L + \alpha\delta Fe \rightleftharpoons \gamma Fe + M_{23}C_6$
U2	1255	$L + M_{23}C_6 \rightleftharpoons \gamma Fe + M_7C_3$
U3	1160	$L + M_7C_3 \rightleftharpoons \gamma Fe + M_3C$
U4	1156	$L + M_3C \rightleftharpoons \gamma Fe + C$

In industrial practice, HCCIs are commonly described as hypoeutectic, eutectic, or hypereutectic depending on the primary phase that is formed. However, their solidification sequence can produce other reactions such those described by Hinckley [13]:

- Peritectic carbides of M_7C_3 , $M_{23}C_6$, and M_3C .
- Secondary carbide precipitation most commonly of the M_7C_3 and $M_{23}C_6$ during slow cooling after solidification or during ageing at elevated temperatures.
- Lamellar pearlite consisting of carbide and ferrite upon slow cooling.

- Martensite or tempered martensite from austenitic ferrous matrixes upon cooling and reheating.
- Transformation of retained austenite to ferrite on reheating.

From the liquidus surface of the Fe rich C-Cr-Fe system, it can also be seen that as the chromium content increases, the carbon composition of the eutectic composition decreases, ranging from 3.8 to 2.7 wt.% for HCCIs with bulk chromium content from 10 wt.% to 28 wt.% respectively, as depicted by figure 2.6 [7, 20]. Similar effect has been observed for most other elements.

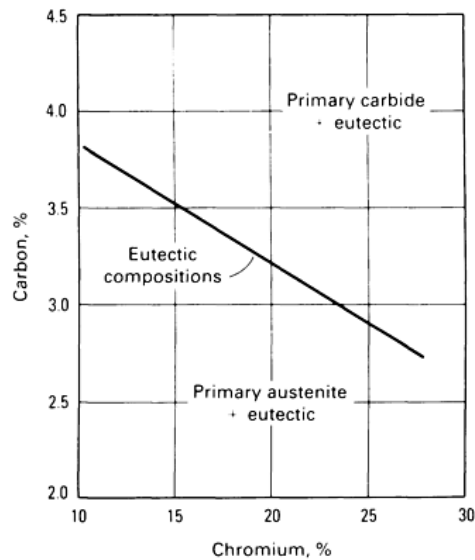


Figure 2.6: Relationship between the eutectic composition and the overall C and Cr content [7].

2.2.4 Heat treatment for HCCIs

Under non-equilibrium conditions, which is the case in most commercial HCCIs, the austenitic matrix becomes supersaturated in carbon and chromium, and a metastable austenitic matrix is retained at room temperature, providing there are sufficient alloying elements to prevent the formation of pearlite and bainite [30, 37].

In order to obtain maximum strength and hardness, a destabilization heat treatment is typically performed. This is achieved by heating to temperatures between 800 to 1000°C where the austenite phase stabilizes, soaking or slowly cooling through the austenitic region for homogenization, follow by an air quenching to room temperature [8, 9, 13, 41, 65-67]. This type of heat treatment for HCCI has been a subject of study for a number of research experiments in order to understand the nature and mechanisms of secondary carbide precipitation [38, 41, 53, 68-71]. Cracking is avoided by slow heating at least until 650°C. The heat treatment process is illustrated in figure 2.7.

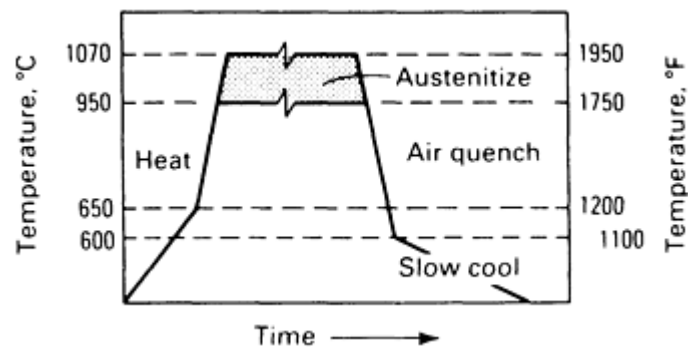


Figure 2.7: Typical heat treatment of high chromium alloys to produce the desired matrix without cracking [65].

The effect of the destabilization heat treatment on the microstructure of a 27 wt.%Cr hypoeutectic HCCIs is illustrated in figure 2.8. The microstructure in the as-cast condition, figure 2.8(a), consists of primary and eutectic austenite free from precipitates and features a hardness of 600 HV. On the other hand, the heat treated microstructure, figure 2.8(b), presents a fine dispersion of secondary carbides in the primary austenite dendrites and the eutectic austenite, which increases the hardness to 800 HV, 33% increases over the as-cast hardness.

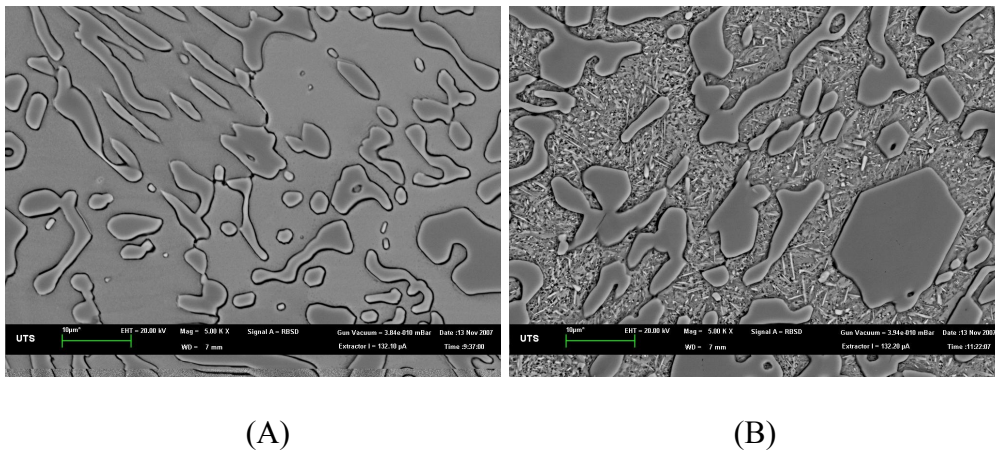


Figure 2.8: Microstructure of a 27% Cr white cast iron: a) as cast; b) after destabilization treatment [13, 72].

It is interesting to note that in hypereutectic HCCIs, only the austenitic matrix is affected, producing the fine dispersion of secondary carbides whereas the primary and eutectic M_7C_3 carbides remain unaffected.

While soaking at austenitizing temperatures, small chromium carbides precipitate from the austenite and become dispersed along the matrix, mostly featuring $M_{23}C_6$ (>25wt.%Cr) as fine interconnected rods, M_7C_3 (>15 wt.%Cr) as

agglomerate rods and plates, or M_3C (<10 wt.%Cr) as plates. The type of secondary carbides also depends on soaking temperature and time [20, 69, 73].

Once these secondary carbides form, the surrounding area becomes depleted in chromium and carbon which increases the martensite start temperature (M_s) and therefore more martensite can be produced lowering the volume of retained austenite after cooling. In some cases, a pre-destabilization anneal between 740 and 780°C is used to soften and stress relief prior machining [53, 74].

Even though destabilization is the most important heat treatment used commercially, other treatments have also been investigated and used for improving specific properties. Quenching to cryogenic temperatures [20, 75-79] has been used to lower the volume of retained austenite in the matrix, which to room temperature is reported to be at least 35%. In view of improving toughness, high temperature heat treatments to spheroidize and breakup interconnected eutectic chromium carbides have been investigated by some researchers [54, 80, 81]. Strain induced martensitic transformation and austempering have also been studied with moderate success [[20, 82].

2.2.5 Toughness and microstructure

Even though HCCI is a brittle material, certain toughness is important to withstand the amount of impact they could be exposed to during the wear process,

for instance, under impact abrasion or slurry erosion. The impact toughness is mainly dependent on the ability of the microstructure to inhibit crack formation and arrest propagation. Therefore, most effort has been made to evaluate the role of different matrix microstructures, and carbide morphology and volume [83].

Several studies agree that an austenitic matrix provides higher toughness than a martensitic one, and as the austenite volume in the microstructure increases, so does the toughness [40, 84-86]. An increase over 30% in the K_{Ic} fracture toughness was reported by Tabrett [20] for a 15 wt.%Cr HCCI when the heat treatment was adjusted to produce an austenitic matrix instead of martensitic [87]. The presence of austenite has also been reported to aid reducing the energy available for cracking through strain-induced martensite formation [20, 83]. The toughness improvement caused by the austenite in the matrix microstructure is generally found to be detrimental for the wear resistance under low-stress abrasion. In this case, some researchers have published that 25 to 30% retained austenite provides the best abrasion resistance, while others have suggested higher content up to 50% as the optimum [88]. On the contrary, under high stress abrasion, the austenite has been found to improve wear resistance due to the strain hardening capability [20].

Reducing the primary and/or eutectic carbide size by inoculation is known to be effective, but difficult and costly to achieve in large scale [20, 23, 88, 89]. Rounding the morphology of the carbides has been found to be beneficial to

reduce the stress concentration at the sharp carbide needles tip, and reduce crack initiation [61, 84, 90, 91]. Studies based on fractographic analysis have shown that impact toughness is limited by the inter-connected carbides in the eutectic cells. On the contrary, as the carbides become more isolated the toughness is favoured by forcing cracks to propagate through the matrix [32]. However, not all carbide spacing provide the same effect. Kootsookos and Gates [92] studied the effect of destabilisation temperature and found that as the temperature increases the impact toughness was improved, which was attributed to the higher secondary carbide mean free path. In general, secondary carbides facilitate the ductile tearing surrounding the carbides as they are believed to impede or restrict the dislocation movement [20].

There is a threshold for the total volume fraction of carbides to which wear resistance is generally improved at the expense of toughness. The optimum value will depend not only on the specific chemical composition and microstructure developed by the HCCI, but also on the nature of the wear mechanism(s) acting on the surface as well as other aspects such as the corrosivity of the environment, temperature, and any other external mechanical requirements. In general, researchers have found that 30% carbide volume in the microstructure provides a good balance between wear resistance and toughness [84, 93, 94].

2.3 Wear modes, mechanisms, and HCCI's performance

2.3.1 Sliding wear

It occurs when two solid surfaces slide against each other, as depicted by figure 2.9. Engineering surfaces consist of multiple micro/macroscale asperities that come into contact at the asperities tip when a normal load to the general plane of the surfaces is applied [95]. The resultant stress at the asperity tip is high enough to cause plastic deformation and bonding of the asperities by solid state welding, which has a higher strength than the weaker of the two materials, and particles removed from one surface are either temporarily or permanently attached to the other surface [95, 96]. Wear debris is generally formed from the weak material and is transferred to the harder surface perhaps at a different location or may remain separated.

The main variables of sliding wear are given by the simple relationship derived by Holm and Archard [95]:

$$V = \frac{KSL}{H} \quad \{ 2.4 \}$$

where V represents the wear scar volume, S is the sliding distance, L is the normal load, H the hardness of the softer surface, and K is a wear coefficient related to other properties of materials, which influence wear, e.g., adhesion, friction, thermal conductivity, and fatigue behavior [134], etc. K is typically determined

experimentally, for instance, through pin-on-disc testing for a specific tribological system.

Even though this equation was originally developed for bare to bare metallic contact, other conditions such as lubrication and oxide films can be represented by adjusting the wear coefficient [35, 97].

In HCCIs, sliding wear resistance is required in applications such as chute liners, hopper and feeder, liner plates, screens, and work rolls for the hot rolling of metals [6, 19, 98].

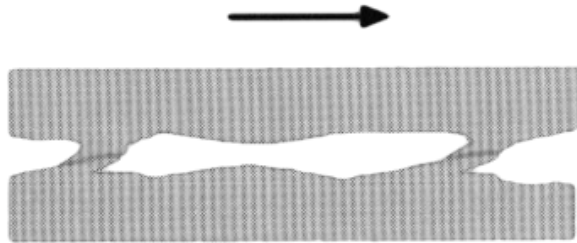


Figure 2.9: Schematic of sliding wear [99].

2.3.2 Abrasive Wear

It occurs when hard particles, most common non-metallic, or asperities move along a softer solid surface, causing a material loss by scratching [35, 99]. Depending on the type of contact, abrasive wear is classified as two-body (see Fig.2.10 (A)), when the particles or asperities slides against the counter-surface,

and three-body when the particles are trapped between two surfaces (see Fig. 2.10 (B)) [35, 95]. Another common classification is based on the applied load. Low stress abrasion refers the situation when particles only exert a light contact with the surface, which is not enough to crush the abrasive [95, 96]. The worn surface feature scratching with minimal subsurface plastic flow and therefore work hardening does not occur [95]. This is typically seen in chute liners, screens, and truck beds; and it is commonly experienced in mining and oil sands extraction [6]. When the applied load is sufficiently large to crush the abrasive particles, scratching, pitting, plastic deformation, and subsequent work hardening occur [95, 100]. High stress abrasion is experienced by crushers, grinding media in mining operations, rolling-contact bearings, and gears. When the high stress abrasion results in coarse grooving and gouges, typically from large abrasive particles, the abrasive wear is referred as to gouging abrasion [35, 101].

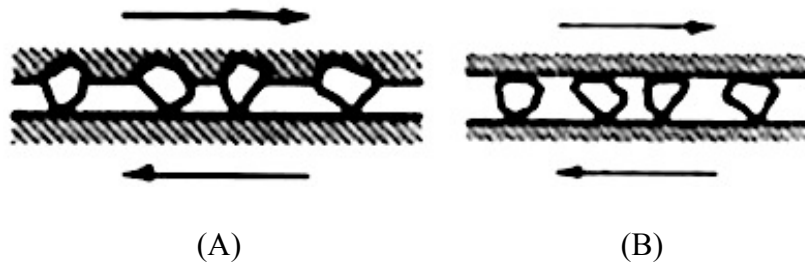


Figure 2.10: Schematic of abrasive wear [99]: (A) two-body; (B) three-body.

To explain the removal of material during abrasion, several mechanisms involving plastic deformation and fracture have been derived, as depicted by figure 2.11

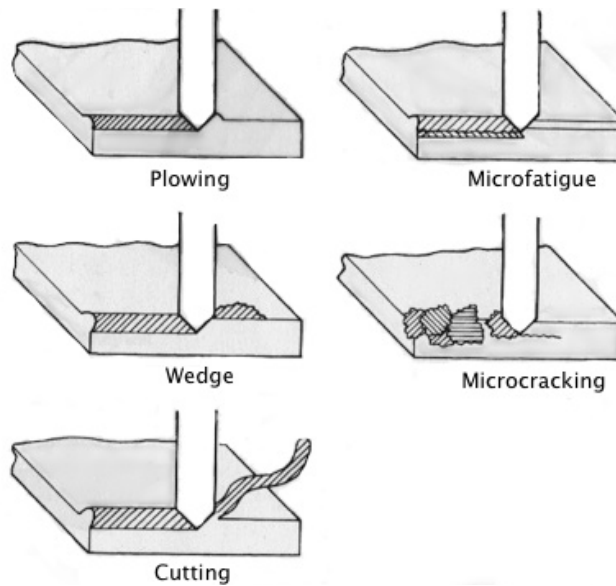


Figure 2.11: Schematic of abrasive wear mechanisms [95].

Plowing occurs when the material is displaced to sides of a scratch with no overall material loss, causing strain hardening near the surface through dislocation build-up [95, 96]. Successive scratching eventually leads to material loss through micro-fatigue. Another mild abrasive wear mechanism is a wedge front of the abrasive tip with little material displaced to the sides, which can form when the contact interface/bulk shear strength ratio lays between 0.5 and 1.0 [95]. When the adhesion of the wedge and the abrasive tip is strong, sliding occurs between the wedge and the solid surface. The most aggressive mechanisms experienced in ductile materials is cutting when the abrasive tip removes a chip from the solid surface similar to a machining tool bit [95]. The cutting nature results in material removal but with little plastic flow relative to the size of the groove. For sharp abrasive particles, there is a characteristic critical angle that determines the transition from plowing to cutting for each material being abraded [35, 95]. In

brittle materials, such as ceramics or even in white cast irons, micro-cracking is another abrasion mechanism, which can be rather severe. Micro-cracking occurs when forces applied by the abrasive particle exceed a critical value corresponding to the fracture toughness of the material [35, 95, 102].

2.3.3 Slurry Erosion

Erosive wear is the progressive loss of material from a solid surface due to the mechanical interaction with a fluid, a multicomponent fluid, or impinging liquid or solid as depicted by figure 2.12 [35, 103, 104]. For this work, slurry erosion is of interest and considered for the research application of HCCIs in oil sands extraction. Slurry is defined as a mixture of solid particles in a liquid (usually water) of such a consistency that it can be readily pumped. In Oil Sands Extraction, slurry erosion is responsible for some of the largest maintenance cost items, and materials are exposed to extreme erodent conditions. Figure 2.13 shows a HCCI worn impeller after 3 months of use in an oil sands slurry pump [4].

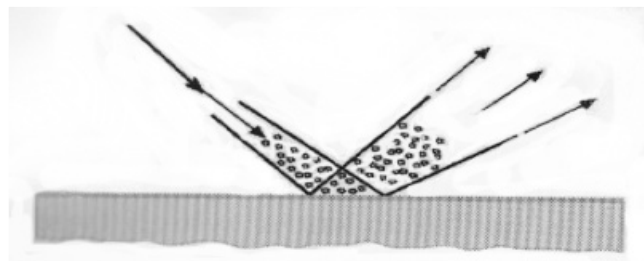


Figure 2.12: Schematic of solid particles erosion [99].



Figure 2.13: A HCCI worn impeller after 3 months of use in oil sands slurry pumps [4].

The term slurry erosion is also defined “as the type of wear by a material exposed to a high-velocity stream of slurry” [105]. This concept is extended to cases where the material is either static or dynamic. In other words, the slurry erosion happens regardless whether the material moves through the slurry or that the slurry moves past the material [104].

High-velocity erosion is one the most destructive wear modes. For instance, when an equipment such as a valve seat, piston, or piping wears to the extent that a slight leak develops, the extremely high velocity of slurry leakage through that small gap can result in catastrophic and rapid failure of the parts. Impellers and cut-water mechanisms of centrifugal slurry pumps can also experience this catastrophic wear mode [4, 6, 98, 104].

The principal mechanism that controls the mass loss of an eroding surface is a combination of plastic deformation and forging at all impact angles [35, 106]. Microstructural studies at different stages of the erosion process have shown that the platelets are initially extruded from shallow craters caused by particle impacts (figure 2.14 (A)). Once the platelets are formed, they are forged into a vulnerable condition (figure 2.14 (B-C)) and eventually get knocked off from the surface by subsequent particle impingements (figure 2.14 (D)) [106].

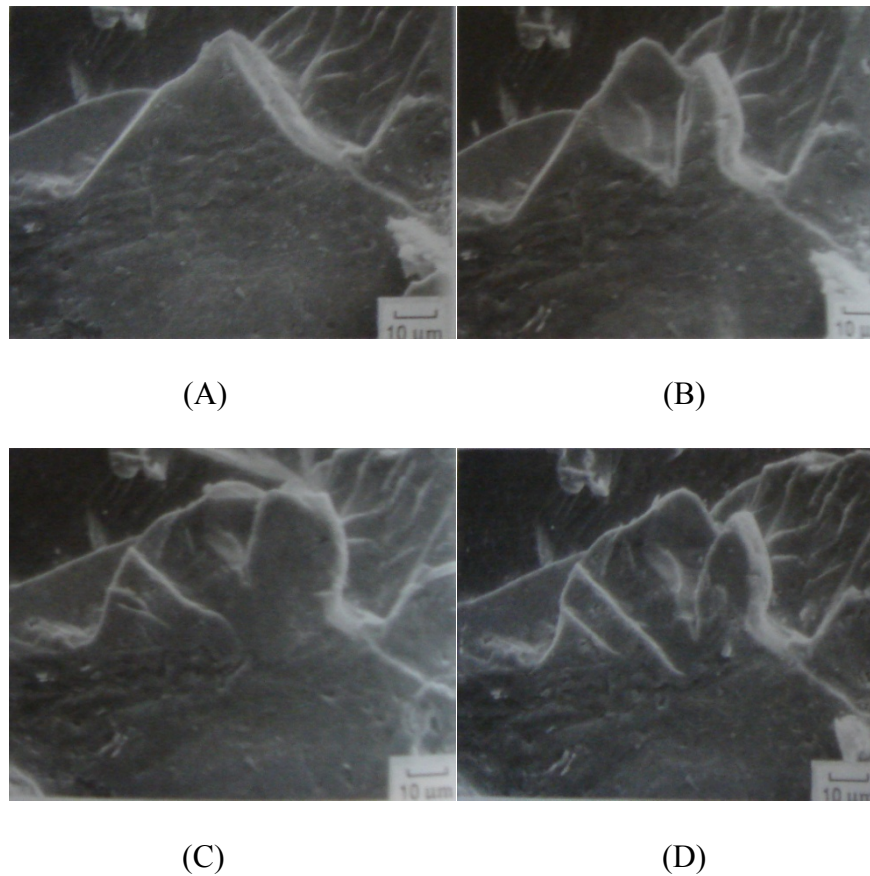


Figure 2.14: Platelets mechanism that controls the mass loss of an eroding surface. (A) formation of the platelets; (B) and (C) forging of the platelets by repeatedly imingements; (D) platelets just before being knocked off from the surface by particle impingement [106].

Figure 2.15 shows the schematic sequence proposed by Levy for the erosion damage mechanism [106]. This shows extrusion as being the first stage of the erosive process leading to the formation of the platelets. They use a 3 μ m layer of copper that was deposited onto a 1020 steel substrate. Then the surface was eroded with a few silicon carbide particles. The cross section of the eroded surface resembles well the schematic sequence shown in figure 2.15 [106].

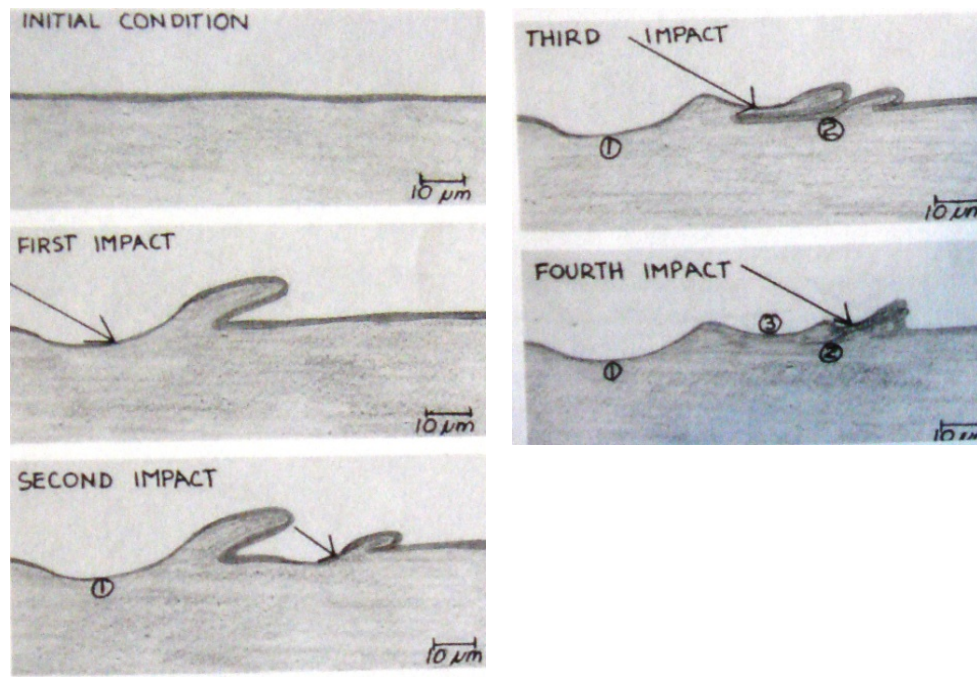


Figure 2.15: Schematic sequence for erosion [106].

Even though the wear mechanisms of solid particle erosion and low stress abrasion are relatively similar, in erosion the tribological system is more complex and involves more variables or parameters to consider. Perhaps the one single most important parameter under slurry erosion is the slurry velocity, which

presents a power law dependency with the volume loss [35]. The velocity exponent, n , is reported to be between 2 and 3 for ductile materials, and between 3~4 for brittle materials [95]. The impingement angle has also an important effect on slurry erosion. It is well established the effect of impingement angle for both extreme cases, the very ductile and the brittle materials. Ductile materials show the highest erosion rate at low angles ($<30^\circ$) being more susceptible to cutting and plowing. As the angle increases, the volume loss decreases reaching a minimum at 90° impingement angle [35, 95, 106]. Ductile materials have the ability to absorb the impact energy exerted by the striking particles without experiencing overall volume loss. On the contrary, brittle materials do not have the capability to withstand the impact component that increases with the impingement angle, and can be severely eroded by micro-cracking caused by the Hertzian stresses produced after particles impingement [35, 106]. As the impingement angle is reduced, the high hardness is rather effective to withstand the micro-cutting and plowing action of the particles and the volume loss reduced, showing the maximum wear at 90° [35].

The flow regime is another consideration that sometimes is overlooked. As it can be expected, laminar flows tend to produce lower wear rates in components as opposed to turbulent flow where multiple impingement angles are developed [95].

As described previously for abrasion, the characteristics of the erodent: particle size, morphology, and physical properties, have a significant impact on the erosion rates [4, 52, 89, 95, 106-108].

2.4 Improving the performance of HCCIs

The outstanding wear performance of high chromium cast iron is attributed to the combination of hard carbides and a relatively ductile ferrous matrix [25, 64, 109, 110]. However, due to the increasing demand of better materials in order to reduce costs of replacement, shutdown, and maintenance, there is a need to further improve these materials, which can only be accomplished by understanding the relationship between microstructure, properties, and performance in the context of the specific wear system [19, 40, 91].

Studies in the past decades have found that the excellent wear properties of HCCI are directly related to volume fraction of chromium carbides in their microstructures [111, 112]. However, a high volume fraction of chromium carbides would reduce the volume fraction of the ferrous matrix, which will be detrimental to the toughness of these alloys [113]. Throughout time, researchers have attempted to balance these properties by variations in compositions and heat treatments [19, 43, 52, 54, 109, 112, 114-129].

The most common HCCIs have featured hypoeutectic microstructures with approximate 25 to 30% eutectic M_7C_3 carbides, that are harder than common abrasives handle in mining operation, listed in table 2.4.

Table 2.4: Hardness of common minerals and various ferrous matrix phases [7, 105].

Mineral	Hardness		Material or Micro constituents	Hardness HV
	Knoop	HV		
Talc	20		Ferrite	70-200
Carbon	35		Pearlite, unalloyed	250-320
Gypsum	40	36	Pearlite, alloyed	300-460
Calcite	130	140	Austenite, 12% Mn	170-230
Fluorite	175	190	Austenite, low alloy	250-350
Apatite	335	540	Austenite, high Cr iron	300-600
Glass	455	500	Martensite	500-1010
Feldspar	550	600-750		
Magnetite	575			
Orthoclase	620			
Flint	820	950		
Quartz	840	900-1280		
Topaz	1330	1430		
Garnet	1360			
Emery	1400			
Corundum (alumina)	2020	1800		
Silicon carbide	2585	2600		
Diamond	7575	10000		

It was a natural step to increase the carbide volume in order to achieve higher wear resistance. Several researchers explored the role of the carbide volume content in different HCCIs in some cases maintaining the microstructure of the ferrous matrix relatively unchanged [4, 34, 46, 51, 83, 130-132].

Surprisingly not always the wear resistance was improved. Under low stress abrasion, when the abrasive was softer than the chromium carbides (but harder than the ferrous matrix), the carbide volume content has a direct effect on improving wear resistance as it reinforces the matrix [4, 46, 87, 132]. In this case, the wear progresses in such a way that the matrix is preferentially abraded until the carbides protrude and become susceptible to spalling and fracture. As the carbide volume increases, the mean free path decreases, and the matrix wear is not as rapid, producing a thinner eroded layer at all times. It is evident that not only the hardness, but also the abrasive particle size with respect to the carbides mean free path are crucial factors that influence the HCCI abrasion performance [35]. In studies conducted with abrasives harder than the chromium carbides, such as silicon carbides and alumina, both the carbides and ferrous matrix were both abraded and increasing the carbide volume content was beneficial but little effect resulted from modifying the matrix macrostructure, as it only provides mechanical support to the carbides [20, 35].

On the contrary, at high stress abrasion or under three-body abrasion, it has been observed that the dominant wear mechanism is changed to microcracking of the carbides tips, especially primary carbides, when indented [20, 34]. When this occurs, there is a threshold value at which further increasing carbide volume content becomes detrimental to the wear resistance. This has been observed with both softer or harder abrasives with respect to the chromium carbides. The angularity of the particles also plays an important role, a high

angularity can also promote micro-cutting which can be quite severe, and has also been reported to produce a larger depth of cut in the carbide phase making it more susceptible to further micro-cracking and spalling [5, 20, 35, 95]. In fact, Tabrett et. al. [20] reported that in low wear resistant materials, the angularity effect can exceed the effect of increasing hardness of the abrasives. The effect of the particles size, as mentioned previously, is dependant on the microstructural spacing of the phases. Larger particle size is associated with higher volume loss as the load per particle increases, and the particles become more effective to induce micro-cracking of the carbides [20, 34]. It has been reported that for a specific microstructure and tribological system, there is a maximum particle size (~100um in HCCI) above which the wear resistance is not affected.

Researchers such as Dogan et. al. have studied the effect of the carbide orientation on the wear performance [25], however there has not been a general agreement. Earlier studies showed that carbides align perpendicular to the wear surface provide the best configuration for maximum support of the matrix to the carbides [20]. The benefits of this configuration have also been recently found in erosion simulations of different perlite orientations in carbon steel [133]. On the contrary, under high stress abrasion, Dogan et. al [10, 25] found that carbides oriented parallel to the wear surface were less susceptible to cracking under high stress.

Another critical microstructural feature in HCCIs is the carbide morphology, unfortunately this has not been widely studied because of the difficulty to modify the carbides without affecting other parameters to isolate such effect. It is expected that the main advantage of lowering the carbide size and producing a rounded morphology is to eliminate carbide micro-cracking at the sharp tips, enhancing both the wear (by attenuating micro-cracking as wear mechanisms) and improving the overall toughness [20, 24]. One of the main concerns in this case is the interfacial strength between carbide and matrix and favouring delamination of carbides from the microstructure. For high stress abrasion applications there is a good potential for improving performance by carbide refinement. Another consideration is that carbide refinement allows for increasing carbide volume fraction and reducing mean free path which can have a tremendous positive impact on performance.

The structure of the matrix can be changed by heat treatment and composition. Austenite, pearlite, martensite, bainite, among others, can be produced as a matrix leading to different overall performances. In steels, it is important to produce the highest hardness microstructures if wear is a concern, and martensite and bainite normally gives the best wear resistance [134]. However, in HCCI, due to the presence of hard chromium carbides it is not necessary to have the hardest microstructure in the matrix (see table 2.4). In fact, it has been observed that an austenitic matrix is beneficial to stop crack propagation and accommodate impact [135]. A pearlitic microstructure is

generally not desirable due to its poor wear and corrosion resistance, and it is avoided by addition of alloying elements such as Mo, Cu, or Ni. Chromium also acts as an austenite promoter but it is mostly tied up in the chromium carbides and therefore it is not sufficient by itself to avoid the pearlite formation [135, 136].

The effect of the matrix on the HCCI wear performance is also dependant on the role of the carbides phase. When the matrix is reinforced by the carbide with a mean free path suitable to the abrasive particles so the matrix is not preferentially worn out, the role of the matrix is limited to support the carbides and there is little effect on changing the matrix microstructure through heat treatment. However, when the matrix with a large carbide mean free path is exposed to the abrasive, the wear resistance of the matrix becomes important and rapid wear of the relatively soft matrix leaves the carbides unsupported causing micro-cracking and spalling [20, 137]. There has been debate whether an as-cast austenitic matrix or heat- treated martensitic matrix is preferable to improve wear performance. In general, under low-stress abrasion the martensitic microstructure has exhibited the best wear performance. Nevertheless, under high stress abrasion and with very hard abrasives, the austenitic matrix has been reported to outperform the martensitic one [10]. Strain hardening capability, strain induced martensite, and higher ductility has been considered to explain these results [20]. Other authors have still found that the martensitic matrix provides the best support to the carbides especially at two-body abrasion [20, 33, 138, 139].

Another important aspect of the heat-treated martensitic microstructure is that it is also accompanied by precipitation of secondary carbides which strengthen the matrix by dispersion hardening [20]. The secondary carbides enhance the mechanical support provided by the matrix and can also improve the wear resistance of the matrix, even though under large abrasive particle size, such as in gouging abrasion, the effect of such small carbides may be negligible. The secondary carbides can also make more anodic the matrix providing larger carbide/matrix interfacial area that is more easily corroded and leaving the carbides unsupported.

The HCCI erosion resistance and relationship with microstructure have not been extensively studied as much as their abrasion behavior. Llewellyn and Dolman [4] studied the erosive wear of hypoeutectic and hypereutectic HCCIs through a Coriolis erosion (low impingement angle) test rig with silica as erodent. In their study, increasing the carbide volume content from 18% (hypoeutectic) to 44% (hypereutectic) was effective to increase wear resistance. They also reported on improved HCCI wear performance with reducing carbide size and increasing hardness. They found that in some cases, coarse primary carbides had a tendency for spalling which was detrimental to the performance of materials. Similar to abrasion, The HCCI erosion behavior can result on the preferential removal of the carbide phase, the loss of carbide phase leaves the matrix exposed to the erodent, resulting in rapid wear, or a preferential removal of the matrix leaves the carbides unsupported, which results in cracking and spallation. HCCI microstructural

aspects discussed for abrasion earlier are also relevant to erosive wear. Several authors have agreed that carbide micro-cracking tends to determine the wear rates in HCCIs [137], however, this cannot be generalized as it largely depends on the tribological system. There have been contradicting results about the HCCI response to varying impingement angles. While Aptekar and Kosel [140] showed that there was no significant effect of changing impingement angle on the rate of erosion, more recent studies have shown a maximum wear rate near 60° , and some others at 90° [52, 107]. To some extent the disagreement is expected because they have not been studied systematically under the same or similar testing conditions. For instance, using harder abrasives, silicon carbides and quartz, on iron based chromium carbide weld overlays, Stevenson and Hutchings [137] found that at high impingement angles mild steel performed better than HCCIs but the trend was reversed at low impact angles or when tested using softer abrasives. Fracturing of primary carbides at high angles with hard abrasives was responsible of the poor performance of HCCI when harder erodent at impingement high angles were used. Particularly it has been noted that the matrix/carbide interface is more prone to cracking. Certainly, when carbide micro-cracking is the dominant mechanism such as at high impingement angle, or when harder erodents are used, increasing the carbide volume content can be detrimental.

The effect of velocity on HCCI erosion has supported the power function dependency found in the literature on erosion mentioned previously. As velocity

increases, the HCCI wear rate increases. Between 30 to 59 m/s velocity, Stevenson and Hutchings [137] also reported that the volume loss increases as the cube of velocity independently of the impingement angle.

It is expected that regardless of the heat treatment, the achieved matrix hardness is usually not as high as the common abrasives or erodent found in mining operations (table 2.4). Therefore, the matrix will generally be worn by erosion in processes involving extrusion, lip formation, and removal of weakened material.

Corrosion is another important aspect in slurry erosion of HCCIs, which has not been extensively investigated in the context of slurry erosion. HCCIs with at least 16 wt.%Cr in matrix are believed to develop a stable passive film [16], however, chromium depletion surrounding the carbides is known to cause preferential localized corrosion on the carbide/matrix interface which can be rather severe and cause carbides to easily fall off or be susceptible to cracking during slurry erosion leaving the matrix unprotected [4, 12, 20, 51, 106, 141, 142]. In this case, the increase of carbide volume content needs to be compensated by higher overall chromium content, or addition of hard carbide forming elements that can allow more chromium to remain in the matrix while promoting hard carbides to withstand wear. Likewise, destabilization treatment for secondary carbides can be rather detrimental making the matrix more susceptible to localized corrosion. It is known that the erosion-corrosion damage is synergistic. For

instance, electrochemical testing of HCCI may show mild corrosion rates due to the small anodic areas mainly around the interface between carbides and the metallic matrix. However, as most of the corrosion damage begins at the matrix/carbide interfaces, the erosion can be greatly enhanced [35, 95].

As mentioned previously, extensive work has been carried out to improve properties of hypereutectic HCCI's while maintaining a relatively high volume fraction of primary M_7C_3 carbides. Most of these studies attempt to refine the carbides through increasing the carbide nucleation rate to obtain dispersed fine carbides. For example, small amounts of foreign elements such as titanium, vanadium, and niobium could act as a substrate for heterogeneous nucleation of carbides [4, 15-20]. This is one of the most viable approaches to implement in large scale foundry without a significant added time and cost. Other alternative to refine the carbide structure is by rapid undercooling during solidification. This has been shown to increase carbide nucleation while restricting the growth of carbides. However, larger nucleation rates only occur in thin sections near the mold wall during casting, which are not the majority of HCCI's products [23, 143].

Long heat treatments have also been studied to spheroidize and modify the morphology of carbides. This has limited effect as the carbides are quite stable at high temperatures [20, 23, 144]. A double-layer or duplex carbide morphology has also been reported to form during heat treatments at chromium content above approximately 30wt.% where the M_7C_3 carbides developed an outer shell

consisting of $M_{23}C_6$ [20]. This softer layer may be beneficial to minimizing the interfacial stress between hard M_7C_3 and the matrix. One of the main limitations of long heat treatment is the significant cost increase and time added to production.

2.5 Bibliography

1. *Engineer Training Manual Extraction*, S.E. Inc., Editor. 2010.
2. Tian, H.H., G.R. Addie, and K.V. Pagalthivarthi, *Determination of wear coefficients for erosive wear prediction through Coriolis wear testing*. *Wear*, 2005. **259**(1-6): p. 160-170.
3. Parent, L.L. and D.Y. Li, *Wear of hydrotransport lines in Athabasca oil sands*. *Wear*, 2013. **301**(1-2): p. 477-482.
4. Llewellyn, R.J., S.K. Yick, and K.F. Dolman, *Scouring erosion resistance of metallic materials used in slurry pump service*. *Wear*, 2004. **256**(6): p. 592-599.
5. M. Anderson, S.C., and S. Hoskins, *Improving reliability and productivity at Syncrude Canada Ltd. through materials research: past, present, and future*, in *CIM Bulletin*. 2004.
6. Llewellyn, R., *Resisting wear attack in oil sands mining and processing*. *Cim Bulletin*, 1997. **90**(1012): p. 75-82.
7. *Properties and Selection: Irons, Steels, and High-Performance Alloys* Vol. 1. 1993, USA: ASM International.
8. Quintero, O., *Aleaciones Ferrosas 2004*, Caracas: Departamento de Ciencia de los Materiales, Universidad Simon Bolivar.
9. Quintero, O., *Fundicion 2006*, Caracas: Departamento de Ciencia de los Materiales, Universidad Simon Bolivar.
10. Dogan, O.N., G. Laird, and J.A. Hawk, *Abrasion resistance of the columnar zone in high cr white cast irons*. *Wear*, 1995. **181**: p. 342-349.

11. Ma, N.H., Q.C. Rao, and Q.D. Zhou, *Corrosion abrasion wear-resistance of 28-percent-Cr white cast-iron containing boron*. *Wear*, 1989. **132**(2): p. 347-359.
12. Tian, H., et al., *Corrosion-wear behavior of some high-alloyed white irons and stainless steels*. *Transactions of the American Foundrymen's Society*, Vol 105. Vol. 105. 1998, Des Plaines: Amer Foundrymens Soc. 595-602.
13. Hinckley, B., et al., *Sem investigation of heat treated high-chromium cast irons*. *Materials Forum*, 2007. **32**: p. 55-71.
14. Jiyang, Z., *Colour Metallography of Cast Iron*. 2011, China Foundry.
15. Huang, X. and Y. Wu, *A high Cr-Mo alloy iron*. *Journal of Materials Engineering and Performance*, 1998. **7**(4): p. 463-466.
16. Zumelzu, E., et al., *Microstructural characteristics and corrosion behaviour of high-chromium cast iron alloys in sugar media*. *Protection of Metals*, 2003. **39**(2): p. 183-188.
17. Tabrett, C.P. and I.R. Sare, *The effect of heat treatment on the abrasion resistance of alloy white irons*. *Wear*, 1997. **203**: p. 206-219.
18. Ruano, O.A., L.E. Eiselstein, and O.D. Sherby, *Superplasticity in rapidly solidified white cast irons*. *Metallurgical Transactions a-Physical Metallurgy and Materials Science*, 1982. **13**(10): p. 1785-1792.
19. Ikeda, M., et al., *Effect of molybdenum addition on solidification structure, mechanical-properties and wear resistivity of high chromium cast irons*. *Isij International*, 1992. **32**(11): p. 1157-1162.
20. Tabrett, C.P., I.R. Sare, and M.R. Ghomashchi, *Microstructure-property relationships in high chromium white iron alloys*. *International Materials Reviews*, 1996. **41**(2): p. 59-82.
21. Christodoulou, P., A. Drotlew, and W. Gutowski, *The effect of carbon, chromium and silicon content on wear resistance of ferritic Fe-Cr-C cast alloys*. *Wear*, 1997. **211**(1): p. 129-133.
22. Yaer, X.B., et al., *Erosive wear characteristics of spheroidal carbides cast iron*. *Wear*, 2008. **264**(11-12): p. 947-957.

23. Bedolla-Jacuinde, A., S.L. Aguilar, and B. Hernandez, *Eutectic modification in a low-chromium white cast iron by a mixture of titanium, rare earths, and bismuth: I. Effect on microstructure*. Journal of Materials Engineering and Performance, 2005. **14**(2): p. 149-157.
24. Jacuinde, A.B. and W.M. Rainforth, *The wear behaviour of high-chromium white cast irons as a function of silicon and Mischmetal content*. Wear, 2001. **250**: p. 449-461.
25. Dogan, O.N. and J.A. Hawk, *Effect of carbide orientation on abrasion of high Cr white cast-iron*. Wear, 1995. **189**(1-2): p. 136-142.
26. Matsubara, Y., et al., *Solidification and abrasion wear of white cast irons alloyed with 20% carbide forming elements*. Wear, 2001. **250**: p. 502-510.
27. Bedolla-Jacuinde, A., *Microstructure of vanadium-, niobium- and titanium-alloyed high-chromium white cast irons*. International Journal of Cast Metals Research, 2001. **13**(6): p. 343-361.
28. Bedolla-Jacuinde, A., B. Hernandez, and L. Bejar-Gomez, *SEM study on the M7C3 carbide nucleation during eutectic solidification of high-chromium white irons*. Zeitschrift Fur Metallkunde, 2005. **96**(12): p. 1380-1385.
29. Laird, G., R.L. Nielsen, and N.H. Macmillan, *On the nature of eutectic carbides in cr-ni white cast irons*. Metallurgical Transactions a-Physical Metallurgy and Materials Science, 1991. **22**(8): p. 1709-1720.
30. Karantzalis, A.E., A. Lekatou, and E. Diavati, *Effect of Destabilization Heat Treatments on the Microstructure of High-Chromium Cast Iron: A Microscopy Examination Approach*. Journal of Materials Engineering and Performance, 2009. **18**(8): p. 1078-1085.
31. Carpenter, S.D., D. Carpenter, and J.T.H. Pearce, *XRD and electron microscope study of an as-cast 26.6% chromium white iron microstructure*. Materials Chemistry and Physics, 2004. **85**(1): p. 32-40.
32. Kootsookos, A. and J.D. Gates, *The effect of the reduction of carbon content on the toughness of high chromium white irons in the as-cast state*. Journal of Materials Science, 2004. **39**(1): p. 73-84.
33. Watson, J.D., P.J. Mutton, and I.R. Sare, *Abrasive wear of white cast irons*. Metals Forum, 1980. **3**(1): p. 74-88.

34. Zumgahr, K.H. and G.T. Eldis, *Abrasive wear of white cast irons*. *Wear*, 1980. **64**(1): p. 175-194.
35. Hutchings, I.M., *Tribology*. 1992, Oxford: Butterworth-Heinemann.
36. Inthidech, S., et al., *Effect of repeated tempering on hardness and retained austenite of high chromium cast iron containing molybdenum*. *Materials Transactions*, 2010. **51**(7): p. 1264-1271.
37. Demello, J.D.B., M. Durandcharre, and S. Hamarhibault, *Solidification and solid-state transformations during cooling of chromium-molybdenum white cast irons*. *Metallurgical Transactions a-Physical Metallurgy and Materials Science*, 1983. **14**(9): p. 1793-1801.
38. Wiengmoon, A., et al., *Microstructural and crystallographical study of carbides in 30wt.%Cr cast irons*. *Acta Materialia*, 2005. **53**(15): p. 4143-4154.
39. Scandian, C., et al., *Effect of molybdenum and chromium contents in sliding wear of high-chromium white cast iron: The relationship between microstructure and wear*. *Wear*, 2009. **267**(1-4): p. 401-408.
40. Inthidech, S., et al., *Two-body and three-body types abrasive wear behavior of hypoeutectic 26 mass% Cr cast irons with molybdenum*. *Materials Transactions*, 2012. **53**(7): p. 1258-1266.
41. Bedolla-Jacuinde, A., L. Arias, and B. Hernandez, *Kinetics of secondary carbides precipitation in a high-chromium white iron*. *Journal of Materials Engineering and Performance*, 2003. **12**(4): p. 371-382.
42. Basak, A., J. Penning, and J. Dilewijns, *Effect of manganese on wear-resistance and impact strength of 12-percent chromium white cast-iron*. *International Cast Metals Journal*, 1981. **6**(3): p. 12-17.
43. Sun, Z.P., et al., *Effect of manganese on As-cast microstructure and hardening behavior of high chromium white cast iron*. *Journal of Iron and Steel Research International*, 2005. **12**(1): p. 34-37.
44. Petrakov, O.V. and A.N. Poddubnyi, *Structure of wear-resistant alloyed white irons*. *Metal Science and Heat Treatment*, 2007. **49**(7-8): p. 409-411.

45. Swindell, N. and J. Burke, *Silicon microsegregation and first stage graphitization in white cast irons*. Metallurgical Transactions, 1971. **2**(12): p. 3257-&.
46. Fulcher, J.K., T.H. Kosel, and N.F. Fiore, *The effect of carbide volume fraction on the low stress abrasion resistance of high Cr-Mo white cast irons*. Wear, 1983. **84**(3): p. 313-325.
47. Demello, J.D.B. and M. Durandcharre, *Phase-equilibria and solidification sequences of white cast irons containing vanadium and chromium*. Materials Science and Engineering, 1984. **67**(1): p. 109-117.
48. Gregolin, J.A.R. and N.G. Alcantara, *Dendritic gamma- to massive (Fe,Cr)₇C₃ transition in Cr-Nb white cast-iron microstructures*. Journal of Materials Science Letters, 1991. **10**(13): p. 751-752.
49. Aso, S., M. Tagami, and S. Goto, *Phase-diagram based on solidification structure in Fe-25-percent-Cr-C-B alloys*. Journal of the Japan Institute of Metals, 1994. **58**(1): p. 1-7.
50. Silman, G.I. and A.A. Zhukov, *A new phenomenon - the transient metastable graphitization of alloyed white iron*. Bulletin of Materials Science, 1995. **18**(2): p. 99-102.
51. Lu, B., J. Luo, and S. Chiovelli, *Corrosion and wear resistance of chrome white irons - A correlation to their composition and microstructure*. Metallurgical and Materials Transactions A: Physical Metallurgy and Materials Science, 2006. **37**(10): p. 3029-3038.
52. Anijdan, S.H.M., et al., *Effects of tungsten on erosion-corrosion behavior of high chromium white cast iron*. Materials Science and Engineering a-Structural Materials Properties Microstructure and Processing, 2007. **454**: p. 623-628.
53. Carpenter, S.D., D. Carpenter, and J.T.H. Pearce, *XRD and electron microscope study of a heat treated 26.6% chromium white iron microstructure*. Materials Chemistry and Physics, 2007. **101**(1): p. 49-55.
54. Karantzalis, A.E., A. Lekatou, and H. Mavros, *Microstructural Modifications of As-Cast High-Chromium White Iron by Heat Treatment*. Journal of Materials Engineering and Performance, 2009. **18**(2): p. 174-181.

55. Thorpe, W.R. and B. Chicco, *The Fe-rich corner of the metastable C-Cr-Fe liquidus surface*. Metallurgical Transactions A, 1985. **16**(9): p. 1541-1549.
56. Raynor, G.V. and V.G. Rivlin, *Phase Equilibria in Iron Ternary Alloys*. The Institute of Metals, 1988. **4**: p. 143-156.
57. Jackson, R.S., J. Iron Steel Inst., 1970. **208**: p. 163-167.
58. W.D. Forgeng and W.D. Forgeng, J., *C-Cr-Fe (Carbon-Chromium-Iron)*. Metals Handbook, 1973: p. 402-404.
59. Rivlin, V.G., Int. Met. Rev., 1984. **29**: p. 299-327.
60. *C-Cr-Fe Ternary Phase Diagrams*. ASM Handbook Online.
61. Hanlon, D.N., W.M. Rainforth, and C.M. Sellars, *The effect of spray forming on the microstructure and properties of a high chromium white cast iron*. Journal of Materials Science, 1999. **34**(10): p. 2291-2301.
62. Randle, V. and G. Laird, *A microtexture study of eutectic carbides in white cast irons using electron backscatter diffraction*. Journal of Materials Science, 1993. **28**(15): p. 4245-4249.
63. Laird, G. and G.L.F. Powell, *Solidification and solid-state transformation mechanisms in Si alloyed high-chromium white cast irons*. Metallurgical Transactions A, 1993. **24**(4): p. 981-988.
64. Dogan, O.N., J.A. Hawk, and G. Laird, *Solidification structure and abrasion resistance of high chromium white irons*. Metallurgical and Materials Transactions a-Physical Metallurgy and Materials Science, 1997. **28**(6): p. 1315-1328.
65. *Heat Treating* ASM Handbook. Vol. 4. 1991, United States: ASM International.
66. Chen, X.A. and Y.X. Li, *Effect of heat treatment on microstructure and mechanical properties of high boron white cast iron*. Materials Science and Engineering a-Structural Materials Properties Microstructure and Processing, 2010. **528**(2): p. 770-775.

67. Farah, A.F., O.R. Crnkovic, and L.C.F. Canale, *Heat treatment in high Cr white cast iron Nb alloy*. Journal of Materials Engineering and Performance, 2001. **10**(1): p. 42-45.
68. Asensio, J., J.A. Pero-Sanz, and J.I. Verdeja, *Microstructure Selection Criteria for Cast Irons with More Than 10 wt% Chromium for Wear Applications*. Materials Characterization, 2003(49): p. 83-93.
69. Powell, G.L.F. and J.V. Bee, *Secondary carbide precipitation in an 18 wt% Cr-1 wt% Mo white iron*. Journal of Materials Science, 1996. **31**(3): p. 707-711.
70. Powell, G.L.F. and G. Laird, *Structure, nucleation, growth and morphology of secondary carbides in high chromium and Cr-Ni white cast irons*. Journal of Materials Science, 1992. **27**(1): p. 29-35.
71. Wang, J., et al., *Effects of secondary carbide precipitation and transformation on abrasion resistance of the 16Cr-1Mo-1Cu white iron*. Journal of Materials Engineering and Performance, 2006. **15**(3): p. 316-319.
72. Dolman, K. *Factors Influencing Standard Operating Procedures for A61*. in *Weir Minerals Foundry Conference*. 2007.
73. Powell, G.L.F., *Morphology of eutectic M₃C and M₇C₃ in white iron castings*. Metals Forum, 1980. **3**(1): p. 37-46.
74. Fernandez-Pariente, I. and F.J. Belzunce-Varela, *Influence of different heat treatments on the microstructure of a high chromium white cast iron*. Revista De Metalurgia, 2006. **42**(4): p. 279-286.
75. Liu, H.H., et al., *Effect of cryogenic treatment on property of 14Cr2Mn2V high chromium cast iron subjected to subcritical treatment*. Journal of Iron and Steel Research International, 2006. **13**(6): p. 43-48.
76. Yang, H.S., et al., *Effect of cryogenic treatment on the matrix structure and abrasion resistance of white cast iron subjected to destabilization treatment*. Wear, 2006. **261**(10): p. 1150-1154.
77. Liu, H.H., et al., *Effects of deep cryogenic treatment on property of 3Cr13Mo1V1.5 high chromium cast iron*. Materials & Design, 2007. **28**(3): p. 1059-1064.

78. Liu, H.H., et al., *Effects of cryogenic treatment on microstructure and abrasion resistance of CrMnB high-chromium cast iron subjected to sub-critical treatment*. Materials Science and Engineering a-Structural Materials Properties Microstructure and Processing, 2008. **478**(1-2): p. 324-328.
79. Wang, J., et al., *Effects of high temperature and cryogenic treatment on the microstructure and abrasion resistance of a high chromium cast iron*. Journal of Materials Processing Technology, 2009. **209**(7): p. 3236-3240.
80. Grant, P.S., *Spray forming*. Progress in Materials Science, 1995. **39**(4-5): p. 497-545.
81. Karantzalis, E., A. Lekatou, and H. Mavros, *Microstructure and properties of high chromium cast irons: effect of heat treatments and alloying additions*. International Journal of Cast Metals Research, 2009. **22**(6): p. 448-456.
82. Hann, S.K. and J.D. Gates, *A transformation toughening white cast iron*. Journal of Materials Science, 1997. **32**(5): p. 1249-1259.
83. Filipovic, M., et al., *Correlation of microstructure with the wear resistance and fracture toughness of white cast iron alloys*. Metals and Materials International, 2013. **19**(3): p. 473-481.
84. Radulovic, M., et al., *The influence of vanadium on fracture-toughness and abrasion resistance in high chromium white cast irons*. Journal of Materials Science, 1994. **29**(19): p. 5085-5094.
85. Zumgahr, K.H. and W.G. Scholz, *Fracture-toughness of white cast irons*. Journal of Metals, 1980. **32**(10): p. 38-44.
86. Inthidech, S., et al., *Effect of repeated tempering on abrasive wear behavior of hypoeutectic 16 mass% Cr cast iron with molybdenum*. Materials Transactions, 2013. **54**(1): p. 28-35.
87. Sare, I.R., *Abrasion resistance and fracture-toughness of white cast irons*. Metals Technology, 1979. **6**(NOV): p. 412-419.
88. Zhang, M.X., P.M. Kelly, and J.D. Gates, *The effect of heat treatment on the toughness, hardness and microstructure of low carbon white cast irons*. Journal of Materials Science, 2001. **36**(16): p. 3865-3875.

89. Adler, T.A. and O.N. Dogan, *Erosive wear and impact damage of high-chromium white cast irons*. *Wear*, 1999. **225**: p. 174-180.
90. Choo, S.H., et al., *Correlation of microstructure with the wear resistance and fracture toughness of hardfacing alloys reinforced with complex carbides*. *Metallurgical and Materials Transactions a-Physical Metallurgy and Materials Science*, 2000. **31**(12): p. 3041-3052.
91. Hanlon, D.N., W.M. Rainforth, and C.M. Sellars, *The rolling/sliding wear response of conventionally processed and spray formed high chromium content cast iron at ambient and elevated temperature*. *Wear*, 1999. **225**: p. 587-599.
92. Kootsookos, A. and J.D. Gates, *The role of secondary carbide precipitation on the fracture toughness of a reduced carbon white iron*. *Materials Science and Engineering a-Structural Materials Properties Microstructure and Processing*, 2008. **490**(1-2): p. 313-318.
93. Zumgahr, K.H., *Fracture-analysis of white cast-iron*. *Zeitschrift Fur Metallkunde*, 1980. **71**(2): p. 103-109.
94. Radulovic, M., M. Fiset, and K. Peev, *Effect of rare-earth elements on microstructure and properties of high chromium white iron*. *Materials Science and Technology*, 1994. **10**(12): p. 1057-1062.
95. *Surface Engineering for Corrosion and Wear Resistance*. 10M Communications. 2005, Ohio, United States: ASM International.
96. Robinson, J.S. and J. McCracken, *Combating Industrial Wear by Hardfacing*. *Materials Forum* 22, 1998: p. 97-121.
97. Ludema, K.C., *Friction, Wear, Lubrication A Textbook in Tribology*. 1996, USA: CRC Press.
98. Llewellyn, R. and C. Tuite, *Hardfacing fights wear in oil sands operation*. *Welding Journal*, 1995. **74**(3): p. 55-60.
99. Neale, M.J. and M. Gee, *Guide to Wear Problems and Testing for Industry*. 2001, Suffolk, UK.
100. Moore, M.A. and R.M. Douthwaite, *Plastic deformation below worn surfaces*. *Metallurgical Transactions A*, 1976. **7**(12): p. 1833-1839.

101. J. Llewellyn, R.A.H., Robert; Du, JunRong, *Assessment of Materials for Gouging Abrasion Applications*. NRC Publications Archive (NPArc).
102. Tabrett, C.P., *The electro-discharge machining surfaces of high-chromium white irons*. *Journal of Materials Science Letters*, 1996. **15**(20): p. 1792-1794.
103. *G40-13 Standard Terminology Relating to Wear and Erosion*, A. International, Editor. 2013: USA.
104. Miller and Schmidt, eds. *Slurry Erosion: Uses, Applications, and Test Methods*. 1987, ASTM USA.
105. *Friction, Lubrication, and Wear Technology in ASM Handbook*. 1992, ASM International: USA.
106. Levy, A.V., ed. *Solid Particle Erosion and Erosion-Corrosion of Materials*. 1997, ASM International: Ohio, USA.
107. Al-Bukhaiti, M.A., et al., *Effect of impingement angle on slurry erosion behaviour and mechanisms of 1017 steel and high-chromium white cast iron*. *Wear*, 2007. **262**(9-10): p. 1187-1198.
108. Adler, T.A. and O.N. Dogan, *Damage by indentation and single impact of hard particles on a high chromium white cast iron*. *Wear*, 1997. **203**: p. 257-266.
109. Bedolla-Jacuinde, A., et al., *Effect of titanium on the as-cast microstructure of a 16%chromium white iron*. *Materials Science and Engineering a-Structural Materials Properties Microstructure and Processing*, 2005. **398**(1-2): p. 297-308.
110. Bedolla-Jacuinde, A., et al. *The effect of titanium on the wear behaviour of a 16%Cr white cast iron under pure sliding*.
111. Adler, T.A. and O.N. Dogan. *Erosive wear and impact damage of high-chromium white cast irons*.
112. Stepina, A.I., V.V. Vagin, and T.N. Doroshenko, *Means of increasing wear-resistance of high-chromium cast-iron*. *Metal Science and Heat Treatment*, 1976. **18**(9-10): p. 828-830.

113. Kitaigora, N.I., *Impact-abrasion wear-resistance of high-chromium cast-iron*. Metal Science and Heat Treatment, 1975. **17**(5-6): p. 417-420.
114. Shadrov, N.S., L.G. Korshunov, and V.P. Cheremnikh, *Influence of molybdenum, vanadium, and niobium on the abrasion resistance of high-chromium cast-iron*. Metal Science and Heat Treatment, 1983. **25**(3-4): p. 284-287.
115. Gureev, D.M., A.E. Zaikin, and S.V. Yamshchikov, *Effect of laser and heat-treatment on the structure and properties of high-chromium cast-iron*. Metal science and Heat Treatment, 1985. **27**(11-12): p. 812-816.
116. Galgali, R.K., H.S. Ray, and A.K. Chakrabarti, *Wear characteristics of TiC reinforced cast iron composites Part 2 - Abrasive wear*. Materials Science and Technology, 1998. **14**(11): p. 1189-1193.
117. Galgali, R.K., H.S. Ray, and A.K. Chakrabarti, *Wear characteristics of TiC reinforced cast iron composites - Part 1 - Adhesive wear*. Materials Science and Technology, 1998. **14**(8): p. 810-815.
118. Tenorio, J.A.S., E. Albertin, and D.C.R. Espinosa, *Effects of Mo additions on the solidification of high chromium cast iron*. International Journal of Cast Metals Research, 2000. **13**(2): p. 99-105.
119. Arikan, M.M., H. Cimenoglu, and E.S. Kayali, *The effect of titanium on the abrasion resistance of 15Cr-3Mo white cast iron*. Wear, 2001. **247**(2): p. 231-235.
120. Wu, X.J., et al., *Effect of titanium on the morphology of primary M7C3 carbides in hypereutectic high chromium white iron*. Materials Science and Engineering a-Structural Materials Properties Microstructure and Processing, 2007. **457**(1-2): p. 180-185.
121. Inthidech, S. and Y. Matsubara, *Effect of Alloying Elements on Variation of Micro-Hardness during Heat Treatment of Hypoeutectic High Chromium Cast Iron*. Materials Transactions, 2008. **49**(10): p. 2322-2330.
122. Qu, Y.H., et al., *Effect of cerium on the as-cast microstructure of a hypereutectic high chromium cast iron*. Materials Letters, 2008. **62**(17-18): p. 3024-3027.

123. Wiengmoon, A., et al., *Effects of heat treatment on hardness and dry wear properties of a semi-solid processed Fe-27 wt pct Cr-2.9 wt pct C cast iron*. Journal of Materials Science & Technology, 2008. **24**(3): p. 330-334.
124. Wiengmoon, A., et al., *Electron microscopy and hardness study of a semi-solid processed 27 wt%Cr cast iron*. Materials Science and Engineering a-Structural Materials Properties Microstructure and Processing, 2008. **480**(1-2): p. 333-341.
125. Zhi, X., et al., *Effect of fluctuation and modification on microstructure and impact toughness of 20 wt.% Cr hypereutectic white cast iron*. Materialwissenschaft Und Werkstofftechnik, 2008. **39**(6): p. 391-393.
126. Zhi, X.H., et al., *Effect of titanium on the microstructure of hypereutectic high-chromium cast iron*. Rare Metal Materials and Engineering, 2008. **37**(1): p. 101-104.
127. Zhi, X.H., et al., *Effect of titanium on the as-cast microstructure of hypereutectic high chromium cast iron*. Materials Characterization, 2008. **59**(9): p. 1221-1226.
128. Zhi, X.H., et al., *Effect of niobium on the as-cast microstructure of hypereutectic high chromium cast iron*. Materials Letters, 2008. **62**(6-7): p. 857-860.
129. Zhi, X.H., et al., *Effect of heat treatment on microstructure and mechanical properties of a Ti-bearing hypereutectic high chromium white cast iron*. Materials Science and Engineering a-Structural Materials Properties Microstructure and Processing, 2008. **487**(1-2): p. 171-179.
130. Albertin, E. and A. Sinatora, *Effect of carbide fraction and matrix microstructure on the wear of cast iron balls tested in a laboratory ball mill*. Wear, 2001. **250**: p. 492-501.
131. Demello, J.D.B., M. Durandcharre, and T. Mathia, *Abrasion mechanisms of white cast-iron Part II Influence of the metallurgical structure of V-Cr white cast irons*. Materials Science and Engineering, 1986. **78**(2): p. 127-134.
132. Chen, H.X., et al., *Effect of niobium on wear-resistance of 15-percent Cr white cast-iron*. Wear, 1993. **166**(2): p. 197-201.

133. Li, L. and D.Y. Li, *Understanding the influence of microstructure features on the erosion resistance of low-carbon pipeline steel through computational simulation*. *Wear*, 2013. **301**(1-2): p. 70-75.
134. Hutchings, I.M., *Tribology Friction and Wear of Engineering Materials*. 1992, Boca Raton: CRC Press
135. Dolman, K. *Metallurgy of white cast iron: effect of alloying elements and heat treatment in 36th Australian Foundry Institute National Conference*. 2005. Sydney.
136. Gundlach, R.B., *High-Alloy White Irons*. ASM Handbook. Vol. 15. 2002, Metals Park, OH.
137. Stevenson, A.N.J. and I.M. Hutchings, *Wear of hardfacing white cast irons by solid particle erosion*. *Wear*, 1995. **186**(1): p. 150-158.
138. Zumgahr, K.H. and D.V. Doane, *Optimizing fracture-toughness and abrasion resistance in white cast irons*. *Metallurgical Transactions a-Physical Metallurgy and Materials Science*, 1980. **11**(4): p. 613-620.
139. Xu, L.Q., C. Vose, and D. Stjohn, *Abrasive wear study of selected white cast irons as liner materials for the mining-industry*. *Wear*, 1993. **162**: p. 820-832.
140. Aptekar, S.S. and T.H. Kosel, *Erosion of white cast irons and stellite*. 1985.
141. McLeod, A.J. and R.E. Clegg, *Effect of exposure time on the morphology of corrosion on high chromium white cast iron in high temperature caustic solutions*. *Materials and Corrosion-Werkstoffe Und Korrosion*, 2013. **64**(5): p. 381-387.
142. Neville, A., et al., *Characterization and corrosion behavior of high-chromium white cast irons*. *Metallurgical and Materials Transactions a-Physical Metallurgy and Materials Science*, 2006. **37A**(8): p. 2339-2347.
143. Parks, J.L., *Characteristics of As-Cast and Subcritically Heat-Treated High-Chromium-Molybdenum White Irons for Thick-Section Castings*. *AFS Trans.*, 1978. **86**: p. 93-102.

144. Tabrett, C.P. and I.R. Sare, *Effect of high temperature and sub-ambient treatments on the matrix structure and abrasion resistance of a high-chromium white iron*. Scripta Materialia, 1998. **38**(12): p. 1747-1753.

3 MICROSTRUCTURE/WEAR MAPPING – GENERAL BEHAVIOR OF HCCI

The objective of this chapter is to present the development of wear mappings of the expanded HCCI system and their general wear behaviors and correlation with microstructural features. In order to provide meaningful rankings and guidelines for material selection, abrasion and slurry erosion testing methods were selected to evaluate the wear behavior of the HCCIs, since these are two of the most frequent wear modes in oil sands mining and extraction. Results of this research have led to a series of publications that report case studies presented in following chapters of the thesis.

This work was conducted in collaboration with the Materials Development Center of Weir Minerals in Australia. Results have been incorporated in a software that has been used to aid materials selection for slurry pumps and wear liners in Alberta oil sands operations and other mining processes throughout the world. Because the outcome of this work is proprietary to Weir Minerals, only a selected group of results is presented. However, established microstructure-property relationships are applicable to the entire HCCI system.

3.1 Experimental techniques

In order to properly compare and understand the wear behavior of the entire expanded range of HCCIs, the most suitable approach is to develop wear

maps using the same experimental techniques with same testing parameters. The tribological systems are complex and direct comparison among results obtained from different testing methods could lead to misleading explanations. This makes it difficult to develop guidelines for material selection based on wear data reported in the literature. Therefore, the entire expanded HCCI system was studied, which included fifty-three alloys in total as shown in figure 3.1. Actual chemical compositions of the alloys are given in table 3.1.

45	45-1	45-2	45-3	45-4	45-5	45-6
40	40-1	40-2	40-3	40-4	40-5	40-6
35	35-1	35-2	35-3	35-4	35-5	35-6
30	30-1	30-2	30-3	30-4	30-5	30-6
25	25-1	25-2	25-3	25-4	25-5	25-6
20	20-1	20-2	20-3	20-4	20-5	20-6
15	15-1	15-2	15-3	15-4	15-5	15-6
10	10-1	10-2	10-3	10-4	10-5	10-6
5	5-1	5-2	5-3	5-4	5-5	
	1	2	3	4	5	6

Figure 3.1: Sample IDs for the expanded HCCI alloys produced for wear and corrosion mapping.

Table 3.1: Actual chemical analysis of the cast plate samples produced.

Nominal								
Wt.%	Composition (wt%)							
Cr-C	C	Cr	Mn	Si	Ni	Mo	Cu	S
5-1	1.36	5.0	1.91	0.38	0.03	<0.01	<0.01	<0.01
5-2	2.09	5.2	1.93	0.44	0.03	<0.01	<0.01	<0.01
5-3	2.87	5.3	1.94	0.49	0.04	<0.01	0.01	0.01
5-4	3.85	5.3	1.96	0.48	0.03	<0.01	0.01	0.01
5-5	4.78	5.3	2.14	0.57	0.04	<0.01	<0.01	0.01
10-1	1.17	10.2	1.80	0.56	0.06	<0.01	<0.01	0.01
10-2	1.96	10.3	1.82	0.53	0.05	<0.01	<0.01	0.01
10-3	2.93	10.4	2.01	0.79	0.05	<0.01	<0.01	<0.01
10-4	4.09	12.0	2.09	0.51	0.07	<0.01	<0.01	<0.01
10-5	4.74	9.5	2.14	0.54	0.07	<0.01	0.01	0.01
10-6	5.61	9.9	2.21	0.70	0.06	<0.01	0.01	0.01
15-1	1.17	14.8	1.65	0.71	0.23	0.03	0.03	0.01
15-2	1.86	15.1	1.85	0.77	0.27	0.04	0.04	0.01
15-3	2.97	14.8	1.90	0.78	0.15	0.01	0.02	0.01
15-4	3.85	14.7	1.96	0.83	0.10	<0.01	0.01	0.01
15-5	4.67	15.0	2.01	0.74	0.09	<0.01	0.01	0.01
15-6	5.58	14.8	2.03	0.71	0.08	<0.01	0.01	0.01

Nominal								
Wt.%	Composition (wt%)							
Cr-C	C	Cr	Mn	Si	Ni	Mo	Cu	S
20-1	1.22	19.4	1.74	0.81	0.10	<0.01	<0.01	<0.01
20-2	1.93	19.5	1.81	0.76	0.14	0.01	0.01	0.01
20-3	2.72	19.8	1.95	0.67	0.12	<0.01	0.01	<0.01
20-4	3.68	19.8	1.94	0.64	0.11	<0.01	0.01	0.01
20-5	4.65	19.7	2.08	0.60	0.11	<0.01	0.01	0.01
20-6	5.69	20.1	2.09	0.64	0.11	<0.01	0.01	0.01
25-2	1.97	24.8	1.69	0.55	0.37	0.04	0.04	0.02
25-3	2.83	24.6	1.73	0.44	0.32	0.04	0.03	0.02
25-4	3.72	24.8	1.56	0.38	0.30	0.03	0.03	0.02
25-5	4.54	24.5	1.83	0.57	0.14	<0.01	0.01	0.01
25-6	5.73	24.2	1.83	0.62	0.11	<0.01	0.01	0.01
25-1	1.21	25.7	1.53	0.44	0.15	0.01	0.01	<0.01
30-1	1.11	29.6	1.71	0.56	0.16	<0.01	0.01	<0.01
30-2	1.84	30.0	1.74	0.38	0.14	<0.01	0.01	0.01
30-3	3.07	30.1	1.74	0.62	0.28	0.01	0.01	0.01
30-4	3.94	29.9	1.81	0.64	0.22	<0.01	0.02	0.01
30-5	4.66	29.0	2.01	1.00	0.19	<0.01	0.01	0.01
30-6	5.63	28.6	1.95	0.95	0.20	0.01	0.02	0.01

Nominal								
Wt.%	Composition (wt%)							
Cr-C	C	Cr	Mn	Si	Ni	Mo	Cu	S
35-1	1.23	34.8	1.70	0.55	0.22	<0.01	0.01	<0.01
35-2	2.06	35.4	1.68	0.49	0.19	<0.01	0.01	0.01
35-3	2.97	34.4	2.00	0.62	0.19	<0.01	0.01	0.01
35-4	4.38	35.1	1.76	0.58	0.19	<0.01	0.01	0.01
35-5	4.73	34.4	1.92	0.71	0.18	<0.01	0.01	0.01
35-6	5.88	33.3	1.99	0.76	0.16	<0.01	0.01	0.01
40-1	1.14	39.2	1.49	0.78	0.21	<0.01	0.01	<0.01
40-2	2.18	39.8	1.55	0.69	0.17	<0.01	0.01	0.01
40-3	3.12	39.6	1.70	0.54	0.15	<0.01	0.01	0.01
40-4	4.58	39.2	1.45	0.42	0.19	<0.01	0.01	0.01
40-5	5.87	38.7	1.67	0.53	0.19	<0.01	0.01	0.01
40-6	7.11	37.4	1.65	0.71	0.18	<0.01	0.01	0.01
45-1	1.36	45.1	1.90	0.49	0.26	<0.01	0.01	<0.01
45-2	2.21	45.2	1.77	0.51	0.22	<0.01	0.01	0.01
45-3	3.20	43.8	1.76	0.50	0.24	<0.01	0.01	0.01
45-4	4.02	41.2	2.61	0.61	0.23	<0.01	0.01	0.01
45-5	5.03	43.0	1.80	0.70	0.20	<0.01	0.01	0.01
45-6	6.06	42.2	2.01	0.78	0.22	<0.01	0.01	0.01

3.1.1 Alloy preparation

All HCCI alloy plates were cast in a sand mold using a Weir Minerals proprietary casting technique. Prior to machining, the cast plates were solution treated at 1160 °C and immediately cooled down by a blast of compressed air, followed by heat treatment at 950 °C for 5 hours and immediately cooled by the compressed air. These plate castings were then cut into specimens with various dimensions: a) 12×12×10 mm for microstructure characterization and electrochemical tests; b) 76×25×10 mm for dry abrasion tests, and c) 50x10x5 mm for slurry erosion tests, all using an Accutom-5 automatic precision cut-off machine (Struers A/S, Denmark). Alloys were identified by their Cr and C nominal content (in weight) separated by a dash. The actual chemical composition of the plates, listed in table 3.1, was determined by optical atomic absorption spectroscopy except for C and S, which were determined by combustion Leco analyzer.

3.1.2 Microstructural characterization and micromechanical properties

Specimens were ground using silicon carbides papers from 60 up to 1200 grit, then polished by nylon cloth with a diamond slurry of 5 um, followed by fine polishing with 1µm diamond suspension on a finer polishing cloth. Samples for optical microscopy were etched using a solution of 50 ml FeCl₃, 20 ml of HCl, and 20 ml of ethanol. This solution attacks preferentially the matrix leaving the carbides relatively unaffected, which provides good contrast between the two

phases [1]. Optical microscopy was undertaken using an Olympus PME3-ADL and images were analyzed with the aid of the software “ImagePro”. The stereographic measurements were performed on three representative micrographs for each sample. XRD patterns were obtained using a Rigaku X-ray diffractometer with Cu K α radiation. Scanning electron microscopy (SEM) and energy dispersive X-ray spectrometry (EDX) analysis were carried out using a Zeiss EVO SEM with LaB6 crystal equipped with an ultrathin window X-ray detector. A Hitachi S-2700 SEM was also used. Micro-hardness was determined on lightly etched samples using a micro-indenter (Fisher Technology Ltd., Winsor, CT, USA) under a load of 100 mN. Each reported micro-hardness value was an average of fifteen measurements.

3.1.3 Abrasion testing

The abrasion wear resistance of the HCCIs was evaluated using ASTM G-65 dry sand/rubber wheel apparatus following Procedure A [2], which gives the most severe testing condition suitable for abrasion-resistant materials such HCCIs. Samples were prepared with conventional metallographic preparation procedures, using silicon carbide papers from 60 to 600 Grit successively, to produce a surface roughness (Ra) below 0.120 μm . Before testing, samples were cleaned thoroughly in ethanol, dry by compressed air, and initial weights were measured. The balance used to measure the mass loss has a sensitivity of 0.1 mg.

The abrasive used was Ottawa sand, AFS 50-70 from U.S. Silica Company, USA, which is fairly common for the ASTM G65 tests. A new batch of sand was used for each test. The particle size distribution is shown in figure 3.2, where 95% of particles have their size in the range of 212 μm . The AFS 50-70 Ottawa sand is well adopted by the oil sands industry for abrasion tests. A comparison between the Ottawa Sand AFS 50-70 and a typical oil sand tailings solid sample has been reported by Clark and Llewellyn [3]. Their overall morphologies are illustrated in figure 3.3.

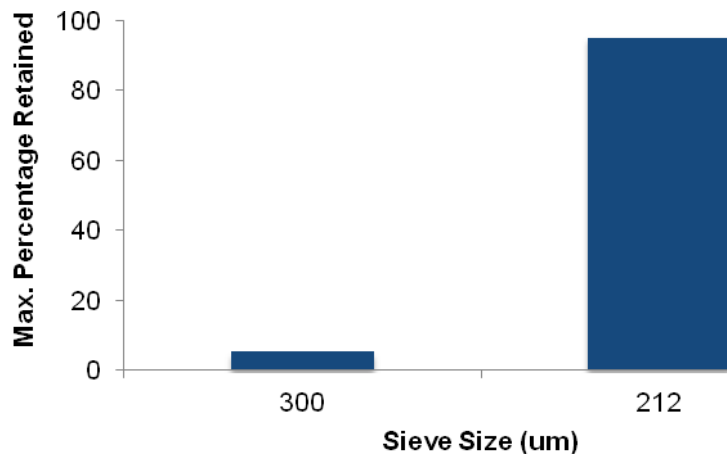


Figure 3.2: Particle size distribution of the Ottawa sand, AFS 50-70, used for dry abrasion tests.

The sand flow rate was adjusted between 300~400 g/min. A contact load of 130 N was selected. The number of wheel revolution was set as 6000 and the rotational speed was set as 200RPM +/- 10, resulting in total abrasion linear distance of 4309 m.

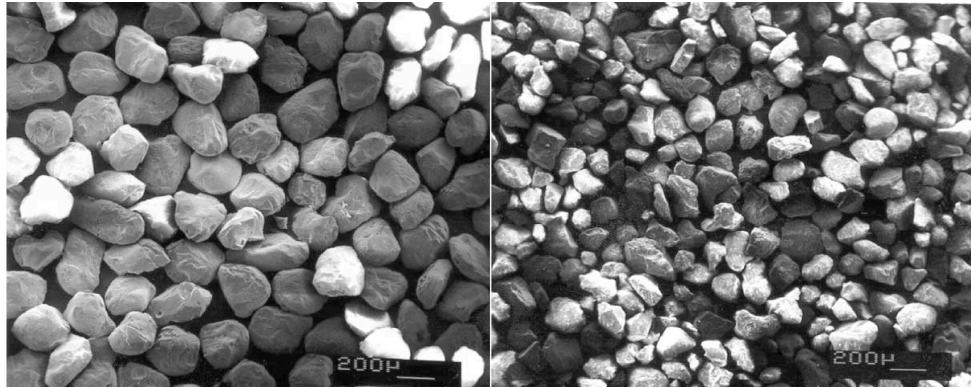


Figure 3.3: Comparison of Ottawa Sand AFS 50–70 used for abrasion tests (left) with typical oil sands tailings solids (right) [3].

After each test, samples were cleaned with ethanol, dried with compressed air, and weighed. The abrasive wear resistance of the HCCIs was reported in terms of volume loss [2, 4, 5]:

$$Volume\ Loss\ (mm^3) = \frac{Mass\ Loss\ (g)}{Density\ \left(\frac{g}{cm^3}\right)} \times 1000 \quad \{3.1\}$$

The wheel diameter and thickness were always measured and visually inspected before and after each test. The actual volume loss was corrected to account for any change in the wheel diameter. Therefore, reported volume loss represents the ones produced by a 228.6 mm (9 in.) wheel. Each test was repeated two times and the average reported. Initial testing of HCCIs in the dry abrasion-testing rig showed standard deviation of approximately 10%.

The adjusted volume loss (AVL) was calculated as follows: [2]

$$AVL = \text{Measured Volume Loss} \times \frac{228.6 \text{ mm (9.00 in.)}}{\text{Wheel Diameter After Use}} \quad \{3.2\}$$

3.1.4 Slurry erosion testing

Samples were prepared following conventional metallographic preparation procedures using silicon carbide papers from 60 to 600 Grit successively to produce a surface roughness (Ra) below 0.120 μm . Before testing, samples were cleaned thoroughly in ethanol, dry with compressed air, and initial weights were measured to a sensitivity of 0.1mg. The slurry consisted of tap water and silica abrasive at 20% volume concentration. The pH was maintained neutral as oil sands slurry is near pH=8. It was worth maintaining a neutral pH to sustain some corrosion during tests. For some particular experiments where corrosion needed to be suppressed, NaOH was added to the slurry as an inhibitor.

The abrasive used was silica sand, AFS 12-50, from Morinville, Alberta. This sand is a high quality close graded sand with sub-rounded characteristics and 5-7 Moh hardness. The particle size distribution is depicted in figure 3.4. Nearly 45% of the particles are in the 600 μm range. The morphology of the sand particles can be seen in figure 3.5. This sand distribution and morphology has been found through preliminary testing in the research group to be adequate for inducing consistent wear in the slurry pot tester.

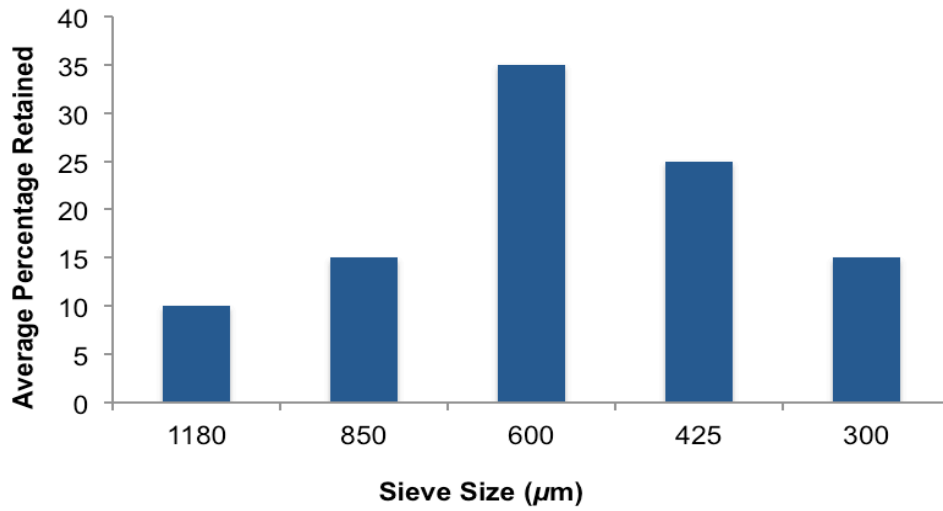


Figure 3.4: Particle size distribution of the silica sand, AFS 12-50, used for slurry erosion tests.

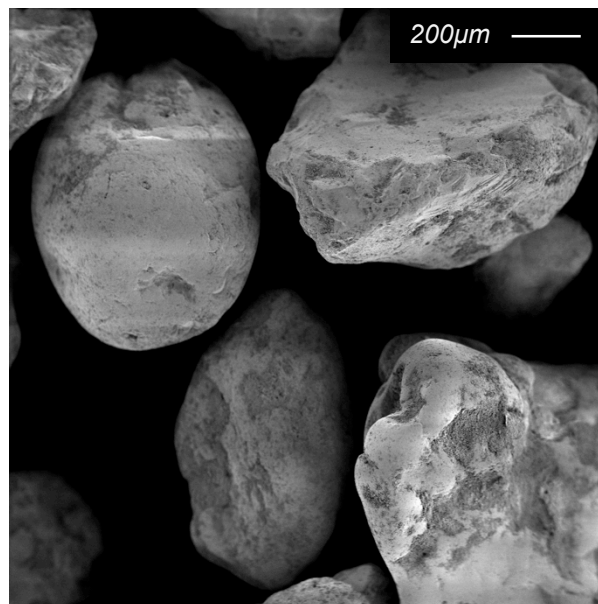


Figure 3.5: A SEM micrograph of the AFS 12-50 silica sand used for the slurry erosion tests.

The slurry temperature was set at $60^{\circ}\text{C} \pm 2$ to simulate working conditions of slurry pumps and slurry pipelines in oil sands extraction. Likewise,

the linear slurry velocity was selected in the range of 2.5 to 8 m/s. All tests were completed with a distance of 25 km for the sample to travel in the slurry at 15°, 30°, 45°, 60°, 75°, and 90° impingement angle. This test distance was selected in order to produce measurable and repeatable results. This was assessed by preliminary experiments with two materials: commercial HCCI used in slurry pumps; and API X70 steel used in hydrotransport pipe. Three different total erosion distances: 15, 25, and 35 km were used for tests with the aim of evaluating the repeatability of test results. Six samples were tested at each distance at 45 deg. impingement angle. It turned out that 25 km produced the lowest scatter among the three distances, with standard deviation of 5%.

After each test was completed, samples were removed immediately, cleaned with ethanol, dried with compressed air, and weight losses were then measured. Throughout the experiment the dissolved oxygen stabilized at approximately 3.8 ± 0.2 ppm at normal aeration. Each experiment was repeated at least two times.

The slurry pot tester configuration, as shown in figure 3.6, consists of a 2HP AC motor, six fluid baffles to disrupt the flow and maintain the erosive stream, and a shaft plate where four sample holders are attached in certain predetermined positions depending on the desired impingement angle. All components in the slurry pot that are in contact with the slurry are made of stainless steel. To maintain the desired temperature, a band heater is used which is

controlled by a thermocouple system with a temperature controller. The system was cleaned thoroughly after each test, so new slurry mixture was always used.

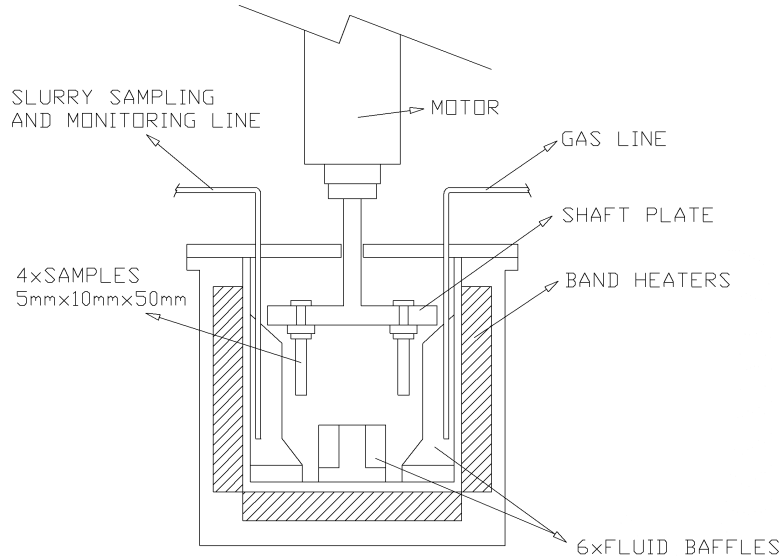


Figure 3.6: A schematic diagram of the slurry pot apparatus.

3.1.5 Electrochemical testing

The corrosion resistance of the HCCIs was evaluated by electrochemical testing in tap water, at pH=3, 5 and 7. The pH was adjusted with NaOH and H₂SO₄. Each specimen of HCCIs was connected to a metal wire and mounted in an epoxy resin with a surface area of approximate 1.44 cm² exposed to the testing solution. The exposed surface was then ground with silicon carbide papers up to 600 grit, and then degreased with acetone and rinsed with distilled water, and finally dried with compressed air. The polarization resistance, R_p , was used to rank the corrosion resistance of HCCIs, since the corrosion current density (I_{Corr}) is inverse proportional to R_p as follows:

$$I_{corr} = \frac{B}{R_p} \quad \{ 3.3 \}$$

where B is a constant for a specific corrosion system [6]. The linear polarization of the samples was recorded with a commercial electrochemical system (PC4-750, Gamry Instruments, Inc., USA) within the range of ± 30 mV versus open circuit potential, E_{ocp} , at a scanning rate of 0.125 mV/s. The R_p was determined as the tangent of the polarization curve at $I = 0$. A Saturated Calomel Electrode (SCE) was used as the reference electrode and a platinum plate with area of 2 cm² was used as the counter electrode. All measurements were repeated at least three times.

3.2 Microstructure

The solidification sequence for the sets of carbon and chromium compositions being studied are depicted on the iron rich corner of the metastable Fe-Cr-C liquidus surface diagram presented in figure 3.7.

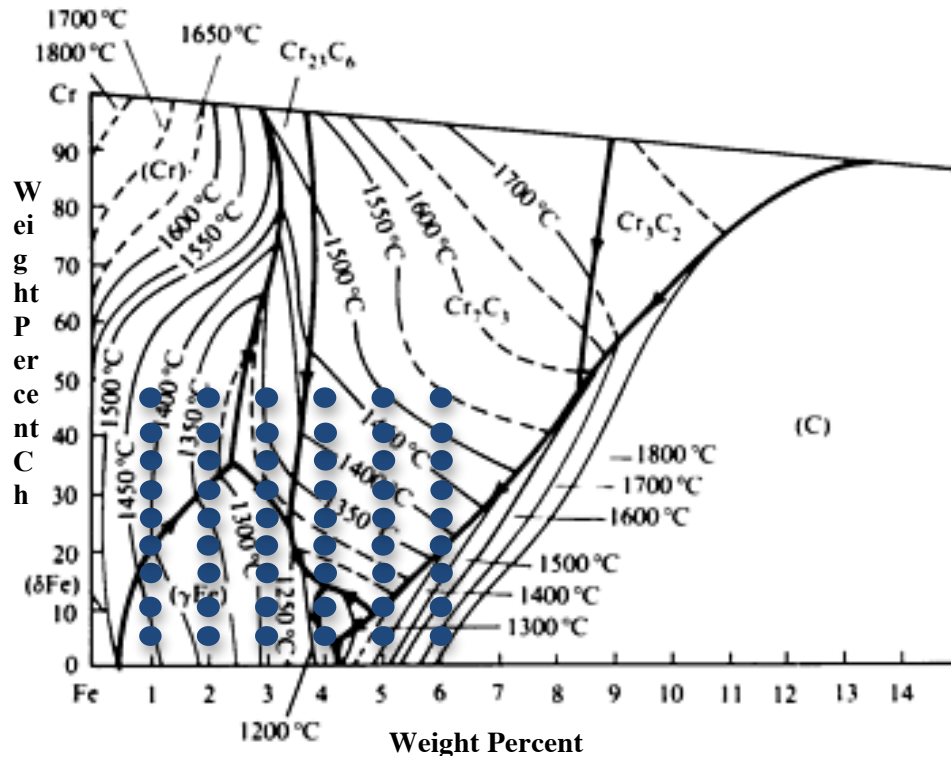


Figure 3.7: Iron rich corner of the metastable Fe-Cr-C liquidus surface showing the set of carbon and chromium compositions investigated in this work [8].

Their solidification path and corresponding microstructural evolution throughout the liquid to solid transformations depend primarily on the carbon and chromium chemical content. Other casting parameters such as cooling rates and pouring temperature are also important [7], and were maintained as uniform as possible for all castings. The microstructure phases can include ferrite ($\alpha\delta$), austenite (γ), M_7C_3 , $M_{23}C_6$, and/or M_3C carbides, in various configurations depending on the reactions that take place.

The resulting microstructures obtained for the entire HCCI compositional range have been grouped according to their primary phase to facilitate their discussion and are presented in the following sections.

3.2.1 Microstructures that began solidification from primary austenite (γ)

A large group of the HCCIs studied began solidification with primary austenite nucleated from the liquid at temperatures ranging from 1500 to 1150°C. There were two different resulting microstructures from this group of hypoeutectic alloys, with carbon ranging from 1 to 4 wt.% C, depending on the eutectic reaction that followed the primary solidification.

Between 10 to 30 wt.% nominal Cr, the final resulting microstructure consisted of austenite dendrites surrounded by a relatively fine distribution of eutectic austenite (γ) and M_7C_3 carbides. After heat treatment, small secondary carbides of M_7C_3 , $M_{23}C_3$, and/or M_3C , precipitated in the austenitic matrix, which depleted chromium and carbon in the ferrous matrix and consequently facilitated the martensitic transformation by increasing the temperature at which martensite begins to form. A microstructure featuring this morphology is shown in figure 3.8, which corresponds to alloy 15-2. The final liquid of this group of alloys solidified by the eutectic precipitation of austenite (γ) and M_7C_3 carbides.

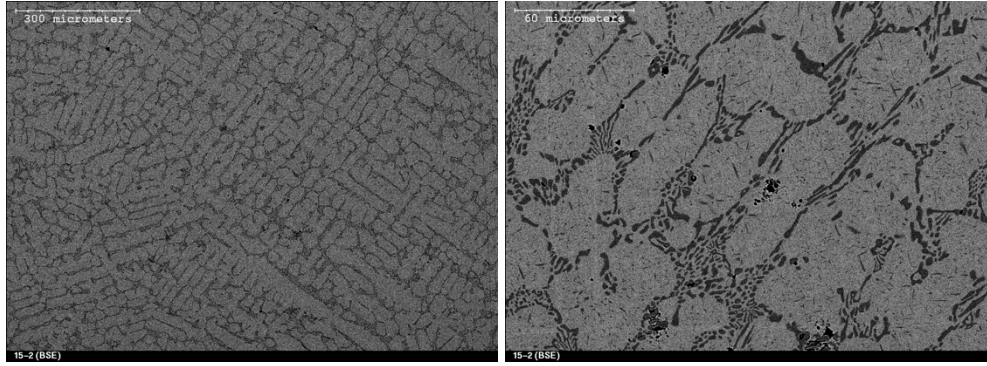


Figure 3.8: Hypoeutectic microstructure of alloy 15-2, at two different magnifications, obtained through SEM backscattered. The resulting microstructure features primary austenite (γ) surrounded by eutectic precipitation of austenite (γ) and M_7C_3 .

Below 10Wt.% Cr, the final microstructure consisted of austenite (γ) dendrites surrounded by a fine mixture of eutectic austenite (γ) and M_3C carbides, as shown in figure 3.9 for alloy 5-1. Their solidification began with the formation of primary austenite (γ) as described previously, but it was completed with a different eutectic reaction in which austenite (γ) and M_3C carbides precipitated instead of M_7C_3 carbides. After heat treatment, the austenitic matrix transformed into martensite aided by the lower chromium levels. Due to reduction in the number of secondary carbides precipitated into the ferrous matrix (low chromium content), they became coarser as seen in figure 3.9.

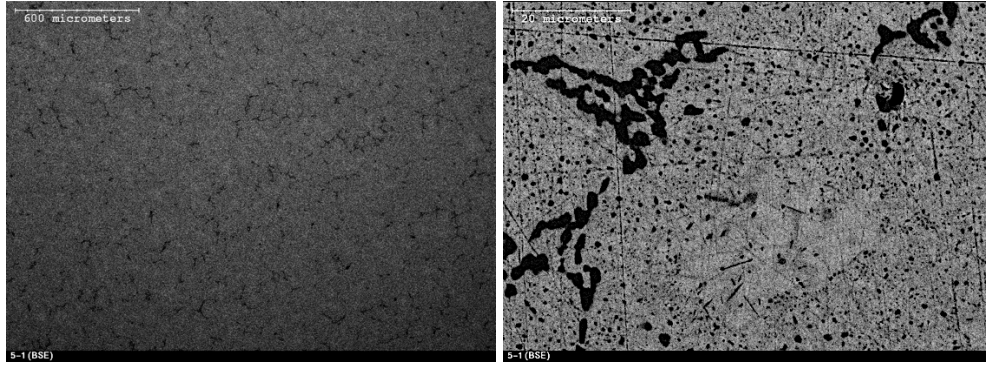


Figure 3.9: Hypoeutectic microstructures of alloy 5-1 at two magnifications (SEM backscattered). The microstructure consists of primary austenite (γ) surrounded by eutectic precipitation of austenite (γ) and M_3C carbides.

3.2.2 Microstructures that began solidification from primary ferrite ($\alpha\delta$)

At the lower carbon content, 1 and 2 wt.%, another group of samples developed microstructures featuring ferrite ($\alpha\delta$) as primary phase. This primary phase nucleates between 1500°C and 1175°C. Depending on the solidification path followed after the primary solidification, two types of microstructures were developed.

Below 30 wt.% Cr, the resulting microstructure consisted of a coarse highly segregated dendritic structure of austenite (γ) with a ferrite ($\alpha\delta$) skeleton or domains within the secondary arms. The interdendritic spaces feature a mixture of peritectic M_7C_3 carbides and austenite (γ). A typical microstructure of this subgroup, corresponding to alloy 15-1, is presented in figure 3.10.

This type of microstructure is produced by the peritectic reaction in which the liquid reacts with ferrite ($\alpha\delta$) to precipitate austenite (γ) until exhausted by formation of an austenite shell surrounding the proeutectic grains (ferrite ($\alpha\delta$)). This reaction is succeeded by a final quasitectic peritectic reaction in which the remaining liquid reacted with the ferrite ($\alpha\delta$) to produce a mixture of peritectic austenite (γ) and M_7C_3 carbides in the final microstructure.

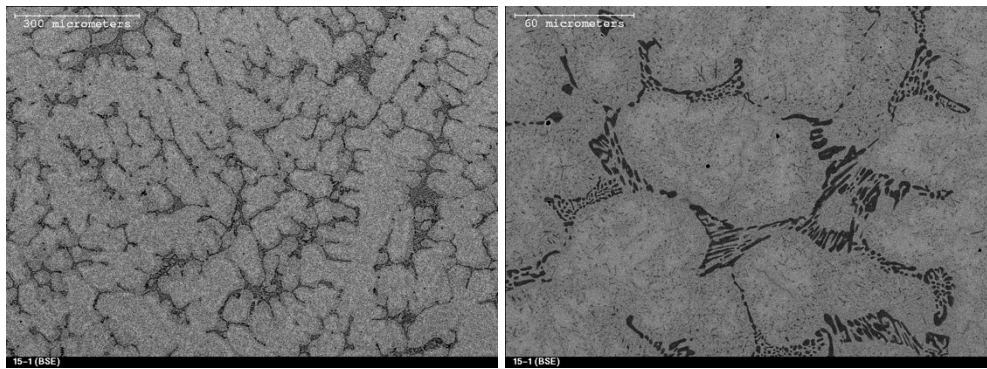


Figure 3.10: Microstructure of alloy 15-1, at two different magnifications (SEM backscattered). The microstructure consists of peritectic formation of austenite (γ) and M_7C_3 carbides from the liquid- ferrite ($\alpha\delta$) reaction.

When the chromium content is above 30 wt.%, the resulting microstructure features a complete ferrite ($\alpha\delta$) grains or matrix structure surrounded by a well dispersed mixture of $M_{23}C_6$ carbides and ferrite ($\alpha\delta$). Upon heat treatment, carbide precipitation occurs in the matrix, mainly of $M_{23}C_6$ carbides.

These microstructures developed through a eutectic solidification similar to the one described for the first type of samples with austenite (γ) as primary phase. In this case, the formation of primary ferrite ($\alpha\delta$) is followed by the precipitation of eutectic ferrite ($\alpha\delta$) and M_7C_3 carbides, and then completed, if there is any remaining liquid, by the quasi peritectic reaction where the final liquid reacts with the ferrite ($\alpha\delta$) to produce a mixture of austenite (γ) and M_7C_3 carbides.

A typical microstructure is shown in figure 3.11, taken from alloy 40-2.

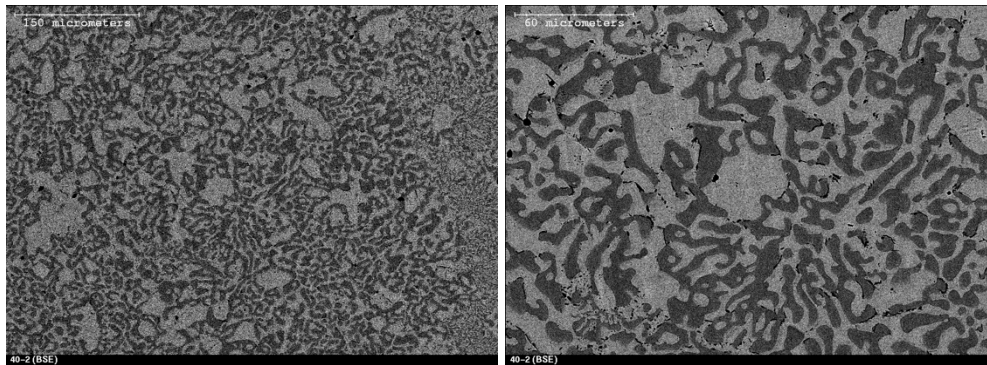


Figure 3.11: Microstructure of alloy 40-2, at two different magnifications (SEM backscattered). The resulting microstructure features primary ferrite ($\alpha\delta$) and eutectic $M_{23}C_6$ carbides.

3.2.3 Microstructures developed from primary M_7C_3 carbides

The final group of microstructures observed belong to the samples with carbon nominal content generally above 3 wt.%, that featured primary M_7C_3 carbides as primary phase with carbon that nucleates from the liquid at

temperatures between 1450 to 1250°C. Within this group, there were two different resulting hypereutectic microstructures depending on the eutectic reaction that occurred following the primary solidification.

Above 10 wt.% Cr, the microstructures featured coarse primary polygonal shaped M_7C_3 carbides surrounded by colonies of austenite (γ) and M_7C_3 carbides. Coarse needle like M_7C_3 carbides were also observed, which are the same polygonal carbide rods but exposed to their longitudinal plane [9-11]. As the overall carbon content was raised, it was evident that the carbides became coarser and their volume fraction increased. For this group, once the primary M_7C_3 carbides nucleated, the solidification proceeded with the eutectic precipitation of a mixture of austenite (γ) and M_7C_3 carbides than completed the solidification. A representative microstructure of this type of hypereutectic alloys is shown in figure 3.12, taken from alloy 25-4.

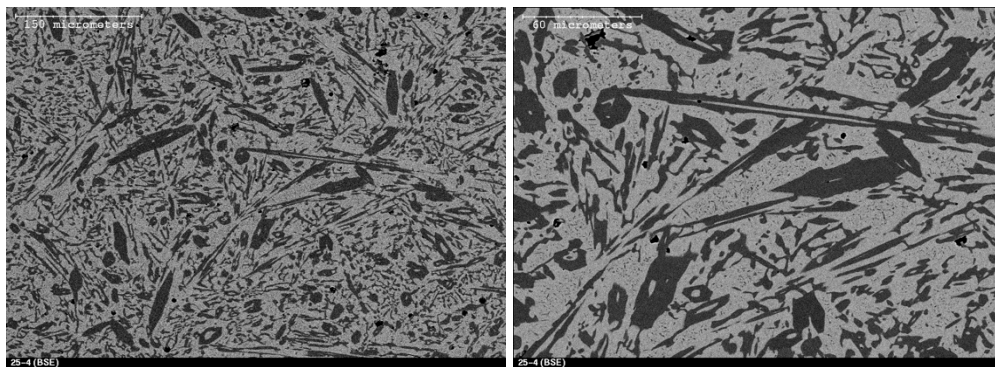


Figure 3.12: Hypereutectic microstructure of alloy 25-4, at two different magnifications (SEM backscattered). The resulting microstructure features primary M_7C_3 carbides surrounded by eutectic colonies of austenite (γ) and M_7C_3 .

When chromium content was below 10 wt.%, the resulting hypereutectic microstructure featured large primary coarse duplex carbides of M_7C_3 core and M_3C shell. The surrounding matrix in this case featured an interesting configuration of domains of alternating plates of peritectic M_3C and austenite (γ) while other domains featured a more rod type of configuration. After heat treatment it was expected that the austenite partially transformed to martensite along with secondary carbides precipitation. In this case M_3C and M_7C_3 were both noticed. A representative microstructure for this type of microstructure is presented in figure 3.13 corresponding to alloy 15-6.

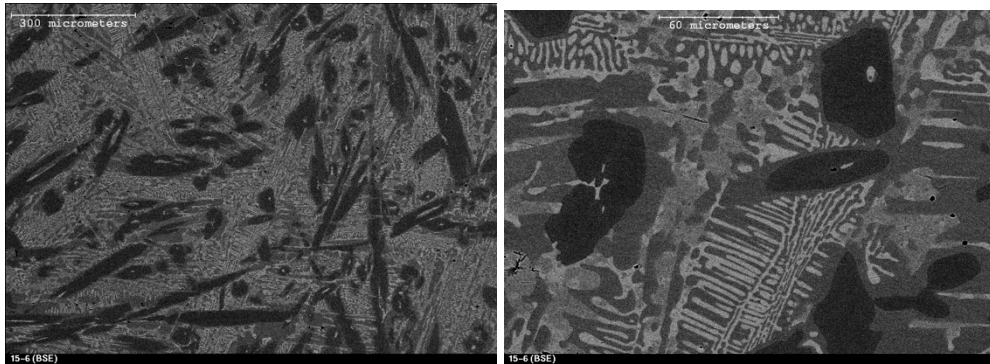


Figure 3.13: Hypereutectic microstructure of alloy 15-6, at two different magnifications (SEM backscattered). The resulting microstructure feature primary M_7C_3 carbide core with a peritectic M_3C carbide shell, surrounded by peritectic austenite (γ).

As can be seen in the iron rich corner of the metastable Fe-Cr-C liquidus surface (figure 3.7), the primary solidification of the M_7C_3 carbides is followed by

the peritectic reaction where the remaining liquid reacts with M_7C_3 carbides to form M_3C which causes the duplex or double layer carbide morphology observed.

A small group of hypereutectic samples above 35 wt.% Cr with 4 wt.% C featured another duplex morphology of primary carbides. In this case, the carbides presented an M_7C_3 core and $M_{23}C_6$ shell. They were both coarse polygonal shaped and needle like type (cross section and longitudinal plane respectively). Their surrounding ferrous matrix consisted of austenite (γ) and $M_{23}C_6$ with an irregular distribution. After heat treatment, the austenite matrix transformed to martensite with retained austenite domains and precipitation of secondary $M_{23}C_6$ carbides. A representative microstructure is presented in figure 3.14 corresponding to alloy 45-4.

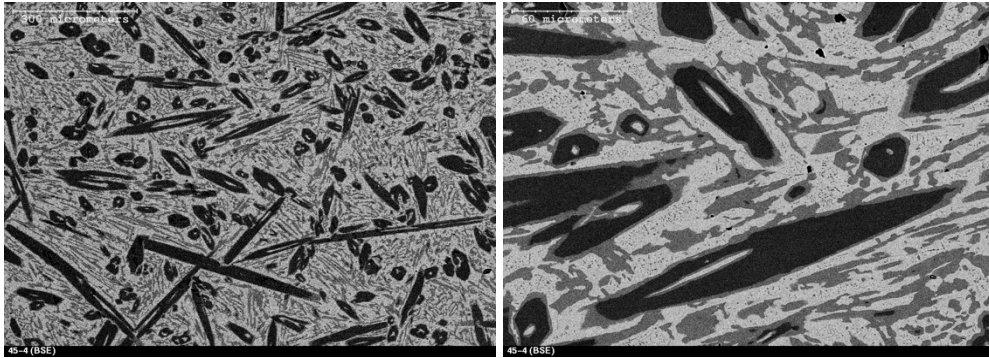


Figure 3.14: Hypereutectic microstructure of alloy 45-4, at two different magnifications (SEM backscattered). The resulting microstructure features primary M_7C_3 carbide core with a peritectic $M_{23}C_6$ carbide shell, surrounded by peritectic austenite (γ) partially transformed to martensite after heat treatment.

This microstructural configuration is produced by the peritectic reaction followed after the primary M_7C_3 carbide nucleation, where the liquid reacts with M_7C_3 carbide to form $M_{23}C_6$ carbides and austenite (γ).

Overall the HCCI system can be treated as a pseudo eutectic system in a binary Fe-C diagram, where the eutectic composition is a function of the chromium content in the alloy. As the chromium increases, the eutectic composition shifts towards lower carbon composition and is given by the eutectic lines in the liquidus surface (figure 3.7).

Throughout the analysis of the thermal history of solidification and the microstructures developed, it was confirmed that the eutectic composition ranges between 4 wt.% C at 5 wt.% Cr to 2.5 wt.% C for the highest chromium of 45 wt.%. This is similar to the information given in published diagrams. An example of a pseudo eutectic diagram obtained for the 15 wt.% Cr series is presented in figure 3.15. Each corresponding microstructure can be seen in figure 3.16, which portrays the microstructural evolution as the carbon composition increases from 1 to 6 wt.% C.

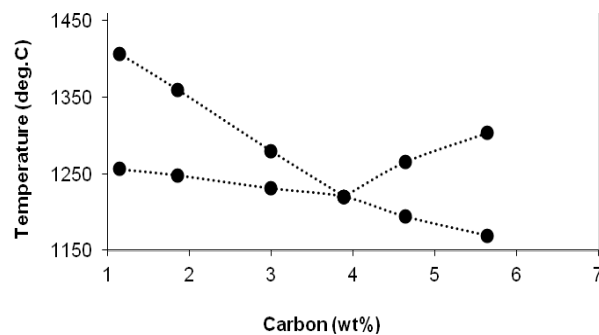


Figure 3.15: Pseudo eutectic diagram for the 15 wt.% Cr series showing the liquidus and solidus lines obtained by the thermal analysis during solidification.

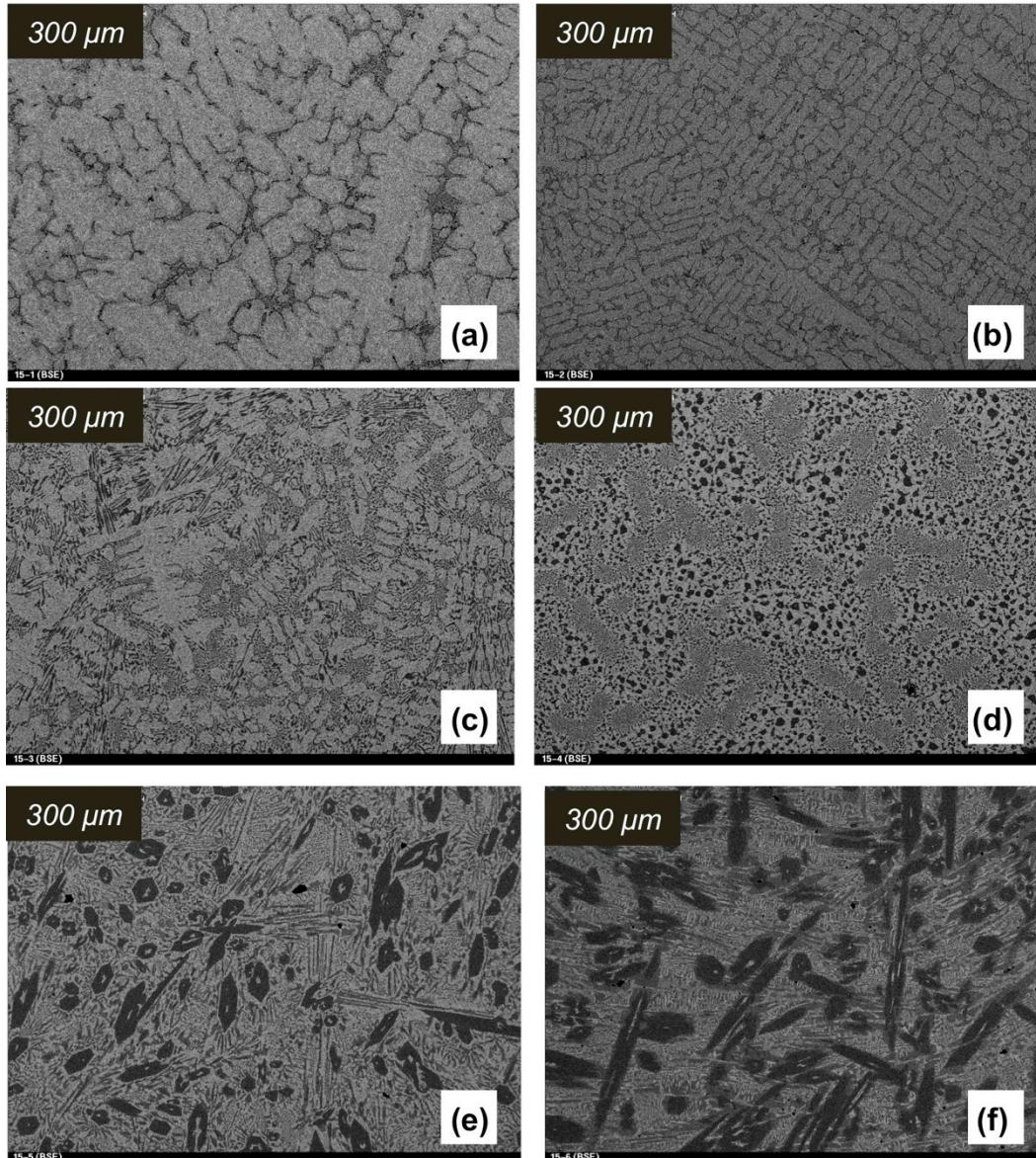


Figure 3.16: Microstructural evolution from a hypoeutectic, eutectic, and hypereutectic state of the 15 wt.% Cr series as carbon nominal composition increases from 1 to 6 wt.% C: (a) 1 wt.% C; (b) 2 wt.% C; (c) 3 wt.% C; (d) 4 wt.% C; (e) 5 wt.% C; (f) 6 wt.% C.

This type of diagram is useful to simplify the analysis of HCCIs. For any given chromium content, the addition of carbon will gradually increase the carbide volume from the hypoeutectic microstructure through a fine distribution

of eutectic carbides, and to the maximum carbide content at the hypereutectic compositions. However, as was discussed earlier, different eutectic reactions can take place and therefore the ferrous matrix and carbide structure can change according to the metastable phases established in the ternary diagram.

3.3 X-ray characterization

The X-ray diffraction patterns for all the alloys were obtained and analyzed. They presented good agreement with the microstructural interpretations made based on morphology of the phases, the liquidus surface, and EDX analysis. Various diffraction patterns are presented in figure 3.17 which correspond to the distinct microstructural groups presented in section 3.2. The major phases identified are listed in table 3.2.

Table 3.2: Summary of phases and crystallographic data encountered through X-ray diffraction patterns.

Phase	Cristal Structure	Space Group
Ferrite ($\alpha\delta$)	BCC	Im3m
Austenite (γ)	FCC	Fm3m
Martensite	Tetragonal	I4mmm
M_7C_3	Hexagonal	Pnma
$M_{23}C_6$	Cubic	Fm3m
M_3C	Hexagonal	Pnma

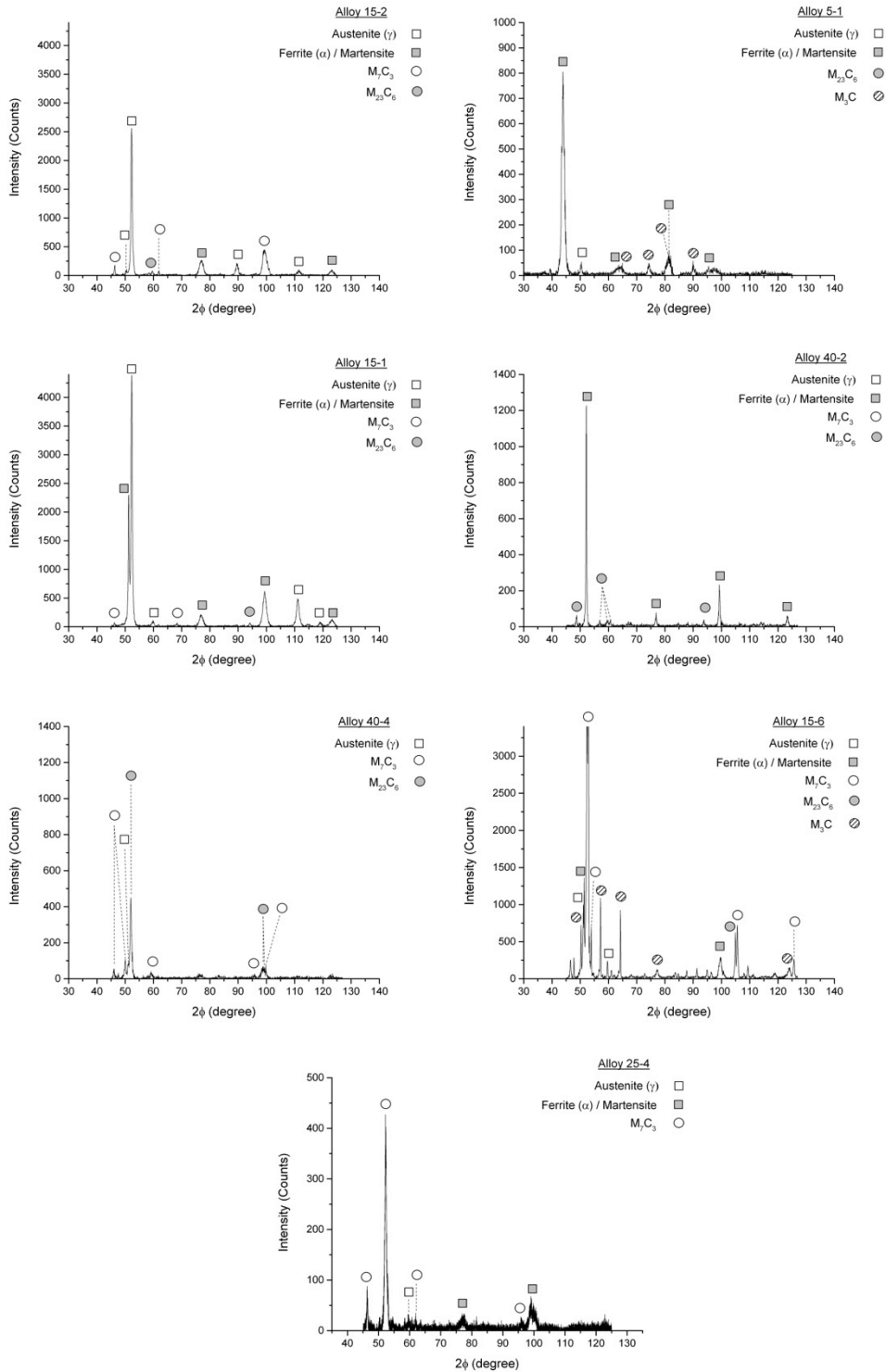


Figure 3.17: X-ray diffraction patterns of various samples corresponding to distinct microstructural configurations presented in section 3.2.

The X-ray diffraction patterns confirmed the final ferrous matrix achieved in the microstructure. In all cases the austenitic matrix transformed to martensite with retained austenite. The presence of secondary carbides of $M_{23}C_6$ and M_7C_3 was also evident. These secondary carbides precipitated into the ferrous matrix preferentially at grain boundaries and sub-grain structures after destabilization treatment [12]. In HCCIs, the tetragonal structure of martensite presents a “c/a” ratio of its lattice parameters near 1 that is a “bcc” crystal structure. This makes it difficult to distinct ferrite and martensite peaks, which is the reason they have been grouped with the same labels. This has been attributed to the larger tetragonal and octahedral interstices formed in the Fe-Cr fcc lattice [13].

3.4 Phase microchemistry

In the HCCI system, the carbides or so called chromium carbides that formed in-situ may have different formula, denoted by M_7C_3 , $M_{23}C_6$, and M_3C . “M” represents Fe, Cr, and other elements that are thermodynamically driven to partition into them [7, 10, 14, 15]. The distribution of these elements has been seen to have an effect on the micro mechanical properties of the carbides [14].

Increasing the overall chromium composition affects the content of chromium in primary M_7C_3 carbides. As shown in figure 3.18, the chromium content in the carbide phase increases rapidly from 5~10% to 60~70% with an increase in the nominal Cr content from 5 to 45 wt.%. At higher overall carbon compositions, the chromium content in the carbide phase is generally lower at any

chromium composition. This trend was observed in all alloys under study, including the hypoeutectic and eutectic ones (1, 2 and 3 wt.% C). The chemical analysis of primary and eutectic carbides did not show any significant difference. This is in agreement with previous studies, e.g., that reported by Atamer and Bhadeshia [16] on HCCIs hardfacing alloys.

The chromium content in the ferrous matrix also increased with an increase in the overall chromium concentration but less rapidly than in the carbide phase. Figure 3.19 shows this behavior for the three hypereutectic carbon compositions, where the maximum chromium in the matrix only reached approximately 16% for the lowest carbon content. With the increase in overall carbon concentration, the chromium in the matrix was also reduced and became more evident as the overall contents of chromium and carbon were raised. This is attributed to the larger number of carbides nuclei formed. Similar results were reported by Dogan and Hawk, who investigated 15 and 26 wt.% Cr hypoeutectic, eutectic, and hypereutectic alloys [7]. This is an important parameter for passivation capability of the ferrous matrix by developing a passive film (Cr_2O_3). For instance, it has been reported that at least 16 wt.% Cr is needed to ensure a stable oxide protective layer [17].

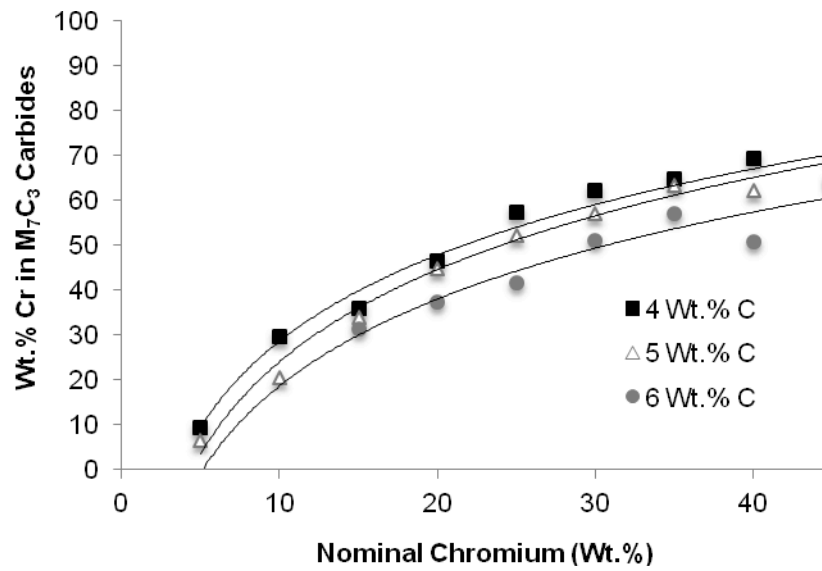


Figure 3.18: Variations in the chromium content in M_7C_3 carbides with increasing chromium and carbon overall concentrations.

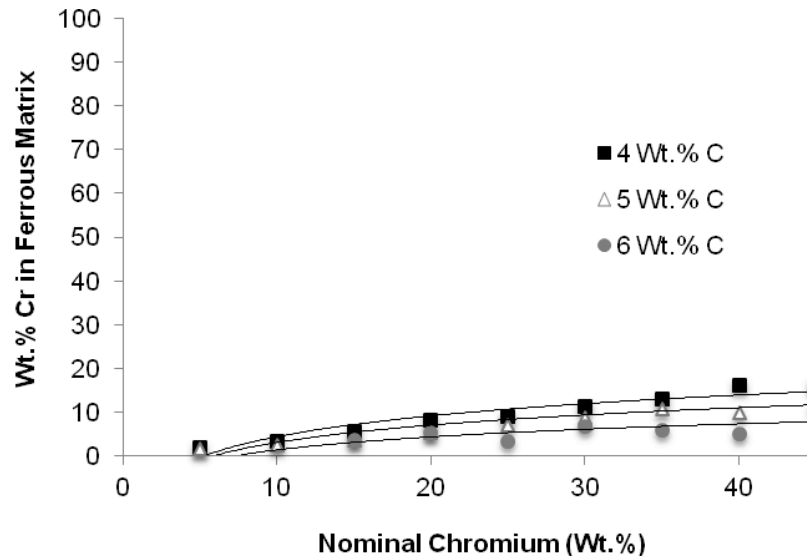


Figure 3.19: Variations in chromium content in the ferrous matrix with increasing chromium and carbon overall concentrations.

The large difference in the variation of Cr between the carbide and matrix phase is expected, as Cr is a strong carbide former. This tendency can be evaluated based on the partition coefficient, which is defined as the concentration of the element in the carbide phase divided by the one in the ferrous matrix. This has been calculated and summarized in figure 3.20 for hypoeutectic, near eutectic, and a hypereutectic carbon compositions. The three carbon series show similar behaviors. As illustrated, partition coefficients of the three compositions present a peak at 10 wt.%Cr where they reach an approximate value of 8 where the chromium precipitation in the carbide phase is the maximum. The incubation type of effect may explain this, where the volume fraction changes little from 1 to 2 wt.% C and therefore more chromium is free to enter the carbide phase. This behavior has been found in all the compositional series under study and is in agreement with those reported in the literature [14, 16].

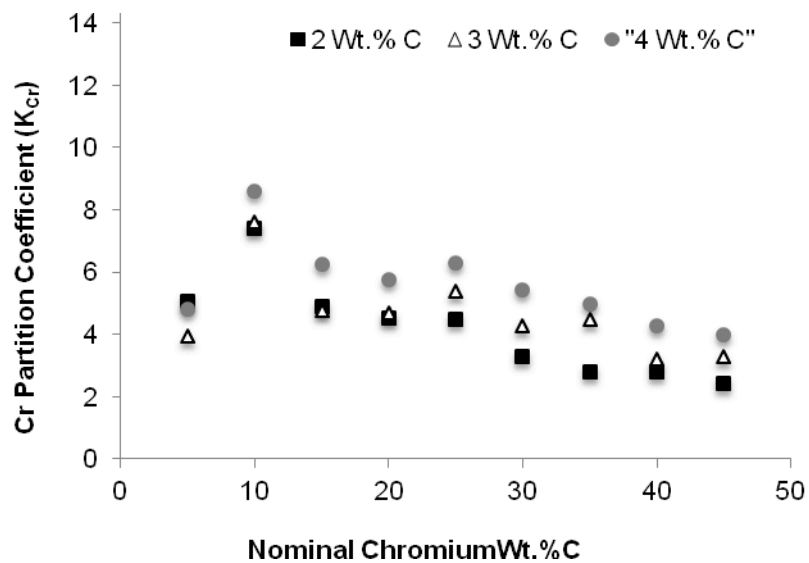


Figure 3.20: Chromium partition coefficient (K_{Cr}) as a function of nominal chromium composition for hypoeutectic, eutectic, and hypereutectic carbon series.

Distributions of Si and Mn in the phases were also analyzed. Mn precipitated in both carbide and ferrous matrix, and its weight content was between 2.6 and 4 % in the carbide phase and between 2.4 and 3.5% in the matrix. This element distribution only underwent small changes as the carbon and chromium bulk content changed (figure 3.21 and 3.22). This can be seen through the partition coefficient presented in figure 3.23, where there is a slight tendency for lowering the partition ratio of manganese as the overall chromium increases, which supports Laird's results [14]. The increasing chromium composition in the carbide phase reduces the Mn solubility in the carbides, and therefore Mn gets rejected into the ferrous matrix. However, overall the changes are small.

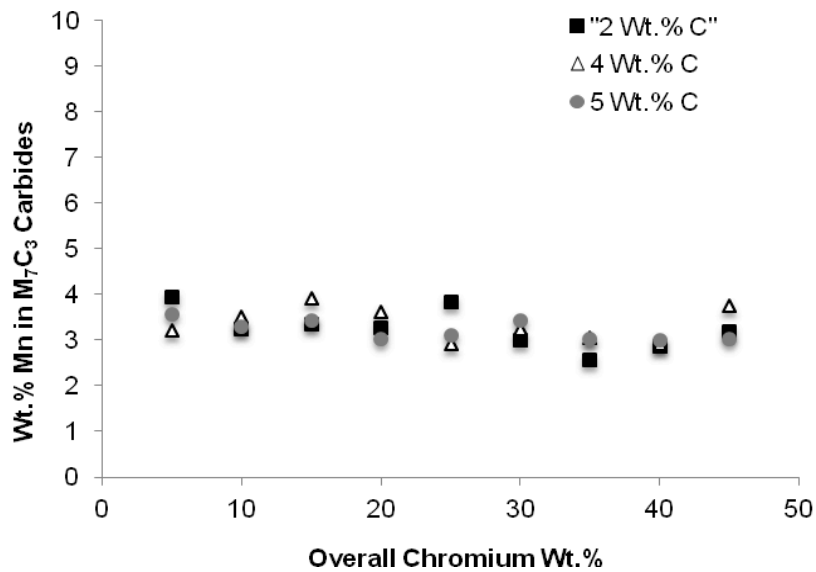


Figure 3.21: Variations in Manganese content in M_7C_3 with increasing chromium and carbon overall composition.

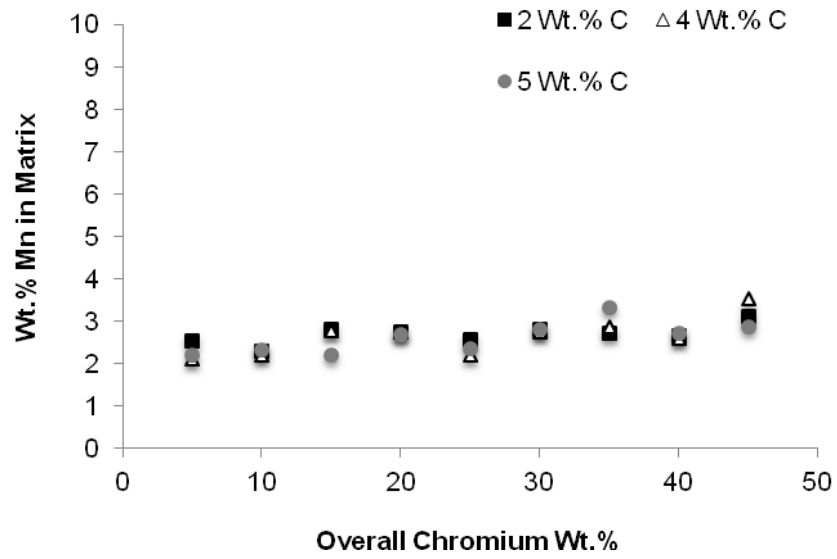


Figure 3.22: Variations in Manganese content in the ferrous matrix with increasing chromium and carbon overall composition.

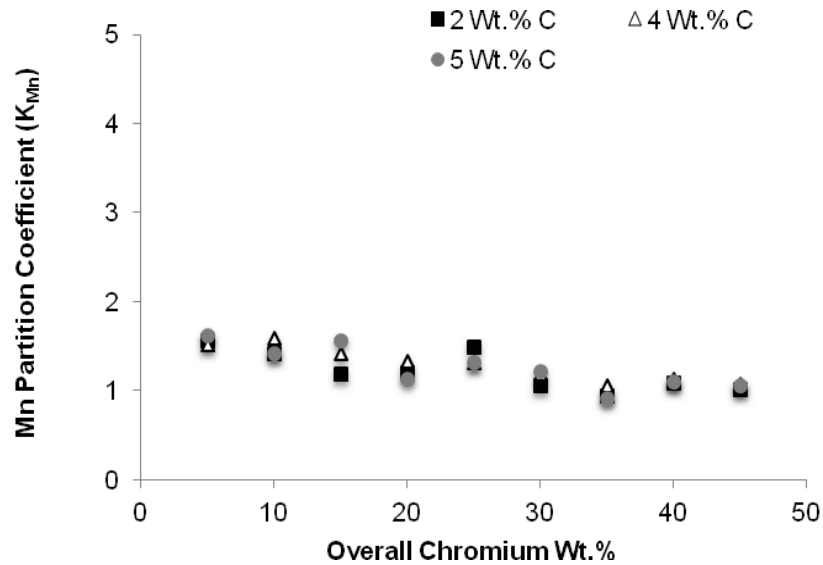


Figure 3.23: Manganese partition coefficient (K_{Mn}) as a function of nominal chromium composition for various carbon compositional series.

In the case of silicon, it was only found in the ferrous matrix phase for all the samples studied, it never partitioned into the carbide phase, therefore its partition coefficient is zero for all compositions. This has also been observed in previous work where it was found that silicon was rejected into the liquid by the carbide/liquid interface [16, 18]. The silicon content in the ferrous matrix as a function of the overall chromium and carbon compositions is illustrated in figure 3.24. As shown, the maximum and minimum contents of silicon are 1.43 wt% and 0.68 wt%, respectively. The Si content in the matrix is slightly raised at the lower chromium, 5 to 10 wt.% Cr, and reaches a valley near 20 wt.% Cr.

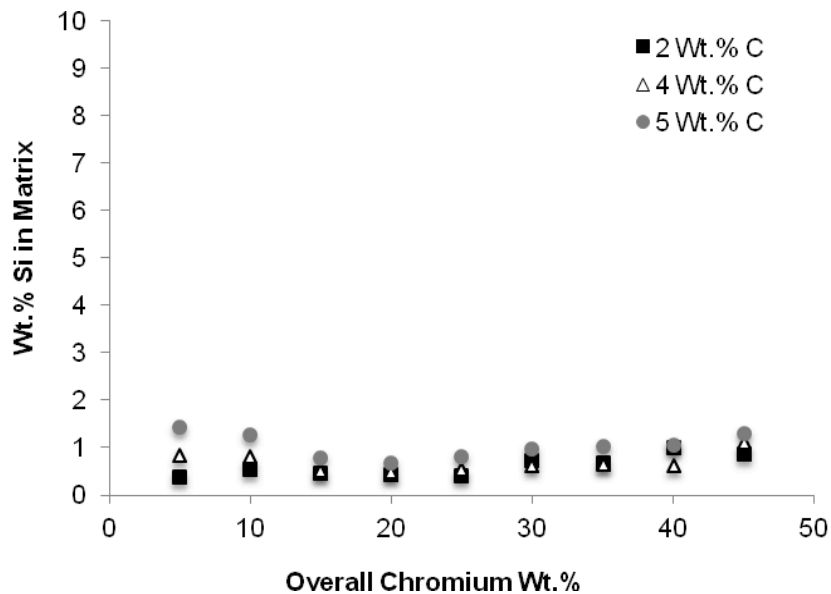
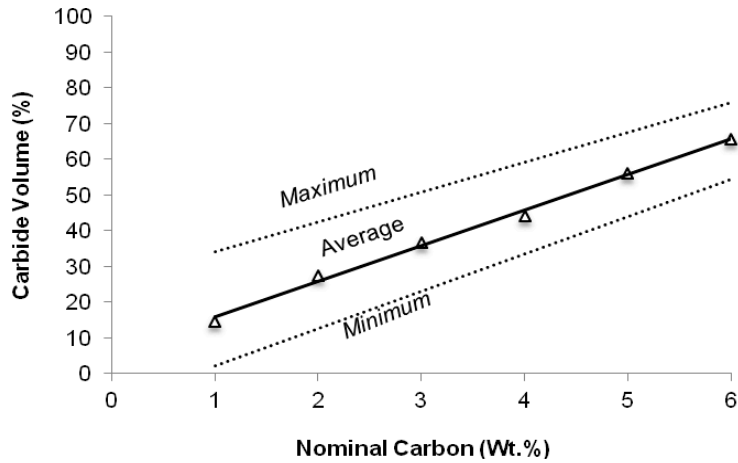


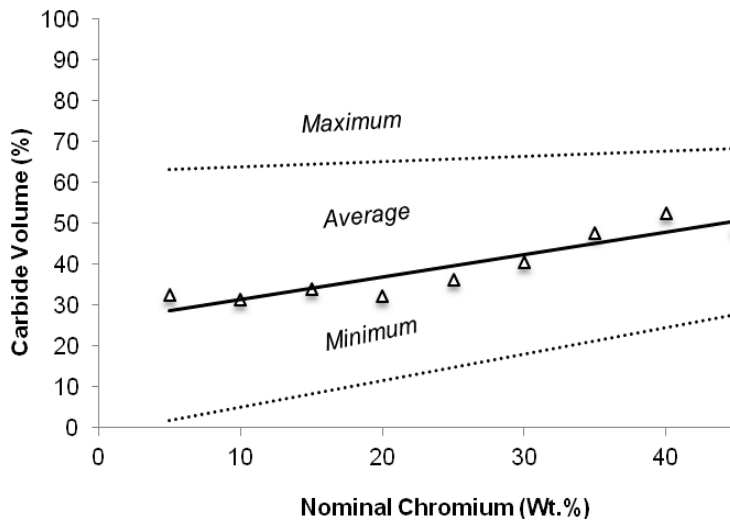
Figure 3.24: Silicon content in the ferrous matrix with increasing chromium and carbon overall composition.

3.5 Carbide volume fraction

The wear resistance of HCCIs is mainly attributed to their high hardness, partly due to the chromium carbides, specially the M_7C_3 , type that is the most desirable phase within the HCCI system for resisting wear [10]. The carbide volume fraction is thus a key parameter to consider when dealing with aggressive abrasion or erosion processes. Figure 3.25 depicts the general effect of the overall carbon and chromium composition on the total average carbide volume in the microstructure. These graphs show a summary of the maximum, minimum, and average carbide percentages found in the entire HCCI compositional series. One may see that even though both carbon and chromium promote the formation of carbides, carbon is more effective for controlling the volume fraction of carbides. As shown, raising carbon from 1 to 6 wt.%, resulted in an increment in carbide volume fraction from 15 to 66% approximately. For comparison, increasing the overall chromium concentration from 5 to 45 wt.% produced an average increment of 17 % carbide volume. Figure 3.25 also shows the maximum carbide volume for the entire expanded HCCI system, being 78% the maximum accomplished without additional reinforcement carbides.



(A)



(B)

Figure 3.25: Effect of the overall concentrations of carbon (A) and chromium (B) on the carbide volume content.

A surface fitting was performed to compare the analysis with the empirical equation derived by Maratray [14]. In this case, it is found that a polygonal fitting of second grade produced better fitting adjustment. Figure 3.26 shows a

comparison of the measured carbides and those obtained for Maratray's equation (1.1) and the one derived in this work. The proposed equation has the following form:

$$CV(\%) = -13.5 + 15.32C + 0.1Cr + 0.08C^2 + 0.02Cr^2 - 0.23 C Cr \quad \{ 3.4 \}$$

In general, their prediction is good when the carbide volume content is below 40%. The deviation somewhat increases at higher volume fraction of carbides.

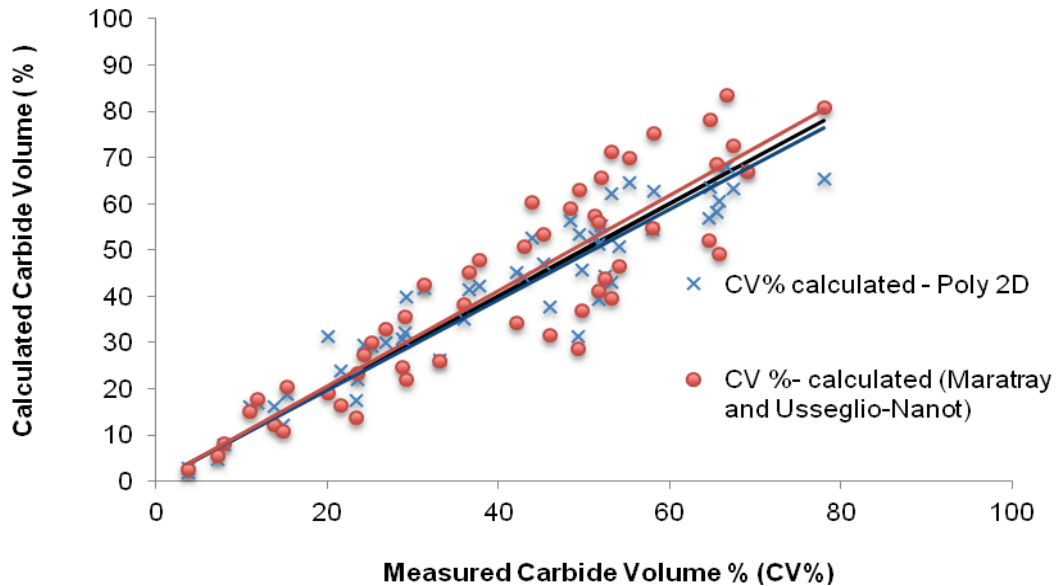


Figure 3.26: Comparison of measured carbide volume fraction with those predicted with an empirical equation proposed by Maratray's[14] and one derived in this work (polygonal 2D).

3.6 Hardness

The mechanical property that is mostly sought to resist wear is the hardness. However, caution should be taken as hardness alone is not sufficient and can be misleading when predicting the wear resistance without considering other properties of the materials, e.g., toughness, and the tribological system.

Hardness of HCCIs is largely dependent on the volume fraction of carbides but also influenced by properties of the matrix. Figure 3.27 presents the hardness obtained for three different Cr series covering the compositional range investigated (low, medium and high Cr). One can observe that increasing the carbon produces a steep increase on the bulk hardness for HCCIs. However, above 30 wt.% Cr, the hardness reached a peak near 4 wt.% C and then the trend was reversed. As overall Cr was raised above 30 wt.% Cr, the hardness drop became more obvious. Similarly, there was a dramatic change in hardness when the ferrous matrix solidified as ferrite above 30 wt.% Cr, such as those seen in sample 30-1 and 45-1 in figure 3.27. This is attributed to the little effect that carbides produced in the hypoeutectic alloys at low carbon (1~2 wt.%) where the hardness of the ferrous matrix is dominant. This is demonstrated by correlating the hardness with the carbide volume content, as depicted by figure 3.28. Definitely, the matrix microstructure plays a key role controlling the hardness until a hypereutectic composition is reached, where the carbide volume content becomes abundant, and the effect of the matrix microstructure begin to be

attenuated by the carbide phase. This is expected to have the same effect on wear resistance, which will be discussed later in this chapter.

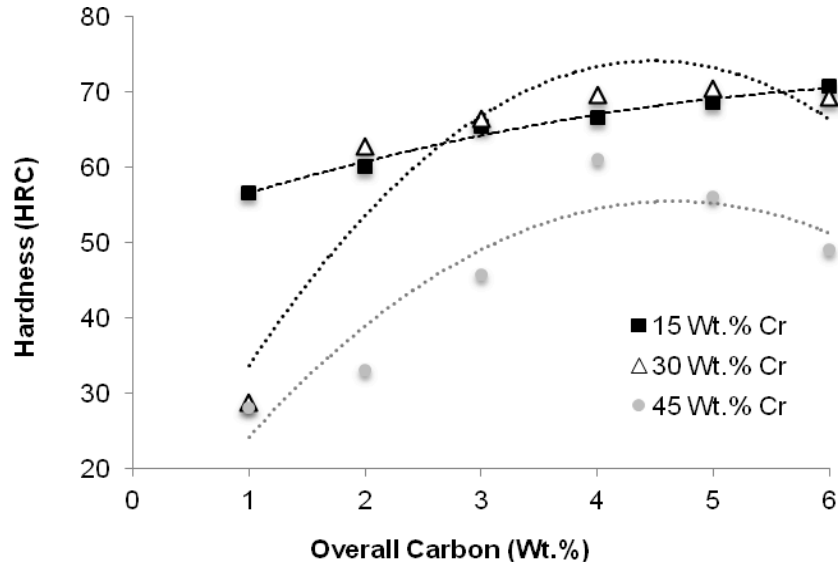


Figure 3.27: Effects of carbon and chromium on bulk hardness of various compositional series studied.

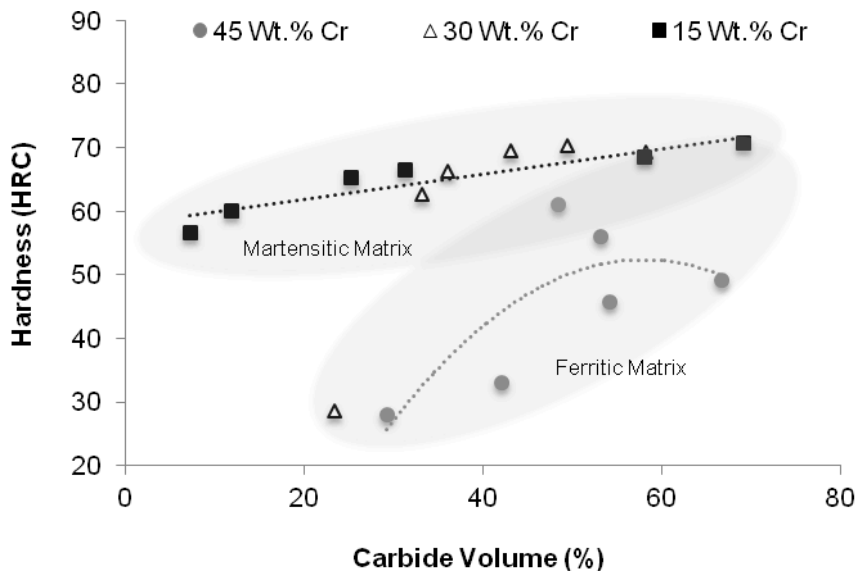


Figure 3.28: Bulk hardness as a function of the carbide volume content for various chromium series featuring martensitic/retained austenite and ferritic matrix.

3.7 Wear behavior

3.7.1 Dry abrasion (three-body)

The abrasion behavior of the entire HCCI system was evaluated under ASTM G65 dry sand/rubber wheel test following procedure A [2]. In general, the results were rather consistent and all the alloys series showed similar behavior, as illustrated in figure 3.29 for HCCIs containing 15, 30, and 45 wt.%Cr respectively. For any given chromium concentration, carbon effectively increases the wear resistance. For instance, in the 30 wt.% Cr series, the volume loss was reduced by 14.6 times when carbon was increased from 1 to 3 wt.%.

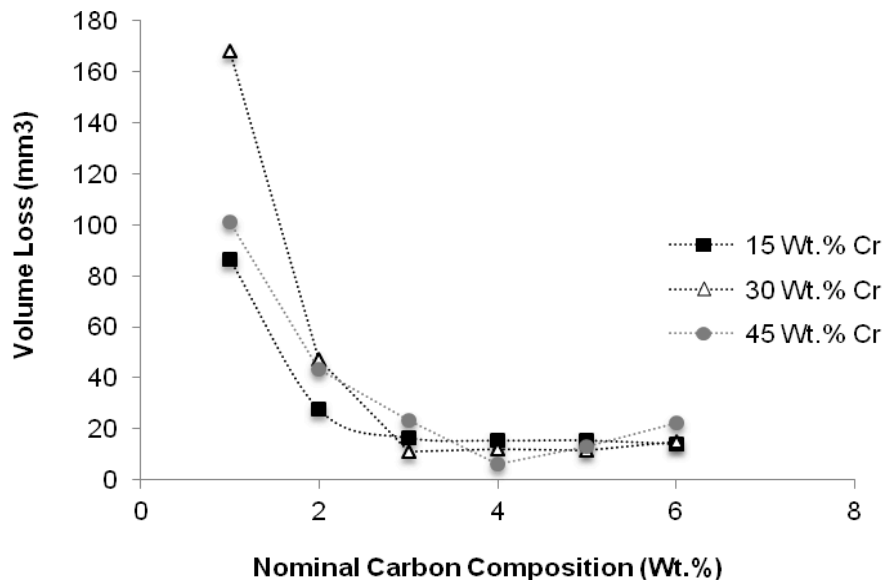


Figure 3.29: Dry abrasion results (ASTM G65 Procedure A) for various HCCI series.

The direct effect of carbon on carbide volume fraction (figure 3.25) and hardness (figure 3.27 and 3.28) explains the significant increment in dry abrasion resistance as carbon nominal levels were raised within a chromium series. It is known that the excellent wear resistance of HCCI is largely due to the in-situ hard carbides, especially M_7C_3 [10, 19] that formed in the microstructure. These results suggest that increasing the carbide volume is extremely effective until approximately 50-60%. Higher values did not produce significant changes under three-body abrasion with silica as the abrasive particle. Similar behavior was observed in the past in Cr-Mo white cast irons under low-stress dry and wet rubber wheel tests with quartz abrasive [19, 20]. It was noticed that at the larger carbide volume content, mostly at high chromium (>30 wt.%) and carbon (>4 wt.% C), the worn surface consisted not only in grooving but also in pits caused by cracking and spalling of the carbides, which was detrimental to the wear performance.

There was no general obvious effect of the overall chromium composition on the dry abrasion behavior. It is important to take into account that chromium, to a large extent, dictates the stability of the different possible carbides and matrix phases, whereas changes occur over a wide range of chromium content as opposed to carbon, so it is expected the chromium effect is more gradual.

As discussed earlier in this chapter, the Cr/Fe ratio on the carbide phase increases with the overall chromium concentration and reaches a peak between 30

to 35 wt.% Cr, depending on the carbon. This has been found to have an effect on micromechanical properties of the complex carbide. Figure 3.30 illustrates variations in micro-hardness of primary carbide with an increase in the Cr/Fe ratio for various samples. One may see that the hardness of the carbide increases considerably and by almost two times at the highest ratio. The increased hardness of the carbide at higher chromium content explains improved anti-abrasion performance of higher chromium (>30 wt.%) hypereutectic alloys at their best carbon composition.

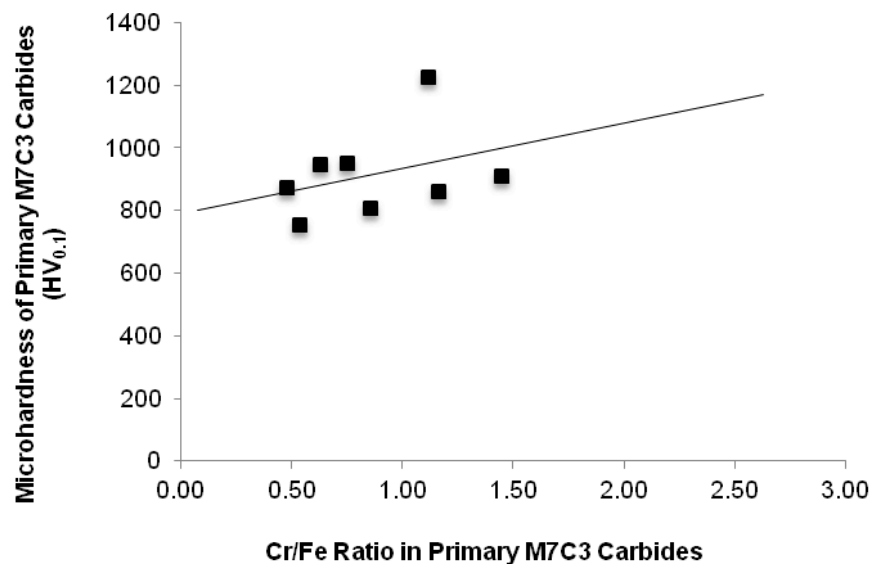


Figure 3.30: Relation between the Cr/Fe ratio and micro-hardness of the primary M_7C_3 carbide.

The wear resistance of the hypoeutectic alloys (<3 wt.% C) largely relies on the ferrous matrix structure. This is why the hypoeutectic samples show such large volume losses. For instance, several of the samples matrix microstructure

and chemical content is not different of that of a tool steel. The Cr/Fe ratio in the matrix was calculated and found to have a reverse effect on the micro-hardness, as shown in figure 3.31. This is attributed to the phase transformation from austenite to Fe-Cr ferrite that occurs at higher overall chromium once the austenitic domain is crossed (figure 3.7).

It is pertinent to mention that the bulk hardness partially resembles the abrasion behavior and the rapid improvement in the wear resistance occurs when the carbon is raised up to 4 wt.%. For chromium content higher than 30 wt.% Cr, it was detrimental when carbon content was beyond 4 wt.%. Thus, although hardness is a good indicator for the wear resistance when improved by increasing the carbon concentration, increasing the carbon content may not always have the expected positive effect as chromium composition has to be considered as well.

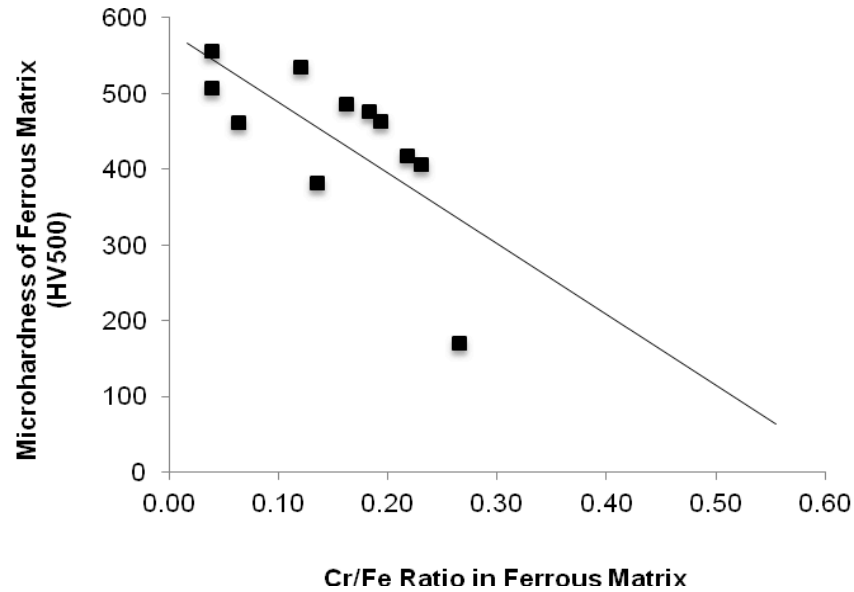


Figure 3.31: Relationship between Cr/Fe ratio and micro-hardness of the ferrous matrix.

For instance, similar abrasion resistances can be found at different hardness values (figure 3.32). Best performances are found generally between 60 to 70 HRC. The explanation for this observation is similar to what is discussed for the carbide volume fraction.

Figure 3.33 compares volume losses of HCCIs under dry abrasion for various carbide volume fractions. There was stronger correlation with carbide content than bulk hardness, even though neither of them fully predict the abrasive behavior. This emphasizes the importance of all microstructural aspects and the tribological characteristics of the system for material selection in wear applications.

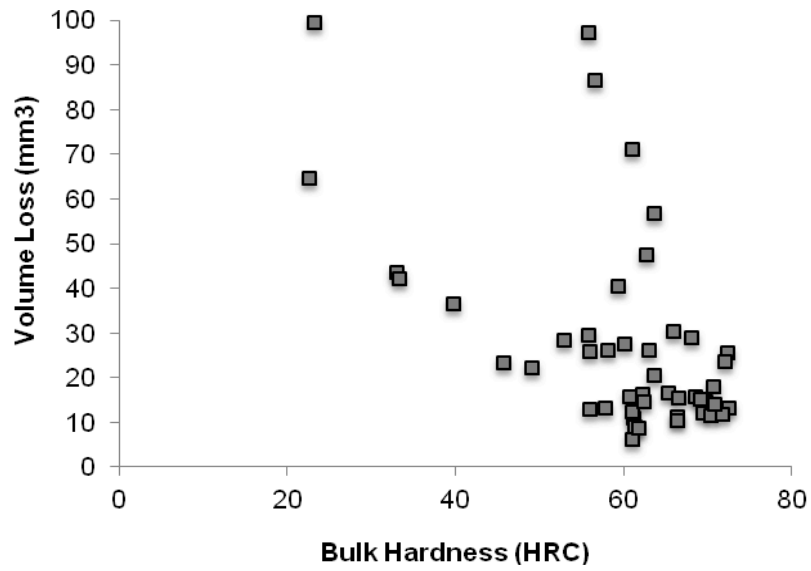


Figure 3.32: Abrasion performance as a function of bulk hardness.

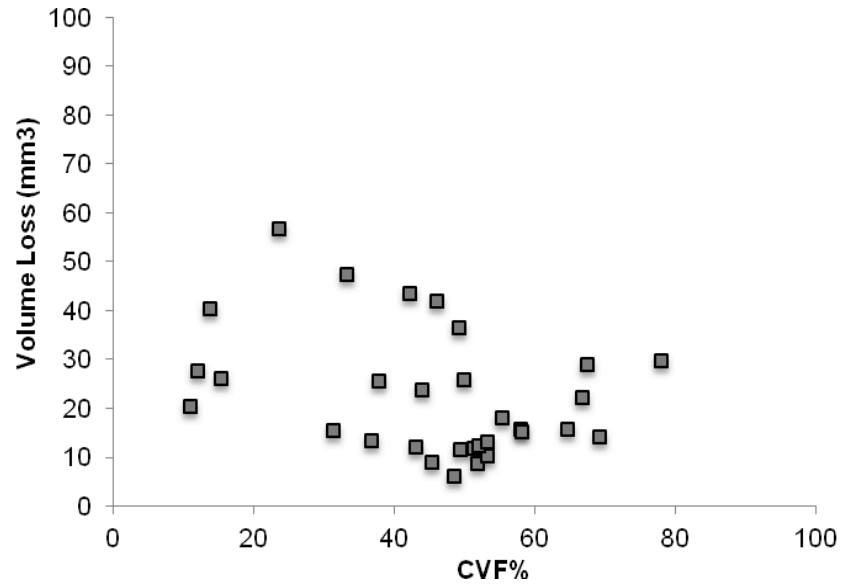


Figure 3.33: Abrasion performance as a function of carbide volume fraction.

3.7.2 Slurry erosion

Unlike dry abrasion testing, the tribological system is more complex during slurry erosion due to the corrosivity of the aqueous slurry, temperature, impingement angle, fluid dynamics of the carrier, and synergy between erosion and corrosion. The slurry erosion testing was conducted at several impingement angles and velocities.

The dependency of HCCIs erosion on the impingement angle is similar to those found in carbon and high strength alloy steels, where impingement angles in the range of 45° generally produce the largest wear damage. Figure 3.34 illustrates this trend for various eutectic or near eutectic alloys. This is a typical behavior for materials that exhibit a balance between hardness and toughness. For reference, table 3.3 lists the fracture toughness obtained for a selected group of the HCCI samples and those typical for carbon steel and aluminum castings. One can observe the reduction in toughness after heat treatment in HCCI samples. This occurred by the destabilization treatment and the precipitation of secondary carbides in the matrix, which tend to be interconnected facilitating the crack propagation through carbides [21]. Experiments conducted by Kootsookos found in a low C hypoeutectic HCCI that the mean-free path of secondary carbides can also be favourable for the toughness and can be controlled by the destabilization temperature[22].

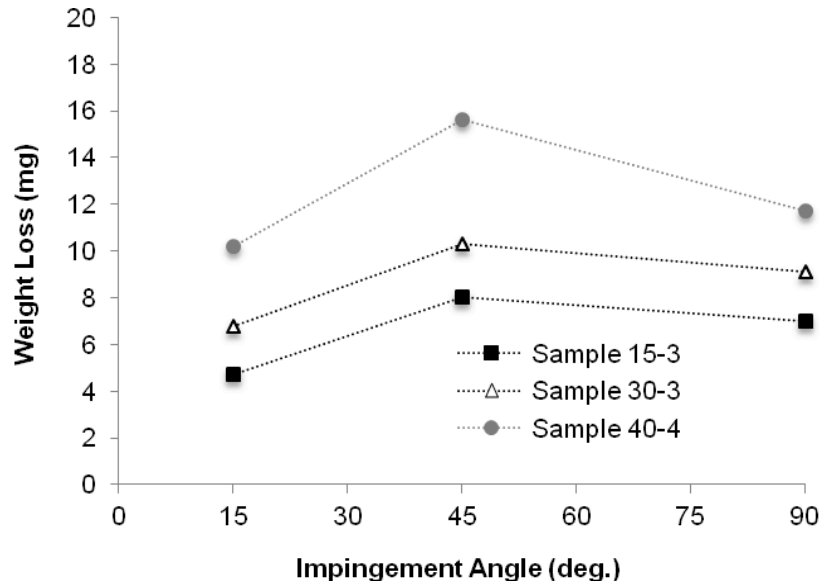


Figure 3.34 Slurry erosion at low (15°), medium (45°), and high (90°) impingement angle for three different samples having near eutectic microstructures.

Table 3.3: Fracture toughness values of various samples and typical ranges for carbon steel and aluminum alloys.

Sample ID	Condition	Fracture toughness (MPa.m ^{0.5})
30-2	As-cast	40
30-2	Heat treated	29
30-3	As-cast	33 - 38
30-3	Heat treated	28 - 29
30-4	As-cast	30 - 33
30-4	Heat treated	31
35-2	As-cast	35
35-2	Heat treated	37
Carbon Steels		50-60
Aluminum Alloys		25-44

Figure 3.35 shows the worn surfaces after slurry erosion at 5 m/s in neutral slurries at low (15°), medium (45°), and high angle (90°) for a hypoeutectic sample (alloy 25-1). It can be seen that 45° impingement caused the more visible damage to the surface. At the low angle, the surface featured evident cutting produced by angular particles and some ploughing. On the other hand, at the high angle, material displaced by ploughing is evident along with a large number of pits and shear lips. At the medium-angle impingement, however, there was a combination of these types of damage causing deeper grooves and more material pile-up. The medium angle was found to be much more effective in causing carbide spalling from the hypereutectic HCCIs.

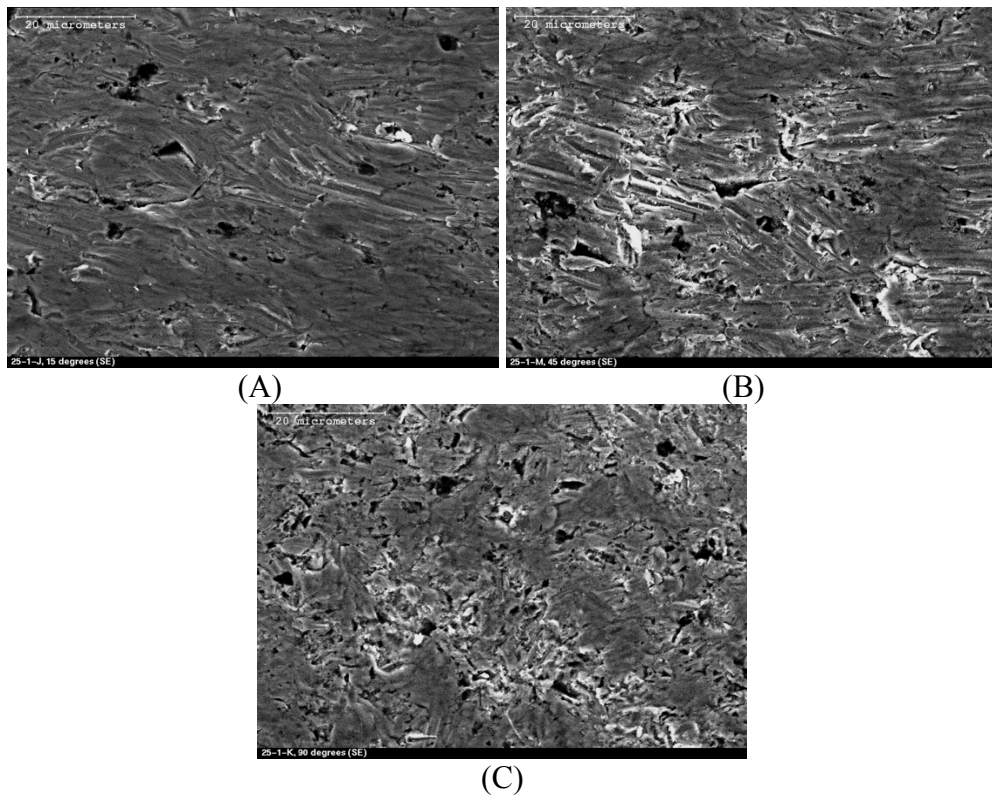
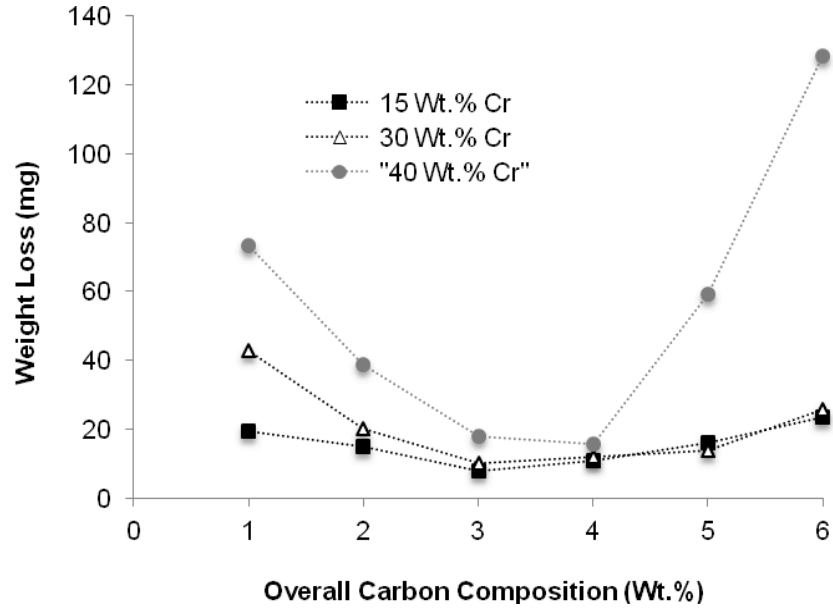


Figure 3.35: SEM images of the worn surfaces of alloy 25-1, after slurry erosion in neutral slurry and 5 m/s slurry velocity, at different impingement angles: (A) 15° ; (B) 45° ; (C) 90° .

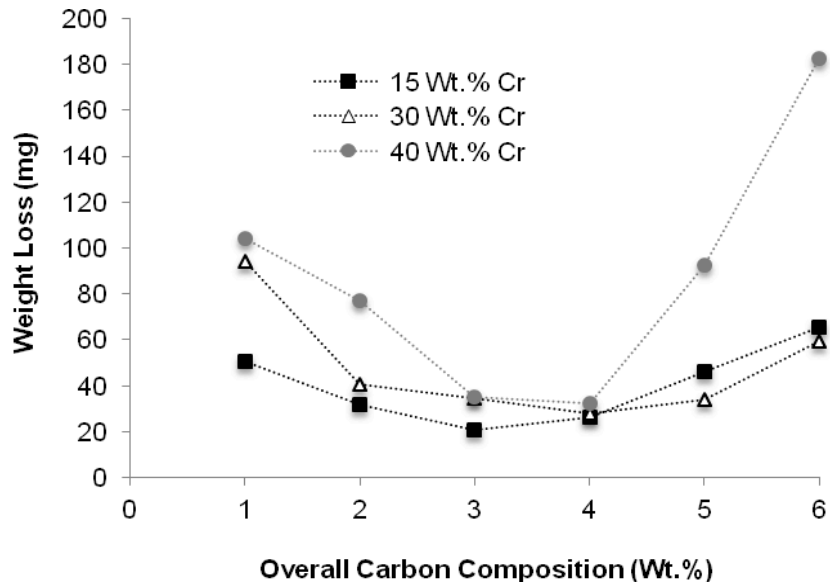
Similar to the three-body abrasion results, the overall slurry erosion behavior is also improved as carbon concentration increased until about 3 to 4 wt.% C (depending on the chromium content), as can be seen in figures 3.36. Similar behavior was observed in all chromium series.

This carbon composition range produced a relatively fine eutectic distribution of carbide and ferrous matrix or a slightly hypereutectic microstructure. For example, the 30 wt.% Cr series featured best erosion resistance at 3 wt.% C, whereas at 4 wt.% C the 40 wt.% Cr system did. Similar relationship between performance and carbon content was found in dry abrasion. However, beyond 4 wt.% C the trend reversed and the erosion damage started increasing. As the overall chromium content was raised, this effect became more noticeable. Therefore, there is a threshold in carbide volume content in the microstructure, fixed by the overall carbon level. Similar trends were found at other slurry velocities tested for all the compositional series.

Once the hypereutectic structure is formed and the carbon concentration is further raised, the volume fraction of primary carbides M_7C_3 starts increasing rapidly. The primary carbides are coarsened, which decreases the toughness as the coarse primary carbides (usually have a needle shape) are brittle and increase stress concentrations at sharp edges. In addition, coarse carbides may result in larger depletion of C and Cr in the matrix, making the regions with less C and Cr more anodic relative to other regions in the matrix.



(A)



(B)

Figure 3.36: Slurry erosion weight loss as a function of overall C content for various Cr-series: (A) 45° impingement, 5 m/s; (B) 45° impingement, 6.5 m/s.

For dry abrasion under stable loading conditions, the high volume fraction of coarse carbides was not as detrimental as that in the case of slurry erosion, since there is not a large impact force involved and a dry environment. Under the erosion-corrosion condition, to resist multiple particle strikes, the material should have reasonably good toughness. Besides, the high volume fraction of coarse carbides also increases the sensitivity of the material to localize corrosion particularly in the chromium depleted regions, leading to considerable synergistic damage. In this case, the carbides are not effective in protecting the surface, and can even be detrimental. Such mechanism can be seen in figure 3.37, which illustrates a worn surface of alloy 25-6 after slurry erosion test at 5 m/s.

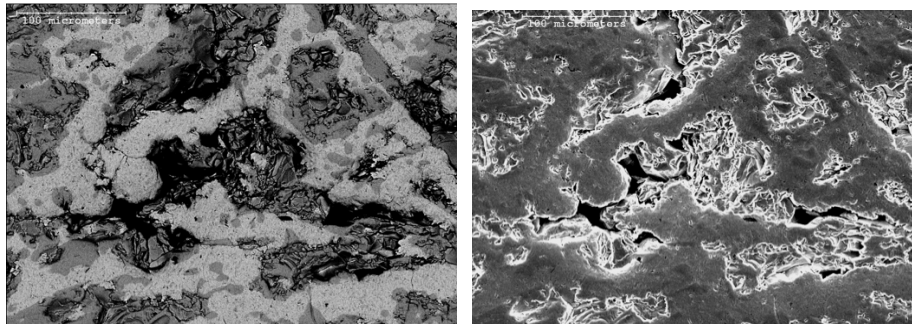


Figure 3.37: Severe carbide fracturing under slurry erosion at 5 m/s, 45° impingement angle. Both micrographs show the same location on backscatter mode (left) and secondary electrons (right).

The overall effect of increasing slurry velocity in nearly all samples studied produced a volume loss increase in agreement with a power law velocity exponent tendency (figure 3.38). However, it was interesting to notice that some samples presented an abnormal behavior where increasing speed reduced the wear

rates which was found to be corrosion related. This behavior can be seen in figure 3.39 and is discussed in detail in chapter 6.

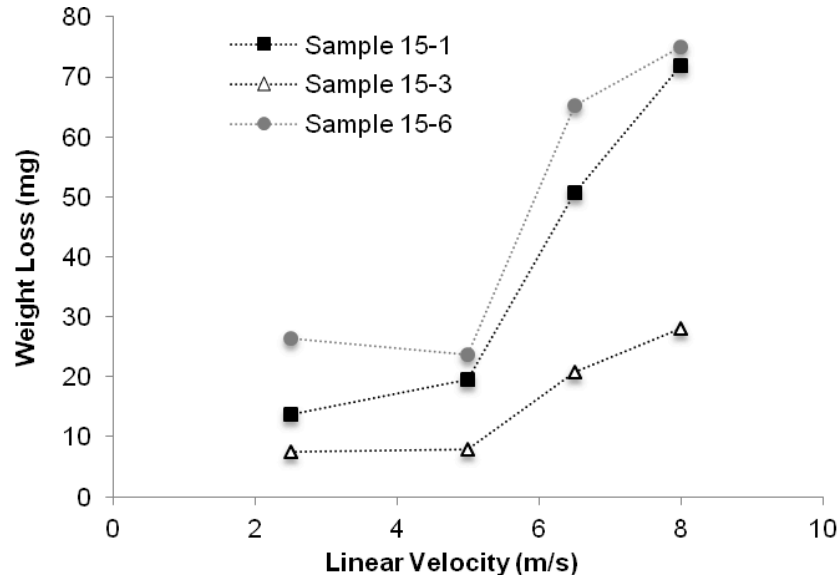


Figure 3.38: Typical slurry velocity – erosion behavior observed for most HCCI samples investigated.

The effect of the ferrous matrix microstructure can be evaluated examining the hypoeutectic alloys, which consist predominantly of matrix and low carbide volume content. The wear behavior of these alloys is mostly controlled by the matrix wear response, and therefore they can be used to assess the influence of the matrix microstructure on the wear behavior. Figure 3.40 shows that under slurry erosion the martensitic matrix outperformed the ferritic structure. Even though the hardness of the matrix is also reduced when the ferritic matrix developed, it can also be seen that the microstructure itself is the dominant factor in these hypoeutectic alloys. This suggests that in hypereutectic alloys, even though the carbide volume becomes a more important factor than the matrix, a

martensitic structure should still be beneficial compared to the ferritic one. This is attributed to the better toughness of the martensitic (in the tempered condition) with respect to the ferrite phase, and also the always present retained austenite in the martensitic matrix which also provides strain hardening capability that is needed to delay the material displacement, ploughing and cutting that is produced by the abrasive particles striking on the surface during erosion. A comparison between the worn surfaces of two hypoeutectic samples featuring martensitic matrix and ferritic matrix respectively is presented in figure 3.41, which shows a more pronounced damage in the ferritic microstructure by cutting and shear lips from ploughing.

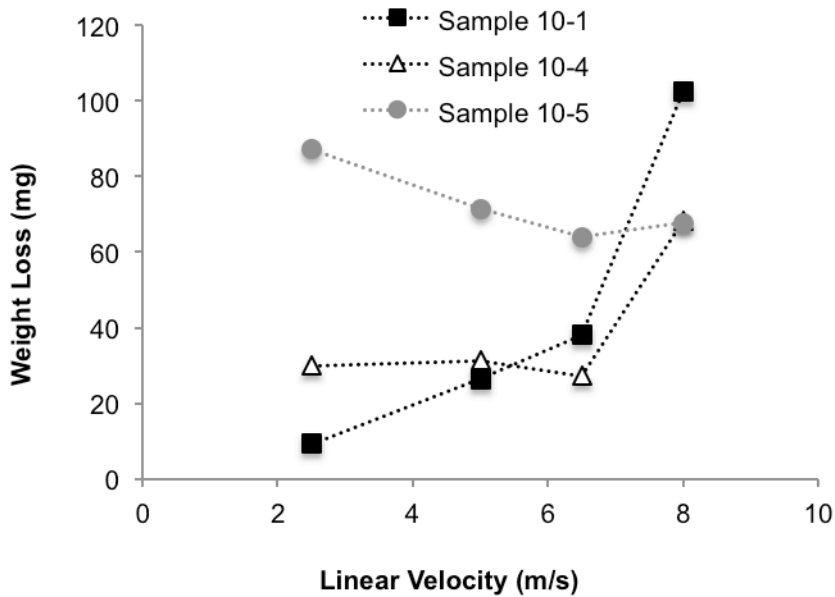


Figure 3.39: An abnormal slurry velocity – erosion behavior observed for a subgroup of alloys featuring lower wear rates as the slurry velocity increased.

When the ferrous matrix behavior was evaluated under abrasion, it was noticed that the matrix microstructure now is not a controlling or dominant factor in the wear response. Similar wear rates were found in martensitic and ferritic matrix microstructures with relatively similar carbide volume content, as shown in figure 3.42. The microhardness of the matrix partially explain the behavior but not completely. In this case, the abrasive particles, which are significantly harder than the matrix (1,200 HV), produce deep grooving and cutting on the ductile ferrous matrix regardless of the matrix microstructure as illustrated by figure 3.43, though slightly shallower grooving was noticed in the martensitic microstructure.

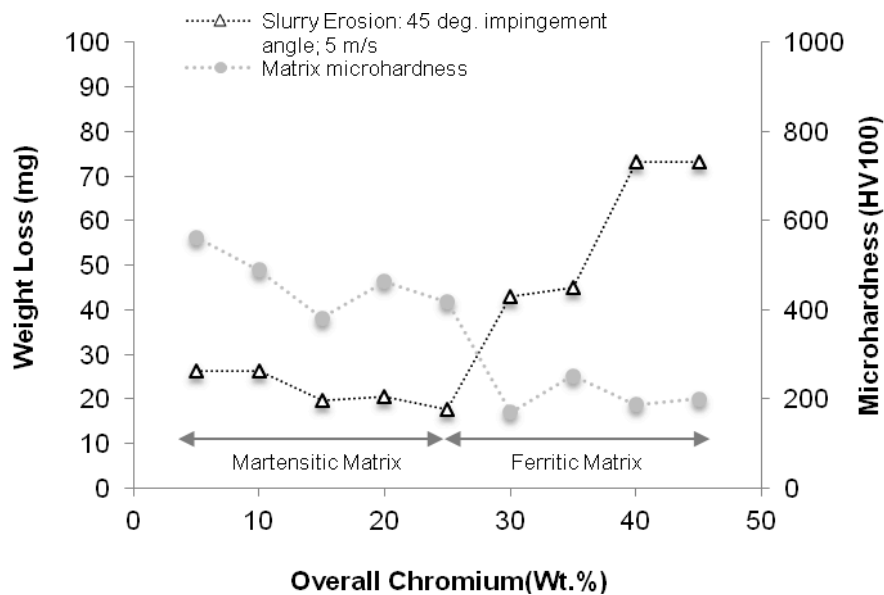


Figure 3.40: Comparison of the slurry erosion performance of hypoeutectic alloys featuring martensitic and ferritic matrixes.

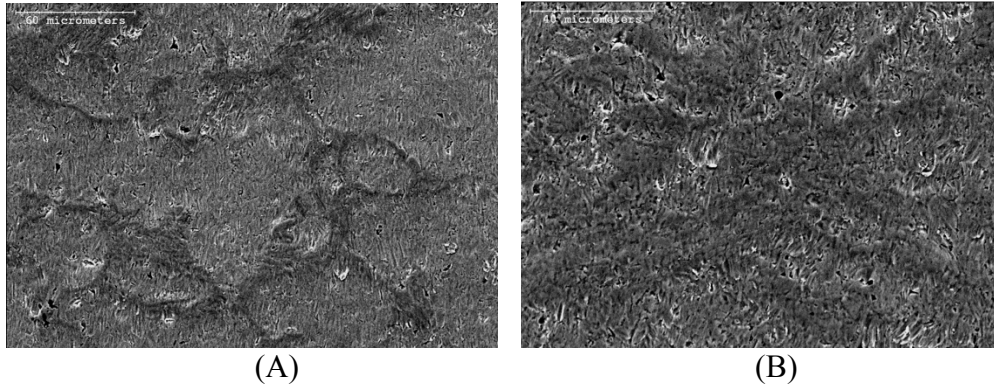


Figure 3.41: Comparison of worn surfaces of two hypoeutectic samples featuring martensitic matrix (A) and ferritic matrix (B). SEM images after slurry erosion in pH=12 slurry, 5 m/s slurry velocity, 45°. pH=12 was used to suppress the corrosion effect and observe the pure mechanical damage.

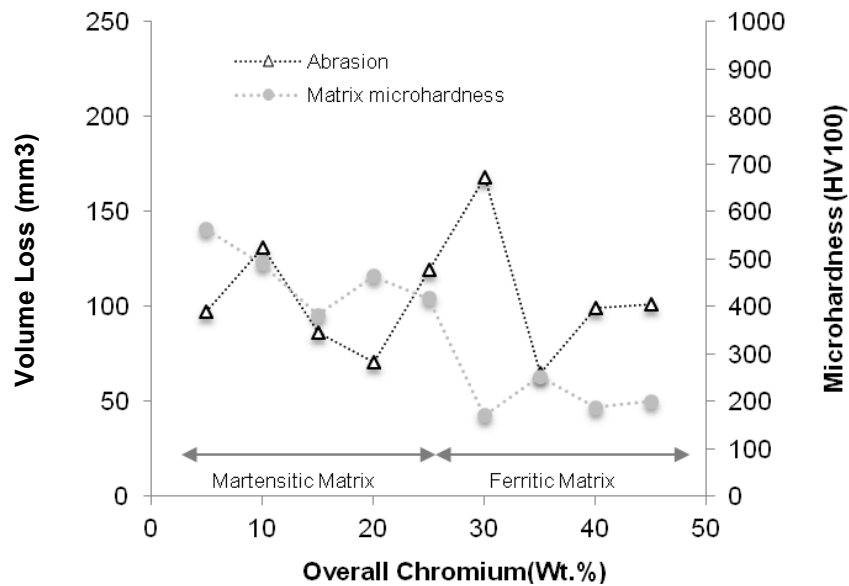
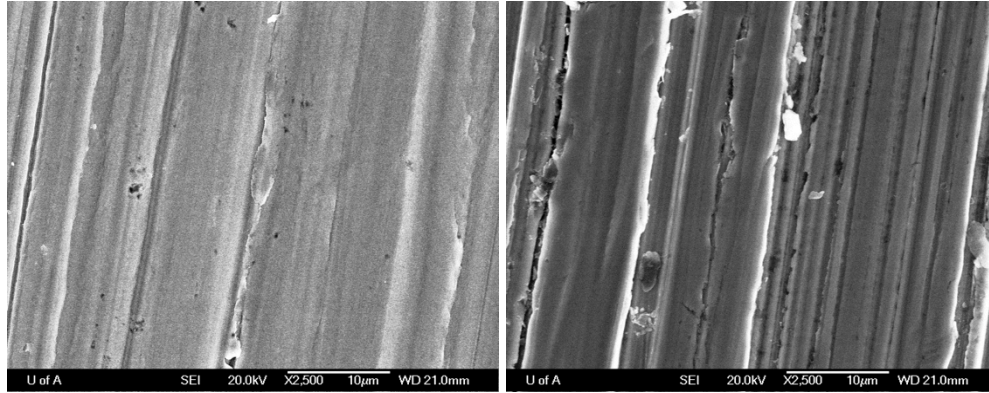


Figure 3.42: Comparison of dry abrasion (three-body) performance of hypoeutectic alloys featuring martensitic and ferritic matrixes.



(A)

(B)

Figure 3.43: Comparison of worn surfaces of two hypoeutectic samples featuring martensitic matrix (A) and ferritic matrix (B). SEM images after dry abrasion testing.

3.8 Corrosion behavior

The corrosion resistance of all samples in the expanded HCCI system was investigated by linear polarization technique. In an aqueous solution, the carbide phase of the HCCI is expected to be inert while the ferrous matrix becomes anodic.

The typical reactions when dissolved oxygen is stable is as follows:

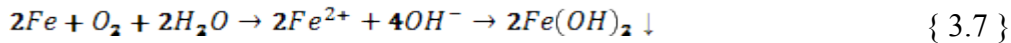
Anodic reaction:



Cathodic reaction:



Overall reaction:



It was observed a very consistent trend in all chromium series where increasing carbon overall content reduces the polarization resistance significantly until the highest carbon content was reached. These results are presented in figure 3.44 for the 15, 30, and 45 wt.% Cr series. Beyond 4 wt.% C, a sharp drop in the polarization resistance generally occurred beyond which even large chromium content did not make a significant contribution to maintain the polarization resistance. These results were expected and attributed to three factors: 1) as shown in figure 3.19, the chromium composition in the matrix is increased with overall chromium content, ranging from 0 to just over 16% by weight. The chromium is essential for the ferrous matrix to form a stable passive film of Cr₂O₃ type, which has been reported to occur above 16%Cr.[17]; (2) The second parameter is the micro-galvanic cells that form between the matrix (anode) and the carbides (cathode), which can be aggravated by the secondary carbide precipitation after heat treatment; (3) the increasing overall carbon content increases the volume fraction of carbides, which in turns, increases the cathode/anode area ratio causing rapid corrosion rates.

At lower pH similar behavior was observed for all the chromium series. However, at acidic pH certain alloys presented reduction in corrosion rates by reaching passivation, which is discussed in chapter 4.

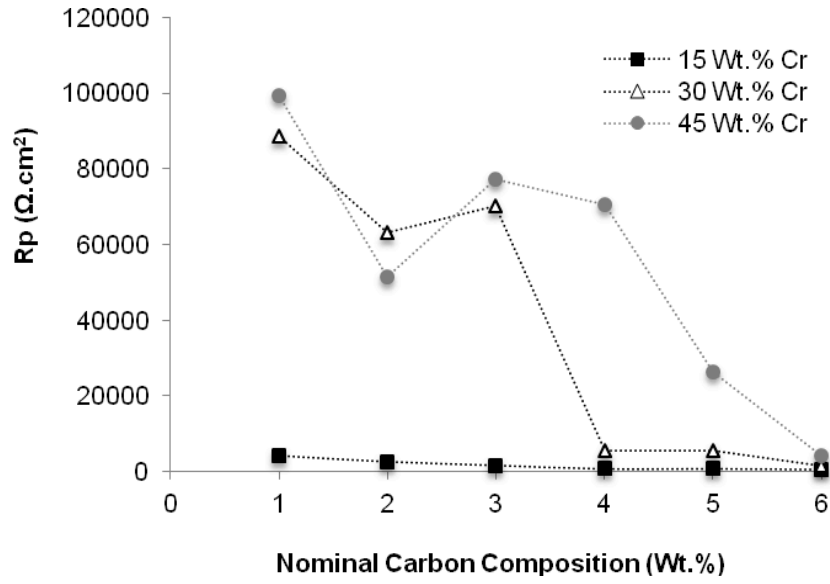


Figure 3.44: Effect of overall carbon composition on polarization resistance for various chromium series.

Figure 3.45 shows the effect of the nominal chromium content on the polarization resistance. It is evident that Cr has a profound effect on the corrosion resistance and is rather effective to increase the polarization. It was interesting to notice that at least 15 wt.% Cr was necessary to see an improvement on the polarization resistance regardless of the carbon content. This is in agreement with the value of 16%Cr reported in the literature to develop an stable passive chromium oxide film [17].

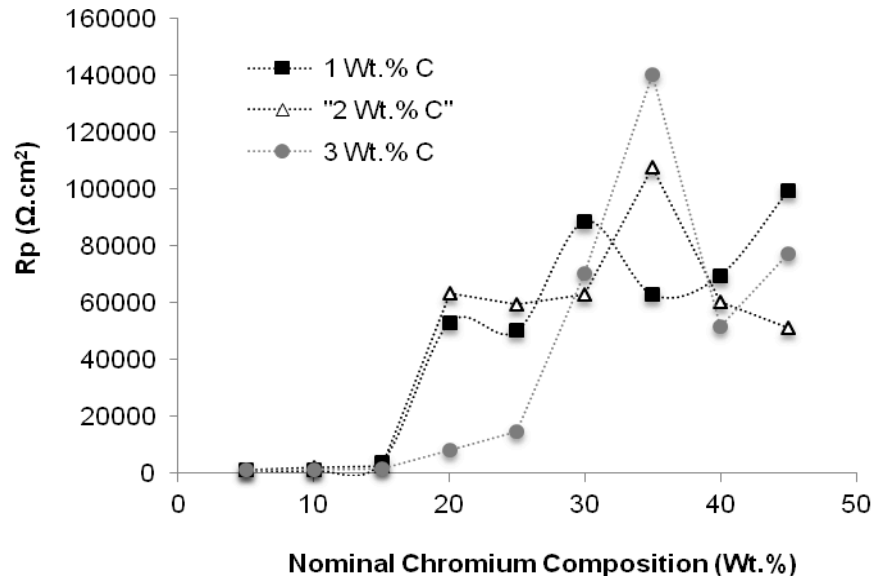


Figure 3.45: Effect of overall chromium composition on polarization resistance for various carbon series.

The morphology of the corrosion damage (in tap water solution) under the SEM can be seen in figure 3.46 for a hypoeutectic, near eutectic, and hypereutectic composition. It is evident that the localized damage occurs in the matrix in the hypereutectic samples where the ferrous matrix is being rapidly attacked. It was observed the onset of the localized attack as small pits form on the carbide/matrix interphase. There was also an indication that the secondary precipitation after destabilizing the microstructure promotes the localized attack. This is explored in chapter 6.

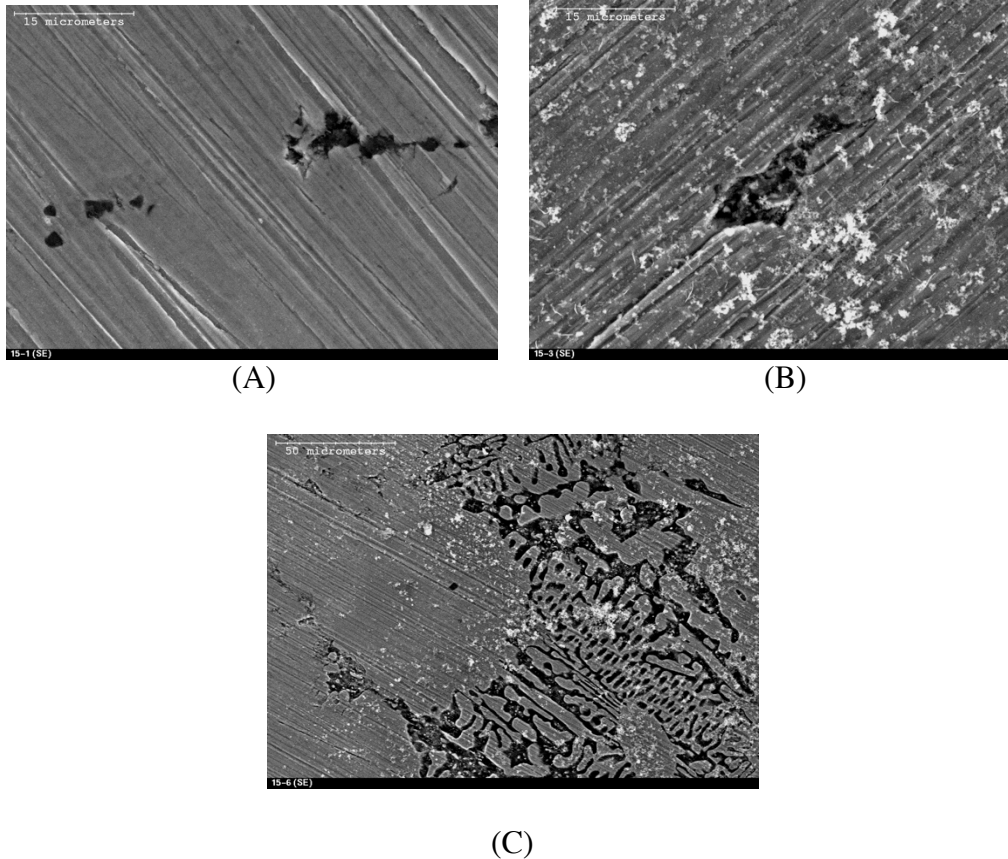


Figure 3.46: SEM micrographs of the corroded surface after electrochemical testing in tap water: (A) 15-1 (B) 15-3; (C) 15-6.

3.9 Conclusions and recommendations

- The microstructures developed in the expanded HCCI system are in good agreement with the metastable liquidus surface of the iron Fe-Cr-C diagram. The existence of the $M_{23}C_6$ domain is noticed but in a narrower carbon compositional zone.

- As the overall chromium composition was raised, the chromium increased in both the ferrous matrix and carbide phase. However, the partition coefficient was largely dependent on the overall carbon content. Higher carbon increased the partition coefficient, meaning a higher ratio of chromium is tied up with the carbide phase.
- The carbide volume fraction and bulk hardness were highly dependent on the overall carbon content for any given chromium concentration, with the maximum carbide volume percentage achieved at about 78%. The chromium was found to have a much less pronounced effect on the carbide volume content.
- Over the entire HCCI compositional range studied, dry abrasion performance was greatly improved as carbon concentration increased. A nominal carbon content in the range of 3 ~ 4 wt.%C resulted in the best performance in terms of wear resistance. Further increments of carbon content did not lead to significant changes in the performance; and in some cases, higher chromium contents (>30wt.%) were detrimental when the carbon content was sufficiently high.
- Volume fraction and bulk hardness of carbides explain the significant improvement in dry abrasion resistance as carbon nominal levels were raised for a given chromium composition. Increasing the volume fraction

of carbides was found effective until approximately 50-60% carbides in increasing the wear resistance. Further increments did not produce significant changes in the dry abrasion behavior and in some cases caused a negative effect. It can be inferred that to further enhance their dry abrasion behavior, one may need to either change the morphology of carbides or use an additional type of carbide.

- Raising the slurry velocity from 5 to 8 m/s significantly increased the weight loss under slurry erosion following an exponential behavior, as the mechanical attack became more severe. At low velocities, several HCCI compositions showed equivalent performance suggesting flexibility for materials selection under such conditions. However, at the highest velocity, the performance between HCCIs differentiates more and became evident that only certain microstructures can maintain the excellent performance.
- The eutectic and slightly hypereutectic compositions produced the best erosion resistance for all compositional series under study. For erosion in neutral slurries, it was found that raising the chromium levels did not show a clear effect on improving the performance of the alloys, like hardness, the volume fraction of carbides did not correlate well with erosion performance.

- Through evaluating the wear behavior of a selected group of hypoeutectic alloys, it was determined that the partially martensitic matrix performed better than a ferritic structure during erosion. However, under dry abrasion conditions there was no a clear correlation between microstructure of the matrix and the wear resistance.
- The electrochemical testing showed a clear trend in all alloy series where the addition of carbon significantly reduced the corrosion resistance of the alloys. On the other hand, raising the chromium content was only effective to enhance corrosion resistance above approximate 15 wt.% Cr. These trends were also observed at lower pHs.
- Analysis of the corroded surfaces confirmed that the ferrous matrix suffered localized attack, even in tap water, which developed rapidly on the carbide/matrix interface and is aided by large cathode/anode area ratios. Such effect made the carbides protrude on the surface causing them to fracture, specially coarse primary carbides; and also the localized corrosion surrounding the interface carbide/matrix favored spalling of carbides and thus reduced their role in protecting the material from erosion-corrosion.

3.10 Bibliography

1. Radzikowska, J.M., *Effect of specimen preparation on evaluation of cast iron microstructures*. Materials Characterization, 2005. **54**(4-5): p. 287-304.
2. *ASTM Standard G65, 2004, "Test Method for Measuring Abrasion Using the Dry Sand/Rubber Wheel Apparatus"*. 2004. DOI: 10.1520/G0065-04R10.
3. Clark, H.M. and R.J. Llewellyn, *Assessment of the erosion resistance of steels used for slurry handling and transport in mineral processing applications*. Wear, 2001. **250-251**(PART 1): p. 32-44.
4. Elalem, K. and D.Y. Li, *Variations in wear loss with respect to load and sliding speed under dry sand/rubber-wheel abrasion condition: A modeling study*. Wear, 2001. **250-251**(PART 1): p. 59-65.
5. Elalem, K. and D.Y. Li, *Dynamical simulation of an abrasive wear process*. Journal of Computer-Aided Materials Design, 1999. **6**(2): p. 185-193.
6. Lu, B., J. Luo, and S. Chiovelli, *Corrosion and wear resistance of chrome white irons - A correlation to their composition and microstructure*. Metallurgical and Materials Transactions A: Physical Metallurgy and Materials Science, 2006. **37**(10): p. 3029-3038.
7. Dogan, O.N., J.A. Hawk, and G. Laird, *Solidification structure and abrasion resistance of high chromium white irons*. Metallurgical and Materials Transactions a-Physical Metallurgy and Materials Science, 1997. **28**(6): p. 1315-1328.
8. *C-Cr-Fe Ternary Phase Diagrams*. ASM Handbook Online.
9. Powell, G.L.F., *Morphology of eutectic M₃C and M₇C₃ in white iron castings*. Metals Forum, 1980. **3**(1): p. 37-46.
10. Laird, G., R.L. Nielsen, and N.H. Macmillan, *On the nature of eutectic carbides in cr-ni white cast irons*. Metallurgical Transactions a-Physical Metallurgy and Materials Science, 1991. **22**(8): p. 1709-1720.

11. Wiengmoon, A., et al., *Microstructural and crystallographical study of carbides in 30wt.%Cr cast irons*. Acta Materialia, 2005. **53**(15): p. 4143-4154.
12. Powell, G.L.F. and G. Laird, *Structure, nucleation, growth and morphology of secondary carbides in high chromium and Cr-Ni white cast irons*. Journal of Materials Science, 1992. **27**(1): p. 29-35.
13. Carpenter, S.D., D. Carpenter, and J.T.H. Pearce, *XRD and electron microscope study of a heat treated 26.6% chromium white iron microstructure*. Materials Chemistry and Physics, 2007. **101**(1): p. 49-55.
14. Tabrett, C.P., I.R. Sare, and M.R. Ghomashchi, *Microstructure-property relationships in high chromium white iron alloys*. International Materials Reviews, 1996. **41**(2): p. 59-82.
15. Jacuinde, A.B. and W.M. Rainforth, *The wear behaviour of high-chromium white cast irons as a function of silicon and Mischmetal content*. Wear, 2001. **250**: p. 449-461.
16. Atamert, S. and H.K.D.H. Bhadeshia, *Microstructure and stability of FeCrC hardfacing alloys*. Materials Science and Engineering A, 1990. **130**(1): p. 101-111.
17. Zumelzu, E., et al., *Microstructural characteristics and corrosion behaviour of high-chromium cast iron alloys in sugar media*. Protection of Metals, 2003. **39**(2): p. 183-188.
18. Azimi, G. and M. Shamanian, *Effect of silicon content on the microstructure and properties of Fe-Cr-C hardfacing alloys*. Journal of Materials Science, 2010. **45**(3): p. 842-849.
19. Zumgahr, K.H. and G.T. Eldis, *Abrasive wear of white cast irons*. Wear, 1980. **64**(1): p. 175-194.
20. Fulcher, J.K., T.H. Kosel, and N.F. Fiore, *The effect of carbide volume fraction on the low stress abrasion resistance of high Cr-Mo white cast irons*. Wear, 1983. **84**(3): p. 313-325.
21. Lee, S., et al., *Correlation of microstructure and fracture toughness in high-chromium white iron hardfacing alloys*. Metallurgical and Materials Transactions a-Physical Metallurgy and Materials Science, 1996. **27**(12): p. 3881-3891.

22. Kootsookos, A. and J.D. Gates, *The role of secondary carbide precipitation on the fracture toughness of a reduced carbon white iron*. Materials Science and Engineering a-Structural Materials Properties Microstructure and Processing, 2008. **490**(1-2): p. 313-318.

4 VARIATIONS IN MICROSTRUCTURE OF HIGH CHROMIUM CAST IRONS AND RESULTANT CHANGES IN RESISTANCE TO WEAR, CORROSION AND CORROSIVE WEAR

Although experimental evidence has indicated that the corrosion rate could be low in the environments (in oil sands industry) in which the HCCIs are used, the synergistic attack of corrosion and wear often results in serious damage to wear-resistant materials. Clearly, in many industrial operation processes, materials with high resistance not only to wear but also to wear in corrosive environments are highly desired.

The objective of this chapter is to study the corrosive wear behavior of HCCIs and its relationship with important microstructural features and chemical composition. The alloy series used for this study contains 30Wt.% Cr, which has been used in making cast components and hard facing products for Alberta's oil sands processes against wear involving synergistic erosion-corrosion attack.

This chapter consists of five sections: (1) experimental methods used for the investigation; (2) microstructural characterization of the six alloys used (Cr = 30 wt.%, C=1, 2, 3, 4, 5 and 6 wt.%); (3) wear resistance; (4) corrosion behavior; and (5) corrosive-wear resistance.

4.1 Experimental procedure

Six HCCIs plates with similar nominal chemical compositions of chromium (30 wt.%), silicon (0.5 wt.%), manganese (2 wt.%), and various contents of carbon: 1, 2, 3, 4, 5 and 6 wt.%, balanced with iron, were casted in a sand mold. Prior to machining, the cast plates were solution treated at 1160 °C and immediately cooled down by a blast of compressed air, followed by annealing at 950 °C for 5 hours and immediately cooled by the compressed air. These plate castings were then cut into specimens with various dimensions: a) 12×12×10 mm for microstructure characterization and corrosion resistance tests; b) 76×25×10 mm for dry sand/rubber-wheel tests, using an Accutom-5 automatic precision cut-off machine (Struers A/S, Denmark).

The wear resistance of HCCIs was evaluated using a dry sand/rubber wheel apparatus [1, 2] with the procedure A described in ASTM G65-04. AFS 50/70 sand (U.S. Silica Company, WV, USA) was used for the testing. The abrasion test was performed under a contact load of 130 N with a sand flow of 300 ~ 400 g/min. The total number of revolution was 6000, responding to a total sliding distance of 4309 m. The wear resistance was ranked in terms of the volume loss, mm³. Initial testing of HCCIs in the dry abrasion-testing rig showed a standard deviation of approximately 10%.

Microstructures and chemical compositions of the as-casted HCCIs were analyzed using a Hitachi S-2700 Scanning Electron Microscope (SEM) equipped with an ultrathin window X-ray detector. The volume fraction of carbides and ferrous matrix were measured quantitatively using an Image-pro plus system (Media Cybernetics, Inc., USA). The crystalline structures were determined by X-ray diffraction (XRD) using a Rigaku rotating Co anode system (40 kV, 160 mA) at a scan rate of $2^\circ/\text{min}^{-1}$ within the range of 45 to 127° .

In order to evaluate the corrosion resistance of HCCIs, tap water and 0.5 mol/L H_2SO_4 solution were used to simulate mediate and harsh environments, respectively. Linear polarization and Tafel measurements were carried out using a commercial electrochemical system (PC4-750, Gamry Instruments, Inc., PA, USA) to determine the corrosion rate of HCCIs. The Tafel plots were recorded by scanning the potential at 1 mV/s in the range of ± 0.25 V vs. Open Corrosion Potential (OCP). Linear polarization resistances were measured at a scanning rate of 0.125 mV/s in the range of ± 30 mV vs. OCP. All specimens were mounted using epoxy resin with a surface area of 1.44 cm^2 exposed to the corrosive solution. Prior to each electrochemical measurement, the target surface was ground with silicon carbide papers of 240-, 400-, and 600-grit successively and then rinsed with deionized (DI) water and acetone in series, followed by stabilization in the corrosive medium for 60 min during which the corrosion potential was recorded. A saturated calomel electrode (SCE) was used as the

reference electrode and a platinum plate with an area of 2 cm² was used as the counter electrode. The corrosion rate (CR) in terms of penetration rate was calculated according to the ASTM G102-89 standard as follows:

$$CR = K \frac{i_{cor}}{\rho} EW \quad \{ 4.1 \}$$

$$i_{cor} = \frac{B}{Rp} \quad \{ 4.2 \}$$

$$B = \frac{\beta_a \cdot \beta_c}{2.303(\beta_a + \beta_c)} \quad \{ 4.3 \}$$

where CR is given in mm/yr; i_{cor} ($\mu\text{A}/\text{cm}^2$) is the corrosion current density; β_a and β_c correspond to the anodic and the cathodic Tafel slopes, respectively; Rp is the linear polarization resistance; B is the Stern-Geary constant; EW is the alloy equivalent weight; ρ is the density in g/cm^3 , and K is a constant, 3.27×10^{-3} mm $\text{g}/(\mu\text{A cm yr})$. All electrochemical measurements were performed at room temperature.

The corrosive wear tests were carried out using a Universal Micro-Tribometer (UMT-2 Multi-Specimen Test System, Center For Tribology, Inc., USA) under a normal load of 30 N for 20 min at a sliding speed of 2 mm/s. A schematic diagram of apparatus for corrosive wear testing was illustrated in figure 4.1. Specimen was mounted using epoxy resin, and polished using silicon carbide papers up to 600-grit, followed by acetone cleaning. The diameter of the circle

wear track was 5.50 mm, and the diameter of ball tip was 4.0 mm. The width of the track on the worn surface was measured using a calibrated microscope system. The volume loss of HCCIs in corrosive wear was calculated by combining the track width and the diameter of the ball tip, and results of volume loss are presented in mm³.

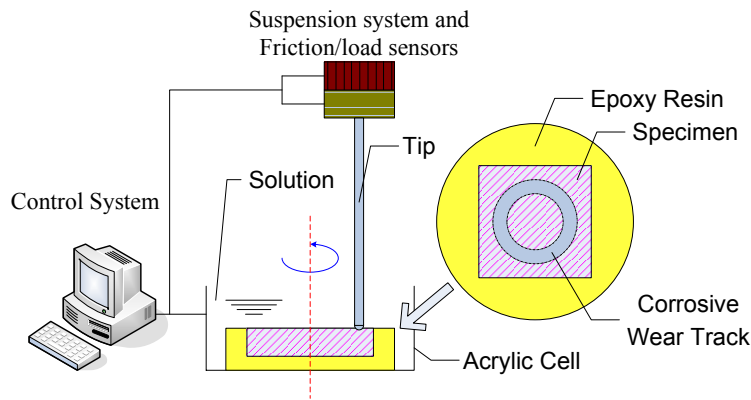


Figure 4.1: Schematic illustration of the apparatus for corrosive wear tests

4.2 Results and discussion

4.2.1 X-Ray diffraction and SEM observation

Figure 4.2 presents XRD patterns of all as-casted HCCI specimens, which indicated that the specimens mainly consisted of ferrous ferrite matrix (PDF: 6-0696) and $M(\text{Fe}, \text{Cr})_7\text{C}_3$ carbides (PDF: 36-1482).

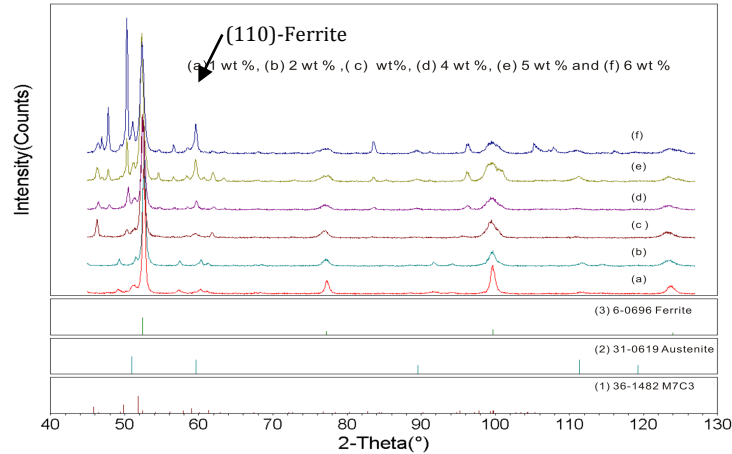


Figure 4.2: XRD patterns of as-casted HCCIs with different nominal carbon contents

It was confirmed that austenite phase expected in the as-casted structure had transformed into martensite after the heat treatment. A small amount of retained austenite (PDF: 31-0619) was observed in all six specimens, consistent with the reported results [3]. With increasing wt.% C, the ferrite fraction in HCCIs decreased, while the volume fraction of carbides increased, since more carbon could react with chromium and iron to form carbides. Besides, by checking the XRD profiles of HCCIs with slightly shifted to a lower angle with increasing wt.% C, it indicated that the lattice constants of ferrite phase increased due to its super-saturated with carbon. The volume fraction of manganese carbide was too small to be found in all XRD profiles.

In order to examine the microstructure of the cast HCCIs in details, all samples were observed under SEM and the obtained images are presented in figure 4.3. As shown, HCCIs consisted of $M(\text{Fe}, \text{Cr})_7\text{C}_3$ carbides dispersing in the ferrous matrix. The coarse dark phase was the primary $M_7\text{C}_3$ carbide and the fine dark phase was eutectic $M_7\text{C}_3$ carbide. The matrix was basically the martensite phase, transformed from austenite during the heat treatment, due to the depletion of carbon and chromium that form eutectic carbide [4]. These alloys fall into three classes: hypo-eutectic ($\%C < 3$), eutectic ($\%C \sim 3$) and hyper-eutectic ($\%C > 3$).

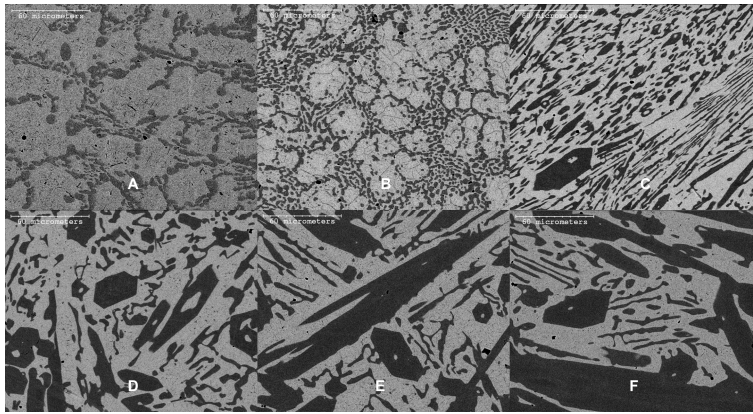


Figure 4.3: SEM images of HCCIs specimens with different nominal carbon contents (A~F: 1, 2, 3, 4, 5 and 6 wt.%)

By quantitatively analyzing the obtained SEM images using the image-pro plus system, the volume fractions of carbides and matrix in different HCCI specimens were determined and are presented in figure 4.4. As shown, the volume fraction of carbides increased with increasing the nominal carbon content. The

changes in the volume fractions of the carbide and ferrous matrix certainly affected the resistances of these alloys to corrosion, wear, and corrosive wear.

Since the corrosion resistance of HCCIs largely depends on the chemical compositions of the ferrous matrix, concentrations of various elements in the matrix were determined using an Energy Dispersive X-Ray Spectrometer (EDS). Results of the compositional analysis were presented in figure 4.5. As demonstrated, Cr was consumed more as wt.% C was increased, resulting a decrease in wt.% Cr of the matrix.

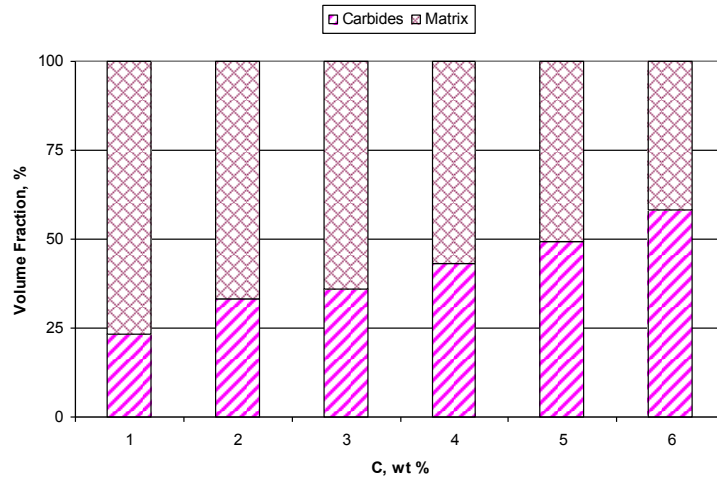


Figure 4.4: The volume fraction of carbides in HCCIs with respect to the nominal carbon content.

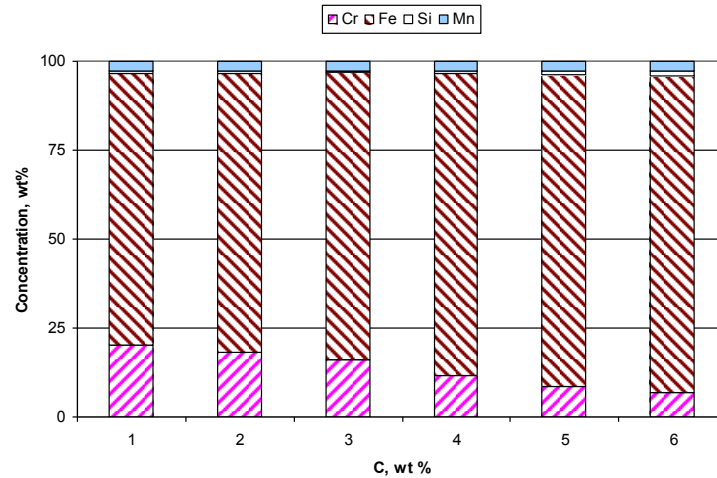


Figure 4.5: Chemical compositions of the ferrous matrix of HCCIs

4.2.2 Wear resistance

The volume losses of the HCCI specimens with different nominal contents of carbon during dry sand abrasion tests were measured following the procedure A of ASTM G65 and the results were illustrated in figure 4.6.

As demonstrated, the wear resistance of the HCCIs was dominated by the nominal content of carbon. The volume loss decreased steeply as the wt.% C increased until a critical value between 2 and 3 wt.% C, above which the volume loss became stable, implying that the wear resistances of HCCIs were almost independent of wt.% C when wt.% C was higher than the critical value. This is understandable. As wt.% C increases, the alloy changes from a hypoeutectic structure to a hypereutectic one with increased amount of carbides (see figure

4.3). When the volume fraction of hard carbides ($\sim 1500\text{HV}$) is high enough, hardness of the HCCIs increases, which enhances the overall wear resistance of the alloy. In this case, the abrasive particles (Size= $212 \sim 300 \mu\text{m}$, 840HV [5]) will have difficulty to attack or remove the relatively softer matrix ($600\sim 800\text{HV}$) and thus dig out the carbides as the spacing between carbides is reduced. Further increasing the volume fraction of carbides would not benefit much the wear resistance of these alloys. Instead, if the volume fraction of carbides was too high without enough matrix support, consequently reduced toughness would have a negative influence on the wear resistance of HCCIs. This may explain the slight decrease in the wear resistance as the carbon content was increased to 6 wt.% C, as shown in figure 4.6.

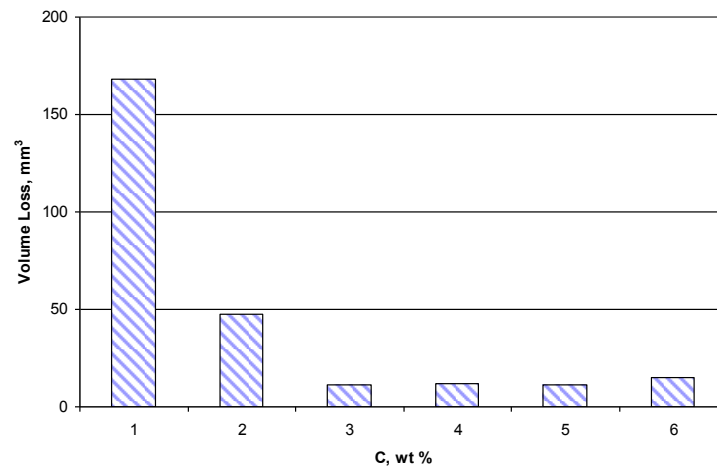


Figure 4.6: Effects of nominal carbon content on the wear resistance of HCCIs.

4.2.3 Corrosion rate and passivation behavior

The corrosion rates of HCCIs in two solutions: tap water and 0.5 mol/L H_2SO_4 , were determined using the electrochemical methods described in the section of experimental procedure. Obtained results are shown in figure 4.7, and values of measured corrosion potentials are summarized in table 4.1. It was interesting to observe that the trend of changes in corrosion rate of the HCCIs with wt.% C in water was opposite to that in the H_2SO_4 solution. In water, as a medium corrosive environment, the corrosion rate increased as wt.% C increased, while in the H_2SO_4 solution that simulated a more corrosive environment, the apparent corrosion rate decreased with an increase in wt.% C. As known, the carbides have a much nobler corrosion potential than the ferrous matrix and could more or less influences the cathodic reaction in corrosion of HCCIs. Therefore, the corrosion rate of HCCIs mainly depends on the corrosion behavior of the ferrous matrix. It has been demonstrated that the corrosion resistance of Fe-Cr alloys depends mainly on the concentration of free Cr, which renders HCCIs possess the passivation capability [6, 7].

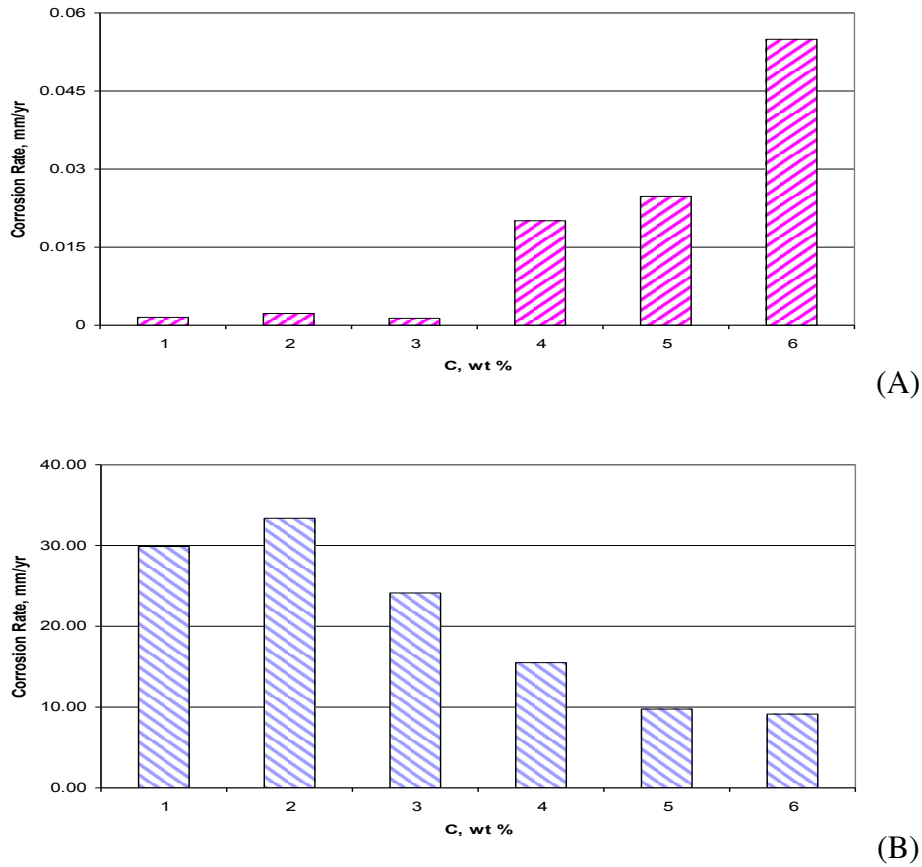


Figure 4.7: The corrosion rates of HCCIs in tap water (A) and 0.5 mol/L H₂SO₄ solution (B)

Table 4.1: Corrosion potentials (CP, mV) of HCCIs in tap water and 0.5 mol/L H₂SO₄ solution

Medium	Nominal contents of Carbon, wt. %					
	1	2	3	4	5	6
0.5M H ₂ SO ₄	-513.9	-494.2	-487.2	-479.3	-477.0	-473.1
Tap Water	-52.7	-62.26	-67.62	-191.6	-370.6	-453.7

In this study, although the nominal chromium content was kept the same for all casted HCCI specimens, its free concentration in ferrous matrix changed significantly as shown figure 4.5. With an increase in wt.% C, Cr concentration in the ferrous matrix decreased accompanied with the formation of more carbides, which explained the increase in the corrosion rate when the samples were corroded in water, as figure 4.7A illustrated. However, the situation was different when the HCCI specimens were exposed to the H₂SO₄ solution (figure 4.7B). As shown, a higher wt.% C, accompanied with the formation of more carbides, corresponded to a lower corrosion rate. In order to explain this unexpected phenomenon, it should be indicated that the corrosion rate mainly represented the dissolution rate of the ferrous matrix rather than the entire surface. As wt.% C was increased, the volume fraction of the ferrous matrix or its surface area exposed to the corrosive solution decreased, which could decrease the overall corrosion rate as figure 4.5B illustrated.

The decrease in the overall corrosion rate of the two-phase HCCIs may not necessarily mean that the material was more resistant to corrosion, since the corrosion rate per unit area of the ferrous matrix could be different from the overall corrosion rate due to the depletion of Cr in matrix when wt.% C was increased as shown in figure 4.5. In particular, severe corrosion could occur locally at the carbide/matrix interface, a preferential region for corrosion. Therefore, even the corrosion rate per unit area of the ferrous matrix (dividing the

overall corrosion rate by the area fraction of ferrous matrix) may not be adequate parameter either to precisely characterize the resistance to electrochemical attack in such a corrosive solution.

As a matter of fact, when the HCCI specimens were immersed in the H_2SO_4 solution, hydrogen bubbles were released. This implied that the HCCIs were attacked by the solution more severely than in water and the preferential corrosion of matrix would loosen the carbides. This should affect the wear performance of HCCIs when attacked by wear in the corrosive environment.

The anodic polarization curves of HCCIs in tap water and 0.5 mol/L H_2SO_4 were recorded to evaluate the passivation behaviors of HCCIs. The curves were illustrated figure 4.8A and 8B, respectively. As shown, HCCIs had strongly passivation capability in the H_2SO_4 solution but not the case when immersed in tap water. In water, it was clear that increasing wt.% C decreased the corrosion potential (more active) and increased the corrosion rate. While in the H_2SO_4 solution, wt.% C did not show a large influence on the corrosion potential, which implied that the corrosion reaction in this solution was more influenced by kinetic factors.

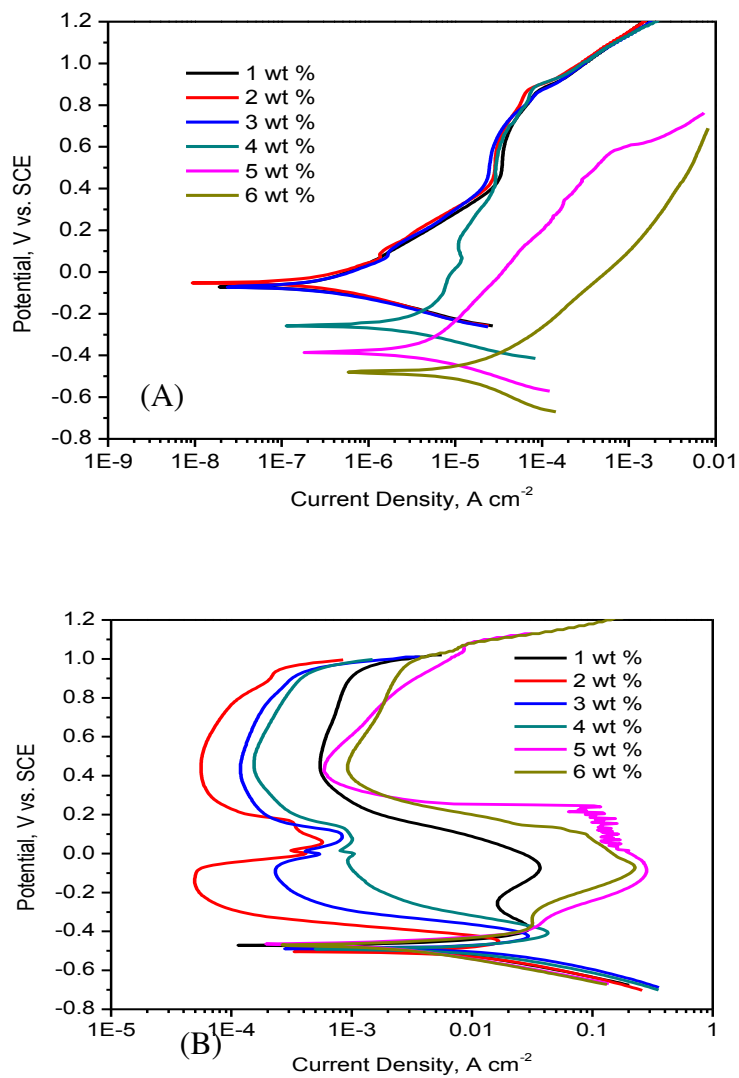


Figure 4.8: Anodic polarization plots: (A) HCCIs in tap water; and (B) 0.5 mol/L H₂SO₄

4.2.4 Corrosive wear

A Micro-Tribometer was used to evaluate the corrosive wear behaviors of HCCIs in tap water and 0.5 mol/L H₂SO₄ solution, respectively, under a normal load of 30 N for 20 min at a sliding speed of 2 mm/s. Results of the wear tests in water were presented in figure 4.9. As shown, the resistance of the HCCIs to wear in water increased as wt.% C increased. This trend of change in the wear resistance was similar to that observed during G65 abrasion tests (figure 4.6), but the difference in volume loss between HCCIs with low %C and high %C decreased. Under the dry abrasion condition, the maximum volume loss (1 wt% C) was about 15 times as high as those with higher wt.% C. While this difference was much smaller (about 2 times) when tested under the condition of sliding wear in water (figure 4.9). This could be attributed to increased corrosion rates of HCCIs with higher wt.% C that made the synergistic attack of wear and corrosion more severely.

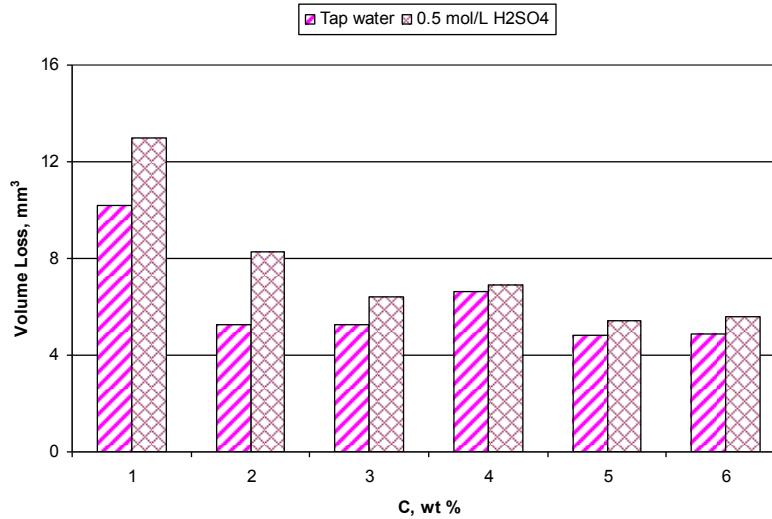


Figure 4.9: The corrosive wear resistance of HCCIs in tap water and 0.5 mol/L H₂SO₄ solution

The situation was similar when the sliding wear tests were performed in the 0.5 mol/L H₂SO₄ solution as shown in figure 4.9. Due to the higher corrosion rate in the H₂SO₄ solution, the volume loss caused by wear in this acidic solution was higher than that in tap water. It may also need to be indicated that for specimens with higher wt% C (2 ~ 6), although the overall corrosion rate decreased with wt% C, their local corrosion especially at carbide/matrix interface could be severe, which may make hard carbides easier to be removed when wear was involved. This may explain the smaller difference in volume loss between samples containing low and high carbon contents, compared to that observed during the dry abrasion tests.

4.3 Conclusions

HCCIs with 30 wt.% of chromium and various carbon contents from 1 to 6 wt.% were casted and solution treated. The microstructure analysis showed that the as-prepared white iron contained $M(\text{Fe,Cr})_7\text{C}_3$ carbides in a martensite matrix. A small amount of retained austenite also was observed. With increasing the nominal content of carbon, the structure of HCCI changed from hypoeutectic, through eutectic, to hypereutectic, successively.

The ASTM G65 tests showed that the wear resistance of HCCIs was dominated by the carbon content, which had a critical value between 2 and 3 wt.%. Below the critical value, HCCIs were in the form of hypoeutectic that showed lower wear resistance. The wear resistance steeply increased as %C was increased. Above the critical value of %C, HCCIs were in the form of hypereutectic, and their wear resistances were stable or approximately independent of %C within the current range of %C.

The corrosion resistance of HCCIs was largely influenced by the free Cr concentration in the ferrous matrix. In water, the corrosion rate increased with increasing C%. While in the 0.5 mol/L H_2SO_4 solution the apparent corrosion rate decreased with an increase in %C (corresponding to an increase in the volume fraction of carbides) probably due to the decrease in the surface area of ferrous matrix that participated in the corrosion reaction.

The resistance of HCCIs to wear in corrosive environments was reduced. The resistance of HCCI to corrosive wear was dependent on its resistance to wear and corrosion as well as the corrosiveness of the solution. Whether in water or 0.5 mol/L H₂SO₄ solution, the corrosive wear resistance of HCCIs was still dominated by their resistance to mechanical wear. Due to the higher corrosion rate in 0.5 mol/L H₂SO₄ solution, their volume loss rate of corrosive wear was larger than that in tap water. Besides, the difference in volume loss between HCCIs with low %C and high %C decreased, this should be attributed to the synergistic attack of wear and corrosion when the HCCIs were worn in the corrosive environments.

4.4 Bibliography

1. Elalem, K. and D.Y. Li, *Dynamical simulation of an abrasive wear process*. Journal of Computer-Aided Materials Design, 1999. **6**(2): p. 185-193.
2. Elalem, K. and D.Y. Li, *Variations in wear loss with respect to load and sliding speed under dry sand/rubber-wheel abrasion condition: A modeling study*. Wear, 2001. **250-251**(PART 1): p. 59-65.
3. Carpenter, S.D., D. Carpenter, and J.T.H. Pearce, *XRD and electron microscope study of a heat treated 26.6% chromium white iron microstructure*. Materials Chemistry and Physics, 2007. **101**(1): p. 49-55.
4. Carpenter, S.D., D. Carpenter, and J.T.H. Pearce, *XRD and electron microscope study of an as-cast 26.6% chromium white iron microstructure*. Materials Chemistry and Physics, 2004. **85**(1): p. 32-40.

5. Tabrett, C.P., I.R. Sare, and M.R. Ghomashchi, *Microstructure-property relationships in high chromium white iron alloys*. International Materials Reviews, 1996. **41**(2): p. 59-82.
6. Huang, X. and Y. Wu, *A high Cr-Mo alloy iron*. Journal of Materials Engineering and Performance, 1998. **7**(4): p. 463-466.
7. Sedriks, A.J., *Effects of alloy composition and microstructure on the passivity of stainless-steels*. Corrosion, 1986. **42**(7): p. 376-389.

5 MICROSTRUCTURE OF HIGH (45 WT.%) CHROMIUM CAST IRONS AND THEIR RESISTANCE TO WEAR AND CORROSION

The objective of studies reported this chapter is to evaluate the wear and corrosion behaviors of a series of HCCI with the highest chromium addition, 45Wt.% Cr, of the expanded compositional range of HCCI. As mentioned previously, recent advances in foundry techniques have made it possible to cast hypereutectic white irons with high carbon and chromium concentrations typified by Warman's A61 and A217 [1]. The erosion mapping demonstrated that HCCIs with their %Cr higher than those of conventional HCCIs show impressive resistances to corrosion and corrosive wear, indicating that the HCCIs with extended %Cr are worth being investigated. The wide literature available for white irons is very limited for HCCIs containing Cr > 40 wt.% and C up to 6 wt.% and their performance during wear and corrosion has not been fully established [2].

This chapter comprises of five sections: (1) experimental methods used for the study; (2) microstructural characterization of the six alloys used (Cr = 45 Wt. %, C=1, 2, 3, 4, 5 and 6 wt %); (3) abrasive wear resistance; (4) corrosion behavior; and (5) erosion-corrosion performance.

5.1 Experimental details

5.1.1 Materials

Six plates of HCCIs with nominal chemical compositions of chromium (45 Wt.%), silicon (0.5 Wt.%), manganese (2 Wt.%), and various concentrations of carbon: 1, 2, 3, 4, 5 and 6 Wt.%, respectively, balanced by iron, were cast in a sand mold. Prior to machining, the cast plates were solution treated at 1160 °C and immediately cooled down by a blast of compressed air, followed by heat treated at 950 °C for 5 hours and cooled by a compressed air flow. These plate castings were then cut into specimens with various dimensions: a) 12×12×10 mm for microstructure characterization and corrosion tests; (b) 50×10×5 mm for erosion-corrosion tests in sand-containing slurry; and (c) 76×25×10 mm for dry sand/rubber-wheel abrasive wear tests.

5.1.2 Characterization

Microstructures and chemical compositions of the HCCIs were analyzed using a Hitachi S-2700 Scanning Electron Microscope (SEM) equipped with an ultrathin window X-ray detector. The volume fraction of carbides in the HCCIs was measured quantitatively with image analysis software of Image-Pro Plus (Version 6.0, Media Cybernetics, Inc., USA). The phase state was analyzed by X-ray diffraction (XRD) using a Rigaku rotating Cu anode system at a scan rate of 1.5 °/min within the angle range from 30 to 120°. The micro-hardness of

individual phases in the HCCIs was evaluated using a micro-indentation probe (H100C, Fischer Technology Inc., USA) with a diamond tip under a maximum load of 300 mN, and a cycle of loading and unloading took 40s. Hardness of each phase was measured at least 5 times, based on which average values were calculated.

5.1.3 Abrasive wear testing

The abrasive wear resistance of the HCCIs was evaluated using a dry sand/rubber wheel apparatus following the “Procedure A/6000 wheel revolutions” described in ASTM G65. AFS 50/70 sand (U.S. Silica Company, USA) was used, and the sand flow rate was adjusted to 300 ~ 400 g/min. A contact load of 130 N was selected. The number of wheel revolution was set to 6000, responding to a total linear sliding distance of 4.3 km. The abrasive wear resistance of the HCCIs was reported in terms of volume loss, mm³ [3-5]. Initial testing of HCCIs in the dry abrasion-testing rig showed a standard deviation of approximately 10%.

$$Volume\ loss, mm^3 = \frac{Mass\ loss\ (g)}{Density\ \left(\frac{g}{cm^3}\right)} \times 1000 \quad \{ 5.1 \}$$

5.1.4 Corrosion testing

The corrosion resistance of HCCIs was evaluated by electrochemistry measurements in tap water at pH 3, 5 and 7, respectively, first two of which were

achieved by respectively adding 1 mol/L NaOH and 0.5 mol/L and H₂SO₄ to tap water. Briefly, each specimen of HCCIs connecting to a metal wire was mounted using epoxy resin with a surface area of ~1.44 cm² exposed to the testing solution. The target surface of mounted specimen was ground with silicon carbide papers up to 600-grit, and then degreased with acetone and rinsed with distilled water, and finally dried by a compressed air flow. The polarization resistance, R_p, was used to rank the corrosion resistance of HCCIs, since the corrosion current density (I_{Corr}) is reverse proportional to R_p as follows:

$$I_{Corr} = \frac{B}{R_p} \quad \{ 5.2 \}$$

where *B* is a constant for a specific corrosion system [6]. The linear polarization of the HCCIs was recorded with a commercial electrochemical system (PC4-750, Gamry Instruments, Inc., USA) within the range of ±30 mV versus open circuit potential, E_{ocp}, at a scanning rate of 0.125 mV/s. The R_p was determined as the tangent of the polarization curve at I = 0. A Saturated Calomel Electrode (SCE) was used as the reference electrode and a platinum plate with area of 2 cm² was used as the counter electrode. All measurements were repeated at least three times.

5.1.5 Erosion-corrosion testing

The erosion-corrosion resistance of HCCIs was measured using a slurry-pot erosion tester, which is schematically shown in figure 5.1. It consisted of a

stainless steel cylinder with 32 cm in diameter and 30 cm in height, 4 buffers attached to the inner wall of cylinder evenly. Specimens were driven by a direct current permanent magnet motor (Leeson Electric Corporation, WI, USA). The slurry was tap water mixed with silica sand (12-50mesh, semi-rounded, Manus Abrasive Systems Inc., Edmonton, Canada), $V_{H_2O} : V_{sand} = 4:1$. The pH level of slurry was adjusted to be 3, 5 and 7, respectively, by adding controlled amounts of NaOH and H₂SO₄ solutions. The impingement angle of the set-up was adjustable. Prior to erosion-corrosion tests, all specimens of HCCIs were ground using abrasive papers up to 600-grit, followed by thoroughly cleaning and weighing before and after testing. Four specimens could be tested simultaneously. The erosion resistance of the HCCIs was reported in terms of volume loss, mm³. The speed of motor rotation was converted to an impingement velocity of 8 m/s, and the impingement angle was set at 45°. The total travel distance of each sample in slurry during the erosion-corrosion test was about 25 km. Results were obtained with a standard deviation of approximately 5%.

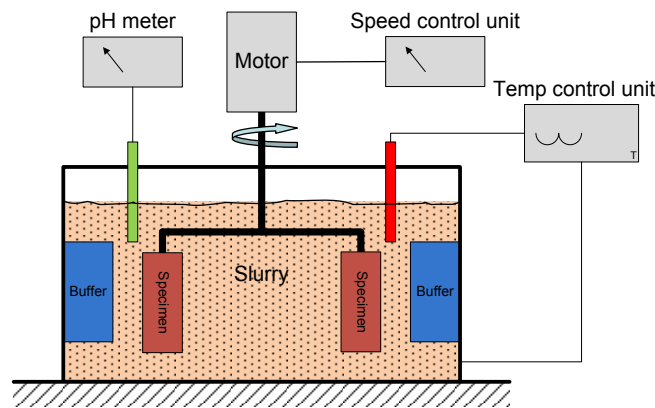


Figure 5.1: Schematic illustration of the slurry-pot erosion tester.

5.2 Results and discussion

5.2.1 Microstructure and chemical analysis

Six specimens of HCCIs with different nominal concentrations of carbon were examined using SEM and obtained images are presented in figure 5.2. As shown, HCCIs with 1 and 2 Wt.% nominal carbon were in the hypoeutectic state; when nominal carbon was above 3 Wt.%, coarse primary carbides showed up along with fine eutectic carbides; the primary carbides became coarser with further increasing the nominal carbon concentration. According to the condition of heat treatment for age hardening, the ferrous matrix of all HCCIs should be in the martensitic state [7]. It was interesting to notice that the primary carbides in 45-4 had a duplex structure consisting of a dark core and a lighter layer or shell, as shown in figure 5.2D. The core is M_7C_3 and the lighter shell is $M_{23}C_6$, based on the local composition analysis with EDX in combination with XRD analysis, which are presented in the following sections.

The volume fraction, types and particle size of carbides in the HCCIs are of importance to their mechanical properties. The volume fractions of total carbides in the 45-series of HCCIs were determined by quantitatively analyzing SEM images using Image-Pro Plus software. At least two images with low magnification (100×) were analyzed, and average values are presented in figure 5.3. As shown, the volume fraction of total carbides in the 45-series of HCCIs

went up with increasing the nominal carbon concentration and this variation was particularly rapid when the nominal carbon concentration was increased from 1 to 3 Wt.%. The HCCIs had three groups of carbides: very tiny secondary carbides dispersing in ferrous matrix, fine eutectic carbides and coarse primary carbides. The primary carbides only appeared in hypereutectic HCCIs, specifically, 45-4, 45-5 and 45-6, as shown in figure 5.2. Compared to primary carbides, eutectic carbides are much smaller and the mean distance among the carbide particles is shorter, which are expected to have positive effects on the abrasive wear and erosion-corrosion resistances. Therefore, the SEM images of HCCIs were further analyzed using the Image-Pro Plus software to determine the volume fractions of the fine eutectic carbides alone. The obtained volume fractions of fine eutectic carbides in 45-series of HCCIs are also presented in figure 5.3. As shown, the 45-4 contains 18 vol% of eutectic carbides, while 45-6 has only 10 vol%. In other words, up to 37 vol% of carbides in 45-4 is eutectic, while only 16 vol% in 45-6. The changes in the amount and types of carbides certainly would affect the performance of HCCIs to abrasive wear and erosion-corrosion.

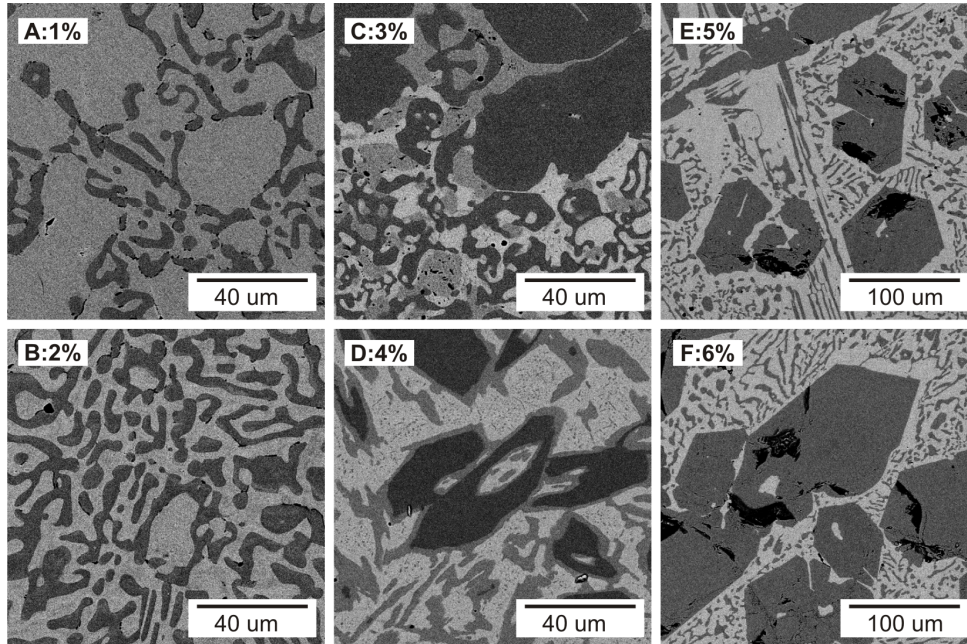


Figure 5.2: Back-scattered Electron images of 45-series of HCCIs (A-F: with varied nominal carbon of 1, 2, 3, 4, 5 and 6Wt.%, respectively).

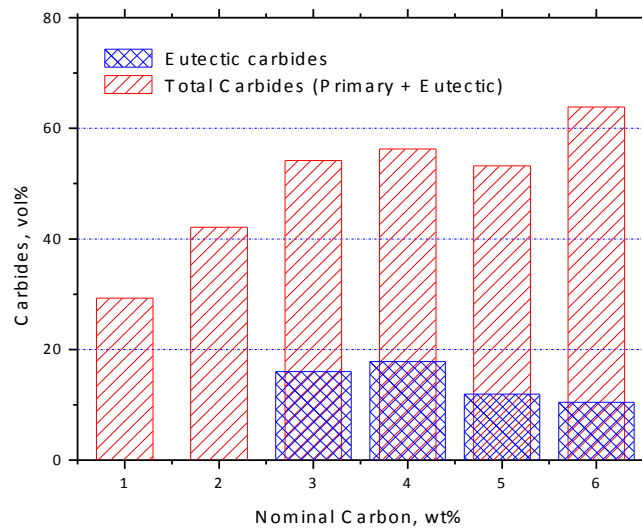


Figure 5.3: Volume fraction of total carbides in 45-series of HCCIs.

In order to determine the crystalline structure of carbides in the 45-series of HCCIs, their XRD patterns were collected and are illustrated in figure 5.4. As shown, the majority of carbides in 45-1, 45-2 and 45-3 were identified as cubic-face centered M_2C_6 (PDF: 5-0721), while both hexagonal close packed M_7C_3 (PDF: 17-0333) and M_2C_6 are found in 45-4: eutectic carbides and those in the outer layers of primary carbides (M_7C_3) are M_2C_6 . The amounts of primary M_7C_3 and eutectic M_2C_6 carbides in 45-4 were also determined using the Image-Pro Plus, which were 24 vol% and 32 vol%, respectively. The M_7C_3 was predominant in 45-5 and 45-6 for both fine eutectic and coarse primary carbides. The crystalline structure of the matrix of HCCIs is consistent with martensitic lattice (PDF: 44-1290), and no diffraction peaks of austenite were found. This confirms that the austenite phase expected in the as-casted structure had transformed to martensitic phase completely after the age-hardening treatment.

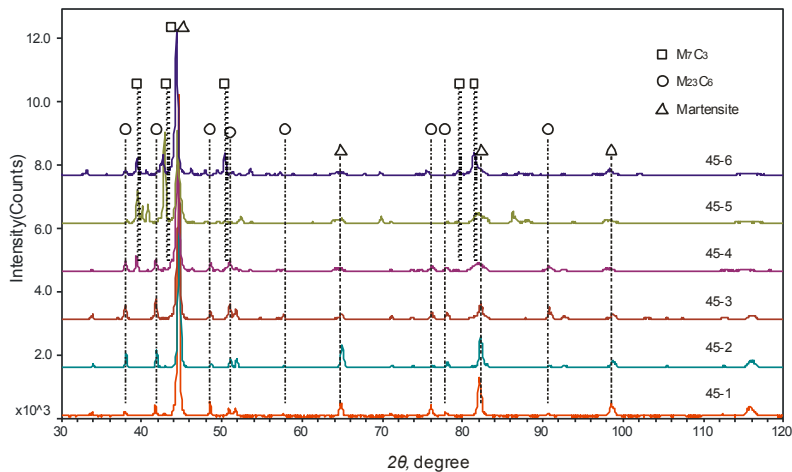


Figure 5.4: XRD patterns of 45-series of HCCIs (A-F: with nominal carbon of 1, 2, 3, 4, 5 and 6Wt.%, respectively).

5.2.2 Abrasive wear resistance of HCCIs

The volume loss of the 45-series HCCIs with different nominal concentrations of carbon during dry sand abrasion tests is illustrated in figure 5.5. As shown, the wear resistance of HCCIs is strongly affected by the carbon content. The volume loss of the 45-series of HCCIs decreased steeply as the carbon content was increased up to 4 Wt.%, above which the volume loss increased with increasing %C instead. This is understandable. With an increasing in the carbon content, the alloy changed from a hypoeutectic state to a hypereutectic one accompanying with an increase in the amount of carbides (see figure 5.3). The increased amount of hard carbides resulted in higher hardness and thus enhanced the overall wear resistance of the HCCIs. In this case, the abrasive particles (Size=212~300 μ m, 840HV) had difficulties to attack or remove the relatively softer matrix (600~800HV) and to dig out carbides as the mean distance between carbides was reduced. However, if the volume fraction of carbides was too high without enough matrix support, the reduced toughness, resulting from brittle carbides, would have a negative influence on the wear resistance of HCCIs. Unlike fine eutectic carbides, coarse primary carbides have less flexibility provided by the surrounding ferrous matrix i.e. less deformation or impact energy would be absorbed by the matrix when the carbides are under external forces or impact. This may explain the decrease in wear resistance of HCCIs as the carbon content was increased to 5 and 6 Wt.%, as shown in figure 5.5. The highest wear resistance of HCCI 45-4 could benefit from its largest amount of fine eutectic

carbides, which reinforced the matrix while better supported by the relatively flexible ferrous matrix.

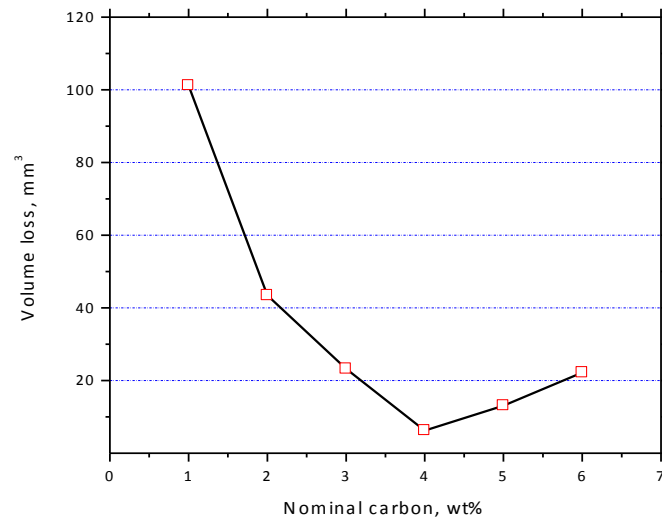


Figure 5.5: Effects of nominal carbon on the wear resistance of 45-series of HCCIs.

The nominal carbon content affects the wear resistance of HCCI by influencing not only the overall mechanical behavior of the material but also local mechanical properties of carbides and the matrix. In order to determine the effect of carbon content on local mechanical properties, micro-indentation tests were performed on both carbides and matrix in the 45-series HCCIs. Results of the local mechanical testing are given in figure 5.6. As illustrated, both carbides and matrix in alloys 45-1 and 45-2 show low hardness. As the carbon content increases up to 4 Wt.%, the hardness of the carbides and the matrix increase, but after that, carbon content > 4%, the hardness of carbides decreases inversely with

increasing carbon concentration. It should be mentioned that the measured may not be the intrinsic properties and the determined local properties should be influenced by the local microstructure. For instance, the increase in the volume fraction of carbides may lead to an enhanced constraint to adjacent matrix, resulting in an increase in hardness of the matrix, which also leads to additional constraint back to the carbides. The increase in hardness of the carbide with the carbon concentration could be attributed to the changes in carbide type from $M_{23}C_6$ to M_7C_3 as well. The highest wear resistance of HCCI 45-4 largely benefited from its high hardness values of both carbides and matrix, compared to other 45-series of HCCIs. However, further increasing carbon content to 5 and 6 Wt.%, the apparent hardness of carbides decreased, likely due to the loss of toughness, resulting in a weakened wear resistance.

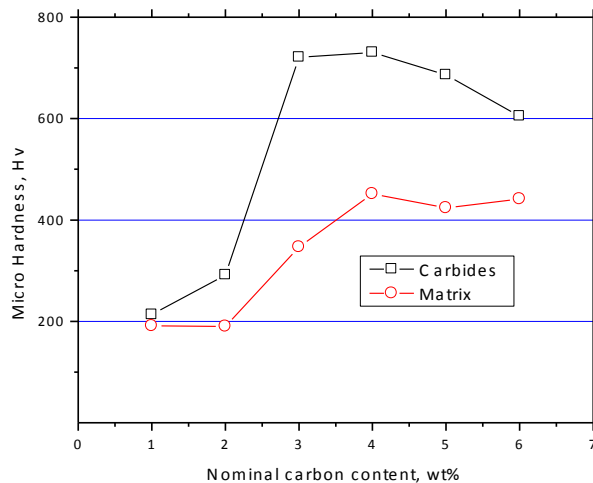


Figure 5.6: Micro-hardness of carbides and matrix in 45-series of HCCIs.

5.2.3 Corrosion resistance

The corrosion resistance of 45-series of HCCIs in tap water at pH 3, 5, and 7 was measured with linear polarization method, and the obtained results are shown in figure 5.7. It was observed that the corrosion resistance of 45-series of HCCIs decreased with increasing the nominal carbon content at all tested pH levels. As known, the galvanic corrosion occurred on the surface of HCCIs due to the difference in corrosion potentials between carbides and the ferrous matrix. The carbides have a much nobler corrosion potential than the ferrous matrix and hence act as cathodes in galvanic corrosion cells.

The corrosion reactions of HCCIs in a solution containing dissolved oxygen with near-neutral pH could be written as follows [6-8]:

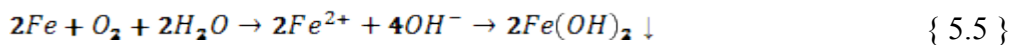
Anodic reaction:



Cathodic reaction:



Overall reaction:



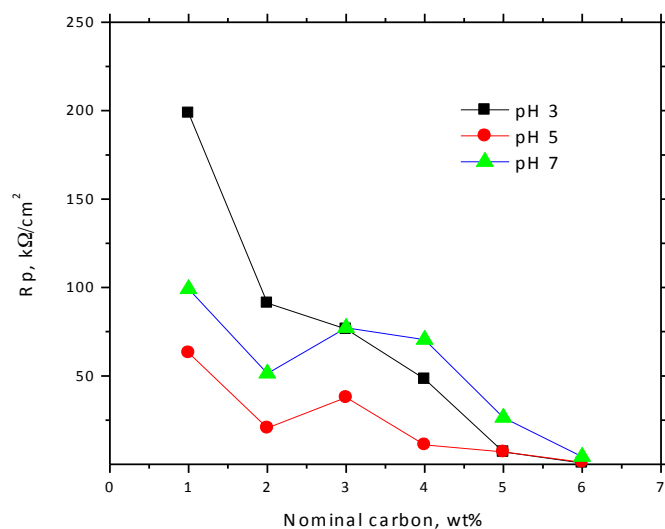


Figure 5.7: Effects of nominal carbon on the corrosion resistance of 45-series of HCCIs in tap water at various pH levels.

As indicated by the overall reaction (5.5), the corrosion resistance of HCCIs mainly depends on the corrosion behavior of the ferrous matrix in a specific corrosive environment where the concentration of dissolved oxygen is stable. It has been well demonstrated that the corrosion resistance of the ferrous matrix of HCCIs is dependent on the concentration of free chromium, which provides the HCCIs the passivation capability [5, 6]. For the 45-series of HCCIs, the concentration of free chromium in the ferrous matrix changed significantly as shown figure 5.8. With an increase in the nominal carbon content, the chromium concentration in the ferrous matrix decreased almost linearly, accompanied with the formation of more carbides, which explains the decrease in polarization

resistance when the alloys were corroded in tap water at all tested pH levels, as figure 5.7 illustrates. In addition, the corrosion current also increases with increasing the cathode/anode area ratio [9]. In the current case, the carbides are the cathodes, and the ferrous matrix is anode. With increasing carbon content, the area ratio of cathode to anode is increased. For instance, the volume fraction of carbides in 45-6 is 64 vol%, which means that the ratio of cathode/anode is as high as 1.78. It may explain why the polarization resistance of 45-6 is close to zero under the current corrosion conditions. Consequently, based on the combination of the concentration of free chromium in matrix and the area ratio of cathode/anode, the polarization resistance of 45-1 is estimated to be 285, 58 and 33 times higher than those of 45-6 at pH 3, 5 and 7, respectively.

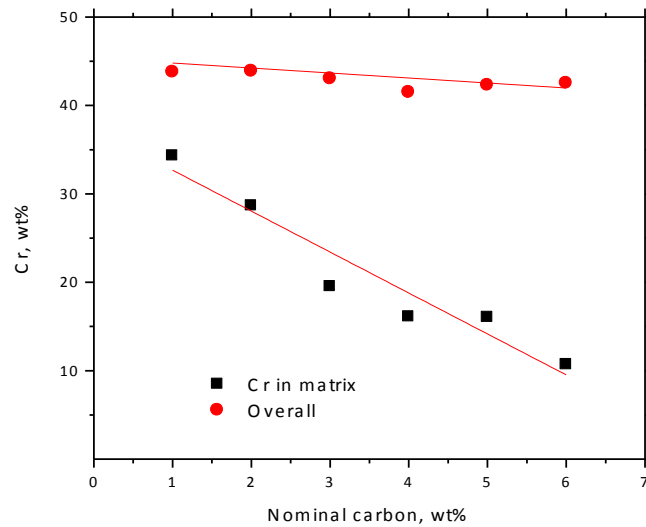


Figure 5.8: The measured overall concentration of chromium in 45-series of HCCIs and the free chromium in their ferrous matrix.

5.2.4 Erosion-corrosion resistance of HCCIs

Slurry erosion testing was performed as described in section 2.3 in sand-containing tap water at pH 3, 5 and 7, respectively. The impingement angle was 45° and the speed, converted from motor rotation, was set as 8 m/s. Volume losses of the HCCIs during erosion-corrosion testing are presented in figure 5.9.

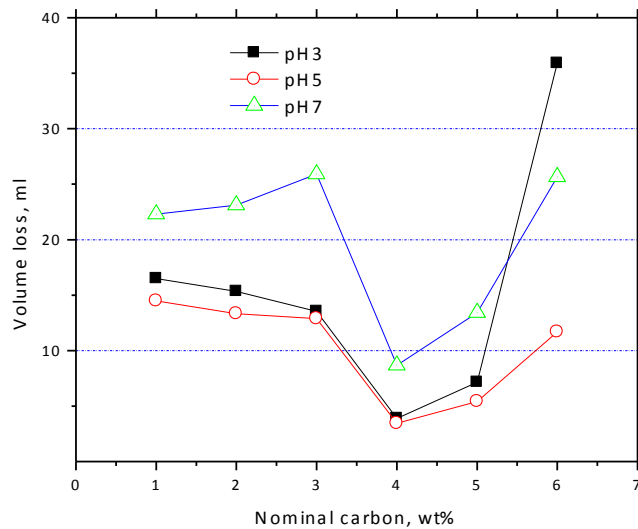


Figure 5.9: Effects of nominal content of carbon on the erosion-corrosion resistance of 45-series of HCCIs in corrosive slurry at pH3, 5 and 7, respectively.

As shown, the volume losses of the HCCIs in water had no significant variation when carbon content was in the range of 1 to 3 Wt.%, but sharply decreased when the carbon content was increased to 4 Wt.%, above which the

erosion loss increased remarkably again. The slurry's pH value influenced the erosion resistance of the 45-series of HCCIs: the volume loss was higher at pH 7 than those at pH 3 and 5, originating from the weakened passivation capability in the neutral water. This trend of change in erosion resistance was somewhat similar to that observed during ASTM G65 abrasion tests (figure 5.5). Under the dry wear condition, alloy 45-4 showed the highest wear resistance. The volume loss of alloy 45-1 (1 Wt.% C) was about 16 times larger than that of the alloy 45-4, while this difference became smaller (about 3~4 times) under the slurry erosion conditions, as shown in figure 5.9. This was caused by elevated corrosion rates of 45-series of HCCIs with increasing the carbon content that made the material less resistant to the synergistic attack of wear and corrosion.

Based on the performed tests, HCCI 45-4 exhibits the best performance in both abrasive wear and erosion-corrosion tests, although its corrosion resistance is lower than those with lower %C. As discussed earlier, hard carbides mainly contribute to the wear resistance and erosion resistance as well if the slurry is not very corrosive. However, coarse carbides usually result in lower overall fracture toughness, compared to fine eutectic carbides. Thus, the wear resistance depends on not only the volume fraction but also the size of carbides. Therefore, alloy 45-4 having the highest volume fraction of fine eutectic carbides may have a positive effect on its wear resistance. Another possible factor responsible for the highest wear resistance of alloy 45-4 is its duplex configuration of primary carbides as

shown in the SEM images of 45-series of HCCIs. The core of the carbides is M_7C_3 and the shell is $M_{23}C_6$. $M_{23}C_6$ is softer but tougher than M_7C_3 . As reported by Lin et al. [10], $M_{23}C_6$ is about 46% softer but 85% tougher than M_7C_3 in a ferrous alloy. This shell thus acted as a transition layer, which would help to reduce the interfacial mismatch between the carbide and the ferrous matrix, resulting in a higher resistance to interfacial fracture during wear processes. Further studies on shell-core carbide structure in 45-series of HCCIs and how it affects the performance of the material in wear and erosion are being carried out.

5.3 Conclusions

The solution-treated and age-hardened 45-series of HCCIs were investigated with regard to their microstructure and resistance to wear and corrosion. The following conclusions are drawn:

- The 45-series of HCCIs are in three states: hypoeutectic ($\%C < 2$), eutectic ($\%C \sim 2$) and hypereutectic ($\%C > 2$). The volume fraction of total carbides increased considerably with increasing the carbon content. The carbides in HCCIs with low nominal carbon concentrations (1~3 Wt.%) were identified as cubic-face centered $M_{23}C_6$, while hexagonal close-packed M_7C_3 existed in HCCIs with higher overall carbon concentrations.

The ferrous matrix was in a martensitic state.

- The abrasion resistance of the 45-series of HCCIs initially increased with an increase in the carbon concentration but decreased with continuously increasing the carbon content after reaching the maximum abrasive wear resistance at 4%C. The performance of the HCCIs during slurry erosion tests showed a similar trend. The HCCI 45-4 performed the best during both the abrasion and erosion tests.
- The corrosion resistance of the HCCIs decreased with an increase in the overall carbon concentration, which is attributed to the reduced free chromium in the matrix and increased area ratio of cathode to anode. Low (≤ 3 Wt.%) and too high (6 Wt.%) carbon concentrations made the HCCIs suffer serious damage during slurry erosion tests, due to enhanced synergy of wear and corrosion attacks.
- A duplex configuration of primary carbides was observed in HCCI 45-4. The core of the primary carbides was M_7C_3 and the shell or outer layer was $M_{23}C_6$. Since $M_{23}C_6$ is generally softer but tougher than M_7C_3 , the duplex carbides could benefit the wear resistance of the material with enhanced interfacial bonding between the carbides and the matrix. This could be one of factors responsible for the highest abrasive wear and erosion-corrosion resistance the alloy 45-4.

5.4 Bibliography

1. Llewellyn, R.J., S.K. Yick, and K.F. Dolman, *Scouring erosion resistance of metallic materials used in slurry pump service*. *Wear*, 2004. **256**(6): p. 592-599.
2. Tian, H.H., G.R. Addie, and R.J. Visintainer, *Erosion-corrosion performance of high-Cr cast iron alloys in flowing liquid-solid slurries*. *Wear*, 2009. **267**(11): p. 2039-2047.
3. Elalem, K. and D.Y. Li, *Dynamical simulation of an abrasive wear process*. *Journal of Computer-Aided Materials Design*, 1999. **6**(2): p. 185-193.
4. Elalem, K. and D.Y. Li, *Variations in wear loss with respect to load and sliding speed under dry sand/rubber-wheel abrasion condition: A modeling study*. *Wear*, 2001. **250-251**(PART 1): p. 59-65.
5. Tang, X.H., et al., *Variations in microstructure of high chromium cast irons and resultant changes in resistance to wear, corrosion and corrosive wear*. *Wear*, 2009. **267**(1-4): p. 116-121.
6. Lu, B., J. Luo, and S. Chiovelli, *Corrosion and wear resistance of chrome white irons - A correlation to their composition and microstructure*. *Metallurgical and Materials Transactions A: Physical Metallurgy and Materials Science*, 2006. **37**(10): p. 3029-3038.
7. Karantzalis, A.E., A. Lekatou, and H. Mavros, *Microstructural Modifications of As-Cast High-Chromium White Iron by Heat Treatment*. *Journal of Materials Engineering and Performance*, 2009. **18**(2): p. 174-181.
8. Chang, C.M., et al., *Effect of carbon content on microstructure and corrosion behavior of hypereutectic Fe-Cr-C claddings*. *Materials Chemistry and Physics*, 2010. **123**(1): p. 241-246.

9. Arya, C. and P.R.W. Vassie, *Influence of cathode-to-anode area ratio and separation distance on galvanic corrosion currents of steel in concrete containing chlorides*. Cement and Concrete Research, 1995. **25**(5): p. 989-998.

10. Lin, C.M., et al., *Hardness, toughness and cracking systems of primary (Cr,Fe)₂₃C₆ and (Cr,Fe)₇C₃ carbides in high-carbon Cr-based alloys by indentation*. Materials Science and Engineering a-Structural Materials Properties Microstructure and Processing, 2010. **527**(18-19): p. 5038-5043.

6 ABNORMAL EROSION – SLURRY VELOCITY RELATIONSHIP OF CHROMIUM CAST IRON WITH HIGH CARBON CONCENTRATIONS

In chapter 3, through the erosion mapping of the expanded HCCI system it was noticed that in a relatively low velocity range (2.5 - 8.0 m/s) some HCCIs showed an abnormal erosion-slurry velocity dependency where an increase in the slurry velocity led to reduced erosion. This was consistently observed during slurry erosion tests for a number of hypereutectic HCCIs.

The objective of this investigation was to understand this abnormal trend in order to select appropriate HCCIs for specific applications against erosion-corrosion. This is also extremely applicable to HCCI hardfacing products that typically feature large carbon concentration in this range.

This chapter consists of five sections: (1) experimental methods used for the investigation; (2) microstructural characterization of the samples used; (3) typical HCCI slurry erosion velocity dependency; and (4) effect of the corrosivity of slurry (changing pH) on the localized corrosion attack and resultant erosion – corrosion behavior.

6.1 Experimental procedure

6.1.1 Sample preparation

The chemical compositions of cast irons used in this work are given in table 6.1. Coupons for testing were cut from plate castings of 12.5 mm thick, which had been previously solution-treated at 1160°C and immediately cooled using a compress air flow, followed by age hardening at 950°C and subsequent cooling using the air flow. The samples' dimensions for slurry erosion and electrochemical testing were 50 x 10 x 5 mm and 10 x 10 x 10 mm, respectively.

Table 6.1: Chemical composition of cast irons under study.

Alloy	Chemical Composition (wt.%)				
	Cr	C	Si	Mn	Fe
10-1	10.2	1.2	0.6	1.8	
10-3	10.4	2.9	0.8	2.0	
10-5	9.5	4.7	0.5	2.1	
15-1	14.8	1.2	0.7	1.7	
15-3	14.8	3.0	0.8	1.9	Balance
15-6	14.8	5.6	0.7	2.0	
25-1	25.7	1.2	0.4	1.5	
25-3	24.6	2.8	0.4	1.7	
25-6	24.2	5.7	0.6	1.8	

6.1.2 Slurry erosion testing

Samples were prepared following conventional metallographic preparation procedures using silicon carbide papers from 60 to 600 Grit successively. Before testing, samples were cleaned thoroughly in ethanol, dry with compressed air, and initial weights were measured. The slurry consisted of tap water and silica abrasive (near-rounded, 6.5-7 Moh hardness) with a particle size distribution as shown in figure 6.1. About 45% of particles were approximately 600 μm in diameter. The slurry temperature was set up at 60°C to simulate working conditions of slurry pumps used in oil sands operations. Likewise, the slurry velocity was selected in the range of 2.5 to 8 m/s. All tests were completed with a distance of 25 Km for the sample to travel in the slurry with a 45° impingement angle.

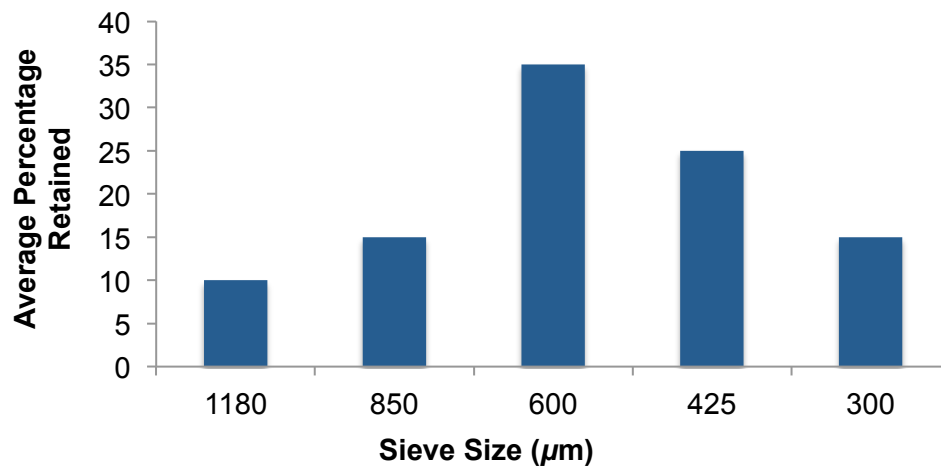


Figure 6.1: Particle size distribution of the silica sand used for the slurry erosion testing.

After each test, samples were cleaned with ethanol, dry with compressed air, and weight losses were then measured. Erosion tests were also performed in slurries at pH12 (adjusted by NaOH) and at a lower level of dissolved oxygen (DO) to determine how the performance of the samples change with the slurry corrosivity. The lower DO level was achieved by continuously blowing nitrogen (industrial grade) into the slurry at a constant pressure of 200 KPa. The measured DO level was lower than 0.06 ppm, compared to the DO level of 3.8 ± 0.2 ppm at normal aeration. Each experiment was repeated two time. Previous studies conducted on HCCIs using this slurry erosion test apparatus and similar parameters have shown a standard deviation of approximately 5%. The slurry pot tester configuration, as shown in figure 6.2, consists of a 2HP AC motor, six fluid baffles to disrupt the flow and maintain the erosive stream, and a shaft plate where four sample holders are attached in certain predetermined positions depending on the desired impingement angle. All components in the slurry pot that are in contact with the slurry are made of stainless steel. To maintain the desired temperature, a band heater is used which is controlled by a thermocouple system with a temperature controller. The system was cleaned thoroughly after each test and new slurry mixture was added.

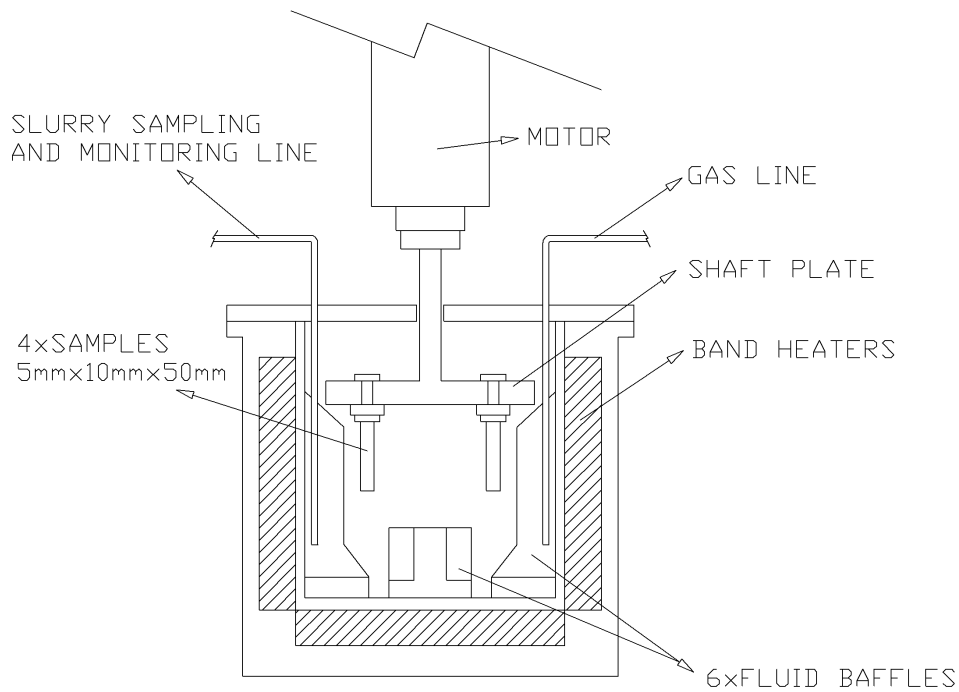


Figure 6.2: Schematic diagram of the slurry pot apparatus.

6.1.3 Electrochemical testing

In order to evaluate the corrosion behavior of the alloys, tafel, linear polarization, and cyclic polarization measurements were carried out using a commercial electrochemical system (PC4-750, Gamry Instruments, Inc., PA, USA). The tafel plots were recorded by scanning the potential at 1 mV/s in the range of ± 0.20 V vs. Open Corrosion Potential (OCP). The linear polarization resistance was measured at a scanning rate of 0.125 mV/s within the range of ± 25 mV vs. OCP. All specimens were mounted in epoxy resin with an exposed surface area of 1.0 cm^2 . Prior to each electrochemical measurement, the target surface was

ground with silicon carbide papers from 60 to 600 Grit successively and then rinsed with deionized (DI) water and ethanol, followed by stabilization in the corrosive solution for 60 min during which the corrosion potential was recorded. A saturated calomel electrode (SCE) was used as the reference electrode and a platinum plate with an area of 2 cm² was used as the counter electrode. Two solutions were used for this study. The first one was the tap water maintained at 60°C. The second solution was the tap water at pH12, adjusted by NaOH, and maintained at 60°C as well. Calculations based on electrochemical measurements were carried out following ASTM G-102 standard. Each experiment was repeated twice.

6.1.4 Characterization and mechanical properties

Specimens were ground using silica carbides papers from 60 up to 1200 Grit, then polished with nylon cloth with a diamond slurry of 5 um, followed by fine polishing with 1um-diamond suspension on a finer polishing cloth. Samples for optical microscopy were etched using a solution of 50 ml FeCl₃, 20 ml of HCl, and 20 ml of ethanol. This solution attacks preferentially the matrix leaving the carbides relatively unaffected, which provides good contrast between carbides and matrix [1]. Optical microscopy was undertaken using an Olympus PME3-ADL and images were analyzed with the aid of the software “ImagePro”. The stereographic measurements were performed on three representative micrographs for each sample. XRD patterns were obtained using a Rikagu X-ray

diffractometer with Cu K α radiation. Scanning electron microscopy (SEM) and energy dispersive X-ray spectrometry (EDX) analysis were carried out using a Zeiss EVO SEM with LaB6 crystal equipped with an ultrathin window X-ray detector. A Hitachi S-2700 SEM was also used for worn surface examination. Micro-hardness was determined on lightly etched samples using a micro-indenter (Fisher Technology Ltd., Winsor, CT, USA) under a load of 600 mN. Each reported micro-hardness value is an average of fifteen measurements.

6.2 Results and discussion

6.2.1 Microstructure

Representative back-scattered electron (BSE) images of the microstructure of the samples under study are presented in figure 6.3. As it was found in our previous work [2], the eutectic point of the cast irons is close to 3.4wt.% C, however, increasing the chromium levels shifts the eutectic point to lower carbon content. Figure 6.3A, D and G illustrate the hypoeutectic alloys 10-1, 15-1 and 25-1 respectively. According to the liquidus projection as shown in figure 6.4, alloys 10-1 and 15-1 contained austenite (γ Fe) as primary phase, which nucleated and grew throughout the liquid until the eutectic solidification of γ -Fe, $M_{23}C_6$, and M_7C_3 consumed the remaining liquid. On the other hand, alloy 25-1 followed a different solidification path where δ -Fe(α -Cr) nucleated as a primary phase followed by the formation of eutectic $M_{23}C_6$ carbides and δ -Fe(α -Cr).

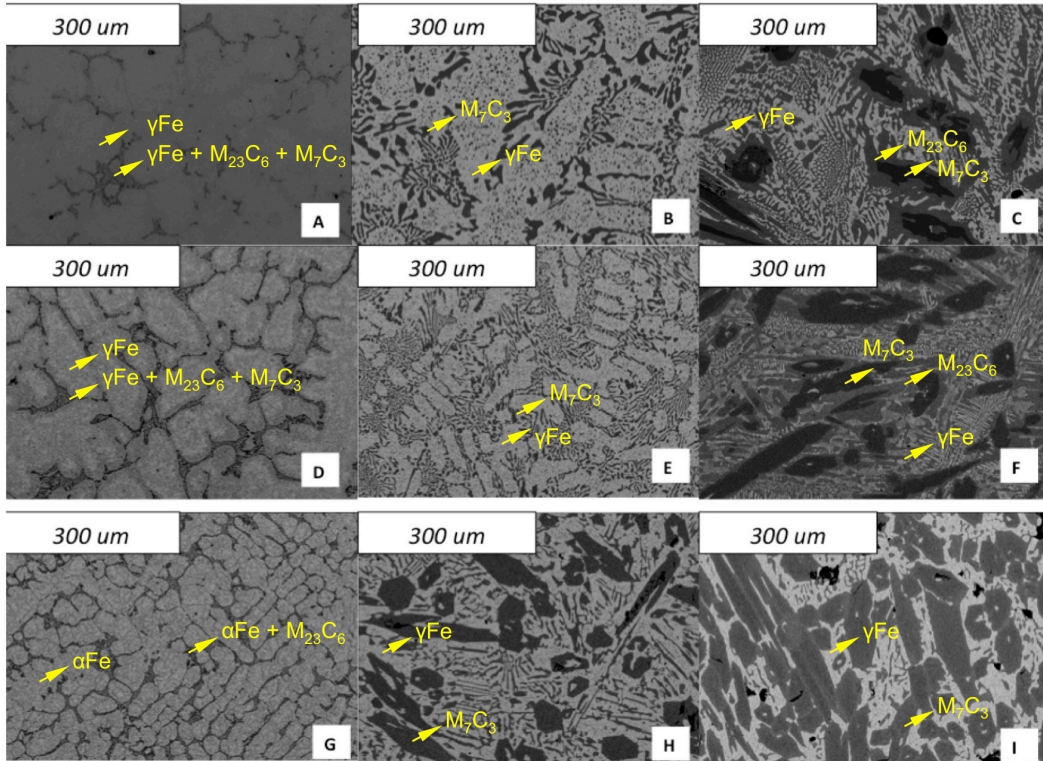


Figure 6.3: Back-scattered electron (BSE) micrographs of alloys being studied: A. 10-1; B. 10-3; C. 10-5; D. 15-1; E. 15-3; F. 15-6; G. 25-1; H. 25-3; I. 25-6.

When carbon content is raised to 3wt.%C the solidification path becomes relatively close to the eutectic composition. If the chromium content also increases, the composition of the invariant point shifts to a lower concentration of carbon and thus produces a more hypereutectic microstructure. In fact, among the three chromium contents, only 25-3 (figure 6.3H) actually formed carbides as primary phase. In this case, solidification began with nucleation and growth of M_7C_3 followed by the precipitation of the eutectic mixture of M_7C_3 and γ -Fe.

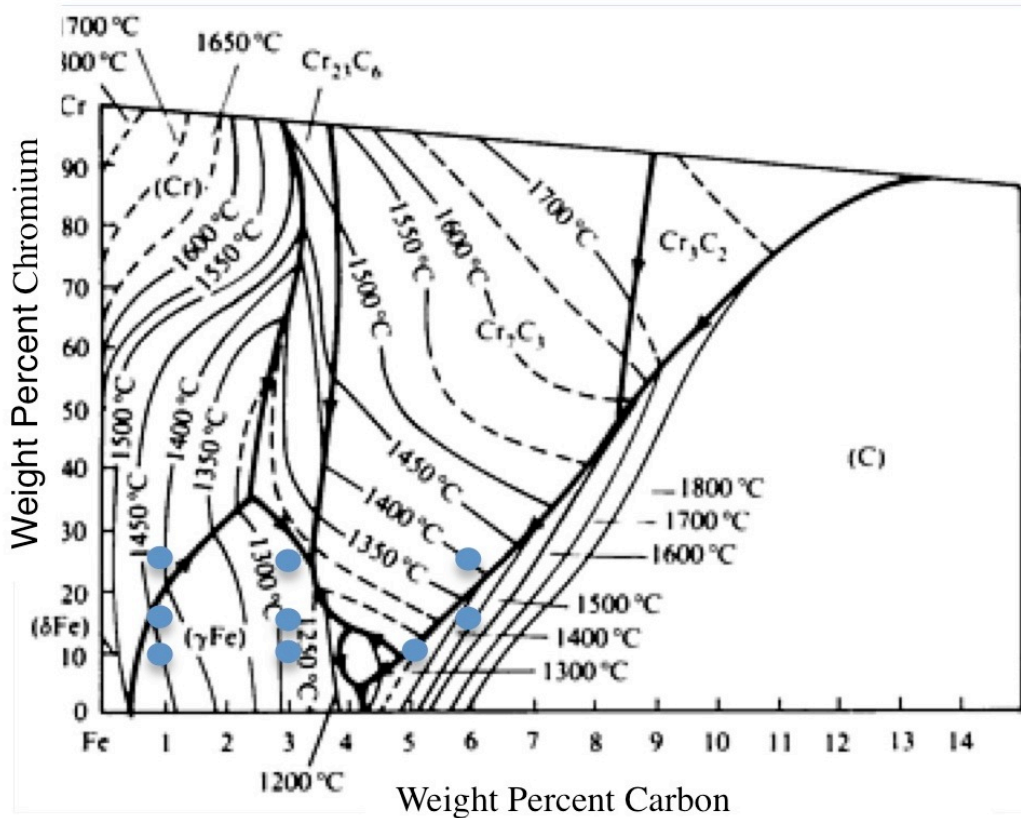


Figure 6.4: Liquidus projection of the Fe-Cr-C system in the Fe-rich corner [3].

The third group of specimens (figure 6.3C, F and I) features high carbon compositions. Their solidification began with the nucleation of primary M_7C_3 carbides. For the alloy 25-6 the formation of primary carbides was followed by the eutectic reaction at which eutectic M_7C_3 and γ -Fe were simultaneously formed. For alloys 15-6 and 10-5 the primary solidification preceded the quasi-peritectic reaction where remaining liquid react with primary M_7C_3 to solidify as $M_{23}C_6$, which can be seen as a lighter outer phase surrounding the large M_7C_3 primary carbides (figure 6.3C and F) [4, 5, 6, 7].

In order to confirm the ferrous phase and the carbide type, alloys were analyzed using X-ray diffraction technique. Representative X-ray diffraction patterns of the nine alloys being studied are presented in figure 6.5, which confirm the phases described in the previous paragraphs and also show the presence of minor carbides such as M_6C and in some cases $M_{23}C_6$ that could have precipitated in the matrix during heat treatment. Besides, small peaks of ferrite/martensite were found in alloys with austenitic solidification, which corresponded to formation of martensite in areas depleted in carbon where the driving force required to form martensite was reduced, for instance, in the proximity of the matrix/carbide interface.

Compositions of the alloys were analyzed using EDX and results of the analysis are given in table 6.2. As shown, with an increase in the nominal %Cr, the matrix's Cr content, the volume fraction of carbides, and the Cr/Fe ratio in the carbides all increased. Increasing the nominal %C considerably raised the volume fraction of carbides. Based on the results, it was expected that increasing the nominal %Cr could enhance the resistance of the material to corrosion and increasing the nominal %C was more effective in enhancing the resistance of the material to wear.

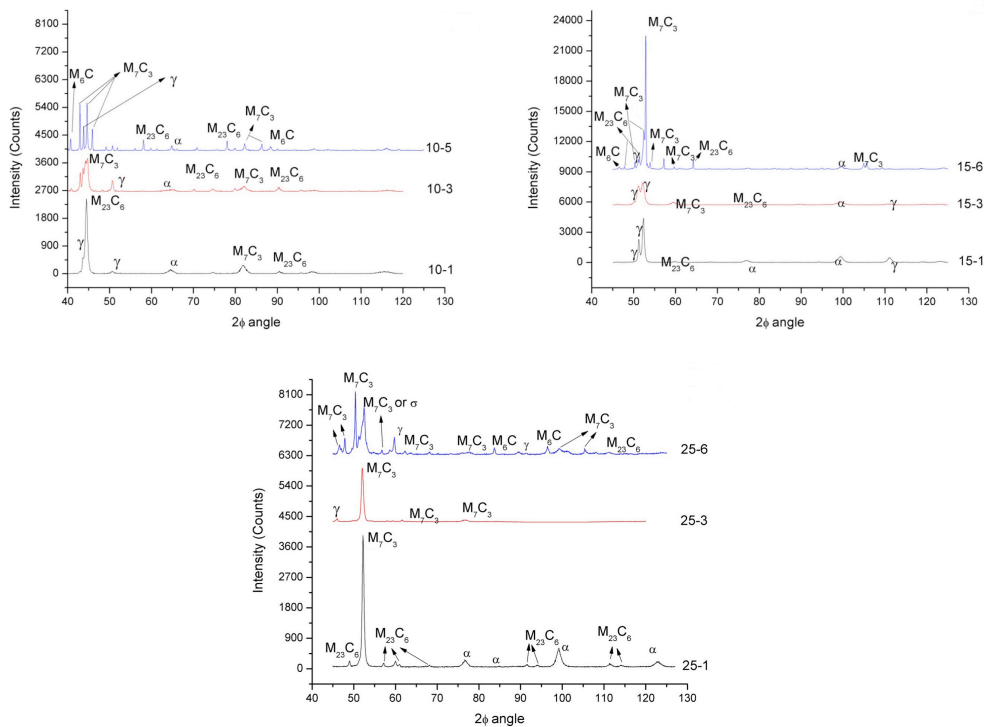


Figure 6.5: X-ray diffraction patterns of the alloy series being studied.

Table 6.2: Microhardness and volume fractions of microstructural components.

	Matrix Hardness (HV_{600mN})	Primary Carbides Hardness (HV_{600mN})	Matrix Chromium Level (wt.%)	Carbides Chromium Level (wt.%)	Matrix Volume Fraction (%)	Carbides Volume Fraction (%)
10-1	170.3		8.62	37.8	96.3	3.7
10-3			4.25	32.3	75.7	24.3
10-5		579.3	2.59	20.5	59	41
15-1	382.4		11.54	49.8	92.74	7.3
15-3		672.7	8.46	40.15	74.80	25.2
15-6		873.1	3.615	31.26	37	63
25-1	417.6		17.30	60.6	85.09	14.91
25-3		834.8	11.55	62.4	70.90	29.1
25-6		948.9	5.7	41.5	43	57

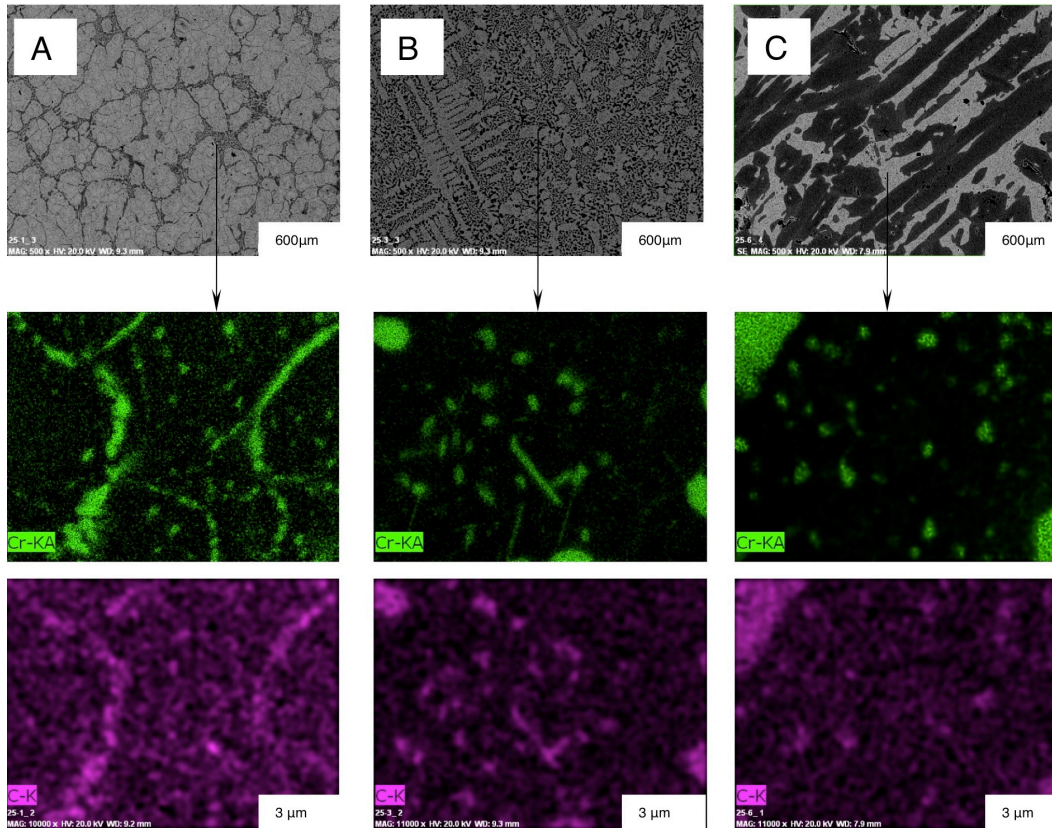


Figure 6.6: EDX compositional mapping of the ferrous matrix of the three HCCIs with 25wt.%Cr. The colour intensities reflect the levels of chromium (green) and carbon (pink).

Local EDX mapping was also carried out. As shown in figure 6.6, the Cr content in the matrix was much lower and unevenly dispersed in the hypereutectic sample, implying that the hypereutectic alloy has a lower resistance to corrosion, which would affect its resistance to erosion-corrosion with an abnormal behaviour as demonstrated in the following sections.

6.2.2 Slurry erosion

It is generally expected that a higher slurry velocity may cause more severe damage to a target surface as the erosive particles carry a larger amount of energy to impact and mechanically interact with the surface. In this study, the erosion behaviour of the HCCI alloys was evaluated and results are presented in figure 6.7. As expected, the erosion loss of the hypoeutectic alloys follows a power law velocity exponent relation between the weight loss and the slurry velocity (see figure 6.7). Even though the ferrous matrix changes from austenite (10-1 and 15-1) to ferrite (25-1) lower weight losses were measured for both 15-1 and 25-1, which showed very similar performance. As depicted by table 6.2, the chromium content in the austenitic matrix of 15-1 was increased near the solubility limit (about 11wt.%Cr), which solution-strengthened the ferrous matrix, improving their hardness and consequently the wear performance. When further raised by increasing the nominal Cr composition to 25wt.%, the matrix became ferrite, featuring a higher hardness and maintaining a similar performance than 15wt.%Cr. It is known that chromium in the ferritic matrix could be detrimental to its mechanical properties and likely to deteriorate the erosion performance if carbon is not increased [8]. Considering the micro-hardness and volume fractions of the ferrous matrix and carbides in each specimen, one may see that the major hardness change in the hypoeutectic alloys coincides with the greater improvement in erosion resistance when increasing the chromium content from 10 to 15wt.%Cr.

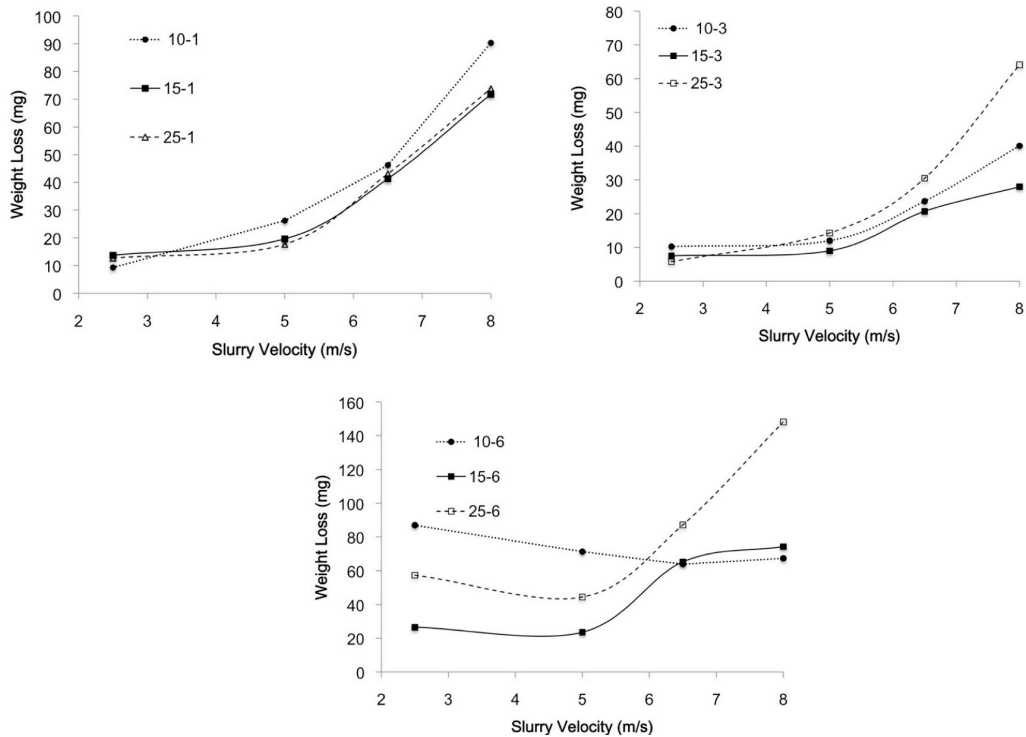


Figure 6.7: Slurry erosion behaviour at four different slurry velocities for the alloys under study.

With the increase in Cr from 10wt.% to 15wt.%, the carbides volume fraction also increased from 3.7 to 7.3%, which contributed to the increase in the erosion resistance. However, the next increment from 7.3 to 14.9%, when the chromium was raised from 15 to 25wt.%Cr, did not have significant effect on their erosion resistance.

The near-eutectic alloys (3wt.%C) presented an erosion-velocity dependency similar to the hypoeutectic alloys where the weight loss increases exponentially with the slurry velocity. These microstructures in general offer a better performance than the hypoeutectic ones, as their weight loss is generally lower than the first group. The best performance of the three near eutectic structures is found in alloy 15-3, followed by 10-3 and 25-3. From table 6.2 one can see that 25-3 has the highest hardness in carbides, which arises from their Cr/Fe ratio. On the other hand, the matrix of the 25-3 contains similar amount of chromium levels than the matrix of the alloy 15-1 which offered the best performance among the hypoeutectic samples. Taking these parameters into account, 25-3 should offer the best performance in such conditions, which is not the case.

Hardness of the microstructural components and their volume fractions is of great importance when designing microstructures to possess a high wear resistance. There are still other parameters influencing the performance of the alloys. For instance, the alloy 15-3 performed the best, which is in a near-eutectic state with finer eutectic distribution of carbides and fewer primary dendrites of the ferrous matrix. A finer microstructure may help to resist fracture more effectively through zigzagging and splitting cracks with increased energy consumption.

6.2.3 Abnormal behaviour of hypereutectic alloys during slurry erosion

The third group of samples, the hypereutectic alloys with high carbon concentrations (10-5, 15-6, 25-6) containing large volume fractions of carbides usually show outstanding performance in dry abrasion testing. Under the slurry erosion condition, their performance was poor, compared to those of the hypoeutectic and near-eutectic alloys. Clearly, the performance of these alloys is strongly affected by their corrosion resistance during the erosion-corrosion process. In this work, as mentioned early, the focus is put on the dependency of the erosion loss on the slurry velocity. As shown, the erosion loss decreased initially with the slurry velocity, after reaching a minimal, and then increased. This abnormal erosion behavior was unexpected and should be clarified.

Logically, during high-velocity slurry erosion, the mechanical behavior or wear resistance may play a predominant role in resisting the erosion-corrosion attack. However, at low velocities, the corrosion attack could be enhanced due to the fact that the target surface has longer time of exposure to a corrosive medium. Our previous studies on erosion-corrosion of stainless steel alloyed with 1 ~ 2%Y that improved the passive film shows that the improvement in the passive film only benefits the resistance of the steel to low-velocity erosion-corrosion [9]. This is an indication that corrosion behavior is of importance to the resistance of materials, particularly for those having low corrosion resistance, to damage during the low-velocity erosion-corrosion processes. In order to confirm this hypothesis,

the hypereutectic alloys were retested in slurries at two pHs levels, pH7 and pH12. The later was achieved by adding NaOH, a corrosion inhibitor. Besides, a slurry containing very low dissolved oxygen (DO) was also used. The low DO level was achieved by blowing nitrogen into the slurry during the erosion test, which reduced the DO level to a value lower than 0.06 ppm, compared to normal DO level (in open air) which was at about 3.8 ppm. Results of erosion tests performed in these slurries are illustrated in figure 6.8. As shown, when tested in the slurry at pH7, the weight loss of the hypereutectic alloys was higher when eroded at the low slurry velocity of 2.5 m/s and is reduced as the velocity is increased to 5 m/s. However, this trend was reversed when the alloys were tested in the slurries at pH12 and lower DO.

It is now clear that at low slurry velocities, the corrosion attack played an important role in causing the damage to the material but at higher slurry velocities the erosion or mechanical damage is dominant. Such a phenomenon is mainly applicable to materials having a low corrosion resistance. For white cast irons, this abnormal trend would not occur if the matrix contained Cr in high concentrations but also with a homogeneous distribution in the ferrous matrix where localized corrosion is suppressed. This is the reason why the hypoeutectic and the near-eutectic alloys, whose matrix contained more and even distribution of Cr, did not show the abnormal erosion behaviour.

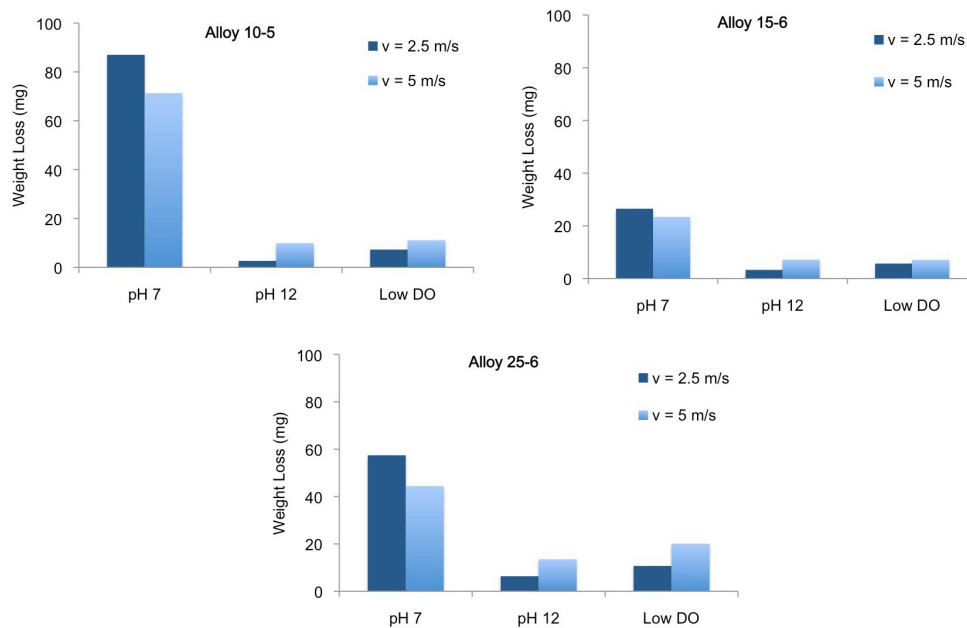


Figure 6.8: Comparison of slurry erosion performance of the three high carbon hypereutectic HCCIs at 2.5 m/s and 5 m/s in three different slurries: pH7, pH12 (adjusted with NaOH), and low dissolved oxygen (DO).

A high Cr concentration helps to generate a passive film to protect the material from further corrosion attack. Cyclic polarization tests were carried out for the 25 wt.%Cr series at pH7 and pH12, respectively. Obtained polarization curves are illustrated in figure 6.9. There it can be seen that the hypoeutectic and near-eutectic alloys 25-1 and 25-3 show an increase in the corrosion potential during the reversed scan at pH7, and also present a positive hysteresis where the reverse scan lays at lower current density, implying the development of a passive

film (Cr_2O_3). In contrast, the hypereutectic alloy 25-6 showed only very slight change in the corrosion potential and featured a large negative hysteresis, where current density on the reverse scan is higher than the first scan, indicating the formation of some sort of localized damage that deteriorate the material stability in such condition and thus lower passivation capability or corrosion resistance of the hypereutectic alloy. The situation was different when the tests were performed in the solution at pH12, which clearly reduced the negative hysteresis after the reverse scan. Interestingly, the corrosion potential obtained by the first scan becomes more negative as the carbon concentration increases indicating that the material was not stable in such conditions, and a uniform rather than localized corrosion damaged still occurred. In other words, localized corrosive attack can enhance the erosion damage in a much more significant way compared to uniform corrosion.

The abnormal relationship has been attributed to the localized electrochemical attack of the ferrous matrix. However, the synergy is found to be severe at the lowest speed, 2.5 m/s, and is attenuated as velocity increases. Two factors have been considered as possible explanations. The first one is that as the slurry velocity increases the electrochemical contribution to the damage becomes less relevant. The second one is that the localized attack is attenuated by higher velocities. In order to qualitatively confirm the latter, cyclic polarization of alloy 25-6 in neutral slurry, at 60°C, with two different slurry velocities were performed

(figure 6.10). “Higher dynamics” corresponds to a larger flow velocity. It is clear that the area of negative hysteresis (indication of localized corrosion) is reduced as the slurry flow increases. This confirms that the local electrochemical attack is suppressed by increasing the slurry velocity, which explains why at the lowest speed 2.5 m/s the erosion damage was more severe than that at 5 m/s for the hypereutectic alloys.

The poor corrosion resistance of the hypereutectic alloy was demonstrated not only by the polarization test but also by the appearance of the worn surface (figure 6.11). For instance, extensive pits were observed on the surface of alloy 25-6, eroded at 2.5 m/s in the neutral slurry (pH7), which were caused by synergistic attack of multiple impacts of silica sand and local corrosion. In contrast, at pH12, little evidence of pitting of the ferrous matrix was found, but surprisingly carbides seemed to be more affected.

We measured the surface roughness of eroded surfaces of alloys 15-1 and 15-6 with erosion time. As shown in figure 6.12, the surface roughness of alloy 15-6 increased with the erosion time, while that of alloy 15-1, which had a higher corrosion resistance, did not show such variations. This confirms our hypothesis: Corrosion played a main role in generating the pits during erosion-corrosion of hypereutectic alloys at low slurry velocities.

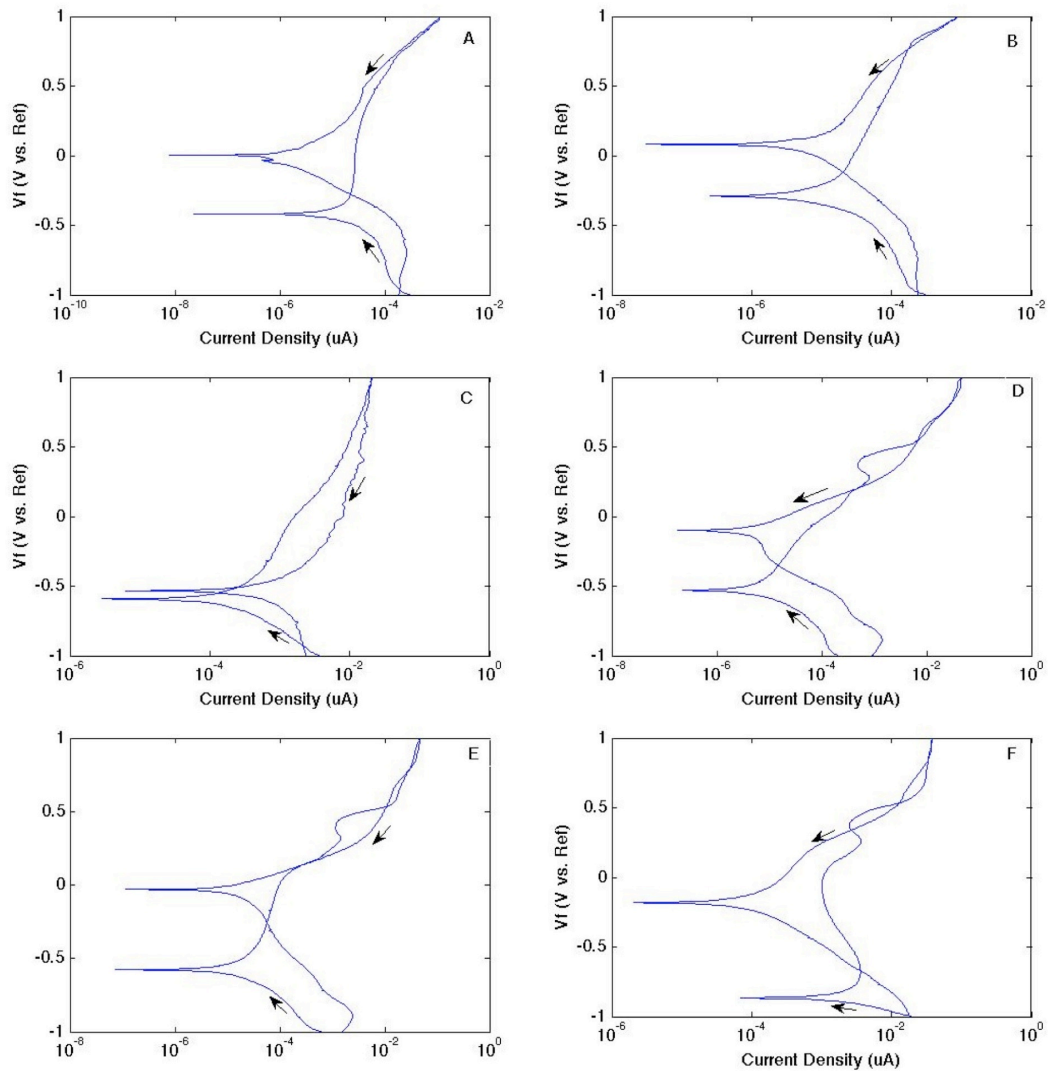


Figure 6.9: Cyclic polarization results obtained for the 25wt.%Cr compositional series. (A) 25-1, pH7; (B) 25-3, pH7, (C) 25-6, pH7; (D) 25-1, pH12; (E) 25-3, pH12; (F) 25-6, pH12.

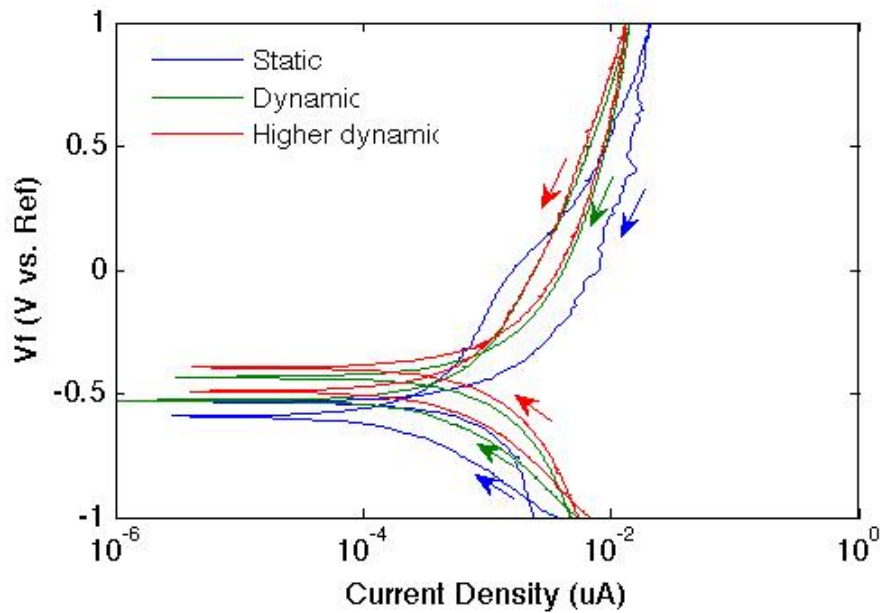


Figure 6.10: Effect of stirring on the cyclic polarization behavior of alloy 25-6.

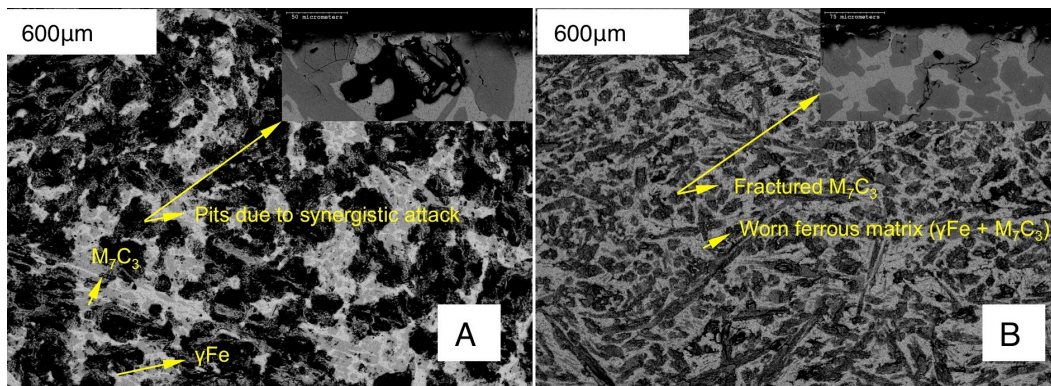


Figure 6.11: Worn surface of alloy 25-6 after 2.5 m/s - slurry erosion testing at two different pH levels: (A) pH7; (B) pH12.

In order to obtain general information on the compositional range within which the abnormal erosion behavior exists at the low slurry velocity, we performed erosion tests in slurries at pH7 for HCCIs with compositions in the

range of 5~45 wt%Cr and 1~6 wt%C, based on which a map was developed, as shown in figure 6.13. Alloys with their composition within the zone where severe local corrosion exists exhibit the abnormal erosion behaviour.

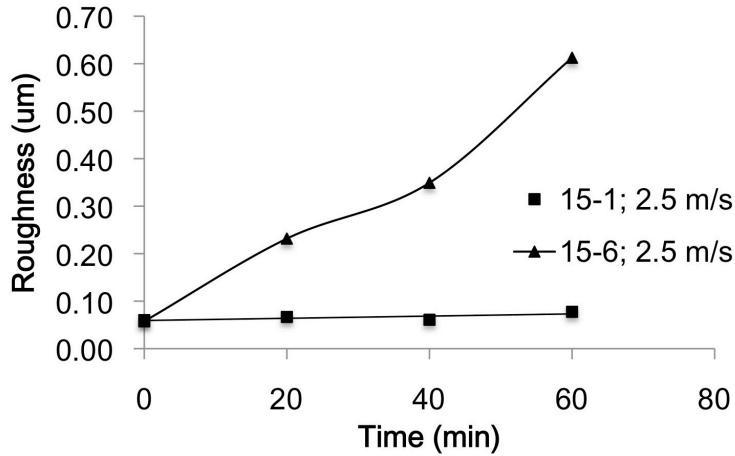


Figure 6.12: Surface roughness of 15-1 and 15-6 as a function of the erosion time.

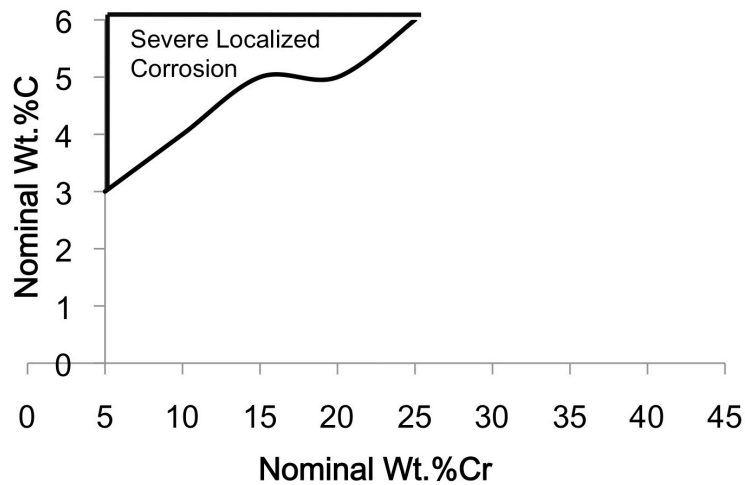


Figure 6.13: The compositional zone of HCCIs shown corresponds to high sensitivity to localized electrochemical attack at fluid velocities below 5 m/s in neutral slurries.

6.3 Conclusions

HCCIs generally exhibit a power-law velocity dependence where weight loss increases with the slurry velocity. However, the abnormal erosion-slurry velocity behavior was observed during erosion-corrosion tests on hypereutectic HCCIs with high carbon concentrations. In this case, the erosion loss was higher at low slurry velocities. As the slurry velocity was raised, the erosion loss first decreased and then increased. The mechanism responsible for this abnormal change in erosion loss with the slurry velocity was investigated by studying the erosion behavior of HCCIs under different erosion-corrosion conditions. It turned out such abnormal erosion-corrosion behavior was due to localized corrosive attack when the target surface had longer time of exposure to the corrosive medium. An approximate map that shows a compositional zone within which the HCCIs exhibit the abnormal erosion-corrosion behaviour was built.

6.4 Bibliography

1. Radzikowska, J.M., *Effect of specimen preparation on evaluation of cast iron microstructures*. Materials Characterization, 2005. **54**(4-5): p. 287-304.
2. Chung, R.J., et al., *Effects of titanium addition on microstructure and wear resistance of hypereutectic high chromium cast iron Fe-25wt.%Cr-4wt.%C*. Wear, 2009. **267**(1-4): p. 356-361.
3. *C-Cr-Fe Ternary Phase Diagrams*. ASM Handbook Online.

4. Adler, T.A. and O.N. Dogan, *Erosive wear and impact damage of high-chromium white cast irons*. *Wear*, 1999. **225**: p. 174-180.
5. Dogan, O.N., J.A. Hawk, and G. Laird, *Solidification structure and abrasion resistance of high chromium white irons*. *Metallurgical and Materials Transactions a-Physical Metallurgy and Materials Science*, 1997. **28**(6): p. 1315-1328.
6. Dogan, O.N. and J.A. Hawk, *Effect of carbide orientation on abrasion of high cr white cast-iron*. *Wear*, 1995. **189**(1-2): p. 136-142.
7. Dogan, O.N., G. Laird, and J.A. Hawk, *Abrasion resistance of the columnar zone in high Cr white cast irons*. *Wear*, 1995. **181**: p. 342-349.
8. Pickering F. B., *High-Strength Low-Alloy Steels - A Decade of Progress*. International Symposium on High-strength, Low-alloy steels, Washington, D.C, 1977. p. 9-30.
9. Zhang T. C., D. Y. Li, *Improvement in the corrosion-erosion resistance of 304 stainless steel with alloyed yttrium*. *Journal of Materials Science*, 2001. **36**: p. 3479-3486.

7 EFFECTS OF TITANIUM ADDITION ON MICROSTRUCTURE AND WEAR RESISTANCE OF HYPEREUTECTIC HIGH CHROMIUM CAST IRON FE-25WT.%CR-4WT.%C

Refinement of primary carbides in hypereutectic HCCI alloys has attracted attention as a possible alternative to produce a step change in wear performance of these already excellent alloys. As it has been discussed in chapter 3, the increasing volume fraction of carbides through raising the overall carbon levels is beneficial to both abrasion resistance and slurry erosion resistance, but there is a threshold where it becomes detrimental due to the natural coarsening of the primary carbides as carbon is raised, in some cases even above 4 Wt.%C.

To maintain a large volume fraction of carbide without coarsening and formation of needle-like primary carbides, researchers have attempted to add small amounts of foreign elements such as titanium, vanadium, and niobium that could act as a substrate for heterogeneous nucleation of carbides [8-12]. This attempted to replicate the ferrous matrix refinement seen mostly in hypoeutectic HCCIs, with Ti as one of the preferred elements. However, considering the fact that titanium is a strong carbide former and likely forms titanium carbides, carbon depletion is expected to precede the normal solidification of the alloy. This would change the matrix's carbon content and thus result in variations in microstructure and consequent changes in properties of the material.

The objective of this work was to confirm this hypothesis through investigating influences of Ti addition (up to 6 wt.%) on the microstructure of a hypereutectic high chromium cast iron (Fe–25wt.%Cr-4wt.%C) and determining corresponding changes in mechanical and tribological properties of the Ti-added alloy.

This chapter consists of three sections: (1) modified alloy preparation and experimental methods used for the investigation; (2) Ti effect on the resultant modified microstructures; and (3) effect of Ti on hardness and wear behavior.

7.1 Experimental details

The HCCI used for this investigation was a hypereutectic alloy, Fe - 25 wt.% Cr - 4 wt.% C, made by Weirminerals Ltd. In addition to the hypereutectic alloy, a hypoeutectic HCCI of Fe - 25 wt.% Cr - 2 wt.% C was also produced for comparison. Pieces of the HCCI were remelted respectively with different amounts of added titanium (see table 7.1) in an arc furnace (MRF INC. SA338-V&G). The titanium was in the form of powder (-325 mesh, 99.99%Ti). The melting and solidification conditions are listed in table 7.2.

During the alloying process, a piece of the base alloy and titanium powder were placed on a water-cooled copper hearth in the arc furnace. In order to minimize the compositional and microstructure heterogeneities, each sample was

turned over and remelted six times. The cast ingot dimensions were 15 x 10 x 30 mm. The set of samples produced for this study are shown in table 7.1.

Table 7.1: Samples with titanium additions.

Ingot #	Base Alloy	wt.% Ti added
1		0
2	Fe – 25 wt.% Cr – 4 wt.% C (Hypereutectic HCCI)	1
3		2
4		6
5	Fe – 25 wt.% Cr – 2 wt.% C (Hypoeutectic HCCI)	0

Table 7.2: Melting and solidification conditions in the arc furnace.

Parameters	Melting Conditions
Vacuum pressure before filling with Ar gas	-90 to -95 kPa
Protection gas	Argon
Pressure during melting and cooling	10 kPa
Electrode type	2% Thoriated Tungsten
No. of turning over and remelting	6 times

Specimens for metallographic observation were prepared following the standard metallographic preparation using silica carbides discs from 80 up to 1200 grit and then polished with nylon cloth in a diamond slurry of 5 um. Samples for optical microscopy were etched using a solution of 50 ml FeCl₃, 20 ml of HCl, and 20 ml of ethanol. This solution attacks preferentially the matrix leaving the carbides relatively unaffected, which provides good contrast between carbides and

matrix [1]. Optical microscopy was undertaken using an Olympus PME3-ADL and images were processed with the help of the software “ImagePro”.

SEM, EDX, XRD, bulk hardness, micro mechanical testing, and pin-on-disc tests were carried out to characterize and evaluate the samples with different amounts of Ti. The XRD analysis was made using a Rikagu X-ray diffractometer with Cu K α radiation. The examinations of SEM and EDS were carried out with a Hitachi S-2700.

Bulk hardness was measured using a conventional Rockwell tester in C scale (150g load and a diamond cone indenter standard for this scale). Five measurements were taken for each sample. Micro-hardness was determined on lightly etched samples using a micro mechanical probe (Fisher Technology Ltd., Winsor, CT, USA) under a load of 100 g. Each reported micro-hardness value is an average of fifteen measurements.

The wear resistance of the samples was evaluated by sliding wear tests using a pin-on-disc tribometer (CSEM Instruments, Neuchatel, Switzerland). The pin was a silica nitride ball of 6 mm in diameter. The wear tests were performed at a sliding speed of 0.5 cm/s along a circular path of 1.6 mm in width under a normal load of 10 N for 10,000 cycles. Wear tracks were observed under an optical microscope and their dimensions were also measured using a contact

profilometer (Tencor Instruments, USA), from which the volume loss was determined.

7.2 Results and discussion

7.2.1 Microstructure and its variation with Ti addition

Microstructures of the hypereutectic HCCI with different amounts of titanium are presented in figure 7.1. The initial state of the as-cast material without titanium addition is shown in figure 7.1(a). This is a typical hypereutectic microstructure of HCCI, which consists of primary M_7C_3 carbides, eutectic M_7C_3 carbides and eutectic austenite. Solidification of hypereutectic HCCI's begins with the nucleation of primary M_7C_3 carbides that start to form at approximately 1300°C [2-6]. The formation of primary carbides is followed by the eutectic reaction at which eutectic M_7C_3 carbides and eutectic austenite are simultaneously formed. XRD diffraction patterns (figure 7.2(a)) and EDS spectrum (figure 7.3(a)) of the sample without titanium addition confirm the presence of M_7C_3 carbides and austenite in the HCCI of Fe – 25 wt.% Cr - 4 wt.% C.

The presence of austenite as a metastable phase in HCCI's is attributed to the high amount of alloying elements such as carbon, which stabilizes the austenite at lower temperatures [7]. The existence of austenite at lower temperatures improves the hardenability of the ferrous matrix [6, 8]. EDS patterns

presented in figure 7.3 show that the primary carbides are rich in chromium. Such coarse primary M_7C_3 carbides found in the sample without titanium made up about 12 vol.% of the alloy, in which the volume fraction of total carbides was 60 vol.%.

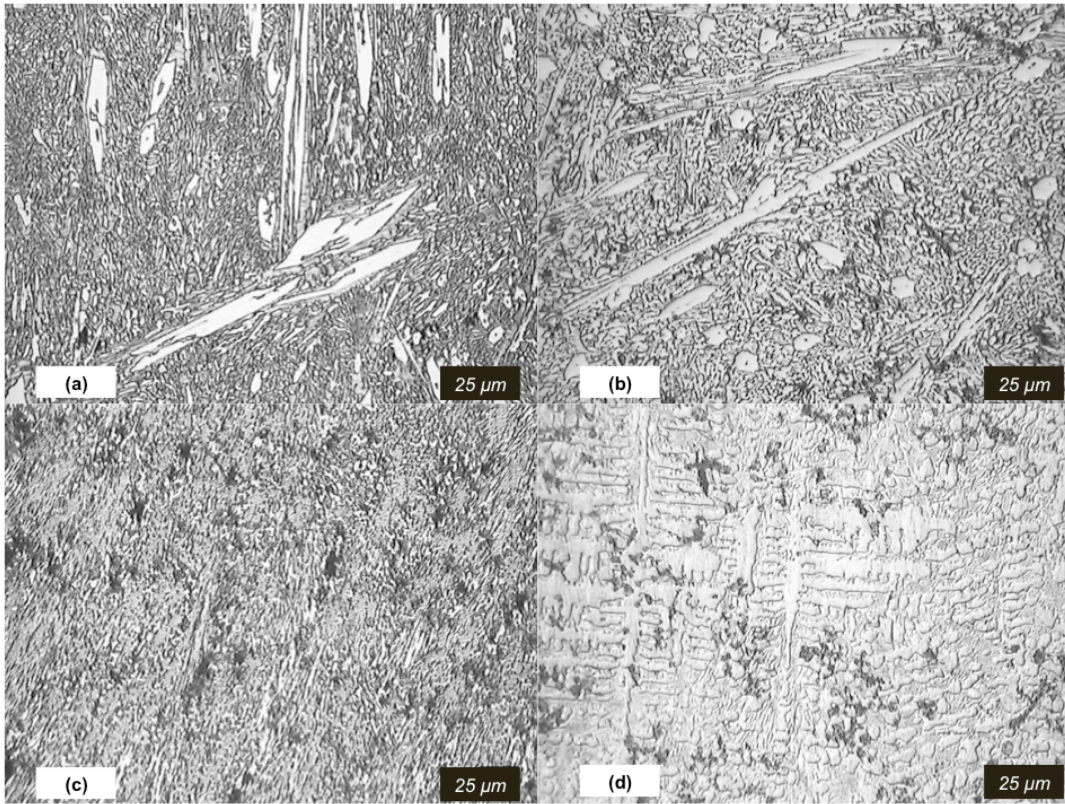
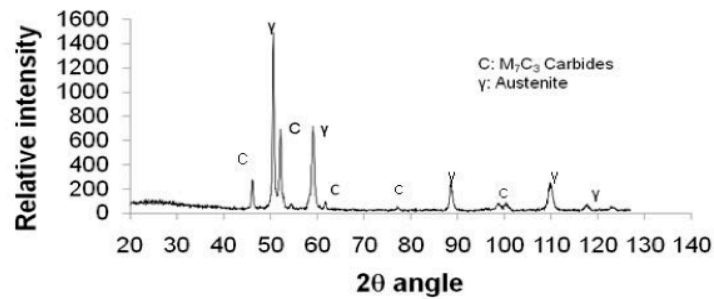


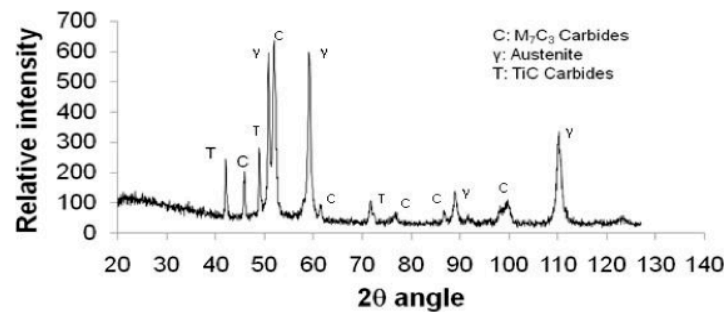
Figure 7.1: Representative optical micrographs of ingots with different amounts of titanium addition: (a) 0 wt.% Ti; (b) 1 wt.% Ti; (c) 2 wt.% Ti; (d) 6 wt.% Ti.

In general, the coarse primary carbides negatively affect HCCI's toughness. It is therefore of importance to refine the microstructure of HCCIs in order to enhance their mechanical properties [2,8-14]. In the present case, adding

Ti changed the size of M_7C_3 carbides and formed TiC domains, confirmed by XRD, EDS and SEM examinations. As the amount of Ti was increased, the TiC domains became larger and extended to a discrete dendritic network such as those in the sample with 6 wt.% Ti (see the SEM image in figure 7.3(c)).



(a)



(b)

Figure 7.2: XRD diffraction patterns of the HCCI with: (a) no titanium addition, and (b) 6 wt.% Ti.

The microstructural changes of the hypereutectic HCCI with three different amounts of titanium addition are illustrated in figure 7.1(b)-(d). As shown, the Ti addition appeared to result in the primary carbide refinement, particularly when 2 wt.% Ti was added. However, when carefully checking the

microstructures, one may notice that as the amount of Ti increased, the microstructure changed from a hypereutectic structure to a hypoeutectic one (see figure 7.1(d)). Therefore, the possible inoculation effect of Ti addition as previously reported [11] is questionable.

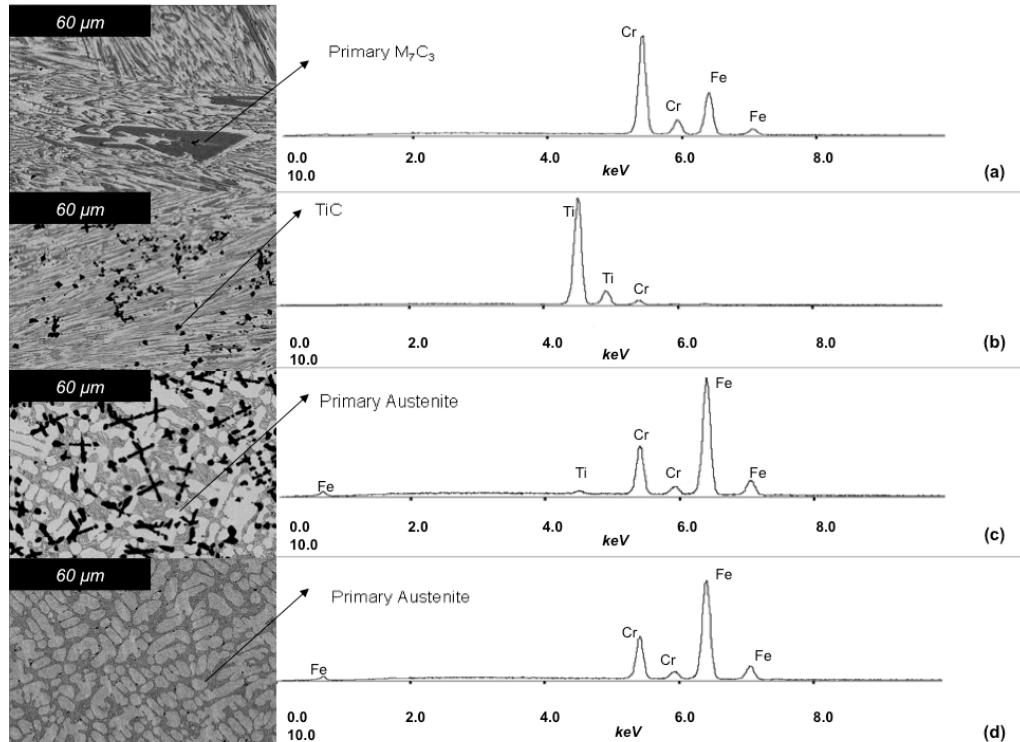


Figure 7.3: Representative backscatter images and EDS patterns of primary phases and TiC in some of the samples under study: (a) 0 wt.% Ti; (b) 2 wt.% Ti; (c) 6 wt.% Ti; (d) Hypoeutectic HCCI of Fe – 25 wt.% Cr – 2 wt.% C.

As a matter of fact, titanium is a carbide former element, which can react with carbon to form TiC at higher temperatures (3000°C) than any other element in HCCI. As a result, the carbon concentration in the matrix becomes depleted,

thus resulting in a shift from the hypereutectic composition to one with a lower carbon content such as the hypoeutectic composition. Or in other words, %C of the matrix would shift to the left hand side of the experimental phase diagram shown in figure 7.4.

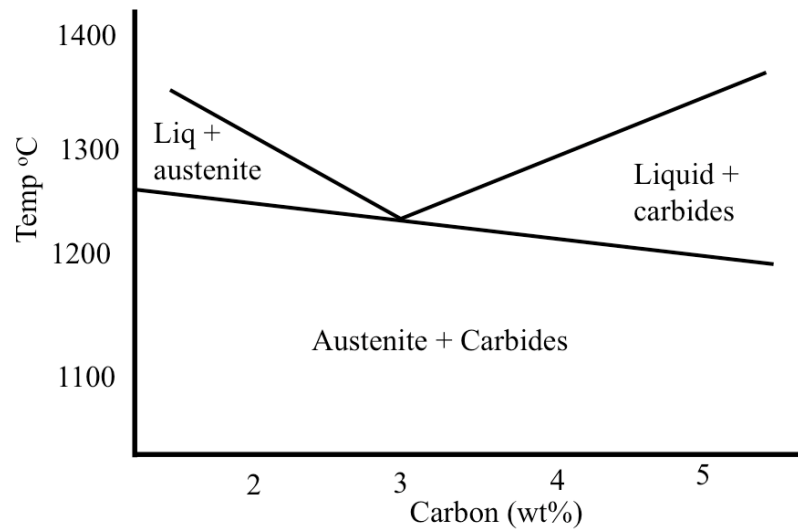


Figure 7.4: An experimental phase diagram obtained through the collection of the thermal history of solidification of a variety of HCCI's [15].

In figure 7.1(b), one may see that 1 wt.% titanium did not cause significant refinement of primary carbides. However, the volume fraction of primary carbides was reduced from 12% to about 9% approximately (figure 7.5). The total carbides's volume fraction was also decreased from 60% to 45%. The reduction in the volume fraction of primary carbides should be attributed to the depletion of carbon caused by the formation of TiC particles. The TiC phase was detected in

samples with added Ti by EDS as shown in figure 7.3 as well as by XRD, shown in figure 7.2(b). TiC domains were observed in different areas, which showed a dendritic structure (see figure 7.3(c)) with platelet/catenulate growth characteristics having an average size of about 10 μ m [16-19].

As shown in figure 7.1(c), 2 wt.% titanium significantly modified the microstructure of the hypereutectic alloy Fe – 25 wt.% Cr – 4 wt.% C, producing a fine eutectic structure without primary carbides. The microstructural changes are attributed to the formation of TiC particles, which consumed carbon and thus brought the alloy from a hypereutectic state to the eutectic one, whose carbon concentration is approximately 3.5 wt.% C [3,7,15].

As the amount of titanium addition was further increased, the microstructure of the alloy completely changed to a hypoeutectic one as figure 7.1(d) and figure 7.3(c) illustrate. For comparison, a sample of Fe – 25 wt.% Cr – 2 wt.% C (hypoeutectic) was made, whose microstructure is shown in figure 7.3(d). This microstructure is similar to the sample of Fe – 25 wt.% Cr – 4 wt.% C with 6 wt.% Ti except that the latter has TiC domains. These further confirm that the added Ti did not act as an inoculant but more like a carbon consumer. Although early formed TiC phase could increase the carbide nucleation rate (heterogeneous nucleation), the depletion of carbon caused by the formation of TiC appeared to play a predominant role in the carbide refinement.

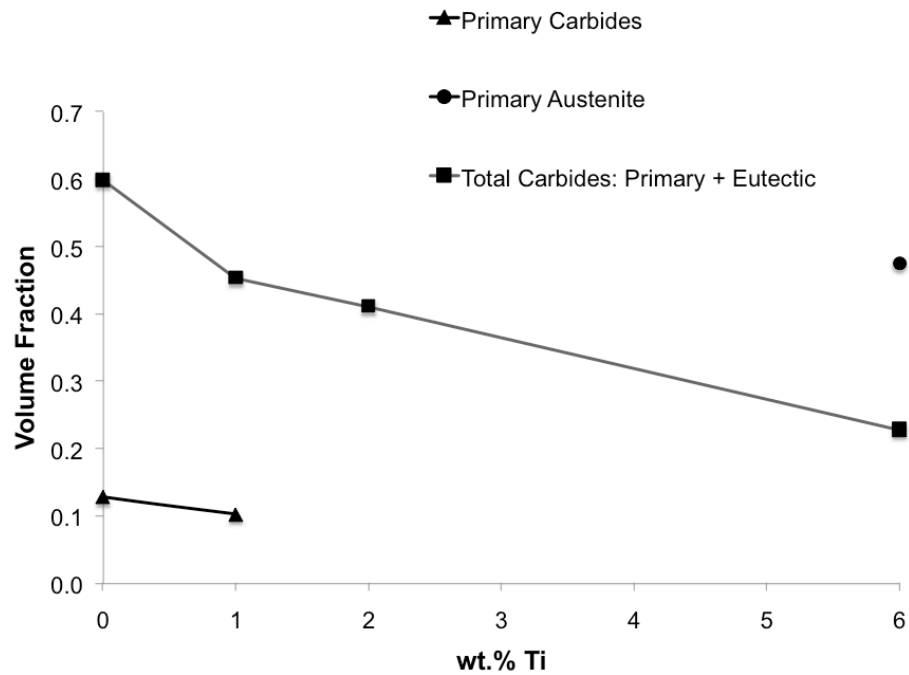


Figure 7.5: Volume fractions of primary phases and total carbides (primary and eutectic M_7C_3) in samples under study.

According to a thermodynamic analysis [17], the change in free energy for the formation of TiC is much more negative than those for other possible reactions such as:



This is a clear indication that TiC particles can grow preferentially in the ferrous liquid solution.

Besides, according to C-Ti and C-Cr phase diagrams [20], the formation of TiC might begin at higher temperatures (e.g., 3000°C) than the formation of chromium carbide (<1800°C), depending on the local composition of the melt. Therefore, it is expected that the added Ti can result in the depletion of carbon in the matrix, leading to the change of the alloy from a hypereutectic microstructure to a hypoeutectic one.

Regarding the composition and morphology of the TiC phase, according to the C-Ti phase diagram [20], TiC does not have a unique stoichiometric composition as the carbon content varies approximately between 10 to 19.3 wt.%. TiC carbides could grow with a dendritic pattern throughout a temperature range of solidification [17-19], especially at higher Ti additions such as 6 wt.% Ti (figure 7.3 (c)).

7.2.2 Effect of titanium on hardness and wear behaviour of the alloy

Microhardness of primary phases and that of the eutectic zone in various samples were measured and the results are presented in table 7.3. As shown, the micro-hardness of the primary carbides slightly decreases with the addition of Ti. This might be attributed to the loss of carbon that was consumed by Ti to form TiC, which possibly influences the configuration of the M_7C_3 carbides. Although it is unclear at present whether the configuration of M_7C_3 carbide could change with the nominal %C, in our other studies on HCCIs with different nominal %C

values we observed that the microhardness of primary carbides in HCCI's decreased with a decrease in the nominal carbon content. Further studies are needed in order to clarify this issue.

Table 7.3: Microhardness (HV) of different phases present in the alloys.

	Primary M_7C_3	Primary ferrous phase	Eutectic Matrix
Fe – 25 wt.% Cr - 4 wt.% C, As Cast	799.3	-	440.1
Fe – 25 wt.% Cr – 4 wt.% C + 1 wt.% Ti	789.4	-	444.9
Fe – 25 wt.% Cr – 4 wt.% C + 2 wt.% Ti	-	-	468.8
Fe – 25 wt.% Cr – 4 wt.% C + 6 wt.% Ti	-	342.0	404.5
Fe – 25 wt.% Cr – 2 wt.% C	-	268.2	401.6

An increase in hardness of the eutectic mixture was noticed when 2 wt.% Ti was added, corresponding to a finer eutectic microstructure. As for the primary austenite in the sample with 6 wt.% Ti, its microhardness was increased to 342 HV_{100mN}, higher than 268 HV_{100mN} of the primary austenite in the hypoeutectic sample. This is consistent with previous observations [8] where an increment in microhardness of the ferrous matrix was observed, which could be attributed to the formation of TiC that acted as a reinforcement to constrain the deformation of

the austenite phase in HCCIs. A small amount of Ti atoms could also exist in the ferrous matrix as a solute, which may strengthen the matrix as well.

The bulk hardness of the samples was measured to evaluate the effect of Ti addition on the overall hardness of the HCCI, which is directly related to the wear resistance of the material. Results of the macrohardness measurements are presented in figure 7.6. As illustrated, the hardness increased with increasing the amount of Ti addition until getting into the range of 2 wt.%. As the amount of Ti addition was continuously increased beyond 2 wt.%, the hardness decreased. Based on the microstructure examination and earlier discussion, such changes in hardness should correspond to the change from the hypereutectic microstructure to the hypoeutectic one as Ti was added. At 2 wt.% Ti, the alloy had a fine eutectic microstructure without coarse carbides, which was beneficial to the mechanical behaviour of the alloy. In addition, the dispersed TiC particles, which are harder than chromium carbides, embedded in a fine eutectic microstructure could further enhance the alloy in the sample with 2 wt.% Ti [21].

Effect of added Ti on the wear behaviour of the HCCI was evaluated using a pin-on-disc wear tester. During the wear test, a ball pin made of silica nitride of 6 mm in diameter slid on a flat sample under a normal load of 10N. Volume losses of various samples are presented in figure 7.6. As shown, the wear resistance increased and then decreased with respect to the amount of added

Ti. The maximum wear occurred at 6 wt.% Ti. The variation in the wear resistance is consistent with that of macrohardness.

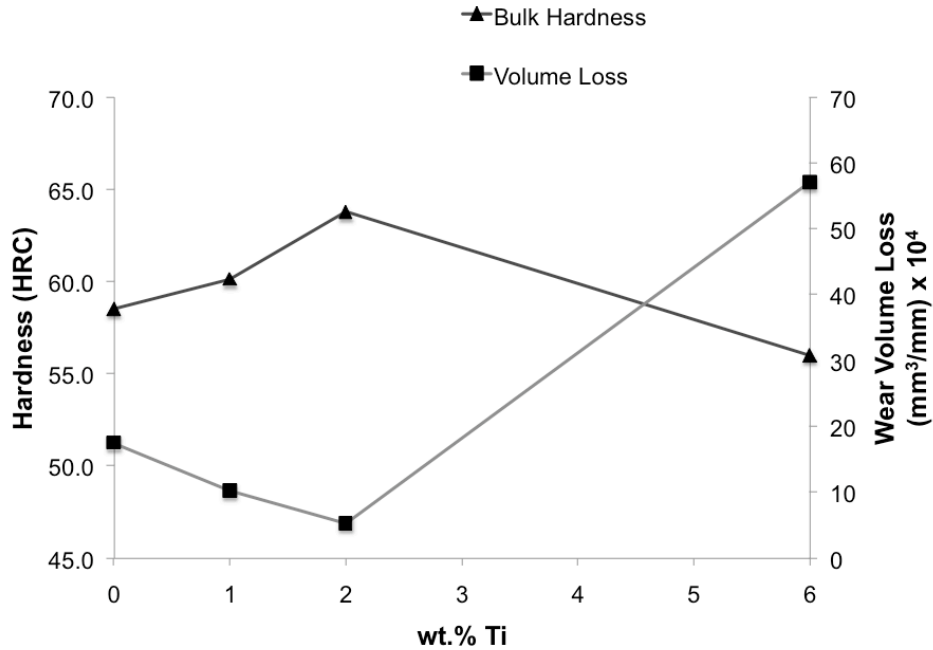


Figure 7.6: Changes in the bulk hardness and sliding wear volume loss of Fe - 25 wt.% Cr - 4 wt.% C with different amount of added titanium.

The variation in the wear behaviour of the alloy with Ti addition should be attributed to two factors that may influence the microstructure and properties of the HCCI. One of the factors is the presence of hard TiC carbides, which are harder than the primary and eutectic M_7C_3 carbides. As reported in literature (e.g., reference [22]), TiC showed its hardness in the range of 3200 ~ 3800 Hv. However, in the present case the TiC phase may not play a main role, since the

overall hardness of the alloy decreased at higher wt.%Ti. For instance, the sample having 6 wt.%Ti showed the lowest macrohardness and the highest wear loss as illustrated in figure 7.6. Nevertheless, the formation of TiC more or less compensate for the loss of M_7C_3 carbides when Ti was added to the HCCI.

The other factor is the refinement of the microstructure, which appears to be the predominant factor that controls the wear behavior of the alloy. Considerable attention has been paid to microstructural refinement for HCCIs using active elements in order to avoid coarse primary carbides that may lower the toughness of the material. However, the active elements do not necessarily act as an inoculant to increase the nucleation rate, since these added elements could react with carbon at temperatures higher than that at which usual M_7C_3 carbides form during solidification of HCCIs. In figure 7.1(b) one may see that the addition of 1 wt.% Ti resulted in a finer microstructure and dispersed TiC domains formed in the Ti-added HCCI (see figure 7.3 (b)). Such refinement, however, came as a consequence of the loss of carbon associated with the formation of TiC, leading to a melt of Fe-Cr-C with lower carbon content available for the formation of primary carbides. As a result, the loss of carbon can cause the change from a hypereutectic alloy to a hypoeutectic one. With a proper amount of added Ti, the alloy could possess an eutectic microstructure so that all M_7C_3 carbides are in the eutectic state without coarse primary carbides. The fine eutectic microstructure consisted of fine eutectic M_7C_3 carbides with a more homogeneous distribution

along with TiC. This eutectic microstructure should be mainly responsible for the highest hardness and wear resistance. When more Ti was added, the alloy was turned into a hypoeutectic microstructure, in which the amount of M_7C_3 carbides decreased although the fraction of TiC was higher, corresponding to a lowered hardness and wear resistance.

The addition of 6 wt.% Ti generated a hypoeutectic microstructure when Ti consumed more carbon and thus shifted the carbon content to a level lower than the eutectic composition. The resultant microstructure (figure 7.1(d) and 7.3(c)) consisted of primary austenite, eutectic microconstituent and TiC phase with a higher volume fraction. However, the lowest hardness and wear resistance of this microstructure may imply that a higher volume fraction of TiC, despite of its high hardness, may not necessarily make a large contribution to the wear resistance, compared to a fine microstructure. Or in other words, in the present case the microstructural refinement plays a predominant role in the improvement of the HCCI's wear resistance.

7.3 Conclusions

Added titanium addition in the Fe – 25 wt.% Cr – 4 wt.% C alloy under study did not act as an inoculant to refine primary M_7C_3 carbides. Instead, Ti consumed carbon with the formation of TiC domains, resulting in a change in microstructure of the alloy from a hypereutectic form to a hypoeutectic one.

With 2 wt.% Ti added, a fine eutectic microstructure with dispersed TiC carbide was achieved.

This microstructure exhibited the highest hardness and lowest wear loss. It appears that the microstructural refinement by limiting the carbon content in the range of eutectic composition plays a predominant role in improving the wear resistance of the alloy.

The variations in the wear resistance of the alloy with respect to the amount of added Ti are consistent with corresponding changes in hardness. The higher hardness, the lower the wear loss. The wear loss of the sample with 6 wt.% Ti is the largest among all samples.

7.4 Bibliography

1. Radzikowska, J.M., *Effect of specimen preparation on evaluation of cast iron microstructures*. Materials Characterization, 2005. **54**(4-5): p. 287-304.
2. Dogan, O.N., J.A. Hawk, and G. Laird, *Solidification structure and abrasion resistance of high chromium white irons*. Metallurgical and Materials Transactions a-Physical Metallurgy and Materials Science, 1997. **28**(6): p. 1315-1328.
3. Thorpe, W.R. and B. Chicco, *The Fe-rich corner of the metastable C-Cr-Fe liquidus surface*. Metallurgical Transactions A, 1985. **16**(9): p. 1541-1549.

4. Carpenter, S.D., D. Carpenter, and J.T.H. Pearce, *XRD and electron microscope study of an as-cast 26.6% chromium white iron microstructure*. Materials Chemistry and Physics, 2004. **85**(1): p. 32-40.
5. Fernández I., F.J. Belzunce, *Wear and oxidation behaviour of high-chromium white cast irons*, Materials Characterization, 2008. **59**: p.669-674.
6. Wiengmoon, A., et al., *Microstructural and crystallographical study of carbides in 30wt.%Cr cast irons*. Acta Materialia, 2005. **53**(15): p. 4143-4154.
7. J.M. Radzikowska, *Metallography and Microstructures of Cast Iron*. ASM Handbooks, Metallography and Microstructures, ASM International, 2004. p.565-587.
8. Bedolla-Jacuinde, A., et al., *Effect of titanium on the as-cast microstructure of a 16%chromium white iron*. Materials Science and Engineering a-Structural Materials Properties Microstructure and Processing, 2005. **398**(1-2): p. 297-308.
9. Bedolla-Jacuinde, A., *Microstructure of vanadium-, niobium- and titanium-alloyed high-chromium white cast irons*. International Journal of Cast Metals Research, 2001. **13**(6): p. 343-361.
10. Galgali, R.K., H.S. Ray, A.K. Chakrabarti, *Wear characteristics of TiC reinforced cast iron composites - Part I - Adhesive wear*. Materials Science and Technology, 1998. **14**: p.810-815.
11. Wu, X.J., et al., *Effect of titanium on the morphology of primary M7C3 carbides in hypereutectic high chromium white iron*. Materials Science and Engineering a-Structural Materials Properties Microstructure and Processing, 2007. **457**(1-2): p. 180-185.
12. Zhi, X.H., J.D. Xing, H.G. Fu. B. Xiao, *Effect of niobium on the as-cast microstructure of hypereutectic high chromium cast iron*. Materials Letters, 2008. **62**: p.857-860.

13. Fan, C., M.C. Chen, C.M. Chang, W.T. Wu, *Microstructure change caused by (Cr,Fe)₂₃C-6 carbides in high chromium Fe-Cr-C hardfacing alloys*. Surface & Coatings Technology, 2006. **201**: p.908-912.
14. Arikan, M.M., H. Cimenoglu, and E.S. Kayali, *The effect of titanium on the abrasion resistance of 15Cr-3Mo white cast iron*. Wear, 2001. **247**(2): p. 231-235.
15. Dolman, K.F., *Metallurgy of White Cast Irons: Effect of Alloying Elements and Heat Treatment*. 36TH Australian Foundry Institute National Conference, Sydney, 2005.
16. Ko, S.H., S. Hanada, *In-situ production and microstructures of iron aluminide TiC composites*. Intermetallics, 1999. **7**: p.947-955.
17. Mei, Z., Y.W. Yan, K. Cui, *Effect of matrix composition on the microstructure of in situ synthesized TiC particulate reinforced iron-based composites*. Materials Letters, 2003. **57**: p.3175-3181.
18. Cui, C.Y., Z.X. Guo, H.Y. Wang, H.D. Hu, *In situ TiC particles reinforced grey cast iron composite fabricated by laser cladding of Ni-Ti-C system*. Journal of Materials Processing Technology, 2007. **183**: p.380-385.
19. Tian, Y.S., C.Z. Chen, L.X. Chen, Q.H. Huo, *Growth model of TiC dendritic crystals produced by laser surface alloying technique*. Modern Physics Letters B, 2006. **20**: p.683-689.
20. ASM Handbooks: Alloy Phase Diagrams, ASM International, Ohio, 2002.
21. Glaeser, W.A., *Wear-Resistant Hard Materials*. E.R. Booser, Tribology Data Handbook: An Excellent Friction, Lubrication and Wear Resource, CRC Press, 1997. p. 544.
22. Suzuki, A., *Effects of multiply charged ions on the Vickers hardness of TiC films*. Jpn J. Appl. Phys., 1999. **38**: p.881 – 885.

8 MICROSTRUCTURE REFINEMENT OF HYPEREUTECTIC HIGH CR CAST IRONS USING HARD CARBIDE-FORMING ELEMENTS FOR IMPROVED WEAR RESISTANCE

Previously, we modified a hypereutectic HCCI by alloying with Ti addition [1]. This strong carbide-forming element was more competitive to react with carbon during casting to form fine TiC particles while the formation of primary M_7C_3 carbides was suppressed as the concentration of carbon in the matrix was reduced due to the formation of TiC. The modified microstructure consisted of refined M_7C_3 carbides (i.e. eutectic carbides) and fine TiC carbides, which demonstrated markedly improved performance during wear processes [1].

The objective of this study was to evaluate the effectiveness of other carbide-forming elements in refining HCCI's microstructure for improved performance, including two strong carbide formers (V, Nb) and less strong carbide formers (B, Mo) that partially partition into HCCI phases; and also to compare these results with the ones obtained by Ti modification. The methodology was the same as that for the study on Ti addition reported in Chapter 7. The base alloy was a hypereutectic HCCI, Fe-25Wt.%Cr-4Wt.%C.

Understanding the individual effect of these carbide-forming elements on microstructure modification and resulting wear behavior helps identify effective paths for HCCI optimization.

This chapter is divided into three sections: (1) alloy preparation and experimental methods used for the investigation; (2) effects of the added elements on the microstructure of the modified alloys; and (3) effects of the additions on the wear behavior and hardness of the modified alloys.

8.1 Experimental details

Modified HCCI alloys were made by alloying a base hypereutectic HCCI, Fe-25Wt.%Cr-4Wt.%C, with V, Nb, B, and Mo, respectively, using an arc melting furnace (MRF INC. SA338-V&G). Concentrations of the added carbide-forming elements were controlled to form desired amounts of their own carbides, e.g., VC, and correspondingly reduced the content of carbon in the liquid to the one of an HCCI with the same amounts of Cr and Fe but having changed carbon concentrations, approximately equal to 3.75, 3.5, 3, and 2.5 Wt.%C, respectively. Such carbon in the liquid is referred to as “Equivalent Carbon” for the normal HCCI solidification (i.e. for forming M_7C_3 or $M_{23}C_6$ and the ferrous matrix). Expected final microstructures are similar to those of HCCIs with their nominal carbon concentrations equal to 3.75, 3.5, 3, and 2.5 Wt.%C, respectively, but embedded with additional carbides of the added carbide-forming elements.

The cast ingot dimensions were 15 x 10 x 30 mm. The set of samples produced for this study are shown in table 8.1 and the melting condition is given in table 8.2. The added elements were in the form of powder (-325 mesh, 99.99%

purity). In addition to the modified HCCIs, the base HCCI and an eutectic HCCI Fe-25Wt.%Cr-3Wt.%C were also made under the same melting condition for comparison purposes. During the alloying process, weighted pieces of the base alloy and powder were placed on a water-cooled copper hearth in the arc furnace. In order to minimize the compositional and microstructure heterogeneities, each sample was turned over and remelted six times.

Table 8.1: Modified HCCI samples produced.

Series Sub ID	Elements in the base Hypereutectic Alloy (Wt.%)				Four modified HCCI alloy series (Sample ID) added with various carbide-forming elements, respectively (Wt.%)				Equivalent Carbon (Wt.%)
	Cr	C	Mn	Si	Mo	V	B	Nb	
1	24.80	3.72	1.56	0.38	6.0 (Mo1)	1.5 (V1)	2.0 (B1)	2.0 (Nb1)	3.75
2					10.5 (Mo2)	2.0 (V2)	4.0 (B2)	4.0 (Nb2)	3.5
3					13.0 (Mo3)	4.5 (V3)	10.0 (B3)	7.5 (Nb3)	3.0
4					16.0 (Mo4)	8.0 (V4)	13.0 (B4)	12.0 (Nb4)	2.5

Table 8.2: Melting and solidification conditions (in an arc melting furnace).

Parameters	Melting Conditions
Vacuum pressure before filling with Ar gas	- 95 kPa
Protection gas	Argon Ultra High Purity (99.999%)
Pressure during melting and cooling	- 75 to -10 kPa
Electrode type	2% Thoriated Tungsten
No. of turning over and remelting	6 times

Specimens for metallographic observation were prepared following the standard metallographic preparation using silicon carbide discs from 80 up to 1200 grit and then polished with nylon cloth in a diamond slurry, 5 μm diamond particle size. Samples for optical microscopy were etched using a solution of 50 ml FeCl_3 , 20 ml of HCl , and 20 ml of ethanol. This solution attacks preferentially the ferrous matrix leaving the carbides relatively unaffected, leading to a good contrast between carbides and matrix. Optical micrographs were taken using an Olympus PME3-ADL and images were processed with the software “ImagePro”.

SEM, EDS, XRD, bulk hardness, micro mechanical testing, and pin-on-disc tests were carried out to characterize microstructures of the samples and evaluate their properties, respectively. The XRD analysis was made using a Rigaku X-ray diffractometer with $\text{Cu K}\alpha$ radiation. A Hitachi S-2700 and a Zeiss EVO SEM with LaB6 crystal equipped with an ultrathin window X-ray detector was used for the SEM and EDS analyses.

Bulk hardness was measured using a Mitutoyo hardness tester with a 30Kgf/mm² load and 30s dwell time. Five measurements were taken for each sample. Micro-hardness was determined on lightly etched samples using a micro mechanical probe (Fisher Technology Ltd., Winsor, CT, USA) under a load of 100 g for 15 s. Each reported micro-hardness value is an average of fifteen measurements.

The wear resistance of the samples was evaluated using a pin-on-disc tribometer (CSEM Instruments, Neuchatel, Switzerland). The pin was a silicon nitride ball of 6 mm in diameter. The wear tests were performed at a sliding speed of 0.5 cm/s along a circular path of 1.6 mm in width under a normal load of 10 N for 10,000 cycles. Wear tracks were observed under SEM and their dimensions were measured using a contact profilometer (Tencor Instruments, USA) along six radial directions, from which the volume loss was determined.

8.2 Results and discussion

8.2.1 Microstructure of the base HCCI Fe-25Wt.%Cr-4Wt.%C

The microstructure of the base hypereutectic HCCI, 25%Cr-4%C, is illustrated in figure 8.1(A), showing a typical hypereutectic HCCI microstructure, which follows the Fe-Cr-C liquidus surface projection that is presented in figure 8.1(B). The first solid phase, M₇C₃, nucleates at about 1300°C and grows in the

liquid to form coarse primary carbides. As solidification precedes the quasi eutectic reaction is reached along which the austenite ferrous matrix (γ), and M_7C_3 carbides simultaneously develop and form the eutectic mixture of carbides (dark phase) and austenite (lighter phase) that surrounds the primary M_7C_3 carbides as shown by figure 8.1(A).

The M_7C_3 carbides typically grow into needle-like rods. Depending on the sample cutting plane or faces where micrographs are taken, M_7C_3 carbides may show different apparent morphologies. The M_7C_3 carbide has its hardness in the range of 1200 - 1800 HV, which is the highest among different types of chromium carbide and chromium-iron carbide species. Thus, it is a desired type of carbide in the HCCI system for high resistance to wear. As seen in figure 8.1(B), other possible carbides are $M_{23}C_6$ (976 – 1,650HV) and M_3C (1,060 – 1,240 HV), depending on the chromium and carbon content.

XRD diffraction pattern of the base HCCI confirms the presence of the M_7C_3 carbides and austenite phase (γ). Through SEM-EDS analysis, chemical compositions of the present phases and their volume fraction in the microstructure were analyzed and estimated. Obtained results are summarized in table 8.3. Relevant information on the eutectic HCCI, Fe-25Wt.%Cr-3Wt.%C, is also given in table 8.3.

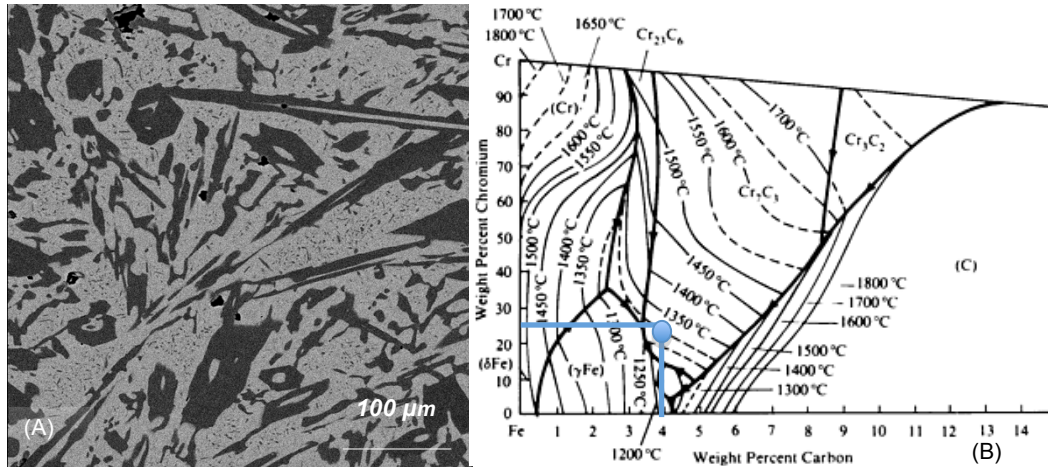


Figure 8.1: (A) Backscatter SEM image of the base HCCI, Fe-25Wt.%Cr-4Wt.%C, consisting of needle-like coarse primary M_7C_3 carbides and a eutectic ferrous matrix; (B) Liquidus projection of the Fe-Cr-C system [2].

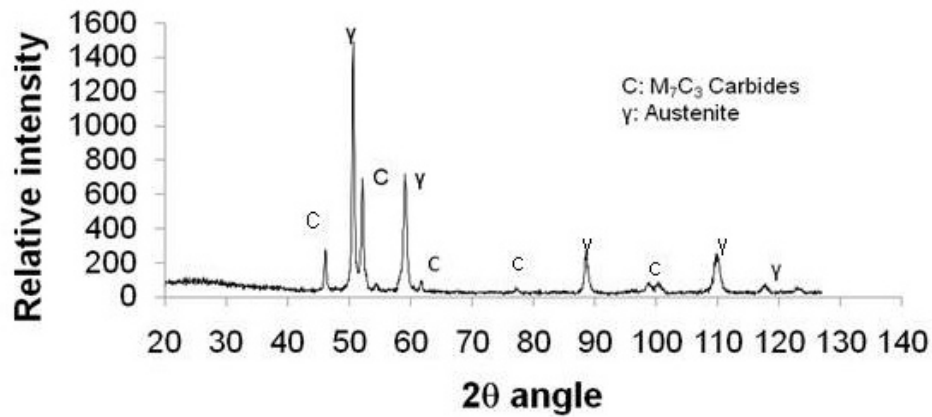


Figure 8.2: XRD diffraction pattern of the base HCCI, Fe-25Wt.%Cr-4Wt.%C, which contains M_7C_3 carbides and austenite [1].

Table 8.3: Microchemistry of phases in the base and eutectic HCCIs (without addition of other carbide-forming elements) determined by SEM-EDS, and their respective volume fractions.

Alloy	Phase	Wt.%		Volume Fraction (Vf)		Micro-hardness (HV ₁₀₀)
		Cr	Fe	Primary Carbides (%)	Total Carbides (%)	
Base HCCI 25Wt.%Cr- 4%C	M ₇ C ₃	57.4	39.7	12	58	1510
	Austenite	9.1	88.2			438-572
Eutectic HCCI 25%Cr-3%C	M ₇ C ₃	57.3	39.4	-	38	-
	Austenite	10.0	88.8			-

8.2.2 Microstructure of the modified HCCI alloys with added carbide-forming elements

Microstructures of four modified HCCI alloy series with added V, Nb, B and Mo, respectively, were characterized and are described in the following sections.

8.2.2.1. *Vanadium Series*

Microstructures of modified HCCIs with added V (Samples: V1 – hypereutectic, V3 – Near-eutectic and V4 – hypoeutectic) are shown in figure 8.3. One may see that the hypereutectic microstructure with the lowest addition (shown in figure 8.3(A)) gradually changes through a near-eutectic (figure 8.3(B)), to a hypoeutectic one (figure 8.3(C)) with the formation of fine vanadium

carbide (VC). As %V increases, VC carbides become visible and their size is in the range of 5 μm . The near-eutectic alloy (sample V3) presents a rather fine structure in which austenite (γ), M_7C_3 carbides, and VC carbides coexist. Their microstructure can be seen in more detail in figure 8.4 along with their characteristics peaks in the XRD diffraction pattern. Figure 8.5 presents EDS compositional maps of various elements in the microstructure. One may see that the element distributions are quite consistent with the microstructure and identified phases as shown, e.g., in figure 8.4(A).

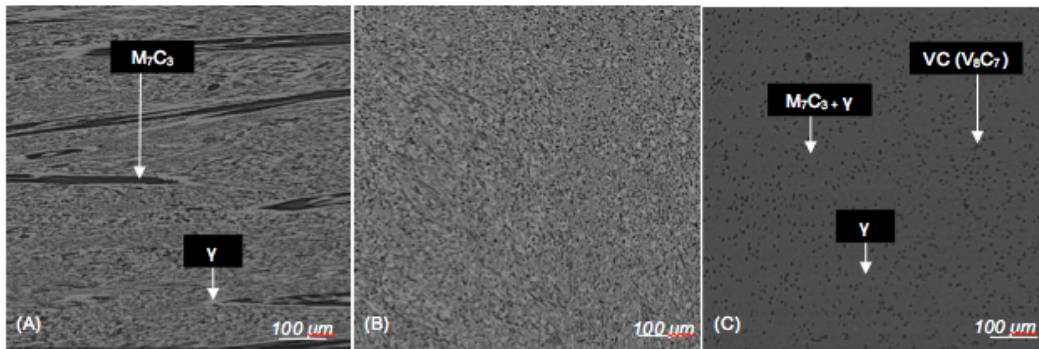


Figure 8.3: Microstructures of Vanadium added HCCI Series. (A) Sample V1 – Hypereutectic HCCI; (B) Sample V3 – Near-eutectic HCCI without distinguishable primary M_7C_3 carbides; Sample V4 – Hypoeutectic HCCI with fine carbides and a primary austenitic matrix.

The addition of V has a relatively minor effect on the solidification path of HCCI. However, the formation of VC in the liquid phase reduces the carbon content prior to nucleation of primary M_7C_3 carbides, producing an equivalent HCCI with lower carbon content in which fine VC phase is embedded. The in-situ

size of VC carbides in the present alloy samples, it has been reported in the literature that the hardness of VC may reach 2,800HV [4].

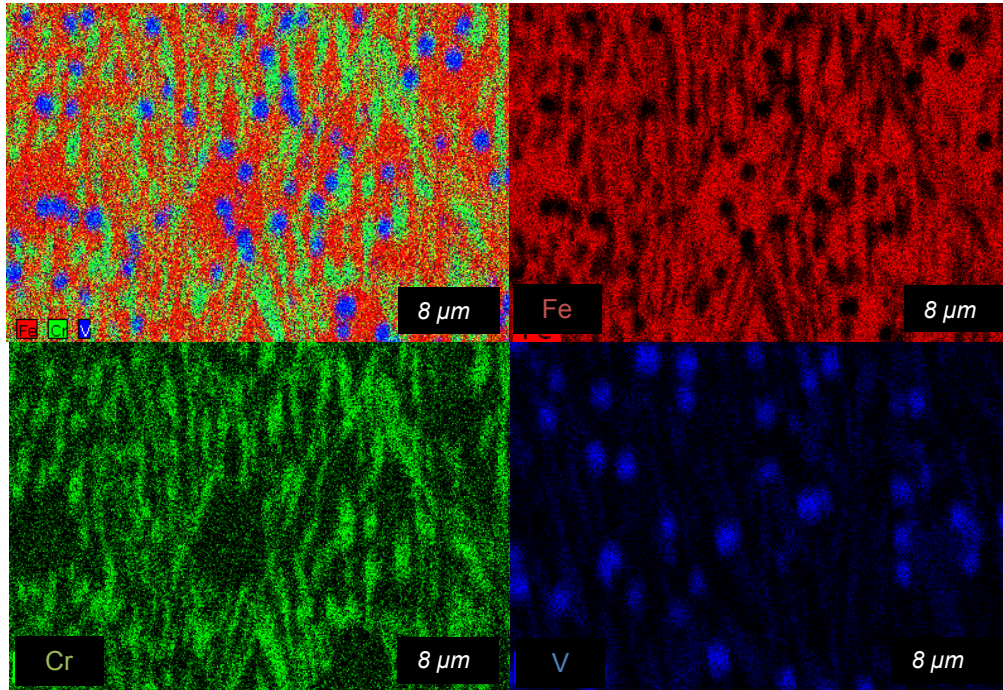


Figure 8.5: High magnification EDS compositional mapping of the sample V3 showing the microstructural distribution of Fe (red), Cr (green), and V (blue).

Table 8.4: Microchemistry of V-HCCI phases determined by EDS, and their volume fractions.

Alloy	Phase	Cr (Wt.%)	V (Wt.%)	Fe (Wt.%)	Primary Carbides (%)	Total Carbides (%)	Micro-hardness (HV ₁₀₀)
V1	M ₇ C ₃	48.8	8.5	41.7	15	43	1727
	Austenite (γ)	14.2	1.3	82.3			644
	VC (V ₈ C ₇)	22.2	60.0	5.0			-
V3	M ₇ C ₃	45.6	21.6	31.7	-	62	-
	Austenite (γ)	15.7	4.4	78.1			639
	VC (V ₈ C ₇)	15.9	68.0	15.6			-
V4	M ₇ C ₃	40.8	16.4	41.7	-	47	-
	Austenite (γ)	14.9	3.5	80.5			-
	VC (V ₈ C ₇)	11.8	85.4	4.9			-

8.2.2.2. Niobium Series

Microstructures of three modified HCCIs with added Nb (Samples: Nb1 – hypereutectic, Nb3 – Near-eutectic and Nb4 – hypoeutectic) are illustrated in figure 8.6. As shown, as the concentration of Nb increased (from left to right in figure 8.6), coarse primary M_7C_3 carbides were eliminated and the hypereutectic structure with primary M_7C_3 carbides was replaced by a mixture of eutectic austenite and M_7C_3 carbides, and eventually by primary austenite (γ) grains with fine niobium carbide phase (NbC).

Nb is a very strong carbide former with a higher melting temperature (3,500 deg.C) than the liquidus temperature of HCCI and a large negative enthalpy of reaction [4,5]. Therefore, the formation of niobium carbides is expected to occur in the liquid, which reduces the carbon content in the liquid, thus shifting the structure of the base alloy from a hypereutectic state, through eutectic one, to hypoeutectic one with embedded fine Nb_4C_3 carbides. The Nb_4C_3 carbides may promote the refinement of the austenitic matrix through heterogeneous nucleation and pinning of the austenitic grains on formed Nb_4C_3 , which is a typical approach used in microalloyed steels.

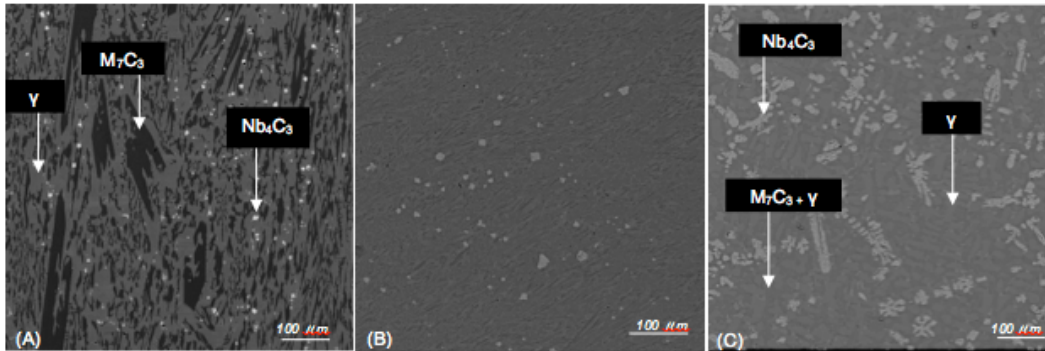


Figure 8.6: Microstructures of the Niobium added HCCI Series. (A) Nb1 – Hypereutectic, (B) Nb3 – Near-eutectic HCCI without distinguishable primary M_7C_3 carbides., (C) Nb4 – Hypoeutectic HCCI consisting of austenitic matrix (γ) and fine NbC.

Unlike V, Nb has extremely low solubility in both the ferrous matrix and M_7C_3 carbides, which lowers the threshold of minimum addition required to form the new carbide species in the liquid in order to reduce the equivalent carbon content towards microstructural refinement and reinforcement. It was estimated that for 1%Nb added, 0.99%Nb would react with carbon to form Nb_4C_3 . According to the XRD diffraction patterns (see figure 8.7(B)), Nb_4C_3 , M_7C_3 and austenite (γ) were present in the Nb-added HCCIs. Traces of $M_{23}C_6$ and Nb_2C were also observed. As the amount of added Nb was increased, the volume fraction of Nb_4C_3 also became larger. The microanalysis (table 8.5) confirmed that Nb only had a very small amount, 0.5%, partitioned into M_7C_3 and 0.1% into austenite (γ).

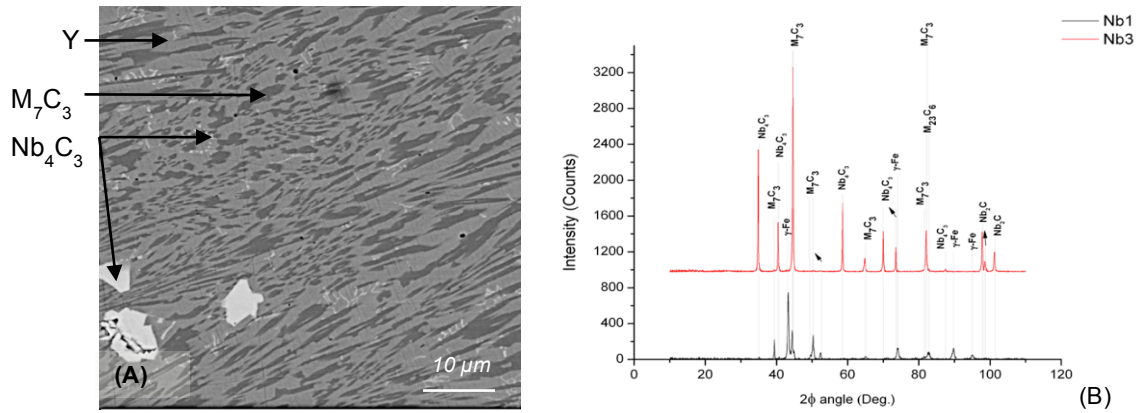


Figure 8.7: (A) A high magnification SEM (backscatter) micrograph of the near-eutectic Nb-HCCI sample (Nb3); (B) Representative diffraction patterns of two Nb-HCCI alloys (Nb1 and Nb3).

The microstructure of the Nb series at higher magnification revealed two morphologies of Nb₄C₃ (see figure 8.7A). Coarse Nb₄C₃ particles of about 5μm, which were formed in liquid phase at temperatures higher than the HCCI liquidus temperature, and a “fish-bone” like structure consisting of fine Nb₄C₃ domains that likely formed following the eutectic solidification of austenite and M₇C₃ carbides. EDS compositional mapping was also obtained. Figure 8.8 illustrates the distribution of various elements at high magnification for the refined near-eutectic Nb added sample, Nb3. The compositional maps are consistent with the observed microstructure features and identified phases. As mentioned earlier, there is no distinguishable Nb partitioned to the other phases other than forming the Nb rich, Nb₄C₃.

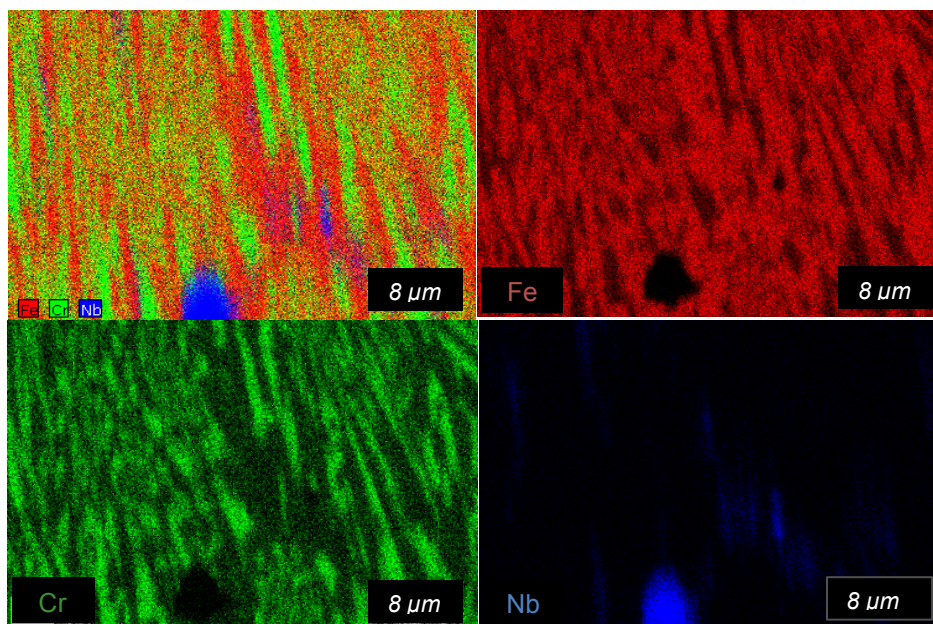


Figure 8.8: High magnification EDS compositional maps of sample Nb3 showing the distributions of Fe (red), Cr (green), and Nb (blue).

Table 8.5: Microchemistry of phases in Nb-HCCI determined by EDS and their volume fractions.

Alloy	Phase	Cr (wt%)	Nb (wt%)	Fe (wt%)	Primary Carbides (%)	Total Carbides (%)	Micro-hardness (HV ₁₀₀)
Nb1	M ₇ C ₃	57.8	0.3	41.9	7	43	1,530
	Austenite (γ)	15.0	<0.1	84.3			385
	Nb ₄ C ₃	5.6	91.1	2.6			-
Nb3	M ₇ C ₃	54.6	0.6	43.3	-	69	-
	Austenite (γ)	14.3	<0.1	83.5			-
	Nb ₄ C ₃	2.6	95.6	1.5			-
Nb4	M ₇ C ₃	54.9	0.6	42.8	-	33	-
	Austenite (γ)	19.0	0.1	79.1			464
	Nb ₄ C ₃	0.8	98.3	0.9			2,200

8.2.2.3. Boron Series

Representative microstructures of B-added HCCI samples (B1-hypereutectic, B3 – near-eutectic, and B4-hypoeutectic) are shown in figure 8.9. One may see that the microstructure of the base HCCI was modified as B was added, which was however different from the trend as those of V and Nb added samples. The effect of B on microstructural refinement was less profound, which could be attributed to the fact that B is a less strong carbide former and more soluble in the HCCI phases. Thus, a fair amount of B could dissolve in the austenite matrix, M_7C_3 , and $M_{23}C_6$ carbides in addition to the formation of M_2B boride [6].

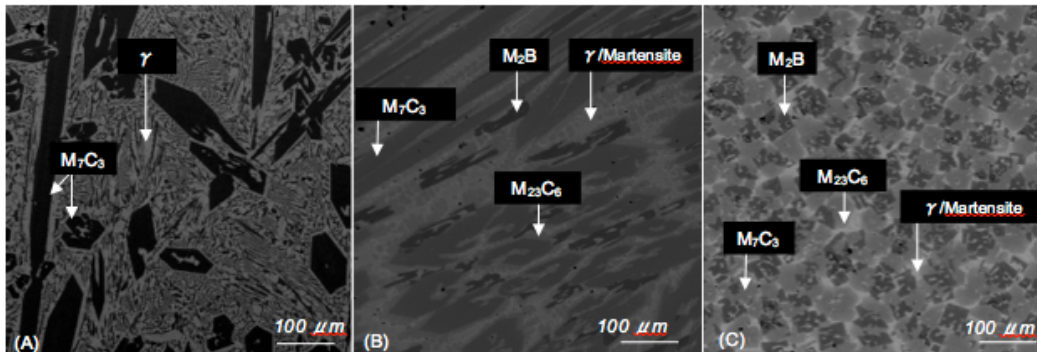


Figure 8.9: Microstructure of the Boron added HCCI series. (A) B1 - Hypereutectic HCCI; (B) B3 - Hypereutectic HCCI with nucleated boride phase. (C) B4 - Hypereutectic HCCI featuring primary M_7C_3 and boride phase.

For all the B additions under study, the M_7C_3 carbide was always present as a primary phase and its volume fraction became higher, being the first solid

phase to nucleate. However, sample B4 with the highest addition of B formed a larger volume fraction of the discontinuous M_2B as it can be seen in figure 8.9.

The effect of B on the solidification and microstructure of the base HCCI is rather interesting. Even though it did not promote the formation of new hard carbide species in the liquid, it increased the volume fraction of carbides as it substituted C atoms in main carbide phases present in the HCCI, which allowed carbon saturation in the melt, thus favoring the formation of a larger number of carbide nuclei which grow during solidification [6].

XRD patterns of samples B1 and B3 are presented in figure 8.10 (B), which show a number of new peaks that become more intense as B content increases. Main peaks come from $M_7(C,B)_3$, $M_{23}(C,B)_6$, and M_2B phases. The austenite phase peaks are attenuated as B increases, since the fraction of carbides is increased, and the austenite has partially transformed to martensite. The analysis of the four samples confirmed that the more B is added, the greater the volume fraction of carbides (M_7C_3 and $M_{23}C_6$) and boride (M_2B) in the microstructure. Morphologies of the phases are illustrated in figure 8.10 (A) and results of the microanalysis for the B series are presented in table 8.6. The distributions of elements in different micro-constituents are depicted by EDS compositional mapping, which is shown in figure 8.11. As mentioned earlier, B is soluble in all phases due to its ability to substitute C. The B concentration is

slightly higher in the darker phase shown in figure 8.10(A), which was identified as M_2B . It is however pertinent to mention that EDS is not accurate for analyzing light elements such as B and C, and therefore the EDS mapping was carried out mainly for demonstrating the boron distribution rather than to quantify boron's contents in the different phases.

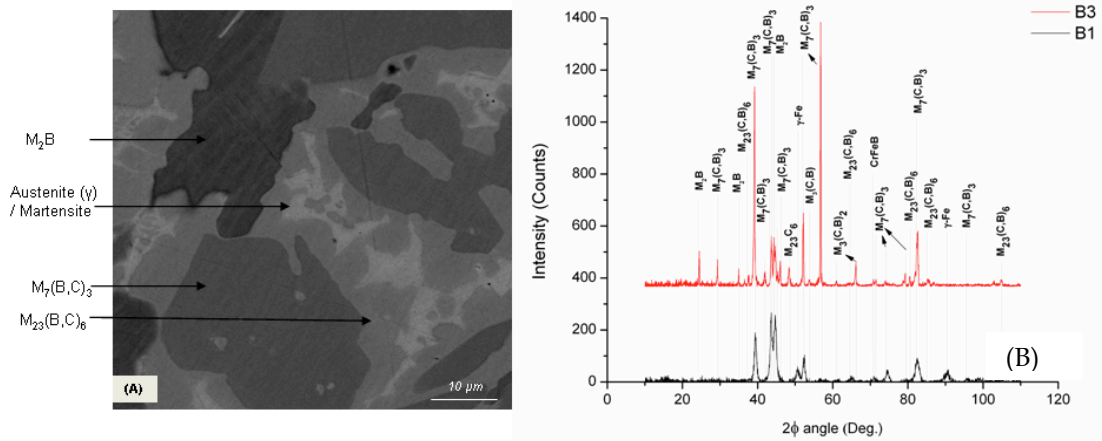


Figure 8.10: (A) High magnification SEM (backscatter) micrograph of sample B3; (B) Representative diffraction patterns of samples B1 and B3.

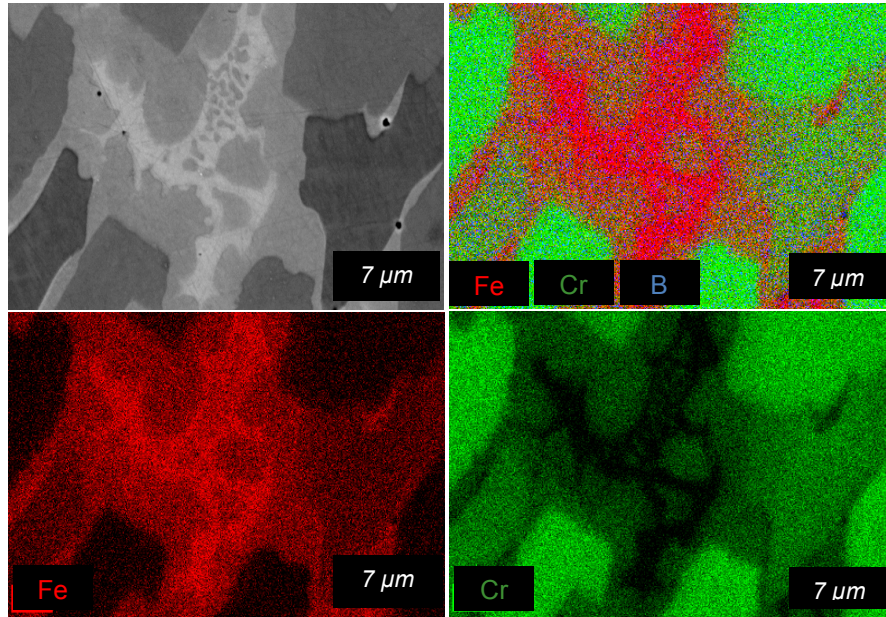


Figure 8.11: High magnification EDS compositional maps of sample B3, showing distributions of Fe (red), Cr (green), and B (blue).

Table 8.6: Microchemistry of the B-HCCI phases determined by EDS, and their respective volume fraction.

Alloy	Phase	Cr (wt%)	Fe (wt%)	Primary Carbides (%)	Total carbides /borides (%)	Micro-hardness (HV100)
B1	M7C3	48.2	47.0	15	55	1,471
	M23(C,B)6	18.2	74.9			-
	Austenite (γ)	10.4	85.4			-
B3	M7C3	36.4	57.4	28	83	1,488
	M23(C,B)6	17.3	75.8			1,276
	M2B	24.3	64.6			1,635
	Austenite	6.2	93.8			-
B4	M7C3	32.0	56.6	46	94	1,432
	M23(C,B)6	14.4	73.9			1,275
	M2B	24.4	59.1			1,694
	Austenite	9.4	77			-

8.2.2.4. Mo Series

Figure 8.12 shows microstructures of the Mo-added HCCI alloy series. Like V and Nb, the addition of Mo refined the microstructure and coarse primary M_7C_3 carbides were eliminated. Sample Mo3 had a near-eutectic microstructure consisting of fine M_7C_3 , M_2C , MC, and austenite (γ) matrix. Further increment of Mo produced a hypoeutectic structure. Although Mo does not change the solidification path of the base HCCI, it is reported that Mo may slightly affect the peritectic reaction of $L + \delta \rightarrow \gamma$ [7]. In the present case, the addition of Mo resulted in the formation of eutectic M_2C and/or MC carbides during the solidification process. The formed molybdenum carbides are fine with a low volume fraction.

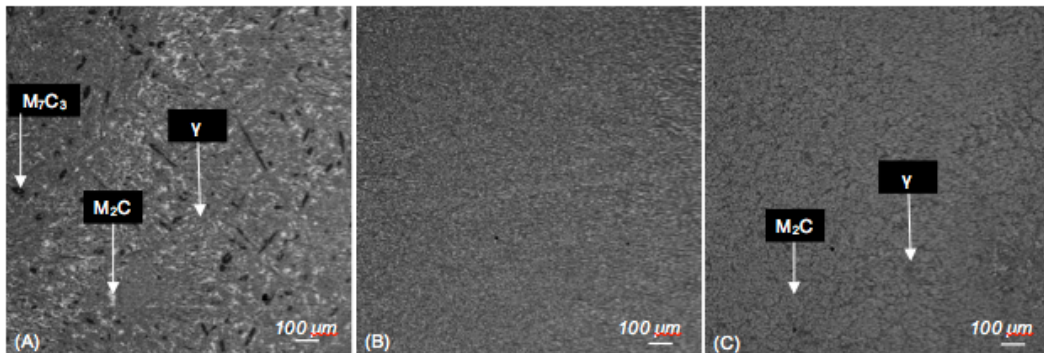


Figure 8.12: Microstructures of the Mo-added HCCI Series. (A) Mo1 – Hypereutectic HCCI; (B) Mo3 – Near-eutectic HCCI without distinguishable primary M_7C_3 carbides; (C) Mo4 – Hypoeutectic HCCI with a primary austenitic matrix.

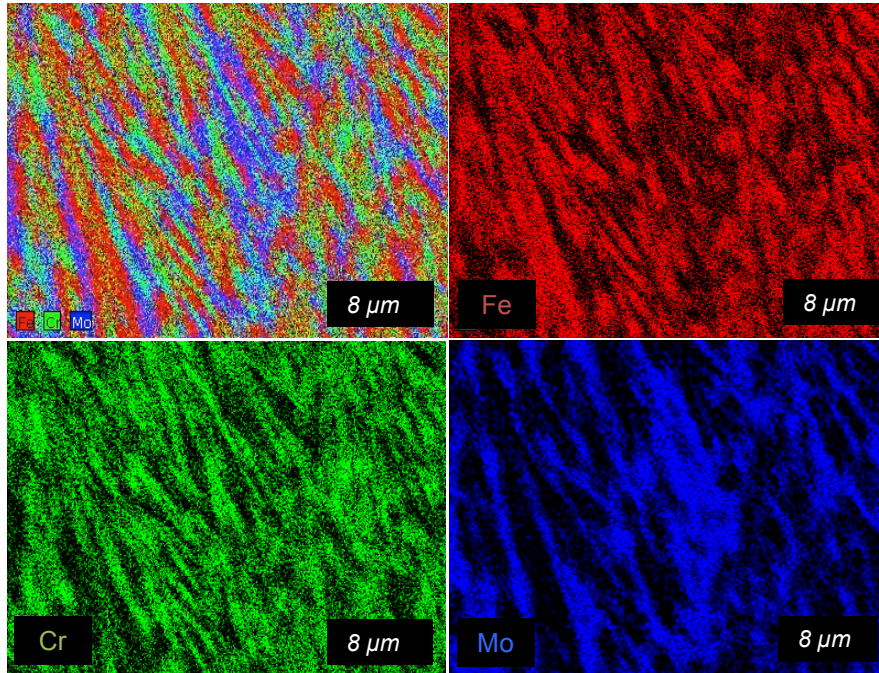


Figure 8.14: High magnification EDS compositional maps of sample Mo3 showing the microstructural distribution of Fe (red), Cr (green), and Mo (blue).

Table 8.7: Microchemistry of the Mo-HCCI phases determined by EDS, and their respective volume fraction.

Alloy	Phase	Cr (wt%)	Mo (wt%)	Fe (wt%)	Primary Carbides (%)	Total Carbides (%)	Micro-hardness (HV ₁₀₀)
Mo1	M ₇ C ₃	56.3	4.9	37.5	11	45	1,476
	M ₂ C	15.2	19.7	62			1,512
	Austenite (γ)	12.7	2.7	81.6			643
Mo3	M ₇ C ₃	38.1	13.0	48.6	-	58	-
	M ₂ C	17.0	21.0	60.0			-
	Austenite	12.7	4.6	80.0			-
Mo4	M ₇ C ₃	38	12.6	47.3	-	73	-
	M ₂ C	17.4	21.3	59.2			-
	Austenite	10.7	6.2	80.5			-

8.2.3 Effects of the carbide-forming elements on hardness and wear behavior of the modified HCCI series

8.2.3.1. *Hardness*

The bulk hardness of each alloy series was measured and plotted in figure 8.15. As shown, the alloys with the added carbide-forming elements had their hardness increased until sample #3 (near-eutectic state), beyond which the hardness sharply dropped (V and Nb series) or reached a plateau (Mo and B series). Sample #3 for each series is the alloy in which the added element and equivalent carbon in matrix resulted in a near-eutectic state, corresponding to the highest level of refinement and reinforcement by the new carbide species which formed in the liquid (V and Nb) or produced later during solidification (B and Mo).

For the V-added and Nb-added series, sample #3 exhibits the highest hardness, which is attributed to two main factors: 1) the highest total volume fraction of hard carbides as shown in tables 8.4 and 8.5, and 2) finer carbides in the near-eutectic microstructures which generate a larger number of barriers and limit the path for dislocations to move. As for the B-added and Mo-added series, their different behavior at higher concentrations of B and Mo, i.e. no hardness drop after sample #3, should be largely ascribed to the continuous increase in the total volume fraction of carbides/borides or carbides as shown in tables 8.6 and 8.7. Corresponding changes in microstructure may also contribute to the increase

in hardness. As shown in figure 8.9, as the amount of added B increased, the carbides became relatively smaller and near equiaxed and so did the hard M_2B borides, which enhance the resistance of the B-added HCCI to plastic deformation. The situation of the Mo-added HCCI is however different in terms of microstructural changes. As figure 8.12, 8.13 and 8.14 illustrates, as the amount of added Mo increases, the ferrous matrix is gradually replaced by an interconnected hard Mo-carbide phase (M_2C). The corresponding increase in the volume fraction of carbides (see table 8.7) should be responsible for the elevated hardness.

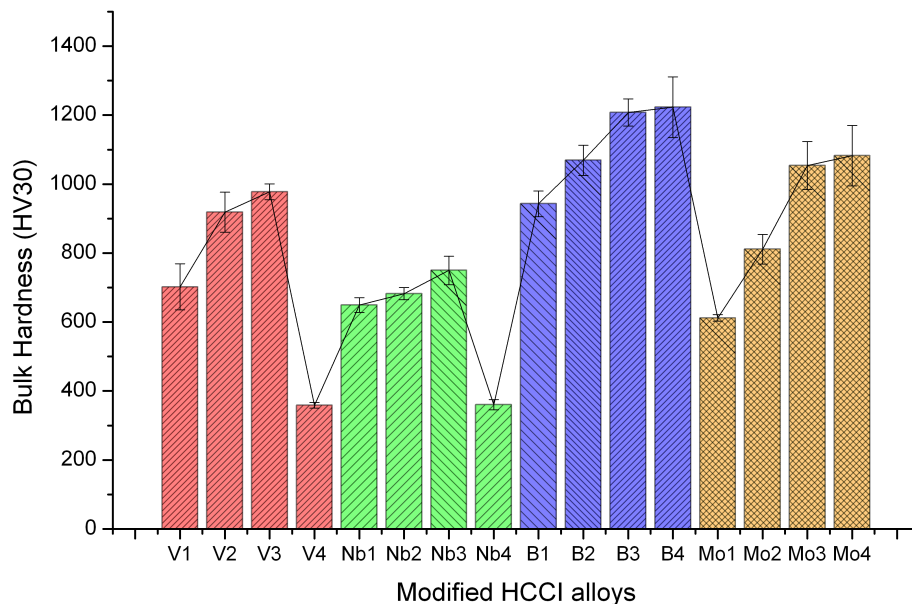


Figure 8.15: Bulk hardness measurements obtained for the modified HCCI alloys series being studied.

Compared to the base HCCI (660 HV), most of the modified HCCI series are harder. Among all the series, the maximum hardness was achieved by the B series (1,222 HV) followed by the Mo series (1,082 HV), and then the V-series (977 HV), and Nb-series (749 HV).

8.2.3.2. *Wear behavior*

The wear behavior of the four modified HCCI series was evaluated using a pin-on-disc wear tester. During the wear testing, a ball pin made of silicon nitride of 6mm in diameter slid on a sample under a normal load of 10N. Measured volume losses of various samples are shown in figure 8.16, which illustrates that the volume loss of the base HCCI decreased as the carbide-forming elements were added, which should be mainly attributed to the increase in hardness. For the V-added and Nb-added HCCIs, the volume loss of sample #3 reached the minimum, benefiting from the near-eutectic fine microstructure with the highest hardness. For the Mo-added and B-added HCCI series, after sample #3, the volume losses reached the minimum and became stable, corresponding to elevated and stabilized hardness at higher concentrations of B and Mo, respectively. As demonstrated in figure 8.16, for all the alloys the changes in their volume loss versus the estimated concentration of equivalent carbon is well consistent with changes in their hardness.

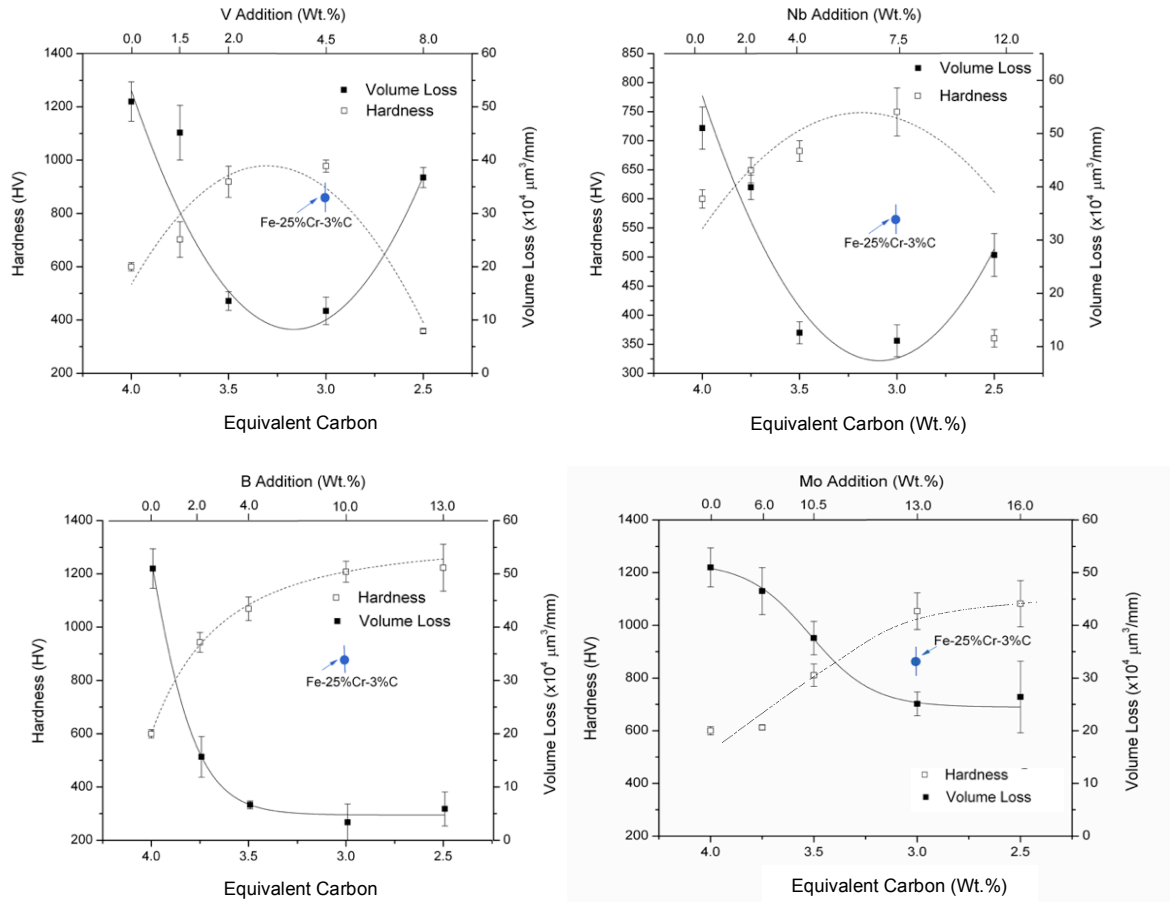


Figure 8.16: Pin-on-disc test results for the modified HCCI alloys under study as a function of the concentration of equivalent carbon, estimated based on the amount of added carbide-forming element.

The added carbide-forming elements eliminated coarse needle-like primary M_7C_3 carbides which deteriorated the fracture toughness and thus the resistance of the material to wear and the ability to withstand mechanical attacks involving impact. These largely benefit the wear resistance of the modified HCCIs. For the B-added HCCIs, the formation of finer equiaxed carbides (figure 8.9, 8.10 and 8.11) and borides without needle-like coarse carbides is also very

favorable for the wear resistance by minimizing the stress concentration when under the wearing force.

It is of importance to note that the reduction of wear damage or volume loss by the addition of carbide-forming elements is significant in all cases, and the B-added series shows the lowest volume loss, followed by the Nb-added series. Compared to a previous study on the wear behavior of Ti-added HCCIs [1], the beneficial effects of V, Nb and B on the wear resistance of HCCI are comparable, but these elements, specially Nb or B which has its carbide's or boride's density close to that of iron, can offer considerable benefits at the foundry consisting of higher compositional homogeneity and easier operation of casting.

One issue that needs to be clarified is the effect of added Mo on the volume loss of the Mo-added series. As shown, the modified HCCI can reach fairly high hardness (up to 1,082 HV), compared to those with added V and Nb, but its volume loss is larger than those of the V-added and Nb-added samples. This could be attributed to the interconnected network of Mo_2C as shown in figure 8.13(A) and 8.14). Such interconnected network of brittle carbides could facilitate crack propagation and thus lower the resistance to wear. For better understanding, worn surfaces of samples in different series having the highest wear resistance were observed and are illustrated in figure 8.17. As shown, micro-cracking

appeared to be more profound on the worn surface of sample Mo3 (figure 8.17(A)).

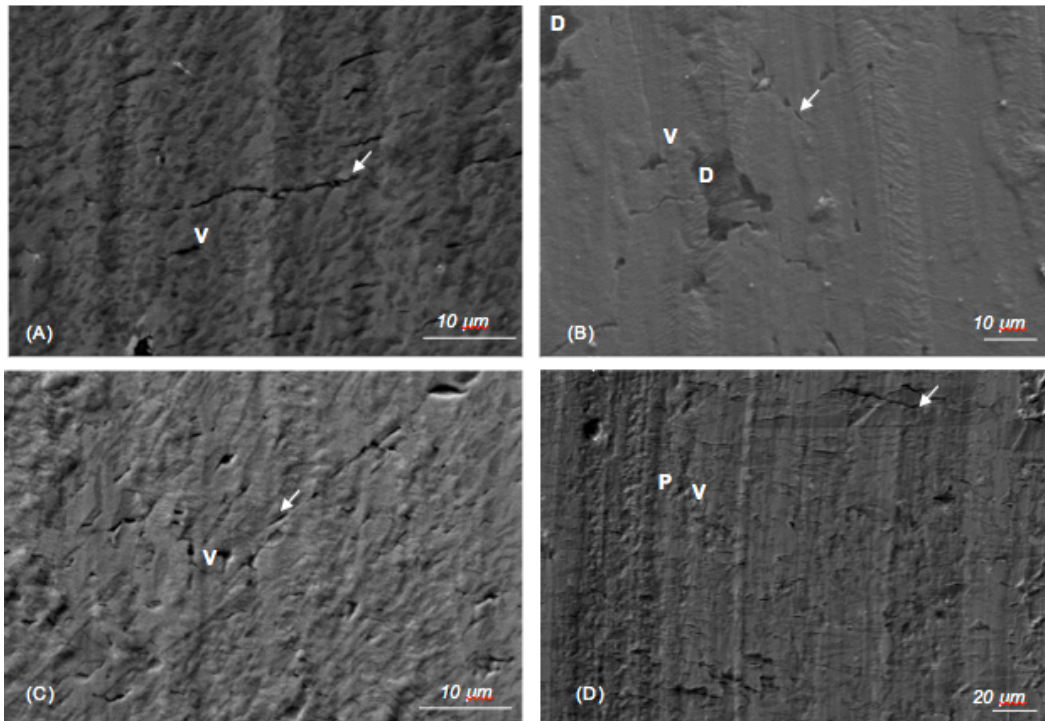


Figure 8.17: Worn surfaces of the modified HCCI samples. (A) Mo-HCCI sample Mo3; (B) B-HCCI sample B4; (C) V-HCCI sample V3; (D) Nb-HCCI sample Nb3. Features are indicated as: micro-cracking (arrow); V (voids), delamination (D), micro-fatigue (F) and plowing (P).

The worn surfaces of the modified HCCIs show general features of worn surface of hard materials without severe plastic deformation. Micro-cracking more or less occurred on the worn surfaces. In addition, wear of the modified HCCIs also involved some of the following processes: formation of voids, delamination and plowing. Figure 8.17(B) shows the worn surface of sample B4.

This hardest sample showed the highest wear resistance and its wear process involved micro-cracking and delamination but less plowing compared to those of others. Wear of relatively soft Nb₃ involved more plowing or plastic deformation (17(D)) but its wear resistance was fairly high. The situation of V₃ was somewhat similar (figure 8.17(C)) and the wear resistances of both Nb₃ and V₃ were higher than that of harder Mo₃, indicating that not only hardness but also toughness are of importance to the wear resistance.

It should be finally mentioned that in the present as-cast condition, the matrix of the HCCIs was mainly austenitic, which happened because the added alloying elements could suppress the formation of pearlite. The ductile ferrous matrix helped accommodate deformation and absorb impact energy, providing toughness that was particularly beneficial to the wear resistance in the situation involving large wearing stresses and especially large impact forces.

8.3 Conclusions

Alloying with appropriate amounts of carbide-forming elements to hypereutectic HCCIs offers an effective mean to improve their wear performance through microstructure refinement and *in situ* formation of fine new carbides.

The modified HCCIs with equivalent carbon to that of a HCCI having its carbon concentration near the eutectic level generally resulted in the highest wear resistance.

Among the four elements under study, B and Nb resulted in the best overall performance under the pin-on-disc testing condition: up to about 15 times lower weight loss, compared to that of the base HCCI, and about 10 times better than a similar HCCI in the eutectic state without being modified by adding the hard carbide-forming elements.

The variations in wear resistance of the alloys with respect to the added carbide-forming elements are mainly caused by the changes in hardness resulting from the introduction of fine carbides and microstructure refinement. The interconnected M-carbide network in the Mo-HCCI series is less beneficial to the performance of the material.

8.4 Bibliography

1. Chung, R.J., et al., *Effects of titanium addition on microstructure and wear resistance of hypereutectic high chromium cast iron Fe-25wt.%Cr-4wt.%C*. *Wear*, 2009. **267**(1-4): p. 356-361.
2. *C-Cr-Fe Ternary Phase Diagrams*. ASM Handbook Online.

3. Wilmes, S., G. Zwick, *Effect of Niobium and Vanadium as an alloying element in tool steels with high chromium content*. Proceeding of the 6th International Tooling Conference, 2002. p.269-287.
4. Radzikowska, J.M., *Metallography and Microstructures of Cast Iron*. ASM Handbooks: Metallography and Microstructures, ASM International, 2004. p. 565-587.
5. Schick, H.L., *Thermodynamics of Certain Refractory Compounds*. Academic Press, 1966.
6. Tomovic-Petrovic, S.M., S.V. Markovic, S. Zec, *The effect of boron on the amount and type of carbides in chromium white irons*. J.Serb.Chem.Soc. 67, 2002.**10**: p.667-707.
7. Breyer, J.P., G. Walmag. *Metallurgy of High Chromium-Molybdenum White Iron and Steel Rolls*. Section I – Chapter III.

9 OVERALL CONCLUSIONS AND POSSIBLE FURTHER RESEARCH TOPICS

This chapter summarizes the general wear behavior of the expanded system of HCCIs under investigation and developed methods for microstructural refinement and reinforcement using carbide forming elements. Further possible research topics are also discussed.

9.1 Conclusions

- Depending on concentrations of C and Cr and casting conditions, various microstructural configurations can be obtained for HCCIs. Heat treatments can be used to further tailor the ferrous matrix phase(s) and precipitation of secondary carbides, but their effects on primary carbides are negligible. In this study, martensite, austenite, and ferrite were observed in the ferrous matrix, and three types of carbide were identified in the HCCIs: M_3C , $M_{23}C_6$, and M_7C_3 .
- The wear performance under both dry abrasion and slurry erosion was greatly improved as carbon concentration increases. In general, HCCIs with the best performance feature nominal carbon content in a range of 3 ~ 4 wt.% C. Above this range, there was plateau where further increments either resulted in small improvements or deteriorated the material, which was more obvious at higher chromium concentrations (> 30wt.%).

- The volume fraction of carbides increases linearly with carbon and chromium concentrations. However, the increase is faster with carbon content. Increasing the volume fraction of carbides was found effective to enhance the wear resistance until approximately 50-60%. The partition coefficient of Cr, bulk hardness, and carbide microhardness are also increased as the carbon content was raised.
- It was determined that the tempered martensitic matrix performed better under slurry erosion than a ferritic matrix. This is particularly a dominant factor for hypoeutectic HCCIs. However, under dry abrasion testing there was no clear correlation between the matrix phase and wear resistance, instead, the carbide volume content dominates the abrasion resistance.
- Results of slurry erosion tests at low velocities reveal the sensitivity of HCCIs to localized corrosion and therefore the synergy between corrosion and erosion due to longer exposure of the target surface to the slurry medium.
- Alloying hypereutectic HCCIs with appropriate amounts of carbide-forming elements has been demonstrated to be an effective means to improve their wear performance through microstructure refinement and *in situ* formation of fine new hard carbides. Lab results have shown up to

about 15 times improved wear performance, which can potentially lead to a step change in service life.

9.2 Further research topics

- In chapter 3, it was shown that the ferrous matrix affects the wear performance, even at hypereutectic compositions where the carbide volume fraction is dominant. This was more evident under slurry erosion testing than abrasion due to the involvement of corrosion which mainly attacks the ferrous matrix. In studies of wear resistance of steel microstructure, it has been found that bainite can achieve almost the same wear resistance as that of martensite despite its lower hardness. For HCCIs, this could be very beneficial to the resistance to wear involving impact, which requires not only hardness but also toughness. However, there is only limited work on this topic.
- Among all the HCCIs, at the highest chromium content, 45 wt.% Cr, the best abrasion performance was obtained in a microstructure containing core-shell structured carbides, which have a $M_{23}C_6$ shell and a M_7C_3 core. During wear and erosion tests, the HCCI with the core-shell structured carbides showed the highest wear resistance among the 45-series. It is worth investigating the influence of the core-shell structured carbides on the wear behavior under different wearing conditions. $M_{23}C_6$ is generally softer and tougher than M_7C_3 carbides. Therefore, the resultant gradual

transition in hardness from the ductile ferrous matrix to the hard and brittle M_7C_3 core may help reduce failure or cracking at the interface between carbide and the matrix.

- It has been observed that the matrix/carbide interface was a preferential zone for localized corrosion. The pitting occurring in the matrix of hypereutectic samples has been attributed to the micro-galvanic effect of secondary carbides in the matrix and also chromium depletion. Understanding in detail this phenomenon can be beneficial to find a balance between wear and corrosion, depending on the intended application. Conductive AFM with an electrochemical cell could be a useful tool to study local corrosion processes, which trigger the overall corrosion.
- The effect of the hard carbide forming elements added in such manner to produce very fine and reinforced near eutectic microstructures has shown excellent performance during lab tests. It is worth continuing this study and including more elements that could lead to similar microstructural refinement effects with new carbide specie(s) having good tribological characteristics. Recommended additions are: Zr, Ce, Ta, and W. High atomic weight brings a challenge in both cast products and hard facing, which needs to be considered as the higher carbide densities limits a uniform distribution in the melt.

- The best-modified microstructures have resulted in significant improvement in the wear resistance, which can be 15 times better than the unmodified base alloy during sliding wear. Next step in this research should include development of effective processes to produce these alloys in larger size in order to test them under abrasion and slurry erosion conditions that are closer to real wear conditions.
- An alternative approach to produce a desired microstructure is to directly add reinforcing carbides to a eutectic or slightly hypereutectic HCCIs, which leads to the formation of HCCI-matrix composites. This is worth investigating, since such an approach makes microstructural manipulation easier or more controllable, e.g., the morphology of carbides. However, it is not clear whether there would be a difference in wear performance between HCCIs respectively with in-situ formed and externally added carbides.
- As discussed in chapter 3, the wear response of HCCI depends on the tribological system characteristics. It would be of interest to perform abrasion and erosion tests with different silica particle distributions. For instance, smaller particles may better reveal the effect of oil sand “fines” (particles $<44\ \mu\text{m}$) on the wear damage. Such studies can help evaluate the optimum mean free path or carbide spacing, and its impact compared with

other factors, for producing appropriate microstructures to resist wear attacked by abrasives having different size distribution.